

Thermal microsensors for *in vitro* and *in vivo* monitoring of chemical and biological processes

THÈSE N° 7017 (2016)

PRÉSENTÉE LE 10 JUIN 2016

À LA FACULTÉ DES SCIENCES ET TECHNIQUES DE L'INGÉNIEUR
LABORATOIRE DE MICROSYSTÈMES 2
PROGRAMME DOCTORAL EN MICROSYSTÈMES ET MICROÉLECTRONIQUE

ÉCOLE POLYTECHNIQUE FÉDÉRALE DE LAUSANNE

POUR L'OBTENTION DU GRADE DE DOCTEUR ÈS SCIENCES

PAR

Rima PADOVANI

acceptée sur proposition du jury:

Prof. C. Guiducci, présidente du jury
Prof. M. Gijs, Dr T. Lehnert, directeurs de thèse
Prof. J. Lammertyn, rapporteur
Prof. M. J. Vellekoop, rapporteur
Dr S. Carrara, rapporteur



ÉCOLE POLYTECHNIQUE
FÉDÉRALE DE LAUSANNE

Suisse
2016

Acknowledgements

It is with great pleasure that I express my sincere gratitude to all the people that have contributed to this important personal and professional achievement, thanks to their advice and encouragement. First and foremost, I am deeply thankful to my advisor Professor Martin Gijs for giving me the opportunity to conduct research in the Laboratory of Microsystems LMIS2, and for supporting me during these intense years. Professor Gijs has always been available for questions, especially during the difficult times of the doctoral studies, he provided extremely helpful guidance and he valorized my achievements, often more than I would have done. I would also like to thank my co-advisor Dr. Thomas Lehnert, for his helpfulness from the very initial phase of the project definition to the final redaction of the thesis.

I am grateful to Prof. Michael Vellekoop, Prof. Jeroen Lammertyn, Dr. Sandro Carrara and Prof. Carlotta Guiducci for accepting to be the jury members of my thesis. I am very thankful for the time taken to evaluate my work, for the scientifically stimulating discussion, and for their fruitful feedbacks.

I would also like to acknowledge the financial support of my research by the EU Ideas program (ERC-2012-AdG-320404). I sincerely thank Professor Johan Auwerx, Dr. Philippe Cettour-Rose and Dr. Raphaël Doenlen for their collaboration and helpful meetings for the project on *in vivo* temperature sensing. Indeed, I would also like to thank Arnaud Bichat, who carried out the surgical procedures and the cold tests and was always available to solve technical issues. I am also greatly thankful to Moullan Norman, who spent much time with me, especially at the beginning of my doctoral studies, for his experience on cell culture and for helping me understanding the stringent requirements of working with living organisms.

I take this opportunity to thank all my colleagues at LMIS2 for their suggestions and advice, and special thanks go to Dr. Raphaël Trouillon, who has always been very helpful, being available for solving practical issues and having an answer for also more theoretical questions. Thanks to my former office-mates Hamideh, Cumhur, Deborah and to the latest office-mates Raphaël and Cristina for the nice chats and friendly atmosphere. I cannot forget to thank two special colleagues, Diego and Matteo, as we have started the doctoral experience in the same year and we passed together the critical turning point, from being the young doctorate students to being the more "experienced" ones. Thanks to the former and present members of the LMIS2&4 "lunch group", in particular Pierre, Fabien, Stefano, Oscar, Amélie, Guillaume, Elodie, Niccolò, Jagoda, Sophie, Josias, Roger, Baris, Gergely, Li, Axel... Thanks to Melis Martin, Lucie Auberson and Marie Halm for their precious help in all administrative aspects. I would also like to thank the EPFL staff of the *Atelier de l'Institut de*

microtechnique (ATPR) and of the *Atelier de fabrication de circuits imprimés* (ACI) for their contribution on the fabrication of the mechanical parts of the experimental setups, and for assistance in temperature sensor preparation, respectively.

Last but not least I would like to thank all my friends in Lausanne for all the nice and funny moments we had together and for their encouragement to overcome the difficult times during these last years. In particular, a special thanks goes to Chiara and Fede, my super-social and super-active friends, to Sara, my personal doctor and friend, to Marina and Giovanni, my always-reliable friends, to Diego and Giovanna, my motivating and attentive friends, to Cristina, my best office-mate ever and friend, to Matteo and Bea, undoubtedly my artistic friends, to Silvia and Marco, my too-sporty friends, to Valentina and Raffaele, to Silvia and Giuseppe, to Marzia and Fabio, to Faiza, my Arabic language teacher and Algerian friend.

Finally, my deepest and most emotional thanks go to my family. I am extremely grateful to my mum and dad, Zabida and Patrizio, for having always supported me, for having always believed on me, sometimes too much, thinking as if I am the genius in the family... and, more seriously, for having taught me to be responsible, to care about the people and to appreciate the important things of life. I am indescribably thankful to my sister Leila and her boyfriend Vito, together with my husband, they are the reference points in my life. Leila and Vito have always been there for me, their love and unconditional support meant and means so much to me. I thank my “little sister” Leila also for always finding the right moments to remind me to take a break from the stress, to take sometimes things less seriously and to enjoy the little things. And really finally, I am infinitely grateful to my husband, Aldo. During our thirteen years together, you managed to support me during all my academic studies, from my very first day at the university. None of this would have been possible without your unconditional love, your support, your patience and your determination. You taught me how to overcome my uncertainties, how to let sometimes things go and be “a bit less” rational, and how to believe more on me. Thanks Aldo, for being a caring husband, the most reliable friend and my personal life coach. Even though I keep the academic title of *PhD* for me, this thesis is dedicated to you.

Rima Padovani
Lausanne, May 11th 2016

Abstract

Metabolism is a highly coordinated biochemical cellular activity indispensable for sustaining life, and is often related to mitochondrial functioning. Innovative technological approaches allowing the study of the thermal signature of chemical and metabolic processes are presented in this thesis. In particular, two solutions are proposed: (i) a nanocalorimetric platform enabling measurements of biochemical heat production *in vitro*, and (ii) a method for localized *in vivo* temperature measurements in mice using implantable miniaturized sensors.

First, the design and development of the nanocalorimetric platform is presented. In particular, this platform is built around a commercial thermopile-based sensor chip, on which an open-well reservoir holding a sample with a volume of a few tens of microliter is directly positioned. Both components are embedded into an isothermal housing providing an excellent temperature stability (± 1 mK), which is a prerequisite for accurate heat power measurements. Furthermore, the platform is characterized by a fast thermalization time to the target temperature (less than 30 minutes) and a fast sensing response time (a few seconds). Numerical simulations, which allowed the optimization of the platform design, are also reported. Electrical calibration of the platform was carried out using resistive heaters positioned either on the sensor chip or in the sample reservoir. A heat power limit of detection of 70 nW was estimated. Then, two reactions for the validation of the nanocalorimetric platform were investigated: (i) the mixing of 1-propanol in water, and (ii) the oxidation of glucose catalyzed by glucose oxidase. The results showed good agreement with literature, confirming that our versatile platform may be applied to many thermochemical studies, including thermodynamic analysis and kinetic reaction analysis.

Furthermore, localized *in vivo* temperature measurements in mice by means of implantable miniaturized sensors are presented. The aim was to monitor mouse metabolism during cold exposure, and to record possible temperature differences between the body temperature measured in the abdomen and the temperature of the brown adipose tissue (BAT) situated in the interscapular area. This approach is of biological interest as it may help unravelling the question whether biochemical activation of BAT is associated with local increase in metabolic heat production. Specifically, the preparation and calibration of miniaturized thermistor sensors are reported and the surgical procedure is also described. Temperature measurements, carried out on mice during cold exposure (6 °C) for a maximum duration of 6 hours, are presented and analyzed. Control measurements with a conventional probe confirmed the good performance of the implanted sensors. Moreover, analysis of the experimental results allowed the identification of two different mouse phenotypes, distinguishable in terms of their metabolic resistance to cold exposure. This difference was investigated from the thermal point of view by computational simulations. A simple physical model of the mouse body

allowed to reproduce the global evolution of hypothermia and to explain qualitatively the temperature difference between abdomen and BAT locations. While with this approach, we have demonstrated the importance and feasibility of localized temperature measurements on mice, further optimization of this technique is foreseen to better identify local metabolism variations.

Keywords

Metabolic heat; Nanocalorimetry; Thermopile; Heat of mixing; Reaction enthalpy; Glucose oxidation; Enzyme kinetics; Brown adipose tissue; Miniaturized temperature sensor; Implantable temperature sensor; *In vivo* localized sensing; Thermistor calibration; Mouse cold exposure.

Résumé

Le métabolisme est une activité biochimique cellulaire hautement coordonnée et indispensable aux êtres vivants dont les mécanismes sont intimement liés au système mitochondrial. Cette thèse présente des approches technologiques innovantes permettant d'étudier la signature thermique de processus chimiques et métaboliques. En particulier, deux méthodes sont décrites: (i) une plate-forme nanocalorimétrique pour quantifier la production biochimique de chaleur *in vitro*, et (ii) des capteurs miniatures implantables pour des mesures locales de température *in vivo* chez la souris.

Premièrement, la conception et le développement de la plate-forme nanocalorimétrique sont décrits. Cette plate-forme est construite autour d'un capteur à thermopile sur lequel est monté un réservoir pouvant contenir un échantillon d'un volume de quelques dizaines de microlitres. Les deux composants sont intégrés dans un boîtier isotherme stabilisant la température (± 1 mK), une condition nécessaire pour une mesure précise de la puissance thermique. En outre, ce système offre un temps de thermalisation à la température cible court (moins de 30 minutes) et un temps de réponse rapide (quelques secondes). Des simulations numériques ont également été réalisées pour optimiser la conception du système. La plate-forme a été étalonnée à l'aide d'éléments chauffants résistifs disposés soit sur le capteur soit dans le réservoir. La limite de détection a été estimée à 70 nW. Deux méthodes de validation de la plate-forme nanocalorimétrique ont ensuite été utilisées: (i) le mélange de 1-propanol dans l'eau, et (ii) l'oxydation du glucose catalysée par la glucose oxydase. Les résultats obtenus sont en accord avec la littérature, établissant ainsi que cette plate-forme polyvalente peut être appliquée à diverses études thermochimiques, y compris thermodynamiques et cinétiques.

Deuxièmement, des capteurs miniatures implantables sont utilisés pour mesurer localement et *in vivo* la température chez la souris. L'objectif est ici d'étudier le métabolisme de la souris lors de l'exposition au froid et d'enregistrer d'éventuelles différences de température entre la température du corps, mesurée dans l'abdomen, et la température du tissu adipeux brun (TAB) situé dans la zone interscapulaire, pour déterminer si l'activation biochimique du TAB est associée à une augmentation locale de la production métabolique de chaleur. Plus précisément, la préparation et l'étalonnage des capteurs miniatures à thermistance sont détaillés et l'intervention chirurgicale est également décrite. Des mesures de température, effectuées sur des souris exposées au froid (6 °C) pendant une durée maximale de 6 heures, sont présentées et analysées. Les mesures de contrôle réalisées avec une sonde classique ont confirmé la bonne performance des capteurs implantés. Par ailleurs, l'analyse des résultats expérimentaux a permis d'identifier deux phénotypes différents de souris se distinguant par leur résistance métabolique à l'exposition au froid. Cette différence a été étudiée thermiquement par des simulations. Un modèle physique simple du corps de la souris a permis de

modéliser l'évolution générale de l'hypothermie et d'expliquer qualitativement la différence de température entre l'abdomen et le TAB. L'importance et la faisabilité des mesures locales de température sur la souris sont ainsi démontrées. Cette technique doit maintenant être optimisée pour mieux identifier les variations du métabolisme local.

Mots-clés

Chaleur métabolique; Nanocalorimétrie; Thermopile; Chaleur de mélange; Enthalpie de réaction; Oxydation du glucose; Cinétique enzymatique; Tissu adipeux brun; Capteur de température miniature; Capteur de température implantable; Détection locale *in vivo*; Etalonnage de thermistance; Exposition au froid de souris.

Sommario

Il metabolismo è una attività biochimica cellulare altamente coordinata e indispensabile per gli essere viventi, i cui meccanismi sono strettamente collegati al funzionamento mitocondriale. Questa tesi presenta approcci tecnologici innovativi che permettono lo studio del profilo termico di processi chimici e metabolici. In particolare, sono proposti due metodi differenti: (i) una piattaforma nanocalorimetrica per misurare la produzione di calore biochimico *in vitro*, e (ii) sensori miniaturizzati impiantabili per monitorare in maniera localizzata la temperatura *in vivo* su topi.

In primo luogo, presentiamo la progettazione e lo sviluppo della piattaforma nanocalorimetrica. Questa piattaforma è realizzata attorno ad una termopila *on chip* commerciale, sulla quale è posizionato un contenitore aperto per tenere in posizione un campione di qualche decina di microlitro. Entrambi i componenti sono inseriti all'interno di una scatola isoterma che garantisce una elevata stabilità termica (± 1 mK), prerequisito essenziale per misure accurate di potenza termica. Inoltre, la piattaforma è caratterizzata sia da un breve tempo di termalizzazione per raggiungere la temperatura di interesse (meno di 30 minuti), sia da un breve tempo di risposta (alcuni secondi). Sono inoltre presentate le simulazioni numeriche, che hanno permesso l'ottimizzazione della progettazione della piattaforma. La calibrazione elettrica della piattaforma è stata effettuata utilizzando microriscaldatori elettrici posizionati o sul *chip* del sensore o nel contenitore aperto in cui è presente il campione. In particolare, è stato misurato un limite di detezione di 70 nW. Due diverse reazioni chimiche sono state studiate per validare sperimentalmente la piattaforma: (i) la miscelazione di 1-propanolo in acqua, e (ii) l'ossidazione del glucosio catalizzata dall'enzima glucosio ossidasi. I risultati ottenuti sono in accordo con la letteratura, confermando l'applicabilità di questa piattaforma versatile a diversi studi termochimici, come l'analisi termodinamica e cinetica di reazione.

In secondo luogo, presentiamo misure di temperatura localizzate *in vivo* su topi utilizzando sensori miniaturizzati impiantabili. Lo scopo di questo studio è stato il monitoraggio del metabolismo del topo durante l'esposizione al freddo, e la registrazione di eventuali differenze tra la temperatura corporea misurata nell'addome e la temperatura del tessuto adiposo bruno (TAB) situato nella regione interscapolare. Questo approccio è di particolare interesse biologico in quanto potrebbe aiutare a comprendere se l'attivazione biochimica del TAB è associata ad un locale aumento della produzione di calore metabolico del tessuto stesso. In particolare, riportiamo sia la preparazione e la calibrazione dei sensori miniaturizzati (termistori), sia la procedura chirurgica utilizzata per l'impianto. Sono quindi presentate e analizzate le misure di temperatura effettuate su topi durante l'esposizione al freddo (6 °C) per una durata massima di 6 ore. Misure di controllo effettuate con un sensore di temperatura convenzionale hanno confermato il buon funzionamento dei sensori impiantati. Inoltre, l'analisi dei risultati sperimentali ha permesso l'identificazione di due diversi

fenotipi nel topo, distinguibili in termini di resistenza metabolica durante l'esposizione al freddo. Questa differenza è stata valutata dal punto di vista termico mediante simulazioni computazionali. Un modello fisico semplificato del corpo del topo ha permesso di riprodurre l'evoluzione globale della temperatura tendente all'ipotermia e di spiegare qualitativamente la differenza di temperatura tra le misure nell'addome e nel TAB. Nonostante si sia dimostrata l'importanza e l'applicabilità della misurazione di temperatura localizzata su topi, si prevede la necessità di un'ulteriore ottimizzazione di questa tecnica per potere meglio identificare le variazioni locali del metabolismo.

Parole chiave

Carole metabolico; Nanocalorimetria; Termopila; Calore di miscela; Entalpia di reazione; Ossidazione del glucosio; Cinetica enzimatica; Tessuto adiposo bruno; Sensore di temperatura miniaturizzato; Sensore di temperatura impiantabile; Sensing localizzato *in vivo*; Calibrazione di termistori; Test di esposizione al freddo su topi.

Contents

Acknowledgements	iii
Abstract	v
Keywords	vi
Résumé	vii
Mots-clés	viii
Sommario	ix
Parole chiave	x
Contents	xi
List of Figures	xv
List of Tables	xxii
List of Equations	xxv
Chapter 1 Introduction	1
Chapter 2 Metabolic studies: biological context and current techniques	5
2.1 Cellular respiration	6
2.1.1 Mitochondria, the cells' power plants	7
2.1.2 The electron transport chain and oxidative phosphorylation	8
2.1.3 Uncoupled respiration	9
2.2 Conventional techniques for <i>in vitro</i> metabolic studies	10
2.2.1 Metabolic oxygen and acidification rate measurements	10
2.2.2 Metabolic heat measurements	12
2.3 The thermogenic function of the brown adipose tissue (BAT)	12
2.3.1 Brown adipose tissue physiology and function	12
2.3.2 Active brown adipose tissue in humans and its clinical implications	13
2.3.3 Importance of the animal model for understanding thermogenesis	14
2.4 Conventional techniques for <i>in vivo</i> metabolic studies	14
2.4.1 The resting metabolic rate	14
2.4.2 Body temperature measurements	15
2.4.3 Localized temperature measurements	15
Chapter 3 Microcalorimetry for biological applications	17
3.1 Classification of calorimeters and historical excursus	18
3.1.1 Lavoisier ice-calorimeter	19
3.1.2 Nernst/Eucken calorimeter	20

Contents

3.1.3	Tian calorimeter	20
3.1.4	Calvet calorimeter	20
3.2	Modern isothermal microcalorimetry	22
3.2.1	Commercial isothermal microcalorimeters	22
3.2.2	Advantages and drawbacks	23
3.3	Applications of isothermal microcalorimetry in biology	24
3.3.1	Cell biology and toxicology	25
3.3.2	Microbiology and antibiotic testing	27
3.3.3	Multicellular organisms	30
3.3.4	Other fields of application	31
Chapter 4	Nanocalorimetry: an emerging technique for metabolic studies	33
4.1	General aspects of miniaturized calorimeters	34
4.2	State-of-the-art of miniaturized calorimeters	35
4.2.1	Thermopile-based nanocalorimeters with open chambers	35
4.2.2	Nanocalorimeters with microfluidics for μl sample volumes	38
4.2.3	Nanocalorimeters with microfluidics for nL sample volumes	41
4.2.4	Microfluidic nanocalorimeters for differential measurements	43
4.2.5	Differential enthalpy arrays with thermistor sensors	45
4.2.6	Nanocalorimeter with paper-based microfluidics	47
4.3	Commercially available nanocalorimeters	47
Chapter 5	Development of the new calorimetric platform	51
5.1	General system requirements for biological nanocalorimetric sensing	52
5.1.1	Nanocalorimeter sensitivity	52
5.1.2	Temperature stability and thermal gradients	53
5.1.3	Thermal time constants of the system	53
5.2	Governing physical equations for heat transfer phenomena	54
5.2.1	Heat transfer by conduction	54
5.2.2	Heat transfer by convection	55
5.2.3	Heat transfer by radiation	56
5.3	Theoretical background for thermopile-based heat flow calorimetry	57
5.3.1	Thermopile sensing principle	57
5.3.2	Working principle of heat flow calorimetry	59
5.3.3	Signal-to-noise ratios for different configurations	60
5.4	Design and assembly of the nanocalorimetric platform	62
5.4.1	Main components of the platform	62
5.4.2	Specifications of the sensor chip	64
5.4.3	Sample reservoir and injection system	65

Contents

5.5	Computational modeling of the nanocalorimetric platform	66
5.5.1	Model definition.....	66
5.5.2	Effect of the external heat source.....	68
5.5.3	Effect of heat generated by the sample	69
5.5.4	Estimation of the thermal time constants.....	70
5.6	The isothermal holder and temperature control system	71
5.6.1	Design and functions of the isothermal holder	71
5.6.2	Temperature control based on PID algorithm.....	73
5.6.3	Integration of the PID control system in the isothermal holder	75
5.6.4	Platform automation and data acquisition	76
Chapter 6	Characterization and validation of the nanocalorimetric platform	79
6.1	Characterization of the platform stability.....	80
6.1.1	Platform thermalization and temperature stability	80
6.1.2	Thermopile signal stability	81
6.2	Electrical calibration and limit of detection.....	83
6.3	Sensing time constant	87
6.4	Quantification of the enthalpy of mixing of 1-propanol in water.....	88
6.4.1	Mixing of 1-propanol in water.....	88
6.4.2	Experimental configuration: single vs sequential injection	89
6.4.3	Evaluation of injection artefacts	89
6.4.4	Detection of mixing of 1-propanol in water	91
6.4.5	Processing of the experimental data for chemical calibration	92
6.5	Enzymatic study of glucose oxidation by glucose oxidase	94
6.5.1	The reaction mechanism of glucose oxidation.....	94
6.5.2	Experimental protocol.....	95
6.5.3	Detection of oxidation of glucose catalyzed by GOx.....	95
6.5.4	Data analysis based on the Michaelis-Menten model	97
6.6	Preliminary metabolic experiments on <i>C. elegans</i> nematodes.....	100
6.6.1	Preparation of the <i>C. elegans</i> nematode suspension.....	100
6.6.2	Experimental configuration.....	101
6.6.3	Preliminary heat power measurements on worms.....	102
6.7	Concluding remarks	103
Chapter 7	Localized temperature measurements during cold exposure for <i>in vivo</i> metabolic studies	107
7.1	Setup for <i>in vivo</i> measurements and sensor preparation.....	108
7.2	Sensor calibration	110
7.3	Animal model: from surgery to cold test	112
7.3.1	Animals.....	112

Contents

7.3.2	Surgical procedure and sensor implant.....	112
7.3.3	Cold test protocol.....	113
7.4	Experimental results during cold exposure	113
7.5	Computational heat transfer modeling	115
7.5.1	Model definition.....	115
7.5.2	Simulating the thermal behavior of mouse phenotype 1	116
7.5.3	Simulating the thermal behavior of mouse phenotype 2	117
7.5.4	Concluding remarks on phenotype difference and BAT activity	117
Chapter 8	Conclusion and Outlook	119
8.1	Results overview and discussion.....	119
8.1.1	Specifications of the nanocalorimetric platform.....	119
8.1.2	<i>In vivo</i> localized temperature sensing in mice	120
8.2	Future opportunities.....	121
8.2.1	Microfluidic integration and new applications of the nanocalorimetric platform	121
8.2.2	Improvements and applications of <i>in vivo</i> localized temperature sensing	122
Appendix A	125
Appendix B	129
References	133
Curriculum Vitae	149

List of Figures

Figure 1 Schematic view of the biochemical pathways involved in cellular respiration. a) Simplified view of catabolic pathways, including nutrient oxidation to acetyl-CoA, further oxidation through the citric acid cycle (Krebs cycle), and finally the electron transport chain coupled to oxidative phosphorylation. Red lines indicate electron paths. b) Typical morphology of a mitochondrion, showing the matrix, the inner membrane, the intermembrane space and the outer membrane. Cristae are also visible, where ATP synthase, also named *complex V*, of the electron transport chain, is located (*image reproduced from [16]*). c) Close-up view on the electron transport chain, identifying the five protein complexes (indicated in red from I to V) involved and proton leaks.7

Figure 2 Bioenergetic studies based on the Extracellular Flux Analyzer by *Seahorse Bioscience*. a) Cross-sectional view of a single well at the bottom, on which cells are plated. The sensor sleeves are visible as well as the two embedded fluorophores (red and white spots), for oxygen and hydrogen ion sensing. Two injection ports allow reagent injections. Upward and downward positions are illustrated. b) Typical protocol and involved compounds for the measurement of bioenergetic parameters via the oxygen consumption rate (OCR). c) Schematics of the electron transport chain, highlighting the sites where the inhibition by the specific compounds, such as oligomycin, rotenone and antimycin A, takes place.11

Figure 3 BAT morphology and location in adult humans. a) Morphological comparison between brown adipocytes and white adipocytes, showing the difference in fat droplet distribution and in mitochondria availability. This difference corresponds also to a functional difference, as the white adipocytes store excess energy, whereas the brown adipocytes dissipate energy to produce heat (*image reproduced from [42]*). b) Computed Tomography (CT) image and overlaid image of CT scan and of Positron Emission Tomography using fluoro-deoxy-glucose (FDG-PET) scan on a patient with endometrial carcinoma. Images were taken on the transverse plane passing through the left and right supraclavicular regions. The white arrows point to the location where unexpected FDG uptake was observed (*image reproduced from [43]*). c) CT/FDG-PET scan comparing FDG uptake on a healthy subject between summer and winter season. During winter season more locations where active BAT are observed (*image reproduced from [39]*).....13

Figure 4 Telemetric temperature sensor by *BMDS* (*images reproduced from [66]*). a) Photograph of a miniature capsule-like sensor (IPTT-300, *BMDS*). b) Sketch showing how this type of sensor is inserted in vivo in a mouse, using a needle loaded with the sensor.15

Figure 5 Schematic views of a) Lavoisier ice-calorimeter and b) the Nernst/Eucken calorimeter in which the suspended sample is heated by means of a platinum wire serving also as a resistance thermometer (*images reproduced from [34]*).....19

Figure 6 Working principle of the Tian calorimeter and of the Calvet calorimeter. a) Tian calorimeter, based on two independent thermoelectric elements, one using the Peltier effect for heat compensation and one using the Seebeck effect for heat measurement, respectively. b) Calvet calorimeter, showing only one unit: a single thermopile located around the sample vessel measures the sample heat flow (*both images reproduced from [34]*). c) Calvet calorimeter used in a twin configuration with a sample and a reference vessel (*image adapted from [81]*).....21

Figure 7 Isothermal microcalorimeter developed by *TA Instruments*. a) Photograph of the model TAM IV, and close up view of the insertion points of the four different calorimetric units. Thanks to the modular approach, each calorimetric unit may hold different sample volumes depending on the application, and independent parallel measurements are possible. b) Drawing of a single calorimetric unit (the “nanocalorimeter” unit) with two access tubes for the 1 ml sample ampoule (visible in the drawing), and the reference ampoule (hidden on the backside) (*images reproduced from [72]*).....22

Figure 8 Metabolic heat production rate as a function of mass, covering 27 orders of magnitude, starting from the smallest size respiratory complexes through a single mitochondrion and a single cell *in vitro*, up to whole mammals. a) The metabolic power of respiratory complexes, mitochondrion and an isolated mammalian cell follows the power scaling law ($B_0 \cdot M^{3/4}$ where M is the corresponding mass and B_0 is a normalization coefficient; red solid line). Considering mammals, for a body mass $M > \mu$, where μ is the mass of the smallest

mammal (*i.e.* the shrew), the metabolic power of whole mammals follows similarly the same power scaling law (blue solid line). b) Assuming the mass of a single cell M_c to be $3 \cdot 10^{-9}$ g, the calculated metabolic power per cell in mammals *in vivo* decreases as a function of the body mass of the animal, following a $M^{-1/4}$ trend (blue solid line). Instead, the metabolic power per cell of cells isolated from different mammals and cultured *in vitro* is independent from the mass of the animal of origin (red line) (*image adapted and reproduced from [98]*).26

Figure 9 Heat power measurements on mammalian cells over several days. a) Heat production rate by lymphocytes due to an allergic response when stimulated at time $t = 0$ with increasing concentration of phytohemagglutinin (PHA) (initial amount of cells 2.5×10^5) (*image reproduced from [73]*, which was modified from [99]). b) Heat power rate of virus-infected BHK-21 cells at time $t = 0$ at 37 °C: (a) FMDV-infected without interferon; (b, c, d) FMDV-infected with increasing concentration of interferon at 0.2, 0.5, 1.0 µg/ml, respectively; (e) uninfected with 1.0 µg/ml of interferon; (f) uninfected without interferon (*image reproduced from [100]*).26

Figure 10 Heat power measurements on *E. coli* (DSM 10142) in M9 medium containing glucose and lactose. Heat production initially increases due to exponential bacterial growth (\approx from hour 5 to 10), and eventually declines (\approx from hour 15) due to a lack of resources in the closed calorimeter ampoule. Three individual peaks, corresponding to glucose respiration, glucose fermentation and lactose fermentation, were obtained by deconvolution, based on the model by Monod (1949) [103] (*image reproduced from [11]*).27

Figure 11 Heat power measurements on platelet suspensions inoculated with increasing concentrations of bacteria, ranging from 1 to 10^5 CFU per ml of platelets. Calorimetric measurements on *E. coli* a), on *S. aureus* b) and on *P. acne* c) are shown, respectively. The heat flow measured in all curves initially increases, corresponding to the exponential bacterial growth, and, for increasing concentration of bacteria, the heat flow peak is reached earlier in time. Then, the heat flow decreases as bacterial growth declines. In particular, the shape of the curves appears to be a characteristic for each bacterial species (*image reproduced from [105]*).28

Figure 12 Heat power measurements for *E. coli* (ATCC25922) incubated at 37 °C, when exposed to increasing concentrations of Cefazolin or Cefoxitin, respectively. For Cefazolin, the minimal inhibitor concentration (MIC) is 2 mg/l (red line), as it is the lowest concentration for which no heat flow increase is observed, corresponding to no bacterial growth. For subinhibitory concentrations (in this case from 0 to 1 mg/l), bacterial growth occurs and is not affected by the exposure to the antibiotic. In particular, no significant difference in the shape of the curve is observed: for example, the time delay (t_1) to reach a detectable heat flow signal is the same, as well as the initial maximum peak, corresponding to initial exponential bacterial growth. For Cefoxitin, instead, the MIC is 8 mg/l and significant differences are observed between heat flow curves of *E. coli* exposed to subinhibitory concentrations of antibiotic (from 0 to 4 mg/l). In particular, for concentrations lower than 1 mg/l, the heat flow curve and, thus, the bacterial growth, is not affected by the exposure to the antibiotic. For higher subinhibitory concentrations (2 and 4 mg/l), the initial maximum peak is significantly smaller. Moreover, for a concentration of 4 mg/l (red line) the time delay to reach a detectable heat flow signal shifts from t_2 (the time delay observed when bacterial growth is unaffected) to t_3 . Thus, starting from a concentration of 2 mg/l, Cefoxitin has an effect on bacterial growth, but only for 8 mg/l it completely inhibits the growth (*image adapted from [106]*).29

Figure 13 Heat power measurements on a) *S. aureus* ATCC 25923 (MSSA, methicillin-susceptible), exposed to different concentrations of antibiotics, and on b) *S. aureus* ATCC 43300 (MRSA, methicillin-resistant), exposed to the same concentrations of antibiotics. In the first case, heat flow curves indicate bacterial activity only when bacteria are not exposed to the drug: in particular, the initial heat flow increase corresponds to the bacterial exponential growth. In the latter case, heat flow curves are observed even after exposure of the bacteria to sufficiently high concentrations of antibiotics. The observable effect of the antibiotic is a reduction of the heat flow peak, thus indicating a reduction in the bacterial activity. The blank is uninoculated bacteria medium (*image reproduced from [107]*).29

Figure 14 Heat power measurements on *C. elegans* nematodes. a) Measurements on a suspension of about 3000 13-day-old worms at 25 °C, in presence (full line) or absence (dotted line) of antibiotics (0.25 mg/ml streptomycin, 250 U penicillin). The increase in heat power is due to bacterial growth. b) Comparison of heat

output of worms suspended in liquid culture medium (open circles) and on worms cultured on the same solidified medium (closed circles) (*images reproduced from [108]*).....30

Figure 15 Heat power, normalized by the protein content (mass), measured on *C. elegans* nematodes during the whole life cycle. The insert shows the real time heat power during worm recovery from dauer stage, induced by food addition (the first 60 minutes were not measured because of the time required for equipment stabilization). L1, L2, L3 and L4 correspond to the four larval stages (*image reproduced from [109]*).31

Figure 16 Nanocalorimeter developed by Johannessen *et al.* a) View of the sensing membrane showing 10 radially distributed thermocouples, a resistive heater, and the open microchamber. b) Top view of the open microchamber, loaded with 10 isolated brown adipocytes, a single cardiomyocyte, and 20 cardiomyocytes, respectively. c) Heat power measurements on 10 cultured brown adipocytes, after the injection of 1.4 μM of noradrenaline (NE) and 14 μM of rotenone: the first measurement is a control, the second is the actual experiment (*images reproduced from [121]*).....36

Figure 17 Nanocalorimeter developed by Xu *et al.* a) Schematics showing the working principle of this open-chamber calorimeter, where a 5 nl droplet was positioned on the suspended nitride membrane. b) Photographs showing the thermopile chip casing (B) and a top view of the membrane with thermopiles (C). c) Heat of mixing measurements consisting of sequential injections of 25 pl of HCl into a 2.5 nL drop of NaOH (plot A), and the control (plot B) (*images reproduced from [132]*).....37

Figure 18 Nanocalorimeter developed by Verhaegen *et al.* a) Photograph of two prototype sensors consisting of a rubber membrane and two distinct open channels for differential measurements. b) Corresponding schematic view, showing also the location of the thermopile and of the isolation chambers (*images reproduced from [133]*).....38

Figure 19 Nanocalorimeter developed by Lerchner *et al.* a) Photograph showing four distinct thermopile sensors (*reproduced from [116]*). b) Cross-sectional view of the nanocalorimeter showing the PMMA frame and microchannel interfaced with the nanocalorimeter chip and the heat sink. Replaceable top and bottom cover foils are used to minimize contaminations between experiments. c) Photograph showing the removable PMMA microfluidic assembly. d) Photograph showing the double nested thermostat for high temperature stability. e) Experiment carried out on *Staphylococcus aureus* bacteria in suspension: first, after injection of the bacterial suspension, a large injection artefact is observed; the signal shift after stopping the flow (SS indicated in the plot) is due to bacterial metabolism; subsequently, the buffer solution is injected, allowing to restore the initial baseline (after another injection artefact). f) Measurement of metabolic heat produced by a growing population of *Staphylococcus aureus* bacteria (corresponding to a time variation of SS in e). The inset shows metabolic heat as a function of bacteria concentrations (*all other pictures reproduced from [114]*).39

Figure 20 Segmented flow calorimeter as a modified version of the nanocalorimeter developed by Lerchner *et al.* a) Schematics showing a Teflon tube clamped on the sensing membrane by means of a PMMA frame. b) Photograph showing a top view of the nanocalorimeter. c) Measurement on human hair follicles after the injection of the mitochondrial uncoupler DNP: the green dots represent the control experiment where no hair follicles were present in the sample; the blue dots report the actual experiment, where hair follicles are exposed to increasing concentration of DNP. As DNP uncouples mitochondrial respiration, it induces an increase in metabolic heat production, which is experimentally observed (*images reproduced from [147]*).41

Figure 21 Nanocalorimeter developed by Zhang *et al.* a) Schematics showing the nanocalorimeter used in the open-chamber configuration with a PDMS chamber. b) Schematics showing the nanocalorimeter used in the close-chamber operation mode where a microfluidic glass structure is bonded to the silicon chip. c) Example of measurements carried out in the open-chamber configuration, showing the oxidation of glucose catalyzed by glucose oxidase: first, a droplet of enzyme was let to dry, then subsequent injections of glucoses were carried out, resulting in increasing voltage peaks for increasing concentrations. d) Comparison of the nanocalorimetric sensitivity of the closed-chamber configuration for different enzyme catalyzed reactions (*images reproduced from [117]*).42

Figure 22 Nanocalorimeter developed by Lee *et al.* a) Cross-sectional schematics showing the different components of the nanocalorimeter developed, including the thermopile sensor, the parylene measurement

chamber, the SU-8 intermediate layer and the PDMS microfluidics. b) Top view of the microfluidic structures fabricated in the PDMS layer, showing fluidic pumps and valves. c) Top picture of the sensing area, showing the thermopile and the resistive heater on the parylene membrane. d) Example of measurements showing urea hydrolysis by urease: heat power generated after the injection of increasing volumes (0.7 nL to 2.8 nL) of 50 mM urea solution into the measurement chamber, previously prefilled with urease solution. The inset shows to the total energy of reaction calculated for increasing sample volumes injected (*images reproduced from* [113])......43

Figure 23 Nanocalorimeter developed by Wang *et al.* a) Schematic view of a closed-chamber nanocalorimeter operated in differential mode. b) Measurement of the oxidation of glucose catalyzed by glucose oxidase, when injecting 0.8 μL of 31.3 mM glucose solution into the sample chamber: initially the voltage signal increases as the chamber is being filled, then it decreases as the glucose available in solution is depleted. c) Maximum of the thermopile voltage measured as described in b) for increasing glucose concentrations in a stopped-flow mode (*images reproduced from* [125])......44

Figure 24 Nanocalorimeter developed by Seung-Il Yoon *et al.* a) Schematic view of the nanocalorimeter, showing the split-flow geometry of the microfluidic channels on top of a thick Si/SU-8 substrate. b) Thermopile voltage resulting from the biotin–streptavidin reaction: 3 μL of 3.4 $\mu\text{g}/\mu\text{L}$ biotin solution was injected three times through the common inlet to obtain a control measurement; then 3 μL of 1.0 $\mu\text{g}/\mu\text{L}$ of streptavidin solution was injected only in the reaction chamber. The first peak indicated in the plot is an injection artefact, whereas the second peak originate from the actual heat of reaction. c) Calorimetric measurement showing the detection of *Neisseria meningitidis* group B for increasing bacteria concentration, and comparison with the optical detection based on ELISA (Enzyme-Linked Immunosorbent Assay) (*a and b reproduced from* [149], *c reproduced from* [148])......45

Figure 25 Enthalpy arrays developed by Torres *et al.* a) Schematic view of a single enthalpy module of the 96 array, showing the two sensing areas for the differential measurement, the thermistor thermometer, and the droplets dispensed on the electrodes of the measurement and the reference area. b) Photograph showing the same module. The electrodes of the two sensing areas are suspended on a polyimide membrane. c) Heat power measurement during the phosphorylation of Kemptide by a specific enzyme in absence and presence of an inhibitor (staurosporine) (*a and b reproduced from* [126], *c reproduced from* [119])......46

Figure 26 Paper-based calorimeter developed by Davaji *et al.* a) Schematic showing the main components of this calorimeter, including the paper-based channel and the RTD sensor. b) Photograph of the calorimeter, realized on the glass substrate (24 x 60 mm²). c) Glucose detection by glucose oxidase where 2 μL of glucose oxidase were first dispensed on the reaction site, then 8 μL of glucose solution was loaded from the sample inlet (*images reproduced from* [150])......47

Figure 27 Nanocalorimeters developed by *Xensor Integration*. a) Photograph as reported in the datasheet of the model XEN-LCMquad with four independent sensors (see appendix). b) Photograph of the model XEN-NCM9924 with a single sensor on a thicker membrane. c) Schematics of a recently developed nanocalorimeter, integrating a closed microchamber for flow-through implementation. d) Photograph of two nanocalorimeters on the same chip of the same type as described in c) (*a and b reproduced from the datasheet, see appendix; c and d reproduced from* [153]).48

Figure 28 Working principle of thermoelectric sensing. a) Schematic of a thermocouple made of two materials A and B connected together. Because of the presence of the temperature gradient $\Delta T = T_{HOT} - T_{COLD}$, a voltage V_{TC} between the two cold junctions is generated. b) Schematic for a thermopile made of a series connection of n thermocouples, exposed to a temperature difference ΔT . The resulting voltage V_{TP} is equal to $n \cdot V_{TC}$. 58

Figure 29 Fast and slow processes with respect to the sensing time constant τ60

Figure 30 Three-dimensional sketch of the nanocalorimetric platform, consisting mainly of a membrane-based sensor chip, a PC sample reservoir positioned on the sensor membrane, and several aluminum parts clamped together (outer size 60 x 60 mm²). The PID temperature control is achieved thanks to a flat polyimide heater (PID heater) on top and a platinum temperature sensor (PID sensor) positioned inside the isothermal holder.63

Figure 31 Photograph of the developed nanocalorimetric platform. The three aluminum parts are visible, together with the top aluminum plate, as well as the PMMA parts (bottom and top plates). The flat PID

resistive heater (orange in the picture) is clamped between the top aluminum plate and the top PMMA plate.63

Figure 32 The thermopile sensor (XEN-NCM 9924, *Xensor Integration*). a) Photograph of the sensor chip, positioned upside down. The bottom face of the membrane is visible in the center of the frame, where the components, such as the resistive heaters, are fabricated. The ceramic Pin-Grid Array (PGA), to which the membrane is glued, is also shown. b) Bottom view of the thermopile sensor chip, indicating the position of hot and cold junctions of the silicon-aluminum thermopile (highlighted in green) and of the integrated aluminum heaters (highlighted in red) on the monocrystalline silicon membrane (area 8.3 x 8.3 mm²). c) Close-up view of a region on the sensing membrane, as indicated by the dashed line in b), showing radially distributed lines corresponding to the thermocouples, and to two different serpentine resistive heaters. d) Cross-sectional sketch of the thermopile sensor chip, showing also the silicon rim.64

Figure 33 Sample reservoir located on the top of the thermopile membrane. a) Cross-sectional view of the core of the platform, showing the 25 μm polystyrene membrane at the bottom of the sample reservoir, which is in direct contact with the sensor membrane. Fluidic connections are fabricated on the sidewalls of the reservoir and are aligned to the corresponding holes in the aluminum holder providing direct access from the outside. b) Photograph of the nanocalorimetric platform, taken after opening the platform and removing one of the three assembled aluminum parts. The polycarbonate reservoir sitting on the membrane at the center of the sensor chip is visible. (The holes in the aluminium parts visible in the photograph are for closing the system with screws, the fluidic connections are hidden by the reservoir).66

Figure 34 Materials assigned to the different parts of the model. a) Full view of the device. b) Closed-up view to show the location of the silicon membrane of the thermopile sensor (dashed line in a), and the PS membrane of the reservoir.67

Figure 35 Boundary conditions applied to the model.68

Figure 36 Computational results for steady-state studies. a) Temperature at the center of the sensing area and temperature difference calculated, based on the temperature on the two positions where the hot and cold junctions are located in the real case, vs the heat power Q_{HEATER} applied to the isothermal holder to reach the setpoint temperature. b) Temperature difference between hot and cold junctions resulting from the production of the heat power Q_{SAMPLE} by the sample (logarithmic scale in the plot).69

Figure 37 Time-dependent computational results when simulating heating the isothermal holder by the flat heater Q_{HEATER} (equal to 145 W/m²) to 25 °C. a) Temperature gradient immediately after switching on Q_{HEATER} ($t = 1$ min, $T_{AMB} = 20$ °C) and after heating for a characteristic time equal to $3\tau'$ ($t = 120$ min). The time constant τ' is estimated to be 40 min. b) (i) Temperature evolution over time in the center area of the chip membrane, when applying the heat source Q_{HEATER} . (ii) Corresponding temperature difference $\Delta T_{HOT-COLD}$ between hot and cold junctions.70

Figure 38 Time-dependent evolution of the temperature in the sensing area after applying the constant local heat source $Q_{SAMPLE} = 10^4$ W/m³ generated by the sample in the reservoir, starting from a platform temperature that is stabilized at 25 °C. a) Simulated temperature gradient immediately after switching on the heat source ($t = 1$ s), and after a characteristic time equal to $3\tau''$ ($t = 24$ s). b) Corresponding temperature difference $\Delta T_{HOT-COLD}$ between hot and cold junctions of the thermopile over time. The second time constant of the system τ'' is about 8 s.71

Figure 39 Schematic explaining shielding of the nanocalorimetric platform. The isothermal holder (depicted as a grey rectangle) with the thermopile sensor, the metal chassis (depicted as a grey rectangle) of the signal re-distribution box, as well as the shields of the cable in between both devices (for the thermopile voltage signal V_{TP} and for the resistive heater signals I_R and V_R) are connected to a common ground. In order to avoid ground loops, the shields of the separate twisted cables for the signals V_{TP} and I_R , V_R connecting the respective equipment are interrupted at specific locations.72

Figure 40 Sketch representing the operation of the PID control system: the output signal of the controller $u_c(t)$ is the sum of the different contributions, i.e. the proportional term (k_p), the integrative term (k_i) and the derivative term (k_D), which are applied for correcting the error signal $e(t)$ at the input.74

- Figure 41 Different elements of the nanocalorimetric platform for fluidic sample injection, electrical signal acquisition and temperature control. The control of the full system is automatized through a Labview (*National Instruments*) interface.77
- Figure 42 Photograph showing the nanocalorimetric platform and the necessary equipment. Acquisition equipment are on the right-hand side (from the top to the bottom): the nanovoltmeter, the sourcemeter and the temperature controller. On the back of the picture, the signal distribution box is visible. The syringe pump used for sample injection is on the left side. The foreground shows the nanocalorimetric platform, including the outer PMMA box surrounding the aluminium holder, which is used for additional insulation from external temperature fluctuations.....77
- Figure 43 Platform temperature T_{PID} stability and baseline signal V_{TP} acquired by the thermopile sensor at a setpoint temperature of 25 °C and 37 °C, respectively. a) Temperature T_{PID} acquired by the PID sensor over time for a setpoint temperature of 25 °C. The flat heater on the top of the platform is activated at $t = 0$ min. After about $t_{STAB} = 20$ minutes of thermal stabilization, the temperature stability of the platform is $T_{PID} = 25.000 \pm 0.001$ °C (see inset). b) Temperature T_{PID} over time for a setpoint temperature of 37 °C. The temperature stability is again in the range of ± 1 mK (see inset). c) Thermopile voltage V_{TP} over time curve at 25 °C. After full thermalization of the platform ($t > t_{STAB}$), the voltage has a slight baseline drift of 0.3 nV/s (see inset). The voltage signal stability $\pm\sigma_V$ is ± 80 nV after baseline correction. d) Thermopile voltage V_{TP} over time curve at 37 °C. In this case, the baseline drift is -8 nV/s (see inset). After baseline correction, the voltage signal stability $\pm\sigma_V$ is ± 100 nV.82
- Figure 44 Sketch of the sample reservoir on the silicon membrane, showing the two configurations used for electrical calibration: (i) the resistive thin-film heater integrated directly on the silicon membrane (R_INT), or (ii) a miniaturized 100 k Ω thermistor used as resistive heater (R_EXT), immersed in the reservoir filled with 50 μ l of deionized water.83
- Figure 45 Electrical calibration carried out at 25 °C and 37 °C. a) Thermopile voltage V_{TP} over time curve (full black line), when applying a periodically increasing electrical power to the integrated resistive heater P_{R_INT} (dashed red line), at 25 °C. b) Calibration curves for the integrated heater R_INT and for the external heater R_EXT, at 25 °C. The corresponding power sensitivities are 2.7 V/W (PS_{R_INT}) and 1.9 V/W (PS_{R_EXT}), respectively. The inset is a close-up of the calibration points for very small heat power (0 – 300 nW) that allows to determine a limit of detection of 70 nW and 170 nW, when using R_INT or R_EXT, respectively. c) Same sequence as described in a) at 37 °C. d) Calibration curves for R_INT and for R_EXT at 37 °C. The inset is a close-up of the calibration points for small heat power (0 – 2 μ W) that allows to determine a limit of detection of 100 nW and 500 nW, when using R_INT or R_EXT, respectively.84
- Figure 46 Thermopile voltage signal V_{TP} over time measured when very low heat power signals P_{R_INT} are applied to the integrated resistive heater R_INT. a) V_{TP} response curves for increasing heat power P_{R_INT} pulses (110 nW, 250 nW and 440 nW, respectively) when the platform is stabilized at 25 °C. b) Measurements carried out at 37 °C for increasing heat power P_{R_INT} pulses (110 nW, 450 nW and 1 μ W, respectively).86
- Figure 47 Experimental evaluation of the sensing time constant of the nanocalorimeter at 25 °C. A heat power pulse P_{R_EXT} of about 30 μ W (dashed red line) was applied at time $t = 0$ s to the external resistive heater R_EXT. The thermopile voltage V_{TP} is acquired with a sampling time of 1 second (black dots), and a fitting according to Equation 6:1 resulted in a sensing time constant τ of 6 seconds.87
- Figure 48 Mixing of 1-propanol in water. a) Schematic showing the mesoscopic molecular interactions taking place when considering a binary alcohol/water mixture at different concentrations (*image reproduced from* [174]). For increasing mole fraction $X(1PrOH)$ of the alcohol in water, different behaviours are observed: for $X < X_1$ water-water molecules interact forming hydration shells; for $X_1 < X < X_2$ hydration structures are less stable and water tends to aggregate around the -OH of the alcohol, forming hydrogen-bonded networks; for $X_2 < X < X_3$ larger alcohol aggregates form; for higher mole fractions isolated water clusters remain. b) Excess molar enthalpy H^E of 1-propanol in water as a function of the mole fraction of 1-propanol $X(1PrOH)$ at 25 °C, as reported by Davis *et al.* in tabulated format [175].88
- Figure 49 Thermopile voltage V_{TP} acquired when implementing three sequential injections of 5 μ l aliquots (at time $t = 30, 60, 90$ min – indicated by the arrows) into the reservoir, prefilled with 45 μ l of different solutions. a) Sequential injection of DIW into the reservoir prefilled with DIW. b) Sequential injection of 1-propanol into

the reservoir prefilled with 1-propanol. c) Injection of 1-propanol into the reservoir prefilled with DIW. Actual mixing peaks are observable in the latter case, which are clearly more pronounced than the injection artefacts in a) and b).....	90
Figure 50 Differential excess enthalpy dH^E_{TOT}/dt over time generated by injecting and mixing 5 μ L of pure 1-propanol into 45 μ L of 1-propanol solutions at different initial concentrations (values are indicated in the figure). $dH^E_{TOT}/dt(t)$ curves were obtained by converting the measured thermopile voltages V_{TP} using a power sensitivity coefficient of 0.6 V/W.....	91
Figure 51 Literature data for the molar excess enthalpy H^E for mixing of 1-propanol in water vs the mole fraction $X(1PrOH)$ (as already reported in Figure 48 [175]). Additionally, the differential molar excess enthalpy dH^E/dX is shown (black solid line), obtained by differentiating the polynomial fit of $H^E(X)$ with respect to the mole fraction $X(PrOH)$ (light grey solid line).	92
Figure 52 Protocol used for data analysis: the measured $dH^E_{TOT}/dt(t)$ curve is first normalized in order to obtain the molar differential excess enthalpy $dH^E/dt(t)$. Integrating over time results in the molar excess enthalpy change ΔH^E between the initial (X_i) and final (X_f) mole fraction. The central mole fraction X_c is then calculated and used to plot ($X_c, \Delta H^E/\Delta X$) data points on the differential molar excess enthalpy $dH^E/dX(X)$ reference curve from literature.	93
Figure 53 Comparison of the differential molar excess enthalpy dH^E/dX derived from literature [175] (dashed line) with the ($X_c, \Delta H^E/\Delta X$) values calculated from our experimental data (red dots).	94
Figure 54 Schematic showing the reaction mechanism of glucose oxidation catalyzed by glucose oxidase (abbreviated as GOD in this figure) (<i>image reproduced from</i> [180]).	95
Figure 55 Measurement of glucose oxidation, catalyzed by glucose oxidase at 25 °C. Heat power $P(t)$ curves are obtained from the measured thermopile voltage V_{TP} with a power sensitivity coefficient $PS_{exp} = 1.0$ V/W. The reservoir was initially filled with 25 μ L of glucose oxidase solution (250 U/ml in PBS), and 1.5 μ L of glucose solution (in PBS with varying concentrations) is injected at $t = 30$ min to achieve an initial glucose concentration [S_0] in the reservoir ranging from 0 to 40 mmol/l.	96
Figure 56 Thermal energy $E(t)$ released during the reaction, obtained by integrating $P(t)$ with respect to time, for different glucose solutions and at a fixed glucose oxidase concentration of 250 U/ml.	97
Figure 57 Fitting of the experimental data by the Michaelis-Menten equation. a) Peak values P_0 of the measured heat power as a function of the initial glucose concentration [S_0] in the reservoir, for different glucose oxidase concentrations: 250 U/ml, 125 U/ml and 0 U/ml (control experiment). The experimental data obtained for [GOx] = 250 U/ml and [GOx] = 125 U/ml were fitted using the Michaelis-Menten equation (dashed lines, adjusted $R^2 \approx 0.99$ and 0.97, respectively). b) P_0 vs [S_0] curve for glucose concentrations below 10 mmol/l (for [GOx] = 250 U/ml, from figure a). This emphasizes the linear region of the Michaelis-Menten curve for glucose concentrations smaller than the Michaelis constant K_M . The proportionality coefficient $\alpha \approx 6.68 \mu\text{W}\cdot\text{l}\cdot\text{mmol}^{-1}$ was determined by linear fitting (dashed line, adjusted $R^2 \approx 0.96$).	98
Figure 58 Suspension of <i>C. elegans</i> nematodes in S Medium, consisting mainly of worms at the larval stage (L3-L4).	101
Figure 59 Preliminary results of heat power measurements carried out on <i>C. elegans</i> nematodes. After thermalization of the platform, 2 μ L of 75 mM of glucose solution in S Medium were injected in the sample reservoir (at $t = 25$ min). The reservoir was initially prefilled with 25 μ L of three different samples: (i) worm suspension (red curve), (ii) <i>E.coli</i> suspension (orange curve), and (iii) S Medium solution (blue curve). The solid lines are the average of 2 worm experiments, and the average of 3 for the control experiments, respectively. The highlighted area corresponds to \pm the standard deviation.	102
Figure 60 Principle of the <i>in vivo</i> temperature measurement on a mouse. a) Schematic view showing the thermistor sensors implanted in the mouse abdomen to record the overall body temperature, and in the brown adipose tissue (BAT). The measurement readout is done via a connector that is surgically fixed on the back of the mouse. After a period of one week for recovery from surgery, the two sensors are continuously read out during cold exposure at 6°C. b) Close-up view of the sensor insertion point in the BAT in the interscapular region underneath the white adipose tissue (WAT) layer.	109

Figure 61 View of the miniaturized temperature sensor assembly. a) Close-up view of the sensor tip, which is 0.5 mm in diameter and 3 mm in length. b) Photograph of the sensor assembly prepared for implant: a pair of sensors is soldered to a common 4-pin connector, then reinforced with dental cement and covered with medical silicon (green colour) to guarantee biocompatibility.109

Figure 62 Exploded view of the custom-built aluminum holder used to set calibration temperatures by means of a PID controller. Specific temperature calibration points in the range of 25 °C to 42 °C were set with a stability of ± 1 mK over a period of 30 min. For each setpoint, the temperature value T_{ref} of a calibrated thermistor reference sensor and the resistance value R_{sens} of each implantable sensor were acquired. 110

Figure 63 Calibration of the temperature sensors. a) Calibration curve based on the Steinhart-Hart equation obtained by fitting three pairs of (R_{sens}, T_{sens}) values per sensor (assuming $T_{sens} = T_{ref}$). b) Calibration error curve at different temperatures, in order to verify the accuracy of the thus-calibrated sensors, by comparing the temperature values T_{ref} from the thermistor reference sensor with the temperature values T_{sens} from the implantable sensors (mean \pm standard deviation). The maximum experimental calibration error is about 2 ± 1 mK.111

Figure 64 *In vivo* temperature measurements during cold exposure at 6 °C for the two different mice phenotypes. a) Average temperature plot for 8 mice of phenotype 1, showing a tendency to hypothermia. Temperature was continuously measured by the implantable sensors positioned in the abdomen and in the BAT. Rectal temperature was also acquired using a conventional rectal probe as a control measurement. b) Average temperature plot for 3 mice of phenotype 2, highlighting a lower resistance to hypothermia (cold exposure lasted less than 4 hours as the mice reached the minimal body temperature allowed). c) Average temperature difference $\Delta T = T_{BAT} - T_{ABDO}$ for phenotype 1, calculated by subtracting the abdomen temperature from the BAT temperature. After more than 5 hours of cold exposure the temperature difference is about -2 °C, indicating faster cooling of the BAT with respect to the abdomen. d) Average temperature difference ΔT for phenotype 2 showing a stronger but also nearly linear decrease over time (data points with error bars: mean \pm standard error of mean, over all mice of a given phenotype).114

Figure 65 Heat transfer computational simulation. The mouse body was modeled as an ellipsoid, considering an overall mouse metabolic rate $Q_M(t)$ and an initial body temperature T_{M0} prior to cold exposure. Additional boundary conditions are determined by natural convection at the surface of the ellipsoid with a heat transfer coefficient h and an external temperature $T_C = 6^\circ\text{C}$115

Figure 66 Comparison between computational and experimental results for mouse phenotype 1. a) Constant body metabolic rate implemented in the model ($Q_M = 0.42$ W). b) Simulation of the temperature gradients on the body surface at different time lapses, considering $t = 0$ min as the starting point of cold exposure. c) Comparison of experimental and simulated temperature over time data for abdominal and BAT sensor locations. Simulated temperature values are taken at a distance of about 8 mm from the surface, both for the BAT and the abdominal temperature.116

Figure 67 Comparison between computational and experimental results for mouse phenotype 2. a) Body metabolic rate $Q_M(t)$ implemented in the model. In order to take into account the breakdown of the cold resistance for phenotype 2, the body metabolic rate $Q_M(t)$ was set constant up to 150 minutes of cold exposure ($Q_M = 0.42$ W), and then decreases linearly. b) Temperature gradients on the body surface simulated at different time lapses, considering $t = 0$ min as the starting point of cold exposure. c) Comparison of the experimental and simulated temperature plots showing good qualitative correspondence.118

Figure 68 Screenshot of the nanocalorimetric interface.130

Figure 69 Screenshot of the calibration interface.131

List of Tables

Table 1 Main parameters of two commercial isothermal calorimeters (as indicated in the corresponding datasheets) and selected examples of chip-based nanocalorimeters (as discussed in more detail in Chapter 4). *Either “resolution” or “limit of detection” is used for commercial devices or chip-calorimeters, respectively, to express the performance of the system.	23
Table 2 Basal heat power generated by living cells and organisms measured by microcalorimetry...52	
Table 3 Summary of relevant specifications of XEN-NCM 9924 chip, as reported in the datasheet by <i>Xensor Integration</i>	65
Table 4 Thermal properties of materials, as specified in the computational modelling.	67
Table 5 Boundary conditions applied for the different computational studies.	68
Table 6 PID control gains used for the integrated control system at the two setpoint temperatures of 25 and 37 °C.	76

List of Equations

Equation 5:1 – Fourier’s law of heat conduction	54
Equation 5:2 – Energy balance for an element of thickness dx	55
Equation 5:3 – Heat conduction equation for a one-dimensional system.....	55
Equation 5:4 – Heat conduction equation for a three-dimensional system	55
Equation 5:5 – Newton’s law of cooling	56
Equation 5:6 – Stefan-Boltzmann law.....	56
Equation 5:7 – Radiative heat transfer between an object and the surroundings	56
Equation 5:8 – Seebeck voltage - temperature difference relationship	57
Equation 5:9 – Seebeck voltage and coefficients defined for two conductors A and B.....	57
Equation 5:10 – Seebeck voltage - temperature difference relationship for a thermocouple	58
Equation 5:11 – Seebeck voltage for a thermopile made of n thermocouples connected in series....	58
Equation 5:12 – Heat power equation for heat flow calorimetry.....	59
Equation 5:13 – Re-written heat power equation for heat flow calorimetry	59
Equation 5:14 –Heat flow equation for an ideal thermopile	59
Equation 5:15 – Tian’s equation	59
Equation 5:16 – SNR of nanocalorimetric measurements for fast processes	61
Equation 5:17 – SNR of nanocalorimetric measurements for slow processes.....	61
Equation 5:18 – Simplified version of Tian’s equation.....	61
Equation 5:19 – Transient temperature profile assuming heating up to the setpoint temperature T_{CENTER}	70
Equation 5:20 – Definition of process error signal.....	73
Equation 5:21 – Proportional gain definition.....	73
Equation 5:22 – Integral controller gain definition.....	74
Equation 5:23 – Derivative control gain definition	74
Equation 5:24 – PID controller output as defined in the <i>Lakeshore</i> PID controller user manual	76
Equation 6:1 – Transient behaviour of the thermopile voltage after applying a heat power to the external heater	87
Equation 6:2 – Oxidation of glucose catalyzed by glucose oxidase	94
Equation 6:3 – Proportionality relationship between measured heat power and reaction rate.....	95
Equation 6:4 – Michaelis-Menten equation	97
Equation 6:5 – Michaelis-Menten equation rewritten for the heat power	97
Equation 6:6 –Linear range of the initial heat power vs initial glucose concentration, for low substrate concentrations.....	98
Equation 6:7 – Exponential decay of the substrate concentration over time	99
Equation 6:8 – Exponential decay of the heat power signal over time	99
Equation 6:9 –Proportionality relation between initial heat power P_0 and initial substrate concentration S_0	99

List of Equations

Equation 7:1 – Steinhart-Hart equation.....111

Chapter 1 Introduction

Most chemical and biochemical processes are either exo- or endothermic, thus having a specific thermal signature. If we consider biological systems, all living organisms generate heat through a complex range of metabolic processes. Therefore, thermal measurements are a powerful and universal method for the investigation of chemical and biological processes in a wide range of applications. In principle, this type of study may be performed in two ways, either by recording the heat power evolution during the process of interest, or by measuring directly the temperature variations. In the frame of this work, we have explored both approaches, as highly sensitive heat power measurements were enabled through the development of a chip-based nanocalorimetric platform, whereas localized *in vivo* temperature sensing in mice was implemented by means of implanted miniaturized thermistors.

Before addressing the technological aspects of this work, we briefly introduce the biological background to highlight the importance of metabolic studies. The term metabolism (from the Greek word *metabolē*, “change”) refers to the set of biochemical reactions indispensable for cell life as they allow cells to “harness energy and channel it into biological work” [1]. This highly sophisticated and coordinated cellular activity involves series of enzyme-catalyzed reactions, named metabolic pathways. By these means, cells are able to break down nutrient molecules, such as carbohydrates, proteins and fats, to obtain chemical energy in the form of adenosine triphosphate (ATP), nicotinamide adenine dinucleotide (NADH), nicotinamide adenine dinucleotide phosphate (NADPH) and flavin adenine dinucleotide (FADH₂) (catabolic pathways). Inversely, cells may consume energy to build up complex molecules, such as polysaccharides, proteins, lipids and nucleic acids (anabolic pathways). The delicate regulation of such processes responds to signals from within the cell, for example the intracellular concentration of a substrate, and also from outside of the cell, for example growth factors and hormones [1]. As a result, metabolic homeostasis is of crucial importance for the maintenance of a healthy organism [2] and, consequently, metabolic alterations are at the very origin of several and seemingly unrelated diseases, such as age-related diseases, neurodegenerative disorders and cardio-metabolic disorders [3], [4]. Thus, technologies enabling the acquisition of additional information on metabolic activities, such as the ones based on thermal measurements, are promising, not only for studying metabolic mechanisms under physiological conditions, but especially for investigation of the causes of its alterations and of possible therapeutic solutions.

Looking at technologies enabling thermal measurements, the heat power generated by a specific sample may be assessed by micro- or nanocalorimetric methods, both of which are typically based on the transduction of heat flow or temperature gradients into an electrical signal. When applied to the study of (bio-)chemical reactions *in vitro*, calorimetric measurements allow full thermodynamic

profiling, including the quantification of enthalpy, free energy and entropy [5] and the kinetic analysis of bioprocesses [6]–[8]. Furthermore, considering biological systems, such as living organisms, heat produced during metabolic activities may be directly measured by calorimetry [9], [10], enabling applications in important biomedical fields, such as disease diagnosis, drug development or toxicology, and also environmental testing [11], [12]. Thanks to its non-invasive nature, calorimetry is considered the gold standard for studying biomolecular interactions [13]. Nevertheless, the need for versatile and customized platforms, responding mainly to the stringent requirements originating from working with living organisms, became more evident in the last years [14]. Moreover, the implementation of high-throughput assays, even if already approached by certain commercial equipment, is currently an emerging requirement [13]. For these reasons, great efforts have been invested in the development of alternative, miniaturized calorimetric approaches that are at the origin of the so-called nanocalorimeters. In fact, using microfabricated heat power sensors brought a technological breakthrough in this field of research, accompanied by a whole set of advantages. Most important features are high sensitivity in the nW range, small sample volumes typically in the nL- μ L range, fast response time in the order of few seconds, and versatility [15]. In particular, the possible use of nanocalorimeters interfaced with microfluidic devices has high potential for the development of versatile and customizable sensing systems. On one hand, the high sensitivity of nanocalorimeters enables the direct measurement of the very small amount of metabolic heat produced by small biological samples. For instance, considering a heat power production of few pW/cell, signals from as low as a few tens of thousands of cells in suspension may be detected. On the other hand, the appropriate design of microfluidic structures allows not only the culture of living organisms on chip, under optimal conditions of nutrient supply and waste disposal, but also the implementation of advanced biological protocols, such as the sequential applications of biochemical stimuli.

The measurement of temperature changes resulting from the production of metabolic heat is another approach for the investigation of biochemical processes. This is particularly convenient when studying the metabolic activity of biological tissues on whole organisms *in vivo*. Commercial implantable temperature sensors have been used for this purpose, but their size does not allow the investigation of the individual metabolic contributions of specific spatially confined tissues in an organism, especially if considering the small size of current animal models, typically mice, as used for the present studies. Thus, also in this case miniaturization plays an important role and the use of very small, possibly microfabricated temperature sensors may provide relevant information on localized metabolic activity of tissues.

In this thesis work, we present the two approaches implemented for the thermal investigation of biochemical processes, both of which based on the use of miniaturized sensors. First, we present the development of a nanocalorimetric platform enabling heat power measurements during biochemical reactions *in vitro*. Second, we report on the use of miniaturized temperature sensors for local monitoring of the metabolic activity of specific tissues *in vivo*. In particular, Chapter 2 provides detailed information on the biological context of this field of research, giving relevant background information on the main metabolic mechanisms related to mitochondria functioning, and on the conventional techniques currently used in life science laboratories. Chapter 3 gives a more in-depth

overview on microcalorimeters, which have been extensively used for heat power measurements in biology, especially on living organisms. The purpose of this chapter is to present briefly some of the major historical devices and then to focus on current applications of microcalorimetry, in particular on some important studies in the biomedical field. Chapter 4 reports the state-of-the-art of miniaturized calorimeters, including information on fabrication processes, performance and some relevant applications. Chapter 5 describes the new nanocalorimetric platform developed in the frame of the present work. The different stages from the initial design to the actual development are presented. Heat transfer computational simulations, the fabrication of the nanocalorimetric platform and the integration with a highly stable and accurate temperature control system are discussed. Chapter 6 is dedicated to the description of the experimental characterization of the nanocalorimeter, in terms of important parameters, such as temperature stability, power sensitivity, time constants and limit of detection. Furthermore, the validation of the platform is presented showing heat power measurements on two different systems, *i.e.* the mixing of 1-propanol in water, and the oxidation of glucose catalyzed by glucose oxidase. In both cases, data analysis is reported and compared with literature. Preliminary results on metabolic heat power measurements on *C. elegans* nematodes are also discussed. Chapter 7 describes localized *in vivo* temperature sensing on mice, based on two implanted miniaturized thermistors. The procedure for accurate calibration of these sensors as well as for implant and *in vivo* measurements is reported. In particular, a possible metabolic response of the brown adipose tissue (BAT) in the mouse during cold exposure was investigated. Experimental results from a small number of mice are presented, together with the computational results obtained by using a simplified thermal model of the mouse body. Finally, Chapter 8 summarizes the main achievements of this thesis work, bringing the discussion further in order to identify potential improvements of the developed systems. Possible more advanced biological experiments are proposed, which may take advantage of the full potential of these technologies in the field of metabolic studies.

Chapter 2 Metabolic studies: biological context and current techniques

"[...] in general, respiration is nothing but a slow combustion of carbon and hydrogen, which is entirely similar to that which occurs in a lighted lamp or candle, and that, from this point of view, animals that respire are true combustible bodies that burn and consume themselves [...]" (from a memoir by A. Seguin and A. Lavoisier, quoted in Lavoisier, A. (1862) Oeuvres de Lavoisier, Imprimerie Impériale, Paris [1]).

This chapter aims at providing the biological context for the technologies that have been developed in this work. From the thermal point of view, both design and development of the sensing devices are strongly influenced by the biological applications. The discussion will be focused on metabolic studies on *in vitro* or *in vivo* biological models, respectively (drawing on the right-hand side of a mitochondrion from [16]).



This chapter begins with an introduction to cellular respiration, which refers to the set of catabolic processes enabling cells to obtain energy under aerobic conditions. Then the focus shifts to mitochondria, which are the cells' organelles where a specific catabolic process called oxidative phosphorylation occurs. More specifically, uncoupled respiration is presented as a peculiar feature of mitochondrial respiration, which is of particular interest when studying the thermal signature of cellular respiration. Available techniques, which are routinely used in life science laboratories to study metabolic processes, are also presented to complete the biological overview. The perspective then moves from the cellular level to the tissue level, introducing the function of the brown adipose tissue, which is considered the major site of non-shivering thermogenesis, *i.e.* the production of heat as a protective mechanism against cold and hypothermia. The biological importance of this phenomenon is presented, as well as the conventional technologies to study it.

2.1 Cellular respiration

Eukaryotic cells typically live under aerobic conditions as they oxidize nutrient molecules to obtain energy, together with byproducts such as carbon dioxide and water. The related biochemical processes occur in different cellular compartments and are typically grouped under the term of cellular respiration. Although cellular respiration is made of many complex and interconnected metabolic pathways, it is possible to distinguish three main stages, from the initial nutrient oxidation to the final energy production, as depicted in Figure 1a. The first stage is the oxidation of sugars, fatty acids and most amino acids, in order to obtain acetyl-coenzyme A (acetyl-CoA). The second stage consist in the oxidation of acetyl-CoA to carbon dioxide through the so-called citric acid cycle, also named Krebs cycle. The energy released during this second stage is stored in the coenzymes nicotinamide adenine dinucleotide (NADH) and flavin adenine dinucleotide (FADH₂), which are electron carriers in their reduced form. The final stage, and the most rewarding in terms of energy released, is the electron transport chain and subsequently the oxidative phosphorylation during which NADH and FADH₂ are oxidized and energy is produced in the form of adenosine triphosphate (ATP) molecules [1], [17].

The overall conversion of energy in the different steps of cellular respiration has an efficiency lower than 100%. Part of the energy is lost to the environment in the form of heat. As metabolic production of heat is innate in living organism, the measurement of heat is a direct approach to quantitatively study cellular respiration, and more generally cellular metabolism. Moreover, not only physiological conditions may be analyzed in terms of their thermal signature, but also altered conditions, for example in the case of pathologic states (such as metabolic disorders) and in the case of "artificially" altered states (such as uncoupled respiration induced by specific biochemical compounds), as it will be described in detail in section 2.2.1.

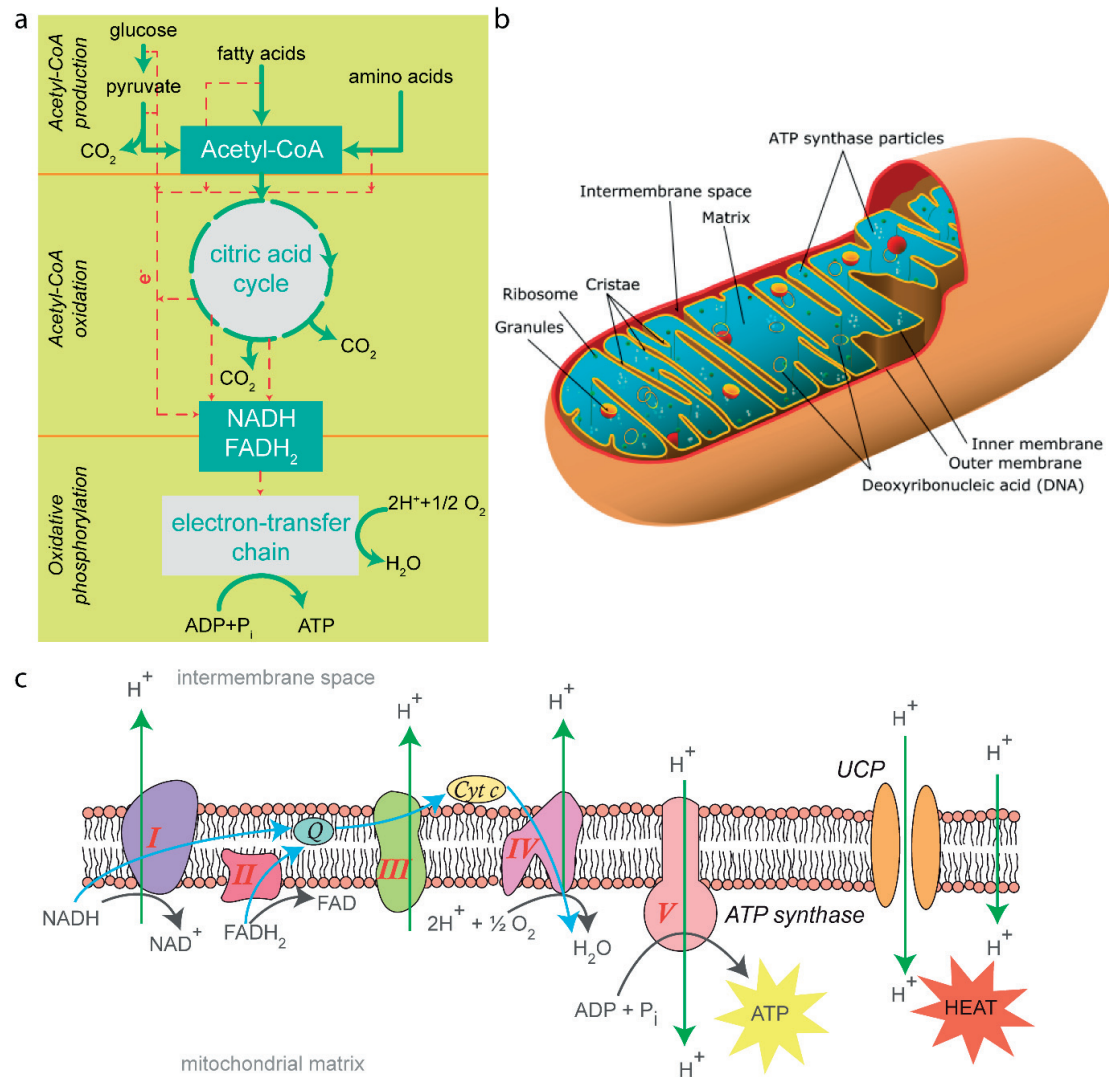


Figure 1 Schematic view of the biochemical pathways involved in cellular respiration. a) Simplified view of catabolic pathways, including nutrient oxidation to acetyl-CoA, further oxidation through the citric acid cycle (Krebs cycle), and finally the electron transport chain coupled to oxidative phosphorylation. Red lines indicate electron paths. b) Typical morphology of a mitochondrion, showing the matrix, the inner membrane, the intermembrane space and the outer membrane. Cristae are also visible, where ATP synthase, also named *complex V*, of the electron transport chain, is located (image reproduced from [16]). c) Close-up view on the electron transport chain, identifying the five protein complexes (indicated in red from I to V) involved and proton leaks.

2.1.1 Mitochondria, the cells' power plants

Mitochondria are cellular organelles, a few μm in length and about $0.5 \mu\text{m}$ in diameter. They are considered the cells' "power plants", as they produce most of the chemical energy indispensable for the cell in the form of ATP. According to the endosymbiotic hypothesis, mitochondria originated from the engulfment of an aerobic prokaryote, capable of oxidative phosphorylation, by another cell. The symbiosis made the engulfed cell dependent on the protective environment provided by the host cell, and at the same time the host cell became dependent on the prokaryote cell for energy production [17].

From a morphological point of view, mitochondria have two major membranes, an outer smooth membrane and an inner membrane, which is folded into ridges called cristae as depicted in Figure 1b. The intermembrane space is the compartment confined between the inner and the outer membrane. The inner membrane encloses the mitochondrial matrix. This matrix is the site of the Krebs cycle, whose main function is the formation of reduced electron carriers NADH and FADH₂ that in turn enter the electron transport chain taking place in the cristae of the inner membrane [1]. In particular, the highly folded structure of the inner membrane results in the presence of a large number of locations dedicated to oxidative phosphorylation. The outer membrane is permeable to many small molecules and ions thanks to pore-forming proteins named mitochondrial porins. The permeability of the inner membrane is much more limited, as only small molecules that are metabolized or required during the bioprocesses occurring in the mitochondrial matrix, are shuttled by membrane transport proteins [17], [18].

Mitochondria are highly dynamic organelles. Their size and shape changes according to the cell type, they constantly move and they can undertake structural changes, such as fusion by merging the membranes and mixing the intramitochondrial content, and fission, in order to increase the number of mitochondria [18], [19]. In particular, mitochondrial fusion and fission play a critical role in the maintenance of healthy mitochondria, and also to dynamically respond to varying cells' energetic requirements [20]. More specifically, energy demand may drive the number of mitochondria present in the cell. For example, liver cells, which are highly demanding in terms of energy requirements, contain from 1000 to 2000 mitochondria per cell, occupying up to one fifth of the total cell volume [18]. In contrast, cells of less demanding tissues, such as skin, may have much fewer mitochondria, as well as fewer cristae within [1].

2.1.2 The electron transport chain and oxidative phosphorylation

As previously mentioned, the most rewarding stage of cellular respiration is oxidative phosphorylation, which occurs at the inner membrane of the mitochondria. The activated electron carriers NADH and FADH₂, which have been produced in the Krebs cycle in the mitochondrial matrix, reach the inner mitochondrial membrane where they enter the electron transport chain. The term electron transport chain refers to the series of electron transfers, occurring through consecutive protein complexes, which is coupled with proton transfers (H⁺ ions) happening through the inner membrane, as depicted in Figure 1c. The accumulation of H⁺ ions in the intermembrane space results in a proton gradient between the mitochondrial matrix and intermembrane space that drives the phosphorylation of adenosine diphosphate (ADP) to ATP. For this reason, these last steps are referred to as oxidative phosphorylation.

The main protein complexes involved are NADH:ubiquinone oxidoreductase (also named NADH dehydrogenase), succinate dehydrogenase, ubiquinone:cytochrome-c-oxidoreductase and cytochrome oxidase, which are also called Complex I, II, III and IV respectively. Electrons are shuttled from a complex to the next one by two electron carriers, which are coenzyme Q (also named ubiquinone) and cytochrome c. More specifically, NADH is oxidized to NAD⁺ by Complex I, with electrons being transferred to ubiquinone and protons released to the intermembrane space. Ubiquinone

shuttles electrons to Complex III, where electrons are transferred to cytochrome c while additional protons are released to the intermembrane space. Similarly, ubiquinone also shuttles electrons from Complex II, where FADH_2 is oxidized to FAD, to Complex III. The main difference compared to NADH oxidation is that, in the latter case, there is no flux of protons to the intermembrane space. Cytochrome c then shuttles electrons to Complex IV. Here electrons are delivered to diatomic oxygen to generate water molecules, while protons are again released to the intermembrane space. Thus, the sequential transfer of electrons from a protein complex to the next one results in the generation of a proton gradient across the mitochondrial inner membrane, also named chemio-osmotic gradient [1], [17].

This proton gradient is the key element of the chemi-osmotic theory, developed by Peter D. Mitchell who won the Nobel Prize in Chemistry in 1978 for this model [21], [22]. According to this theory, the proton gradient generated in the electron transport chain, which is also an electrochemical gradient, is used by the protein complex ATP synthase, also called Complex V, to phosphorylate ADP and generate ATP [17]. Therefore, the production of energy as ATP is coupled to the electron transport chain and, thus, to the proton gradient and to the consumption of oxygen. For this reason, cellular respiration under these conditions is also named coupled respiration [23].

2.1.3 Uncoupled respiration

Mitchell's theory also predicted that proton leaks across the inner mitochondrial membrane into the mitochondrial matrix not coupled with ATP synthesis would result in energy loss in the form of heat, which is thermogenesis. In particular, this process is called uncoupled respiration, as ATP synthesis is interrupted, being uncoupled from the electron transport chain and, thus, from the oxygen consumption [24], [25]. Indeed, a certain degree of proton leak is an inherent property of inner mitochondrial membranes, even though the molecular basis of such phenomenon are still not completely understood [26], [27]. Specifically, the correlation between the membrane proton permeability and the presence of carrier proteins such as the adenine nucleotide translocase (ANT) suggests that such proteins may play a role in proton leak. ANT is a transmembrane protein, which shuttles ATP and ADP across the mitochondrial inner membrane, and the interface between such proteins and the lipid bilayer of the inner membrane may be a site of proton leak [26]. Interestingly, results from literature raise the possibility that "mild uncoupling", that is a mild increase in proton leak, limits oxidative stress, thus protecting mitochondria against reactive oxygen species [27].

This basal proton leak is unregulated, in contrast to an inducible proton leak, which is mediated by specific transmembrane proteins in the inner mitochondrial membrane, also named uncoupling proteins (UCP). The most known of such proteins is thermogenin (also called UCP1), which acts as a proton channel and is a peculiarity of the mitochondria in the brown adipose tissue (BAT) [25], [26]. In fact, UCP1 are abundant in the BAT and, as will be discussed more in detail in the following sections, they are responsible for nonshivering thermogenesis in hibernating animals, small rodents and newborn mammals [23], [26], [27]. The protein-mediated proton leak is regulated, for example, UCP1-related proton leak is inhibited by purine nucleosides and activated by free fatty acids [26].

Finally, uncoupled respiration can be “artificially” induced by specific compounds, called proton ionophores, such as 2,4-dinitrophenol (DNP) [28] and carbonyl cyanide-4-(trifluoromethoxy)phenylhydrazone (FCCP) [29], which shuttle the hydrogen ions back across the inner mitochondrial membrane, thus reducing drastically the efficiency of ATP synthesis. Based on such molecular mechanism, DNP has been a potential candidate as a drug for the treatment of obesity as it was found to effectively stimulate metabolism [30]. However, such compound was banned by the Food and Drug Administration as its pharmacokinetics made it unsafe for human use [31]. FCCP is used in bioenergetics studies, when investigating mitochondria respiration. In particular, FCCP allows the measurement of the mitochondrial maximal respiration.

As uncoupling pathways and, in general, the molecular basis of proton leak are still not completely established and as the main physical effect of such phenomena is the release of heat, it is clear that the development of accurate technologies aiming at the direct measurement of the related thermal effects / temperature variations holds great potential.

2.2 Conventional techniques for *in vitro* metabolic studies

There are two main approaches to study metabolic processes in mitochondria. At the molecular level, it is possible (i) to carry on enzymatic assays targeting a specific enzyme and looking at its activity, (ii) to quantify the concentration of specific metabolites, such as the detection of ATP based on the bioluminescence of the enzyme luciferase, (iii) or even to study specific gene expression directly at DNA level [32]. Another approach is to look at “macroscopic” effects of cellular metabolism, *i.e.* oxygen consumption, acidification level (hydrogen ion concentration) and heat production. This second type of approaches is not meant to supplant the more specific molecular approach. However, they may be used together to get a more complete understanding into metabolic pathways and possibly facilitate the identification of new therapies for metabolic diseases [9].

In the specific context of this work, the investigation of the macroscopic effects of metabolism is the main target and for this reason, the two main conventional techniques allowing such studies are introduced in the following section (microcalorimetry will be discussed in more detail in the following chapter).

2.2.1 Metabolic oxygen and acidification rate measurements

Metabolic studies are routinely carried out in life sciences laboratories, using commercially available equipment, such as the Extracellular Flux Analyzer by *Seahorse Bioscience* [33]. In particular, this equipment allows the measurement of the oxygen consumption rate (OCR) and the extracellular acidification rate (ECAR) on cells, which are seeded on cell culture microplates interfaced with sensing cartridges. In particular, the sensing cartridges consist of an array of sleeves in which the sensing elements are embedded. Two fluorophores are used, one which is quenched by oxygen, thus measuring oxygen consumption during mitochondrial respiration, and another one which is sensitive to hydrogen ions, providing more information on glycolysis. As shown in Figure 2a, optic fibers may be inserted in the sensing cartridge for the fluorescent measurements. The sensing tips are lowered to a small distance from the cell layers in the well plate in order to create a transient microchamber

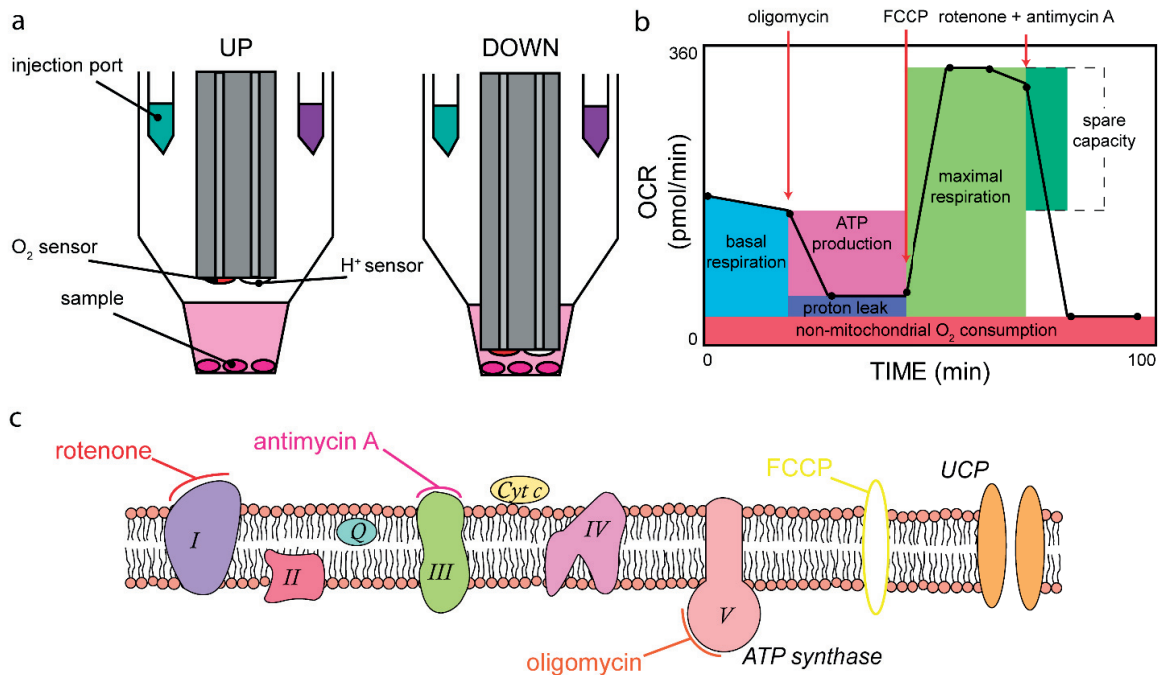


Figure 2 Bioenergetic studies based on the Extracellular Flux Analyzer by *Seahorse Bioscience*. a) Cross-sectional view of a single well at the bottom, on which cells are plated. The sensor sleeves are visible as well as the two embedded fluorophores (red and white spots), for oxygen and hydrogen ion sensing. Two injection ports allow reagent injections. Upward and downward positions are illustrated. b) Typical protocol and involved compounds for the measurement of bioenergetic parameters via the oxygen consumption rate (OCR). c) Schematics of the electron transport chain, highlighting the sites where the inhibition by the specific compounds, such as oligomycin, rotenone and antimycin A, takes place.

and to allow real time measurements. Injection ports are also used for subsequent injections of reagents, such as inhibitors or substrates, enabling studying their effects.

As shown in Figure 2b, this type of technology enabled the direct investigation of important bioenergetic parameters of mitochondria in terms of oxygen consumption, such as basal respiration, proton leak, ATP turnover, maximal respiration, spare respiratory capacity and non-mitochondrial respiration [27]. The driving biological interest in the development of the nanocalorimetric platform presented in this work is to perform similar studies, but in terms of heat production. Combining both approaches could help giving new insights into mitochondrial respiration and, possibly, into investigating mitochondria-related diseases. Typical protocols used for oxygen consumption measurements, which consist in the ordered sequential injection of specific compounds, will therefore be adapted to our metabolic heat production experiments. More specifically, four main compounds are typically used for such purpose, as indicated in Figure 2b-c:

- Oligomycin, which is an inhibitor of ATP synthase, thus blocking oxidative phosphorylation. This allows quantifying the proton leak, as protons re-enter the mitochondrial matrix only through it [27].

- FCCP, which is a proton ionophore and uncouples the electron transport chain from ATP synthesis. The maximal respiration, which depends on substrate delivery and electron transport, can thus be measured [27].
- Rotenone and antimycin A, which are inhibitors of Complex I and of Complex III, respectively. Thus, they inhibit completely the electron transport chain from the initial steps, and they allow the quantification of non-mitochondrial respiration [27].

2.2.2 Metabolic heat measurements

Heat power measurements are possible by using commercially available microcalorimeters, which allow the detection of signals as small as few μW , corresponding to temperature differences in the order of magnitude of few tens of μK [34]. Microcalorimeters and, in general, conventional calorimetric equipment, have been used for a wide range of applications in the last decades. For this reason, the presentation of microcalorimetric measurements for biological applications is discussed in more detail in Chapter 3, where detailed information on equipment working principles and on relevant biological studies will be presented.

2.3 The thermogenic function of the brown adipose tissue (BAT)

Thermogenesis is the conversion of biochemical energy into heat and mechanical work by metabolic processes within a living organism. In particular, obligatory thermogenesis relates to the basal metabolic activities, which are indispensable for cell life. In contrast, facultative thermogenesis depends on external factors, such as diet, exercise and cold exposure. Diet-induced thermogenesis may occur in the BAT, especially in conditions of overeating. Exercise-induced thermogenesis occurs in the skeletal muscles due to mechanical work. Finally, cold exposure may induce shivering thermogenesis in the skeletal muscles and non-shivering thermogenesis in the BAT [35].

2.3.1 Brown adipose tissue physiology and function

The BAT is made of brown adipocytes, which derive their name from the abundance of iron-containing mitochondria. They are specialized in dissipating energy in the form of heat and they are indispensable for hibernating animals and newborn mammals. Therefore, their function is rather different from white adipocytes, which store excess energy in the form of lipids [36]. This functional difference is also reflected in their morphology, as is compared in Figure 3a. White adipocytes are made of single, large lipid droplets, which are taking up most of the cell volume, while brown adipocytes contain dispersed smaller lipid droplets and much more mitochondria [37], [38]. Moreover, brown adipocytes are characterized by an extensive vascular and nerve network [36], [37].

Non-shivering thermogenesis in the BAT is possible thanks to the molecular mechanism based on the presence of a unique protein, UCP1, on the inner mitochondrial membrane of the brown adipocytes. UCP1 uncouples the chemio-osmotic gradient, generated in the mitochondrial intermembrane space by the mitochondrial electron transport chain, from ATP generation when the protons flow back into the mitochondrial matrix through ATP synthase [39]–[41]. The action of the UCP1 in

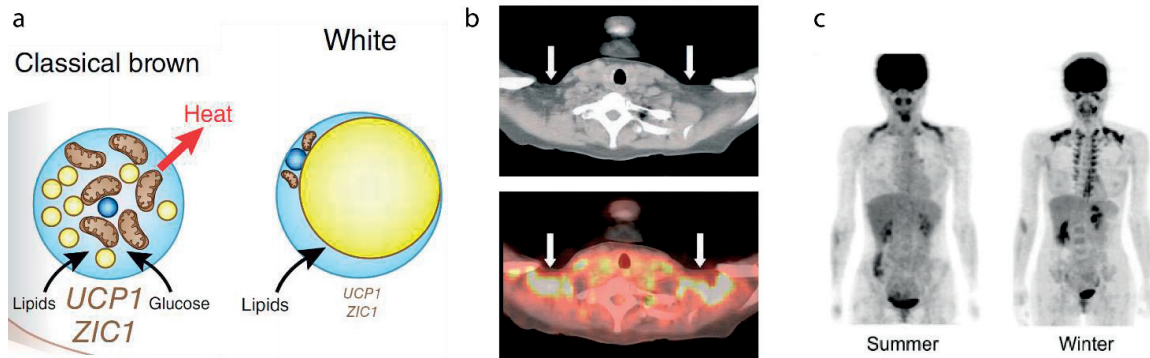


Figure 3 BAT morphology and location in adult humans. a) Morphological comparison between brown adipocytes and white adipocytes, showing the difference in fat droplet distribution and in mitochondria availability. This difference corresponds also to a functional difference, as the white adipocytes store excess energy, whereas the brown adipocytes dissipate energy to produce heat (*image reproduced from [42]*). b) Computed Tomography (CT) image and overlaid image of CT scan and of Positron Emission Tomography using fluoro-deoxy-glucose (FDG-PET) scan on a patient with endometrial carcinoma. Images were taken on the transverse plane passing through the left and right supraclavicular regions. The white arrows point to the location where unexpected FDG uptake was observed (*image reproduced from [43]*). c) CT/FDG-PET scan comparing FDG uptake on a healthy subject between summer and winter season. During winter season more locations where active BAT are observed (*image reproduced from [39]*).

brown adipose tissue hence uncouples mitochondrial respiration from ATP production, thereby increasing loss of energy in the form of heat.

2.3.2 Active brown adipose tissue in humans and its clinical implications

For long time it was believed that active BAT is present only in infants and that it progressively loses its function during growing-up. Instead, radionuclide imaging allowed recently the identification of metabolically active BAT in human adults [39], [43], [44]. At the very origin it was an accidental discovery, while investigating metastasis in lymph nodes in patients with carcinoma. Images were taken by Computed Tomography (CT), and by Positron Emission Tomography (PET) using fluoro-deoxy-glucose (FDG), an analogue of glucose, as tracer. By comparing such images, an uptake of FDG was observed, which did not correspond to neither muscle nor lymph node uptake, and it was located in the supraclavicular region (as shown in Figure 3b). This finding was not completely understood at that time and it was suggested to be related to BAT [43]. Since then, further studies were carried out on healthy adults by exposing them to cold conditions. Evidence then came along about BAT presence in adult humans mainly in the neck and in the supraclavicular region, but also in the paravertebral and suprarenal region (as shown in Figure 3c). The BAT is metabolically active as it is distinctly identified during cold exposure [39], [44].

These findings triggered much interest in conducting more focused studies on BAT, for instance in view of the possible development of new therapeutics against obesity and metabolic disorders [45]. The key point of this strategy is to reach a comprehensive understanding of BAT activation in order to directly act on the delicate equilibrium of energy homeostasis, *i.e.* on the regulation between energy expenditure and food intake [46].

2.3.3 Importance of the animal model for understanding thermogenesis

Animal models are still necessary for the discovery of new therapeutic approaches against obesity and related metabolic disorders. In this specific field of investigation, animal models allow to study directly *in vivo* the balance between food intake and energy expenditure, and to evaluate the effect of potential drug candidates. In particular, they are indispensable in order to evaluate effects such as weight loss, fat loss, and general improvements, such as insulin concentration in blood. At the same time, animal models allow the investigation of behavioral changes after treatment, such as satiety variations [47]. Different approaches against obesity are being investigated, which target the reduction of food intake, or the increase of energy expenditure or a combination of both. Animal models for such investigation are chosen accordingly, for instance, an acute model of food intake may be more adequate when the strategy is targeting food intake, while a chronic model of food intake may be more interesting when aiming at increasing energy expenditure [47]. Moreover, chronic models of food intake include dietary-induced obesity models, for example providing high-fat diet, and genetically modified models, for example evaluating the effects of overexpression, inactivation or downregulation of BAT activity.

It should be noted that animal models allow identifying drug candidates against obesity and help providing a deeper understanding of thermogenesis *in vivo*, but they have limitations too. They cannot provide conclusive therapeutic information for humans, because of the species differences in terms of pharmacokinetic disposition, efficacy and tolerability. Moreover, foreseeing rare and possibly human-specific adverse effects may be very difficult with such studies [47].

2.4 Conventional techniques for *in vivo* metabolic studies

2.4.1 The resting metabolic rate

Conventional techniques allow quantifying body metabolism as a whole in terms of the resting metabolic rate (RMR) or of the body temperature. The RMR is defined as the metabolic rate of animals during exposure to thermoneutral temperatures [48]–[50], *i.e.* to a range of temperatures at which the animal is able to maintain body temperature without significant effort, such as activating additional heat production during cold exposure or evaporation in the case of heat stress [35]. RMR is typically measured by respirometry or calorimetry, the former one, also referred to as indirect calorimetry, being predominantly used. It estimates the RMR based on the measurement of respiratory gases (oxygen and carbon dioxide) exchanged by the animal inside a closed and controlled environment [31], [35], [51]. This approach is based on a model that relates the volume of oxygen consumption and the volume of carbon dioxide production to the metabolic heat generated [52]. However, specific assumptions of this model, *e.g.* for the amount of heat released per liter of oxygen consumed by oxidation of carbohydrates, fats and proteins, are based on estimations that are not widely accepted in literature [31]. Moreover, this model cannot take into account possible anaerobic processes [35]. On the other hand, calorimetry, or direct calorimetry, measures directly the total amount of heat released by the animal. Even though, in principle, this is the most accurate technique to quantify RMR, direct calorimetry is still technically challenging as it requires the development of

custom-built platforms [31], [51], [53]. Consequently, there is an ongoing scientific debate to identify the best approach to quantify RMR [54], [55]. In particular, recent studies show that results obtained with these two methods may differ significantly, and that data relying on respirometry alone may be misleading when studying new therapies [31], [54].

2.4.2 Body temperature measurements

A different approach to quantify whole body metabolism consists in measuring the body temperature. Typically, the core body temperature of laboratory mice is measured as the rectal temperature using a hand-held thermistor probe [49], [56]. Nevertheless, as reported extensively in literature, this simple procedure may impact the temperature measurements, in particular by causing stress-induced hyperthermia [57]–[59]. Furthermore, this procedure does not allow continuous temperature measurements over time. On the other hand, the core body temperature of mice has also been measured as the intra-abdominal temperature using implantable telemetric devices. These measurements are based on commercially available capsule-like sensors of a few centimeters in size, which are implanted abdominally under anesthesia. They have been used for a variety of studies, such as studying strain, age or gender effects [60], analyzing environmental influence on temperature instability [61], and evaluating the effects of biological manipulations [62]–[64]. Similar kinds of sensors have been implanted near the brain, especially in settings where diverging rectal and brain temperatures are expected, *e.g.* during global ischemia [65].

2.4.3 Localized temperature measurements

The methods described above provide information on the global body metabolism of the animal without the possibility to distinguish local variations inside the body. More localized approaches for *in vivo* temperature measurements have been, therefore, developed in recent years. Infrared imaging has been used to monitor the mouse temperature around the BAT area [67]. However, with infrared imaging the body surface temperature is recorded, reflecting only indirectly the local BAT temperature, which is situated a few millimeters under the skin and below the white adipose tissue depot. As shown in Figure 4, localized temperature measurements have also been implemented

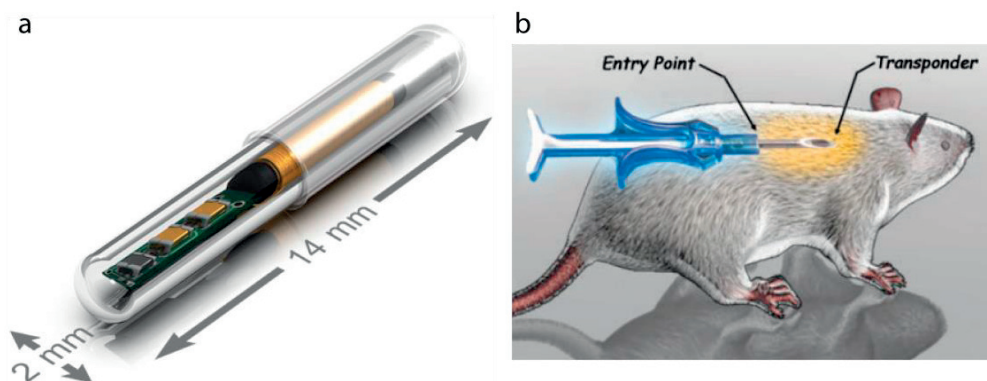


Figure 4 Telemetric temperature sensor by BMDS (images reproduced from [66]). a) Photograph of a miniature capsule-like sensor (IPTT-300, BMDS). b) Sketch showing how this type of sensor is inserted *in vivo* in a mouse, using a needle loaded with the sensor.

using commercially available miniaturized telemetric encapsulated sensors, among which the smallest is 14 mm in length and 2 mm in diameter, which is still relatively large compared to the size of a mouse body [66]. Nevertheless, temperature measurements underneath the BAT, together with other critical parameters, allowed to selectively study BAT metabolism [68], [69], to investigate the effects of drugs such as bombesin receptor subtype-3 agonists, and possibly to identify potential candidates for the treatment of obesity [70]. BAT temperature measurements also allowed the investigation of psychological stress-induced hyperthermia [71]. These studies demonstrate the applicability of local temperature measurements on mice and the great potential in the field of thermal physiology and energy homeostasis that would bring along this kind of technology.

Chapter 3 Microcalorimetry for biological applications

This chapter first provides a short overview of calorimetric techniques and then focuses on modern highly sophisticated and sensitive calorimetric equipment. The advantages of these systems are presented together with their main drawbacks, which may limit the application of the technique in the biological field. Main applications of isothermal microcalorimetry in the biomedical field are discussed, as based on recent studies using commercial equipment (a detail of such a device is shown on the right hand side [72]).



This chapter presents an introduction to microcalorimetry for biological applications. Starting from the eighteenth century, several calorimeters have been developed based on different working principles, which have greatly inspired the realization of modern calorimetric equipment. The first section of this chapter is therefore dedicated to a short historical excursus of the development of calorimetric techniques. The second part of this chapter presents examples of modern commercially available equipment that are nowadays used for calorimetric biomedical studies. Different fields of application of microcalorimetry in biology and some important results are reported in more detail in the remainder of this chapter.

3.1 Classification of calorimeters and historical excursus

Over the centuries a great variety of calorimeters has been developed, characterized by different working principles. All of them consisted of at least one calorimeter vessel, in which the sample is loaded, and a surrounding enclosure (often called thermostat). They differ from each other in terms of how the heat produced/released by the sample in the calorimeter vessel is managed and detected. According to their working principle, calorimeters may be classified into: (i) isothermal calorimeters based on compensation, (ii) isothermal calorimeters based on heat conduction, and (iii) adiabatic calorimeters [10], [73].

(i) Isothermal calorimeters operate at constant temperature, *i.e.* by ideally keeping both the calorimeter vessel and the surrounding at exactly the same temperature. One mode of operation is to compensate heat produced/absorbed by the sample and to maintain in this way the isothermal condition. Compensation may be implemented in different ways, for instance by taking advantage of a phase transition of the calorimeter substance in which the calorimeter vessel is immersed (*e.g.* Lavoisier calorimeter) [74], or by using the Peltier effect for electrical compensation (*e.g.* Tian calorimeter) [34].

(ii) Isothermal calorimeters based on heat conduction are characterized by having the thermal path between the calorimeter vessel and the thermostat carefully designed in order to minimize the thermal resistance. As the thermostat is held at constant temperature, sample heat production/absorption generates a small temperature gradient resulting in heat flow. Heat flow sensing is based on the Seebeck effect (see Chapter 5) [34]. Today, this type of calorimeter is generally referred to as “isothermal calorimeter”, even if it would be more appropriate to define them as *quasi-isothermal*, as the working principle is based on a small temperature difference between sample and thermostat (typically within few mK, but not exceeding 100 mK). In 1982, Suurkuusk and Wadsö realized the first multichannel system of this type allowing up to 4 simultaneous independent measurements [75]. The first miniaturized chip calorimeter based on heat flow measurement have been developed by *Xensor Integration* in 1990 [76].

(iii) Adiabatic calorimeters are characterized by no heat flow between the calorimeter vessel and the surroundings. This is achieved by placing the calorimeter vessel inside a vacuum container and by minimizing connections between calorimeter vessel and surroundings [34]. This type of calorimeter is not isothermal, as the working principle is based on a temperature rise of the sample.

In the following, four milestones in calorimeter development are briefly presented. A more complete historical outline and detailed descriptions are given by Sarge *et al.* [34].

3.1.1 Lavoisier ice-calorimeter

The ice-calorimeter is the first ever calorimeter, developed by Lavoisier and Laplace in 1780. The word itself for calorimeter, *i.e. calorimètre*, was also coined by Lavoisier (1789) [74], [77], [78]. It is also the first example of isothermal calorimeter as it relied on the phase transition of ice to water in order to measure the heat produced inside the device. The calorimeter was quite cumbersome, consisting of three nested compartments, as shown in Figure 5a [34]. The innermost compartment held the sample of interest in place. The middle compartment contained ice at the melting point. Heat produced by the sample melted the ice and the corresponding water was collected and weighted. The outermost compartment contained ice as well, but its purpose was to isolate the inner compartments from the environment. Heat input from the environment would melt this second layer of ice, and not the ice in the middle compartment. In the ideal case, no heat loss occurs and the weight of water collected would be proportional to the amount of heat produced by the sample. The main drawback was that such calorimeter could be used only in wintertime. Nevertheless, preliminary experiments allowed measuring the heat produced by small animals, and the first conclusions on animal respiration were drawn [10].

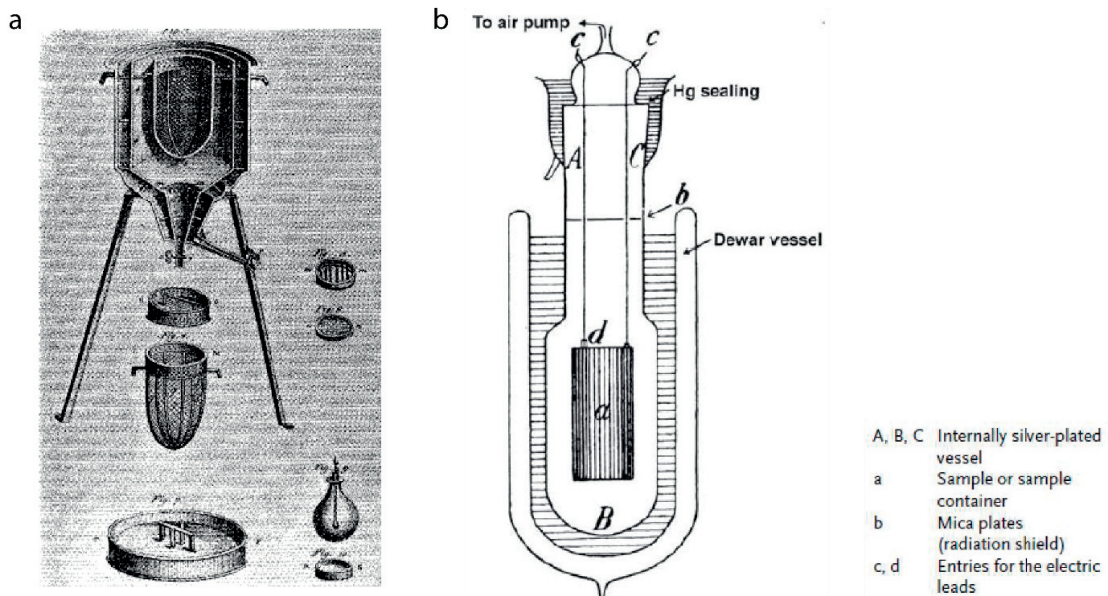


Figure 5 Schematic views of a) Lavoisier ice-calorimeter and b) the Nernst/Eucken calorimeter in which the suspended sample is heated by means of a platinum wire serving also as a resistance thermometer (*images reproduced from [34]*).

3.1.2 Nernst/Eucken calorimeter

The calorimeter developed by Eucken and Nernst in 1909 is the first example of an adiabatic calorimeter, and it allowed the measurement of the specific heat capacity of samples at low temperatures. As depicted in Figure 5b, the calorimeter vessel was suspended in an evacuated vessel, surrounded by liquid hydrogen as cooling fluid [34], [79]. The sample in the calorimeter vessel was heated up by Joule effect through a platinum wire, whereas a temperature sensor inserted into the vessel allowed recording the temperature. Under adiabatic conditions, the heat capacity of the sample may be calculated through the proportionality of the applied heat and the measured temperature increase of the sample.

3.1.3 Tian calorimeter

An isothermal calorimeter, which compensated heat production/absorption of the sample electrically, was first developed by Tian in 1923. Tian calorimeter consisted of a calorimeter vessel and an outer enclosure, which in this case was kept at constant temperature with a precision of ± 10 mK. Two thermoelectric elements connected the vessel to the surroundings, one to measure the heat flow and the other one to cool or heat the vessel by the Peltier effect. As soon as the sample produced/absorbed heat, the temperature difference between vessel and surroundings was recorded and compensated to restore the isothermal condition [34], [80]. Figure 6a reports schematically the working principle of this calorimeter.

3.1.4 Calvet calorimeter

In 1948, Calvet developed a twin calorimetric system by modifying Tian calorimeter. The Tian-Calvet calorimeter consisted of two identical calorimeter vessels, a sample vessel and a reference vessel, that were arranged symmetrically in a thermostat. Each vessel was surrounded by a thermoelectric sensing element that measured the temperature difference with the thermostat [34], [80]. In this way, temperature fluctuations of the thermostat, which influence both calorimeter units synchronously, were cancelled out, thus improving the sensitivity of the instrument by reducing fluctuations of the baseline caused by the surroundings. The resulting measured heat flow was merely generated by the thermochemical process occurring in the sample vessel. A proper balance between the heat capacities of the two vessels was achieved by filling the reference vessel with an inert control, having similar thermal properties as the sample. Figure 6b-c illustrate the working principle of the calorimeter.

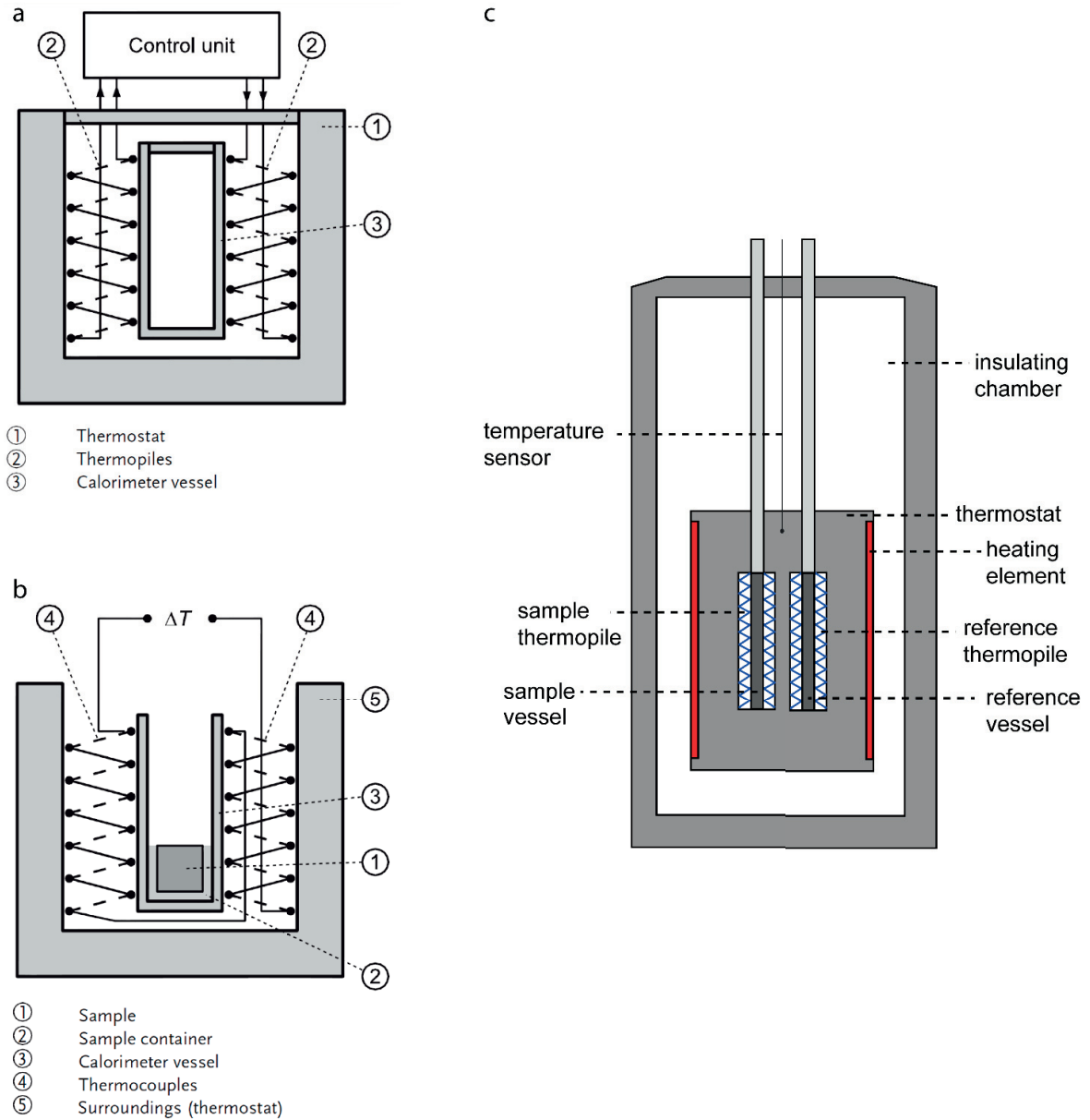


Figure 6 Working principle of the Tian calorimeter and of the Calvet calorimeter. a) Tian calorimeter, based on two independent thermoelectric elements, one using the Peltier effect for heat compensation and one using the Seebeck effect for heat measurement, respectively. b) Calvet calorimeter, showing only one unit: a single thermopile located around the sample vessel measures the sample heat flow (*both images reproduced from [34]*). c) Calvet calorimeter used in a twin configuration with a sample and a reference vessel (*image adapted from [81]*).

3.2 Modern isothermal microcalorimetry

3.2.1 Commercial isothermal microcalorimeters

Isothermal microcalorimetry (IMC) is the preferred calorimetric technology for measuring metabolic heat production of living organisms [82]. The twin configuration, inspired by the Calvet calorimeter, consisting of a measurement ampoule and a reference ampoule is mostly used, as it allows to increase sensitivity and accuracy [11]. This type of calorimeter is commercialized by different companies, such as the models TAM IV and TAM IV-48 by *TA Instruments* [72], the model C80 by *Setaram* [83], and the model μ RC by *Thermal Hazard Technology* [84]. The sensing principle is based on the thermoelectric detection of heat flow produced/consumed by any exo-/endothermic process in the sample (see Chapter 5). The reference with a nearly identical inert control reduces baseline noise by eliminating the effect of any small thermostat fluctuations on the measured heat flow.

All commercial microcalorimeters are equipped with a high-performance thermostat characterized by a high temperature stability. This feature enables accurate and sensitive calorimetric measurements for long time windows and even for the study of very slow processes, such as biomaterial degradation (drugs or food, for instance) or material stability in general. Typically thermalization at the setpoint temperature is allowed for several hours (up to about 24 hours) prior to a series of measurements to ensure maximum temperature stability. Additional thermalization of about 1 hour is required after the introduction of the ampoules in the calorimeter. Ampoule volumes of conventional microcalorimeters typically range from 1 ml [72] to up to 12.5 ml [83]. As an example for a

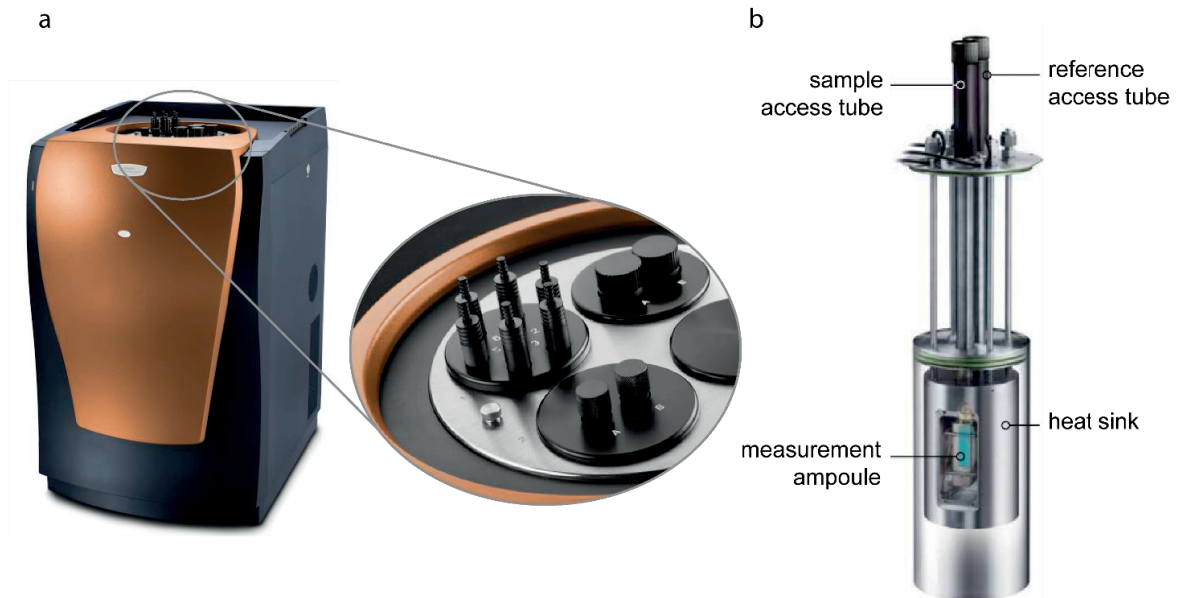


Figure 7 Isothermal microcalorimeter developed by *TA Instruments*. a) Photograph of the model TAM IV, and close up view of the insertion points of the four different calorimetric units. Thanks to the modular approach, each calorimetric unit may hold different sample volumes depending on the application, and independent parallel measurements are possible. b) Drawing of a single calorimetric unit (the “nanocalorimeter” unit) with two access tubes for the 1 ml sample ampoule (visible in the drawing), and the reference ampoule (hidden on the backside) (*images reproduced from [72]*).

commercial microcalorimeter, the TAM IV by *TA Instruments* is shown in Figure 7. With this instrument, a heat power precision of ± 100 nW is achieved when equipped with the “nanocalorimeter unit” (as named by the company, see Figure 7b) which accepts measurement ampoules of 1 ml. Another version of the same instrument is designed for high throughput (TAM IV-48 by *TA Instruments*) allowing up to 48 simultaneous and independent measurements. In this case, the ampoule size is 4 ml with a maximum precision of ± 200 nW. The sensing time constant is typically in the order of tens of seconds up to 150 seconds [83], [84]. Commercial microcalorimeters may also be equipped with open ampoules connected to a syringe pump and/or a mass flow controller, thus enabling the manipulation of the sample while the experiment is taking place (e.g. sequential injections, gas or liquid perfusion, etc.) [72].

Great efforts have been done during the last decades towards the miniaturization of calorimetric techniques, aiming at overcoming existing limitations of conventional equipment and at providing more flexible and convenient solutions for biological studies. Table 1 compares the main properties of some commercial isothermal calorimeters with that of miniaturized chip-based nanocalorimeters. The latter will be discussed in detail in the following chapter.

Calorimeter type	Thermostat stability	Sample volume	
Commercial microcalorimeter			Resolution*
TA Instruments TAM IV & IV-48 [72]	± 100 μ K (over 24h)	1-20 ml	± 100 nW ± 200 nW
Setaram – C80 [83]	± 50 mK	12.5 ml	100 nW
Chip-based nanocalorimeter			Limit of Detection*
Johannessen <i>et al.</i> [85]	-	700 μ l	13 nW
Lee <i>et al.</i> [86]	± 500 μ K (over 1h)	3.5 nl	4.2 nW
Xu <i>et al.</i> [87]	-	50 nl	22 nW
Lerchner <i>et al.</i> [88]	± 100 μ K	10 μ l	50 nW

Table 1 Main parameters of two commercial isothermal calorimeters (as indicated in the corresponding datasheets) and selected examples of chip-based nanocalorimeters (as discussed in more detail in Chapter 4). *Either “resolution” or “limit of detection” is used for commercial devices or chip-calorimeters, respectively, to express the performance of the system.

3.2.2 Advantages and drawbacks

IMC presents many advantages as listed in the following [11], [12], [73], [89], [90]:

- Simplicity. It is a label-free technique, which does not require specific sample preparation.
- Passivity and non-invasivity. The nature of the sample is not altered allowing further analyses after thermal measurements [12].

- High sensitivity and continuous real-time measurements. Heat power as low as about 0.2 μW may be detected, corresponding to the metabolic heat production of a population of only 10^5 of bacteria (assuming 2 pW of heat produced per bacterium) [11]. Real-time bacterial population growth may be monitored as heat production increases.
- Accuracy and stability. The temperature of the thermostat can be set with an accuracy lower than ± 0.1 $^\circ\text{C}$ and with a long term stability of ± 100 μK over 24 hours (see Table 1 and [72]). Typical baseline drifts for heat power signals are about 0.2 μW for 24 h [11], but may be as low as 0.04 μW for the same time window [72].
- Versatility. IMC can be applied to many applications, provided that the chemical reaction process involves an enthalpy variation [89]. Moreover, it is not limited by sample opacity, in contrary to the use of optical characterization methods [11], [12].

Some limiting parameters of IMC may be stated, in particular when considering applications involving living organisms:

- Non-specificity. Heat is a non-specific signal because of the omnipresence of thermochemical phenomena in nature. Thus, unwanted reactions, nonspecific molecular binding events and also evaporation may cause misleading interpretation of the experimental data [10]–[12], [89], [91]. Careful design of the IMC experiment may circumvent such problems.
- Long equilibration time. In order to reach maximum sensitivity and accuracy, an equilibration time of at least 1 hour after inserting the ampoule is required during which no meaningful data can be acquired [11]. Long equilibration time may also negatively affect the quality of delicate biological samples, such as mammalian cells.
- Unwanted variations of the culture environment. As living organisms consume oxygen and release different metabolic waste products, the culture environment changes during the measurement, especially for long term experiments in closed ampoules [11]. Attempts have been made, for example by using a porous seal on the ampoule, in order to allow exchange of oxygen and carbon dioxide without significant evaporation.
- Equipment cost and inflexibility. Current microcalorimeters are highly sophisticated equipment, which can not be adapted in a straightforward way to every application. For example, culture of adherent mammalian cells or of biofilms may be difficult in ampoules. Moreover, high-throughput based on multiwell plate, which are extensively used in bio-laboratories, is currently not implementable [14].

3.3 Applications of isothermal microcalorimetry in biology

IMC has been used to measure directly the metabolic heat produced by living organisms [9], [10], enabling applications in disease diagnosis, drug development, toxicology, and environmental testing [11], [12]. Some examples of applications are reported in the following.

3.3.1 Cell biology and toxicology

Several studies, starting from the 1970s, have been carried out aiming at measuring the metabolic heat produced by mammalian cells. A review by Monti in 1990 reports on different calorimetric measurements performed on healthy and diseased cells [92]. For example, considering healthy human subjects, it was found that erythrocytes are responsible for 50% of the heat production rate of blood, whereas lymphocytes, granulocytes and platelets account for a smaller amount (20%, 20% and 10% of the total heat production, respectively) [73], [93]. Interestingly, it was observed that the metabolic heat production rate may be related to the activity and progression of a disease, thus indicating some potential of calorimetry as a diagnostic and, possibly also as prognostic, clinical tool. For instance, it was found that the metabolic heat production rate of erythrocytes collected from patients with anemia was much higher than in healthy subjects [94]. Additionally, in the case of non-Hodgkin lymphoma, microcalorimetry allowed to discriminate the metabolic heat production rate of tumor cells collected from patients undergoing treatment. In fact, the heat production rate of tumor cells was higher in patients with disease progression compared to patients who responded to the treatment. This strong correlation made the calorimetric value a possible prognostic parameter [95]. Other diseases investigated were obesity, anorexia nervosa, peripheral arterial disease and diabetic cardiomyopathy [92].

Kemp published several relevant reviews on metabolic heat production of mammalian cells [96], [97]. His approach was more oriented to a multi-parametric analysis, for instance relating heat production to oxygen consumption, to carbon dioxide production or to ATP production. The calorimetric-respirometric ratio, *i.e.* the ratio between measured heat and oxygen flux, was compared for different cells types, highlighting the importance of multiple simultaneous measurements in order to discriminate between aerobic and anaerobic catabolic processes.

A more recent study by West *et al.* presented the allometric scaling of metabolic rate, *i.e.* the relationship between body weight and metabolic heat production rate, over 27 orders of magnitude in nature [98]. Figure 8 summarizes metabolic heat power data for respiratory complexes (*i.e.* mitochondria transmembrane proteins involved in cell respiration), a single mitochondrion, cells *in vitro* and *in vivo*, and whole mammal bodies. An interesting observation was that heat production rate per cell of cells cultured *in vitro* was independent from the mammal of origin, whereas cells *in vivo* show some decrease as function of the body mass. This difference was explained by considering the transport of metabolic substrates, which is increasingly constrained in macroscopic systems of increasing mass (larger mammal bodies) and is overcome in *in vitro* culture.

Recently, IMC has been used for various other applications. For instance, in the context of allergic drug reactions, the effect of specific antigens on lymphocyte proliferation was evaluated. Figure 9a shows the effect of phytohemagglutinin (PHA) on lymphocytes heat production rate for increasing concentration [99]. In another study, the metabolic heat production of cells (BHK-21 cell line) infected by foot-and-mouth disease virus (FMDV) was investigated [100]. As demonstrated in Figure 9b, it was possible to observe a clear difference in heat production rate between infected cells and

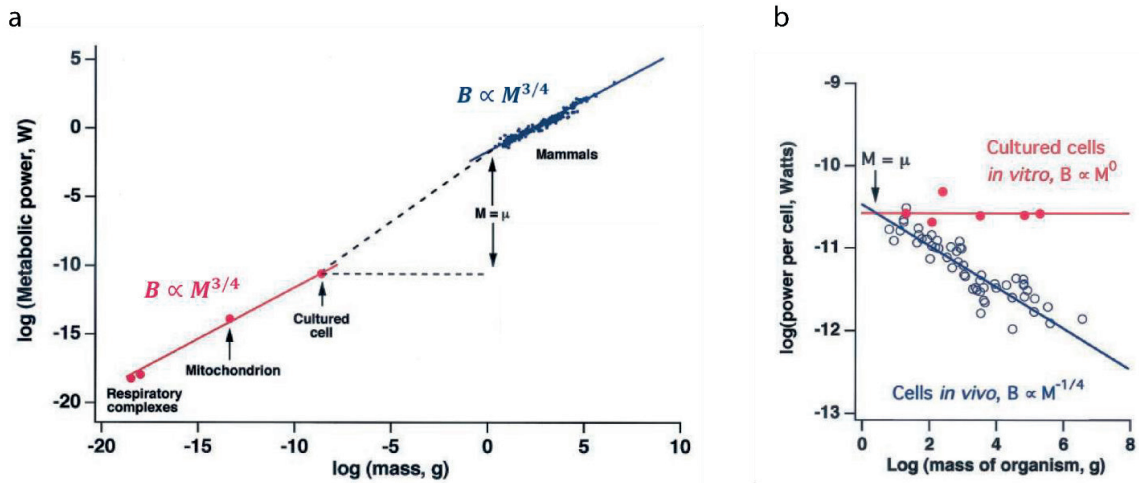


Figure 8 Metabolic heat production rate as a function of mass, covering 27 orders of magnitude, starting from the smallest size respiratory complexes through a single mitochondrion and a single cell *in vitro*, up to whole mammals. a) The metabolic power of respiratory complexes, mitochondrion and an isolated mammalian cell follows the power scaling law ($B_0 \cdot M^{3/4}$ where M is the corresponding mass and B_0 is a normalization coefficient; red solid line). Considering mammals, for a body mass $M > \mu$, where μ is the mass of the smallest mammal (*i.e.* the shrew), the metabolic power of whole mammals follows similarly the same power scaling law (blue solid line). b) Assuming the mass of a single cell M_c to be $3 \cdot 10^{-9}$ g, the calculated metabolic power per cell in mammals *in vivo* decreases as a function of the body mass of the animal, following a $M^{-1/4}$ trend (blue solid line). Instead, the metabolic power per cell of cells isolated from different mammals and cultured *in vitro* is independent from the mass of the animal of origin (red line) (*image adapted and reproduced from [98]*).

uninfected cells (curve (a) and curve (e, f) in Figure 9b). Also the effect of treatment with 1b recombinant homo interferon on infected cells was visible (curve (b-d) in Figure 9b).

The study of heat production rate of mammalian cells has been used also in toxicology. Liu *et al.* evaluated the toxic effect of hexavalent chromium Cr(VI) on human fibroblasts [101]. They observed a reduction in metabolic heat production of the fibroblasts when exposed to increasing concentration of Cr(VI) and correlated the findings with cell mortality. They also compared the calorimetric

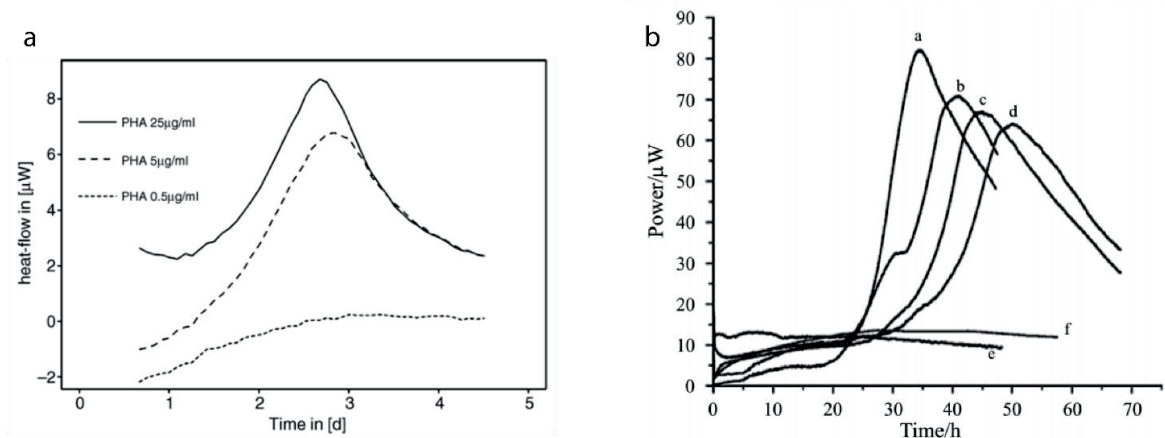


Figure 9 Heat power measurements on mammalian cells over several days. a) Heat production rate by lymphocytes due to an allergic response when stimulated at time $t = 0$ with increasing concentration of phytohemagglutinin (PHA) (initial amount of cells 2.5×10^5) (*image reproduced from [73], which was modified from [99]*). b) Heat power rate of virus-infected BHK-21 cells at time $t = 0$ at 37°C : (a) FMDV-infected without interferon; (b, c, d) FMDV-infected with increasing concentration of interferon at 0.2, 0.5, 1.0 $\mu\text{g}/\text{ml}$, respectively; (e) uninfected with 1.0 $\mu\text{g}/\text{ml}$ of interferon; (f) uninfected without interferon (*image reproduced from [100]*).

results with cytotoxicity assays (WST-1), suggesting that mitochondrial respiration may be impaired by Cr(VI). The effect of cell exposure to different materials used for biomedical implants was also investigated in order to evaluate the potential of new materials [12]. For example, Doostmohammadi *et al.* demonstrated that well-known ceramic biocompatible materials, such as 63S bioactive glass particles and bone-derived hydroxyapatite particles (diameter < 50 μm), had no significant effect on the metabolic heat production rate of yeasts (*Saccharomyces cerevisiae*) and of human chondrocytes, which is consistent with the known non-toxicity of these materials [102].

3.3.2 Microbiology and antibiotic testing

The heat production rate of bacteria has been extensively measured by IMC. In particular, Braissant *et al.* demonstrated how heat production rate measurements on *Escherichia coli* (*E. coli*) under controlled conditions, in culture medium containing glucose and lactose, could be used to identify individual contributions of glucose respiration, glucose fermentation and lactose fermentation to bacterial growth [11] (see Figure 10). At initial phases of bacterial culture, bacterial metabolism relies mainly on glucose respiration, *i.e.* on the catabolic pathway during which glucose and oxygen are consumed in order to obtain chemical energy in the form of adenosine triphosphate (ATP) together with carbon dioxide and water molecules (see Chapter 2). After several hours, oxygen is depleted and energy is produced through glucose fermentation, during which glucose is consumed without needing oxygen, yielding less efficiently energy and lactic acid. Finally, in the last stage, when all glucose is consumed, bacteria use the lactose available in the culture medium to produce energy through lactose fermentation: lactose is first hydrolyzed to galactose and glucose, then the products undergo the fermentation process, providing again chemical energy and lactic acid. This last two-fold process is observable in the original data, even though only a single Gaussian component was considered in the fitting model. As soon as all required nutrients start to be depleted, bacteria metabolism gradually declines.

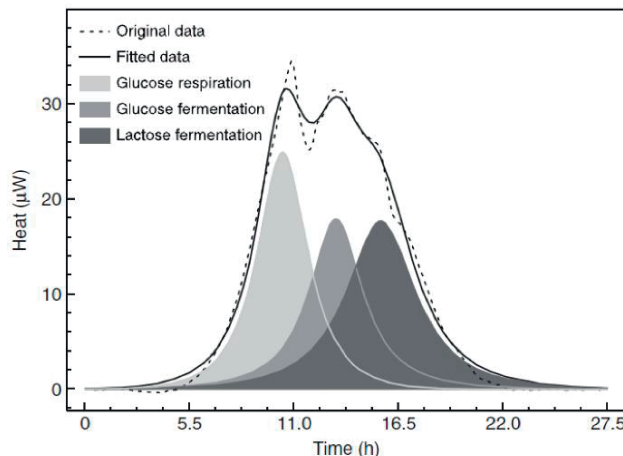


Figure 10 Heat power measurements on *E. coli* (DSM 10142) in M9 medium containing glucose and lactose. Heat production initially increases due to exponential bacterial growth (\approx from hour 5 to 10), and eventually declines (\approx from hour 15) due to a lack of resources in the closed calorimeter ampoule. Three individual peaks, corresponding to glucose respiration, glucose fermentation and lactose fermentation, were obtained by deconvolution, based on the model by Monod (1949) [103] (*image reproduced from* [11]).

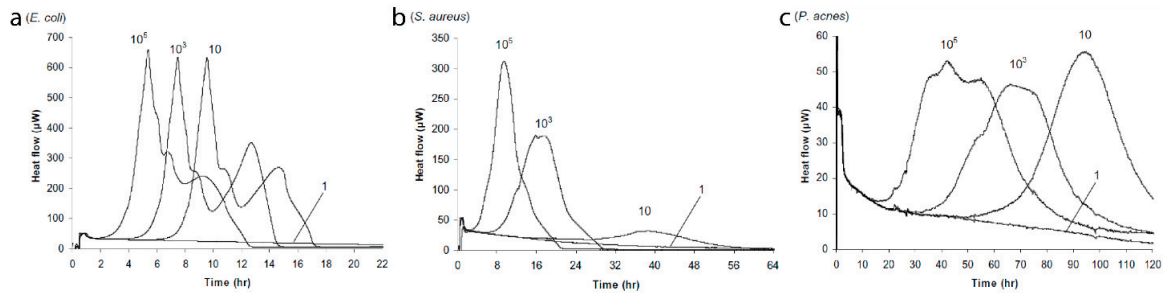


Figure 11 Heat power measurements on platelet suspensions inoculated with increasing concentrations of bacteria, ranging from 1 to 10^5 CFU per ml of platelets. Calorimetric measurements on *E. coli* a), on *S. aureus* b) and on *P. acnes* c) are shown, respectively. The heat flow measured in all curves initially increases, corresponding to the exponential bacterial growth, and, for increasing concentration of bacteria, the heat flow peak is reached earlier in time. Then, the heat flow decreases as bacterial growth declines. In particular, the shape of the curves appears to be a characteristic for each bacterial species (*image reproduced from* [105]).

More often, microcalorimetry has been used for the detection of bacterial infection or contamination [11], [12], [104]. For instance, Trampuz *et al.* were able to discriminate between different degrees of bacterial contamination on human blood platelets, suggesting the use of microcalorimetry for testing platelet products before transfusion, potentially allowing the reduction of transfusion-related sepsis and of the sample shelf life [105]. Figure 11 shows the evolution of the heat production rate over time, when platelets were inoculated by *E. coli*, *Staphylococcus aureus* (*S. aureus*), and *Propionibacterium acnes* (*P. acnes*), respectively, for concentrations from 1 to 10^5 colony forming units (CFU) of bacteria per ml of platelet suspension. Defining the detection time as the time at which the heat flow rises over $10 \mu\text{W}$, the detection of *E. coli* contamination took less than 10 hours for an initial concentration of 10 CFU and about 4 hours for 10^5 CFU. In contrast, a contamination with 10^5 CFU of slow growing *P. acnes* was detected after about 40 hours.

In the context of antibiotic testing, microcalorimetry allowed the identification of the minimal inhibitor concentration (MIC), *i.e.* the lowest concentration required to inhibit bacterial growth after overnight incubation. Several antibiotics have been tested on *E. coli* and *S. aureus* [106]. Heat power measurements on bacteria exposed to subinhibitory concentrations of different antibiotics also allowed to discriminate between different antimicrobial modes of action, for example to distinguish between bacteriostatic antibiotics, which stop bacteria reproduction, from bacteriocidal antibiotics, which directly kill the bacteria [106]. Figure 12 shows a comparison of heat power measurements on *E. coli* exposed to two different antibiotics, which are both cephalosporins that act in disrupting the bacterial cell wall. The MIC was correctly estimated by heat power measurements as 2 mg/l and 8 mg/l, respectively.

Microcalorimetric measurements on bacteria also allowed investigating resistant bacteria strains, which became a critical issue in the medical field and in clinical infrastructures. Von Ah *et al.* reported on microcalorimetric measurements on two different types of *S. aureus* bacteria, the methicillin-susceptible *S. aureus* (MSSA) and the methicillin-resistant *S. aureus* (MRSA) [107]. They were able to determine the MIC and also to identify the resistant bacteria within 4 hours, which is significantly shorter than the time required by standard techniques (typically 24 hours). Figure 13 reports the comparison of the heat power curves for the two bacterial strains.

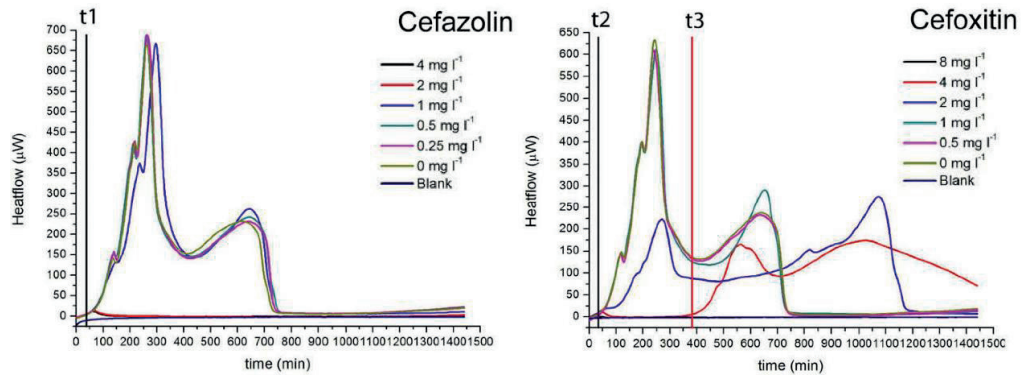


Figure 12 Heat power measurements for *E. coli* (ATCC25922) incubated at 37 °C, when exposed to increasing concentrations of Cefazolin or Cefoxitin, respectively. For Cefazolin, the minimal inhibitor concentration (MIC) is 2 mg/l (red line), as it is the lowest concentration for which no heat flow increase is observed, corresponding to no bacterial growth. For subinhibitory concentrations (in this case from 0 to 1 mg/l), bacterial growth occurs and is not affected by the exposure to the antibiotic. In particular, no significant difference in the shape of the curve is observed: for example, the time delay (t1) to reach a detectable heat flow signal is the same, as well as the initial maximum peak, corresponding to initial exponential bacterial growth. For Cefoxitin, instead, the MIC is 8 mg/l and significant differences are observed between heat flow curves of *E. coli* exposed to subinhibitory concentrations of antibiotic (from 0 to 4 mg/l). In particular, for concentrations lower than 1 mg/l, the heat flow curve and, thus, the bacterial growth, is not affected by the exposure to the antibiotic. For higher subinhibitory concentrations (2 and 4 mg/l), the initial maximum peak is significantly smaller. Moreover, for a concentration of 4 mg/l (red line) the time delay to reach a detectable heat flow signal shifts from t2 (the time delay observed when bacterial growth is unaffected) to t3. Thus, starting from a concentration of 2 mg/l, Cefoxitin has an effect on bacterial growth, but only for 8 mg/l it completely inhibits the growth (*image adapted from [106]*).

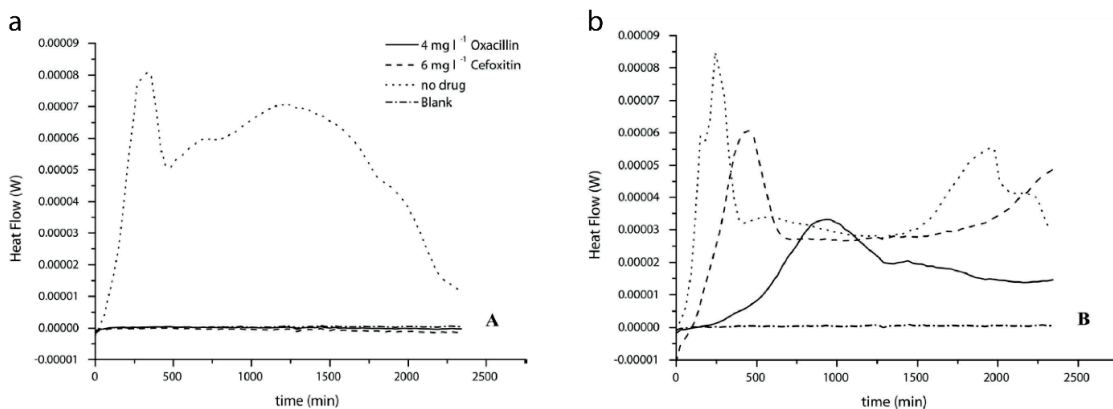


Figure 13 Heat power measurements on a) *S. aureus* ATCC 25923 (MSSA, methicillin-susceptible), exposed to different concentrations of antibiotics, and on b) *S. aureus* ATCC 43300 (MRSA, methicillin-resistant), exposed to the same concentrations of antibiotics. In the first case, heat flow curves indicate bacterial activity only when bacteria are not exposed to the drug: in particular, the initial heat flow increase corresponds to the bacterial exponential growth. In the latter case, heat flow curves are observed even after exposure of the bacteria to sufficiently high concentrations of antibiotics. The observable effect of the antibiotic is a reduction of the heat flow peak, thus indicating a reduction in the bacterial activity. The blank is uninoculated bacteria medium (*image reproduced from [107]*).

3.3.3 Multicellular organisms

IMC has been used to study the metabolic heat production of multicellular organisms, such as *C. elegans* nematodes, a non-parasitic roundworm (a more detailed description of *C. elegans* will be given in Chapter 6). Braeckman *et al.* have studied the metabolic activity of ageing nematodes, looking simultaneously at different parameters, such as oxygen consumption, carbon dioxide production, metabolic heat production, ATP and ADP content [108]. Figure 14a reports the heat production rate of worms suspended in culture medium containing *E. coli* as a food source and antibiotics (250 $\mu\text{g}/\text{ml}$ of streptomycin and 250 U penicillin) to suppress bacterial growth. They also compared the heat production rate of worms when suspended in liquid medium and when cultured on the surface of the same medium solidified with agar (Figure 14b). They observed that the second culture condition, which reproduces better the actual living conditions in nature, corresponds to an about 60% higher heat production rate.

The same research group carried out studies investigating the metabolism during the different developmental stages of *C. elegans* growth [109]. Interestingly, they observed that the heat power normalized by the protein content is higher in juvenile stages, reaching the maximum at larval stages L2-L4, and then decreasing significantly during adulthood. They also measured the heat power production of worms during “dauer stage”, which is an apparently non-ageing larval stage that worms may enter by arresting development under unfavorable environmental conditions, thus allowing them to survive several times the normal life span. In dauer stage, heat power was found to be significantly lower compared to worms of the same age that develop normally. Additionally, heat power was measured when worms were leaving the dauer stage, showing a sudden increase in metabolism. Figure 15 presents these results.

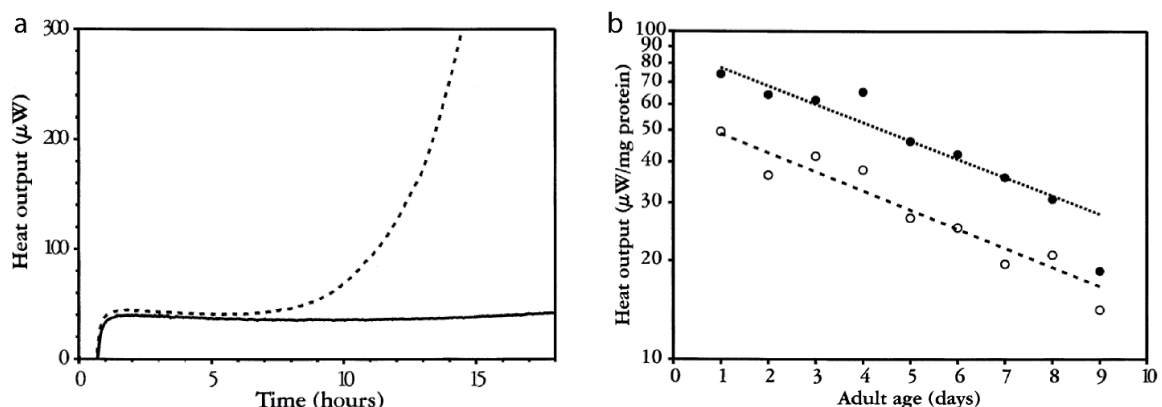


Figure 14 Heat power measurements on *C. elegans* nematodes. a) Measurements on a suspension of about 3000 13-day-old worms at 25 °C, in presence (full line) or absence (dotted line) of antibiotics (0.25 mg/ml streptomycin, 250 U penicillin). The increase in heat power is due to bacterial growth. b) Comparison of heat output of worms suspended in liquid culture medium (open circles) and on worms cultured on the same solidified medium (closed circles) (*images reproduced from* [108]).

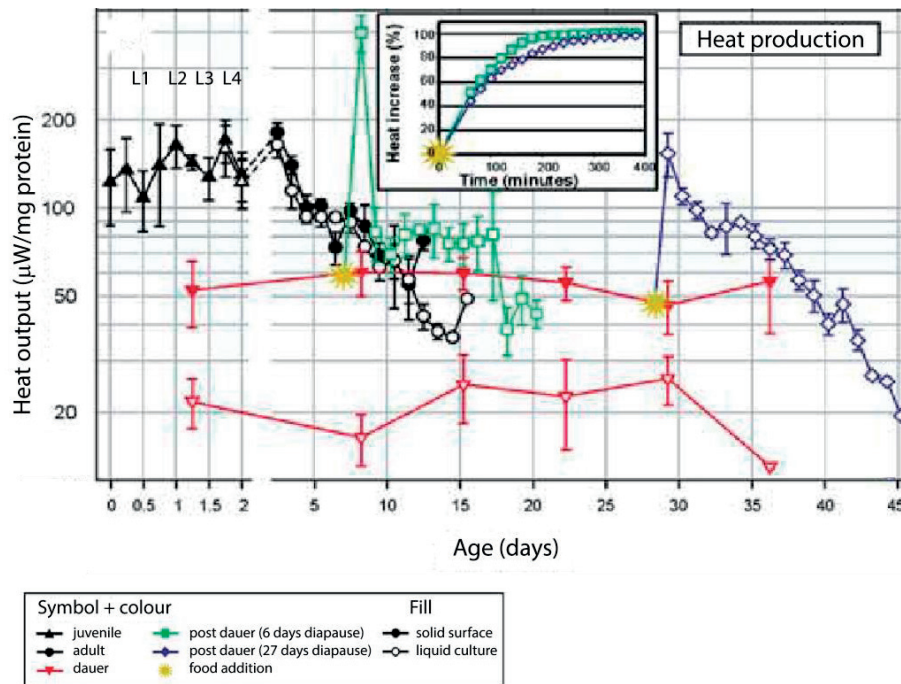


Figure 15 Heat power, normalized by the protein content (mass), measured on *C. elegans* nematodes during the whole life cycle. The insert shows the real time heat power during worm recovery from dauer stage, induced by food addition (the first 60 minutes were not measured because of the time required for equipment stabilization). L1, L2, L3 and L4 correspond to the four larval stages (*image reproduced from [109]*).

More recently, Manneck *et al.* demonstrated the applicability of IMC to study drugs against parasitic worms, such as *Schistosoma mansoni* [110]. The standard technique to evaluate drug effects against this parasitic worm is microscopic inspection, which is labor-intensive and may also depend on the observer's subjective interpretation. The authors obtained a good correlation between morphological readouts of viability and microcalorimetric data, and also were able to identify drug effects that were not previously observable.

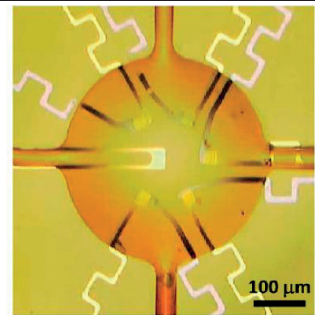
3.3.4 Other fields of application

IMC has been used in the field of soil and environmental sciences [11], [104]. Rong *et al.* presented a review, summarizing the different types of study carried out by IMC in this field [111]. More specifically, the soil may be considered as a unique ecosystem, where numerous physical and biochemical reactions are taking place and whose health is critical for the environment. Calorimetric measurements were implemented for measuring the soil microbial activity (bacteria and fungi are the most active components in soils), and also to investigate the effect of different parameters, such as moisture, soil organic matter content, and the effect of agricultural activities. Additionally, IMC has been used in environmental toxicology to study the effect of pesticides and metals, and to evaluate the bioremediation capacity of soils.

Several applications in the field of food science have been reported in a review paper by Wadsö and Galindo [112]. They span over a wide range, from studying fermentation processes to predicting shelf life and preventing microbiological spoilage.

Chapter 4 Nanocalorimetry: an emerging technique for metabolic studies

This chapter summarizes the state-of-the-art of miniaturized calorimeters, so-called nanocalorimeters or chip calorimeters, including information on performance, fabrication processes, implementation mode and some applications, especially with respect to biologically oriented experiments. For this purpose, nanocalorimeters reported from literature have been classified according to sensing principle, sample-handling strategy, and sensing configuration. The photograph on the right-hand side shows a top view of a thermopile based nanocalorimeter [113].



4.1 General aspects of miniaturized calorimeters

The development of nanocalorimetric devices aims at overcoming the major limitations of conventional calorimeters and microcalorimeters. This is possible thanks to the combination of small sample volumes in the nL- μ L range with highly sensitive miniaturized sensors, thus enabling the detection of heat signals as low as some tens of nW [114]. In particular, the prefix “nano” is used for calorimeters that may detect heat power signals in the nW range, whereas “micro”-calorimeters are designed for and limited to the μ W range. Moreover, nanocalorimeters are often called chip-calorimeters, as they are based on a miniature chip sensor. The versatility of nanocalorimetry has now been demonstrated by a wide range of applications in the biomedical field [115]. More specifically, nanocalorimeters have been used for thermochemical studies at the molecular level, investigating biomolecule interactions, enzymatic assays, protein unfolding and denaturation and protein crystallization [115]–[119]. At the cellular level, direct measurements of the metabolism of single cells, populations of cells, biofilms and multicellular organisms became possible [114], [115], [120], [121].

The working principle of the type of nanocalorimeter we have used will be discussed in more detail in chapter 5. Here, three main parameters will be identified in order to classify the great variety of nanocalorimeters available in literature:

(i) The sensing principle

Heat sensing in nanocalorimeters is mainly based on thermopiles, *i.e.* serial arrangements of several thermocouples [113], [121]–[125]. A few nanocalorimeters use resistive sensors, *e.g.* thermistors, for heat sensing [119], [126]. Nanocalorimeters generally comprise a thin membrane with integrated sensing elements. The membrane has extremely low heat capacity and high thermal resistance, and is suspended on a thicker silicon frame [115], [127]. The sensing principle of thermopile-based nanocalorimeters relies on the thermoelectric (Seebeck) effect [128]–[130]. Thin film leads of two different materials form the junctions on the sensing area and close to the heat sink, respectively (typically called hot and cold junctions). The voltage signal generated is proportional to the thermal gradient and determined by the Seebeck coefficient. The ratio of voltage signal vs temperature difference defines the temperature sensitivity of the device (generally measured in mV/K). Moreover, connecting several thermocouples in series allows to significantly improve the sensitivity [127]. Thermistor-based nanocalorimeters use ceramic or semiconductor sensors whose resistivity depends strongly on temperature [130]. In this case, best fitting of the non-linear relationship of resistance vs temperature is obtained with the Steinhart-Hart equation, which is a 3rd order polynomial equation [131]. However, when working within a small temperature range, it is possible to make a linear approximation characterized by the temperature coefficient of the resistance.

In both cases, additional resistive heaters are microfabricated on the same membrane in order to calibrate the sensor by Joule’s effect. The ratio of the voltage recorded by the sensor and the corresponding dissipated resistive heat power is expressed by the power sensitivity coefficient (measured in V/W) [127]. It is worth to note that the sensitivity of a device strongly depends on the thermal insulation from the external environment.

(ii) The sample handling strategy

Batch-mode, open-chamber nanocalorimeters may be distinguished from flow-through mode, closed-chamber nanocalorimeters. In the batch-mode configuration an open-chamber or a small well holds the sample in thermal contact with the sensing element that is located on the membrane [121], [132]–[135], whereas in the flow-through configuration a closed-chamber is used, which is typically interfaced to microfluidic structures in order to allow dynamic sample/reagent injections and waste removal [113], [117], [124], [125], [136]–[138]. The latter approach is more suitable for integration and automation of measurement protocols. However, fluidic connections to the surroundings introduce additional heat loss paths and may worsen the thermal insulation to the environment, thus affecting the sensitivity of the device [113], [115]. Among others, one critical parameter for the device performance is the membrane thickness of the thermopile sensor. Thinner membranes have higher insulation but are also more fragile, whilst thicker membranes are more robust. In general, the thickness ranges from tens of nm for thinner membranes, to tens of μm for thicker membranes [122], [127].

(iii) The sensing configuration

Nanocalorimeters may rely on single measurements, measuring a temperature difference between the sample and the environment or on twin configurations providing differential measurements being between the sample of interest and a reference [118], [125], [126], [139]. The critical aspect of the first configuration is the accurate control of the temperature of the environment, as temperature fluctuations adversely affect sensitivity [140]. In the second configuration, instead, the critical issue is to guarantee that sample and reference are exactly under the same thermal conditions, so that measured temperature differences between the two are imputable only to the heat generated by the sample. The advantage of differential measurements is that environmental temperature fluctuations affect much less the performance of the device. However, implementing dual measurements is more complex with respect to device design and experimental protocols.

4.2 State-of-the-art of miniaturized calorimeters

4.2.1 Thermopile-based nanocalorimeters with open chambers

Johannessen *et al.* developed a nanocalorimeter based on a 800 nm thick silicon nitride membrane with an outer size of 300 x 300 μm^2 [121], [135], [141]. As shown in Figure 16a, the thermopile is made of a series of ten gold-nickel thermocouples, which are radially distributed around a central circular region, on which a nickel resistive heater is integrated. In particular, the cold junctions of the thermopile are peripherally located and kept at ambient temperature, whereas the hot junctions are closer to the center of the membrane. The resulting temperature sensitivity is 220 $\mu\text{V}/\text{K}$. A polyimide open microchamber is integrated on top of the membrane to hold the sample in the central region. It has an inner diameter of 200 μm and a total volume of 700 μl . The setup comprises also an external water circulating system used to keep a constant ambient temperature, and an additional transparent enclosure to improve insulation from outside. Electrical calibration carried

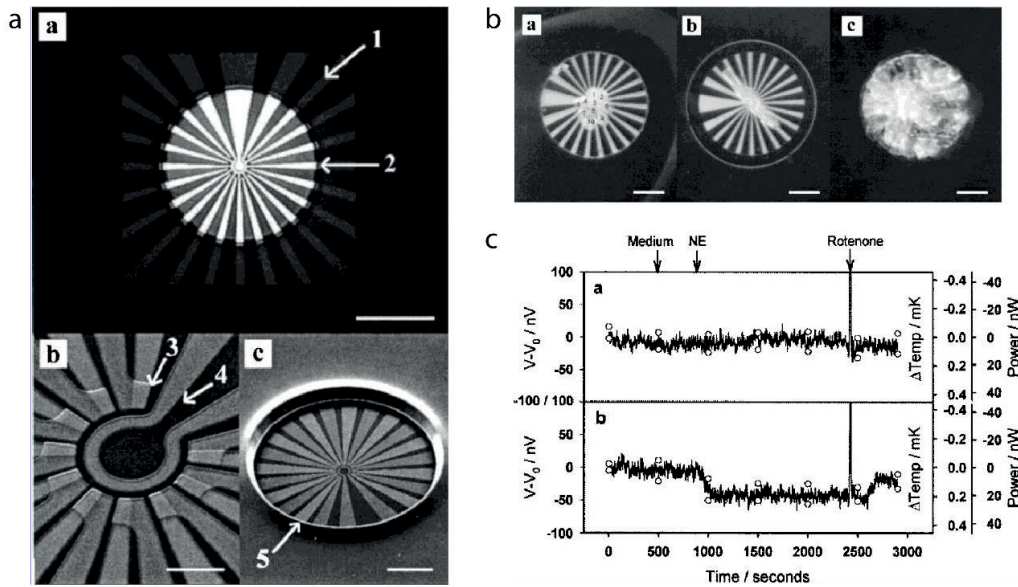


Figure 16 Nanocalorimeter developed by Johannessen *et al.* a) View of the sensing membrane showing 10 radially distributed thermocouples, a resistive heater, and the open microchamber. b) Top view of the open microchamber, loaded with 10 isolated brown adipocytes, a single cardiomyocyte, and 20 cardiomyocytes, respectively. c) Heat power measurements on 10 cultured brown adipocytes, after the injection of 1.4 μM of noradrenaline (NE) and 14 μM of rotenone: the first measurement is a control, the second is the actual experiment (*images reproduced from [121]*).

out using the integrated nickel heater allowed to span a range of heat power values from 1 to 750 nW, with a limit of detection of 15 nW and a thermal time constant of 12 ms [135].

Preliminary experiments aimed at measuring the heat generated during the hydrolysis of hydrogen peroxide catalyzed by catalase, and at quantifying catalase activity on mouse hepatocytes [141]. For this purpose, a micromanipulator was used to position cells on the measurement chamber, and a layer of paraffin was applied on top of the sample in order to prevent evaporation. Injections were carried out by a micropipette, which was filled with a few pl of the reagent of interest. Later results demonstrated the applicability of such device to metabolic studies on small cellular populations down to 10 cells, as shown in Figure 16b [121]. Brown adipocytes have been tested and the effect of noradrenaline (NE)-induced thermogenesis was successfully measured, as reported in Figure 16c [121]. NE is a hormone released by the cold- or diet-stimulated sympathetic nervous system, which induces thermogenesis in the adipocytes by interacting with the adrenergic receptors (β , α_2 , and α_1), being the β -adrenergic pathway the most significant for thermogenesis [142]. The average metabolic heat production of NE-stimulated brown adipocytes is reported as 1.63 ± 0.73 nW per cell. Rotenone was also injected in order to measure metabolic heat reduction, resulting from complete inhibition of the mitochondrial respiration [121]. Similar experiments were carried out on cardiomyocytes and on mitochondria from rat liver, whose thermogenic capacity was stimulated by the injection of carbonyl cyanide *m*-chlorophenyl hydrazone (CCCP), which is an uncoupler agent of mitochondrial respiration similar to FCCP. The reported CCCP-induced heat production is 1.71 ± 0.94 nW per cell and 0.12 ± 0.9 mW/mg, respectively [121].

Xu *et al.* presented a thermopile-based open-chamber nanocalorimeter, obtained by adapting a commercially available infrared (IR) sensor (S25 from *Dexter Research Center, Inc.*) [134]. Such sensor is based on a 1.5 μm thick silicon nitride-silicon oxide membrane on which 20 bismuth/antimony thermocouples are connected in series, giving a temperature sensitivity of 480 $\mu\text{V}/\text{W}$. A microchamber on top of the membrane holds sample volumes of a few nl up to 50 nl (Figure 17a-b). No specific control over the ambient temperature is carried out, only a two-layer insulating system is used for thermal shielding from the environment. The most critical aspect of such system is to minimize evaporation. For that purpose, the measurement chamber was closed with a cover glass on which a hole was machined to allow access and injection by a micropipette. Oil was used to locally seal interfacing parts. Chemical calibration consisted in measuring the heat of mixing of two pairs of acid and base (H_2SO_4 with HEPES buffer and HCl with NaOH, respectively). Initially a 50 nl droplet was placed on the membrane, whereas 1 nl droplets were injected subsequently with the micropipette. The documented power sensitivity was 2.90 V/W, the time constant was 1.1 s and the limit of detection was 22 nW. Further improvements of this nanocalorimeter consisted in minimizing sample volumes down to 2.5 nl, resulting in an enhanced power sensitivity of 60 V/W and a much smaller time constant of about 100 ms. Heat of reaction values down to 1.4 nJ were reported when measuring the temperature variations induced by the injection of 25 pl droplets of HCl into 2.5 nl of NaOH [132]. An example is shown in Figure 17c.

An example of thermopile-based open-chamber calorimeter based on a twin configuration is given by Verhaegen *et al.*, who presented a calorimeter consisting of a 20 μm rubber-based membrane with 666 polysilicon-aluminum thermocouples in series, resulting in a temperature sensitivity of 130 mV/K [133]. Two open channels, etched into bulk silicon, are located on each side of the thermopile, one on the cold junctions and the other one on the hot junctions. A thin layer of silicon is kept over most of the rubber membrane, except for some regions in order to improve insulation. The open channels can hold sample volumes of several tens of μl up to 600 μl . Figure 18a-b shows the main components of such calorimeter. Electrical calibration, using an integrated resistive heater, with channels filled with 50 μl of water allowed to calculate a power sensitivity of 20 V/W and a time constant of 70 s. Some preliminary results were presented for experiments on kidney cells at room

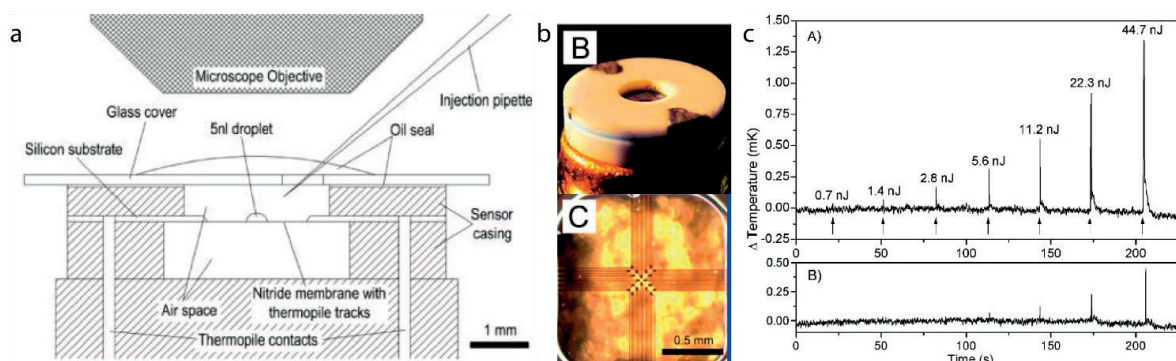


Figure 17 Nanocalorimeter developed by Xu *et al.* a) Schematics showing the working principle of this open-chamber calorimeter, where a 5 nl droplet was positioned on the suspended nitride membrane. b) Photographs showing the thermopile chip casing (B) and a top view of the membrane with thermopiles (C). c) Heat of mixing measurements consisting of sequential injections of 25 pl of HCl into a 2.5 nL drop of NaOH (plot A), and the control (plot B) (*images reproduced from* [132]).

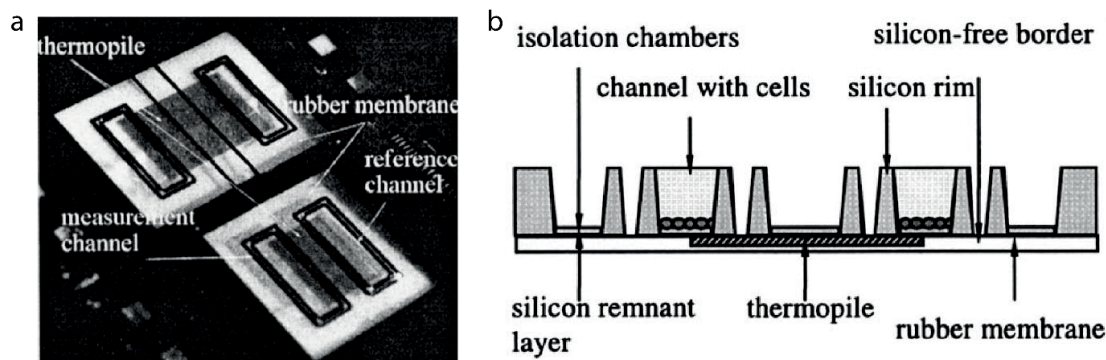


Figure 18 Nanocalorimeter developed by Verhaegen *et al.* a) Photograph of two prototype sensors consisting of a rubber membrane and two distinct open channels for differential measurements. b) Corresponding schematic view, showing also the location of the thermopile and of the isolation chambers (*images reproduced from [133]*).

temperature. About 10^6 cells were cultured on a carrier membrane, which was then placed in the measurement channel filled with 100 μl of culture medium. The reference channel, instead, was filled only with 100 μl of culture medium. Metabolic heat was quantified as 330 pW/cell, and variation on heat production was observed when stimulating chemical transport mechanisms across cellular membrane.

4.2.2 Nanocalorimeters with microfluidics for μl sample volumes

Lerchner *et al.* developed a thermopile-based nanocalorimeter for biochemical applications and worked with tens of μl of sample volumes [123], [140], [116]. Over the years, this device was applied to a wide range of applications, in particular for the study of metabolic activities of living organisms and biofilms. Initially, it was used for the study of the heat generated by enzymatic assays, such as the oxidation of glucose, the oxidation of ascorbic acid, and the hydrolysis of penicillin G [116]. The nanocalorimeter is based on a 1 μm thick silicon nitride membrane on which 118 bismuth-antimony thermocouples are located, together with a nickel-chromium resistive heater [116], [123]. Furthermore, a few μm thick layer of SU-8 photoresist was added on the top of the membrane, both to improve the mechanical stability of the silicon nitride membrane, and to provide a passivation layer with high chemical stability [123]. As shown in Figure 19a, such structures were replicated four times, in order to obtain four independent sensing areas. The four thermopile modules are aligned along a flow channel, so that it was possible to investigate the different stages of mixing from the initial mixing close to the inlet, to the ideally completed mixing close to the outlet. The system was fixed on a copper heat sink. Figure 19b-c shows the interfacing of the microfluidic structure with the thermopiles. The removable poly(methyl methacrylate) (PMMA) chip consists of a microchannel (20 mm in length, 1 mm in width, 0.5 to 1.2 mm in height), which is closed at the bottom by a 50 μm PMMA foil. A thin layer of paraffin film was used to guarantee good thermal contact between the PMMA foil of the microfluidic chip and the thermopile membrane. In this way, the uncontaminated chip could be reused for subsequent experiments. The PMMA structure also has two inlets and one outlet machined in the chip.

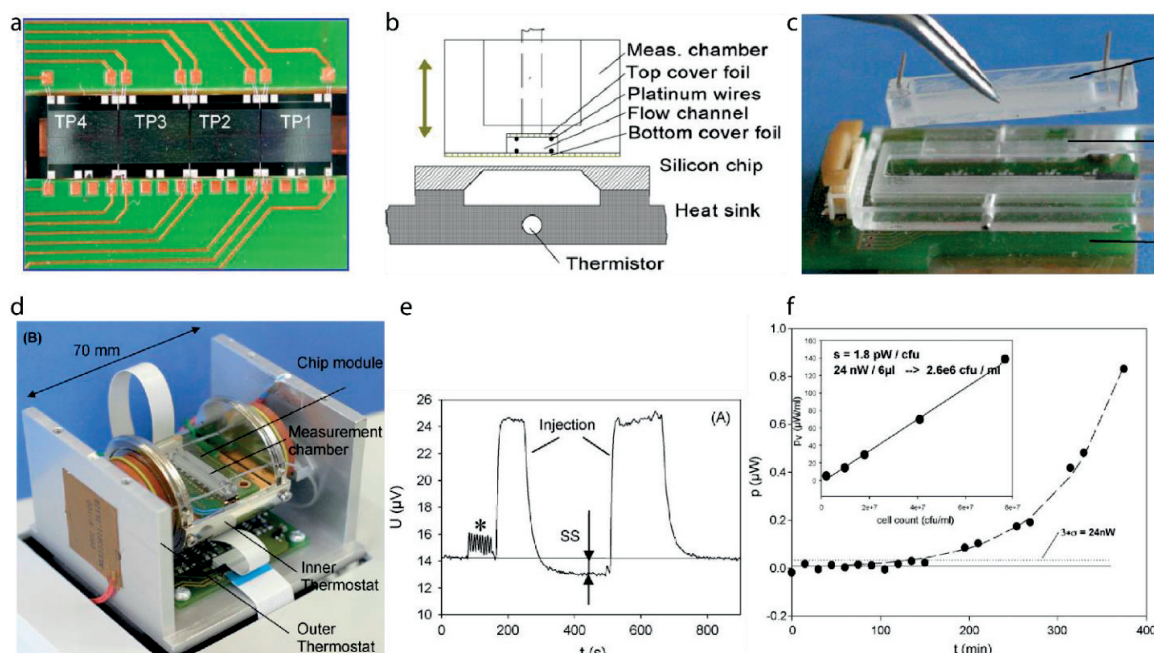


Figure 19 Nanocalorimeter developed by Lerchner *et al.* a) Photograph showing four distinct thermopile sensors (reproduced from [116]). b) Cross-sectional view of the nanocalorimeter showing the PMMA frame and microchannel interfaced with the nanocalorimeter chip and the heat sink. Replaceable top and bottom cover foils are used to minimize contaminations between experiments. c) Photograph showing the removable PMMA microfluidic assembly. d) Photograph showing the double nested thermostat for high temperature stability. e) Experiment carried out on *Staphylococcus aureus* bacteria in suspension: first, after injection of the bacterial suspension, a large injection artefact is observed; the signal shift after stopping the flow (SS indicated in the plot) is due to bacterial metabolism; subsequently, the buffer solution is injected, allowing to restore the initial baseline (after another injection artefact). f) Measurement of metabolic heat produced by a growing population of *Staphylococcus aureus* bacteria (corresponding to a time variation of SS in e). The inset shows metabolic heat as a function of bacteria concentrations (all other pictures reproduced from [114]).

In this context, it was observed that fast temperature perturbations may induce significant signal fluctuations, *i.e.* the heat power resolution strongly depends on the precise temperature stabilization of the environment [116]. For this reason, a high-precision thermostat was developed with a temperature stability better than 100 μK . As shown in Figure 19d, it consists of two nested thermostats with sensing elements and heaters for two independent proportional integrative derivative (PID) temperature control systems. Additionally, a temperature sensor was placed on the copper heat sink, in order to measure the cold junctions temperature and, thus, to cancel out possible residual temperature fluctuations [116]. Furthermore, micromachined heat exchangers were used to minimize temperature perturbations due to sample injections. Two main operation modes were tested, the continuous injection mode, during which reactants were continuously injected at a fixed flow rate, and the stopped-flow injection mode, which consisted in alternating injection and waiting periods. The latter mode showed to be the most convenient, as it allowed correcting baseline drifts [114], [116].

Such system was extensively characterized, first by measuring the heat generated by the protonation of trishydroxy methylaminomethane in aqueous solution, and by the hydrolysis of methylparaben. In particular, the reported heat power sensitivities decreased from 7.2, 6.6 to 5.4 V/W for

channel heights increasing from 0.5 to 1.2 mm, *i.e.* for increasing sample volumes from 10 μl to 24 μl . A limit of detection of 50 nW was estimated, as well as a time constant of 12 s was calculated for the smallest volume. Subsequent experiments showed the applicability of this nanocalorimeter to biochemical studies, by investigating the oxidation of glucose catalyzed by glucose oxidase and catalase, the hydrolysis of penicillin G catalyzed by β -lactamase and the oxidation of ascorbic acid catalyzed by ascorbate oxidase [116]. The same system was also applied to the real-time study of bacterial growth [143], either in suspension or in biofilm, highlighting its applicability for bioprocess control. In particular, when studying heat production by bacteria suspension, such as *Escherichia coli*, alternating injections of bacteria suspension and buffer solution were carried out in a stopped-flow mode. For investigating the heat production of biofilms, instead, biofilms were allowed to grow for up to two weeks. Subsequent injection of high concentration of the mitochondrial uncoupler 2,4-dinitrophenol (DNP) in buffer showed toxic effects. Examples of measurements on bacteria are reported in Figure 19e-f.

Further improvements of such system allowed to reach a temperature stability better than 40 μK near the cold junctions of the thermopile [114], [136]. Heat power measurements were done on bacteria suspensions and on zebrafish embryos, allowing the calculation of heat power values of a few pW/cell and of few hundreds of nW/embryo, respectively. Furthermore, extensive studies were done on biofilms, especially to investigate bacterial resistance mechanisms which have become of particular concern for antibiotic treatment [144], [120], [145]. In this case, heat power signals of untreated biofilms were compared to signals of biofilms treated with antibiotics, as well as of biofilms exposed to bacteriophages.

As with the developed system usually only relatively slow processes could be studied, magnetic beads coated with the reactant of interest and packed on the top of the sensing area, were used to increase the reaction surface area and, thus, to extend the reaction duration beyond the nanocalorimeter time constant [136]. As a result, heat power measurements of fast reactions were also demonstrated, such as for the binding reaction of streptavidin-coated beads and biotin dissolved in solution, and for the hybridization of two strands of DNA, one immobilized on the magnetic beads and the other one in solution.

More recently, such system was adapted and combined with the so-called segmented flow technology, which consists in repetitive sequential processing of sample segments separated by immiscible inert segments [146], [147]. As depicted in Figure 20a, the PMMA microfluidic chip was substituted by a Teflon tube having an inner diameter of 1.7 mm and a wall thickness of 80 μm , which was clamped on the sensing area by a PMMA mold to provide good thermal contact. A photograph of the new arrangement is shown in Figure 20b. Additionally, the nanocalorimeter was positioned vertically in order to help sedimentation of particles inside the sample segments. Experimental results showed its applicability to study the heat produced by biofilms grown on glass beads, by solid soil samples, and also by tridimensional cellular structures, such as spheroids and human hair follicles (as shown in Figure 20c).

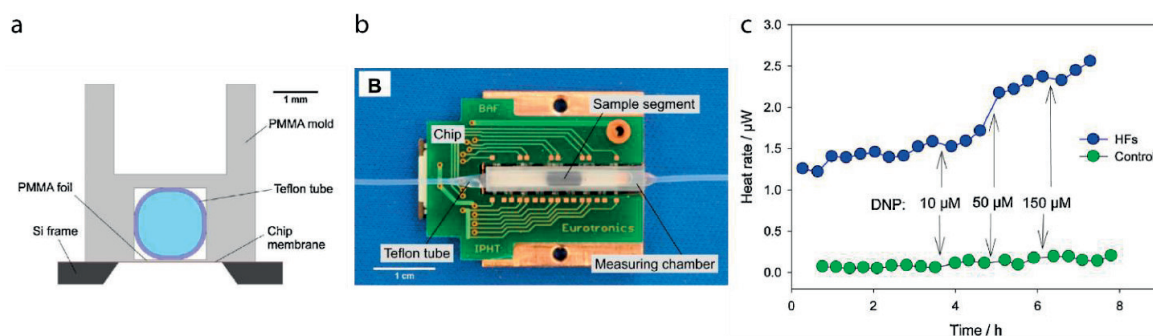


Figure 20 Segmented flow calorimeter as a modified version of the nanocalorimeter developed by Lerchner *et al.* a) Schematics showing a Teflon tube clamped on the sensing membrane by means of a PMMA frame. b) Photograph showing a top view of the nanocalorimeter. c) Measurement on human hair follicles after the injection of the mitochondrial uncoupler DNP: the green dots represent the control experiment where no hair follicles were present in the sample; the blue dots report the actual experiment, where hair follicles are exposed to increasing concentration of DNP. As DNP uncouples mitochondrial respiration, it induces an increase in metabolic heat production, which is experimentally observed (*images reproduced from [147]*).

4.2.3 Nanocalorimeters with microfluidics for nl sample volumes

Zhang *et al.* developed a nanocalorimeter based on a 2 μm thick silicon nitride–silicon dioxide membrane, on which a thermopile was fabricated by connecting in series 16 polysilicon–gold thermocouples [117]. The hot junctions were located on the central area of the membrane, and the cold junctions on the peripheral area. The expected temperature sensitivity was 5.6 mV/K. A polysilicon heater was also fabricated on the membrane to allow electrical calibration. In particular, the power sensitivity calculated by electrical calibration was 0.94 V/W and a time constant smaller than 100 ms was estimated. Such device was tested both on an open-chamber mode (Figure 21a), and subsequently on a closed-chamber mode (Figure 21b). For the open-chamber mode, polydimethylsiloxane (PDMS) was used to fabricate sidewalls to hold the sample in place on the center of the membrane and a thin tubing was positioned to allow liquid injections. Such configuration was tested for the measurement of glucose oxidation catalyzed by glucose oxidase. For that, a droplet of enzyme solution was first left to dry on the top of the sensing area, and subsequently 1 μl aliquots of glucose solution were injected. An example is reported in Figure 21c. The limitation of this approach was the poor reproducibility, depending also on the limited accuracy of dosing and positioning of the injected droplet. The closed-chamber configuration, instead, was made possible by interfacing the sensing membrane with microfluidic structures. In particular, 30 μm deep structures were fabricated on a glass substrate resulting in a measurement chamber with a volume of 15 nl. Continuous flow measurements were run by injecting two reacting solutions through the two inlets and allowing mixing in the measurement chamber. As shown in Figure 21d, the oxidation of glucose catalyzed by glucose oxidase was measured, as well as the hydrolysis of urea by urease and the hydrolysis of hydrogen peroxide by catalase.

Lee *et al.* developed a nanocalorimeter based on a 2 μm parylene membrane embedding a thermopile made of 5 gold–nickel thermocouples connected in series [113]. The resulting temperature sensitivity was 110 $\mu\text{V/K}$. Parylene was also used for fabricating microfluidic channels and a 3.5 nl measurement chamber on the top of the membrane.

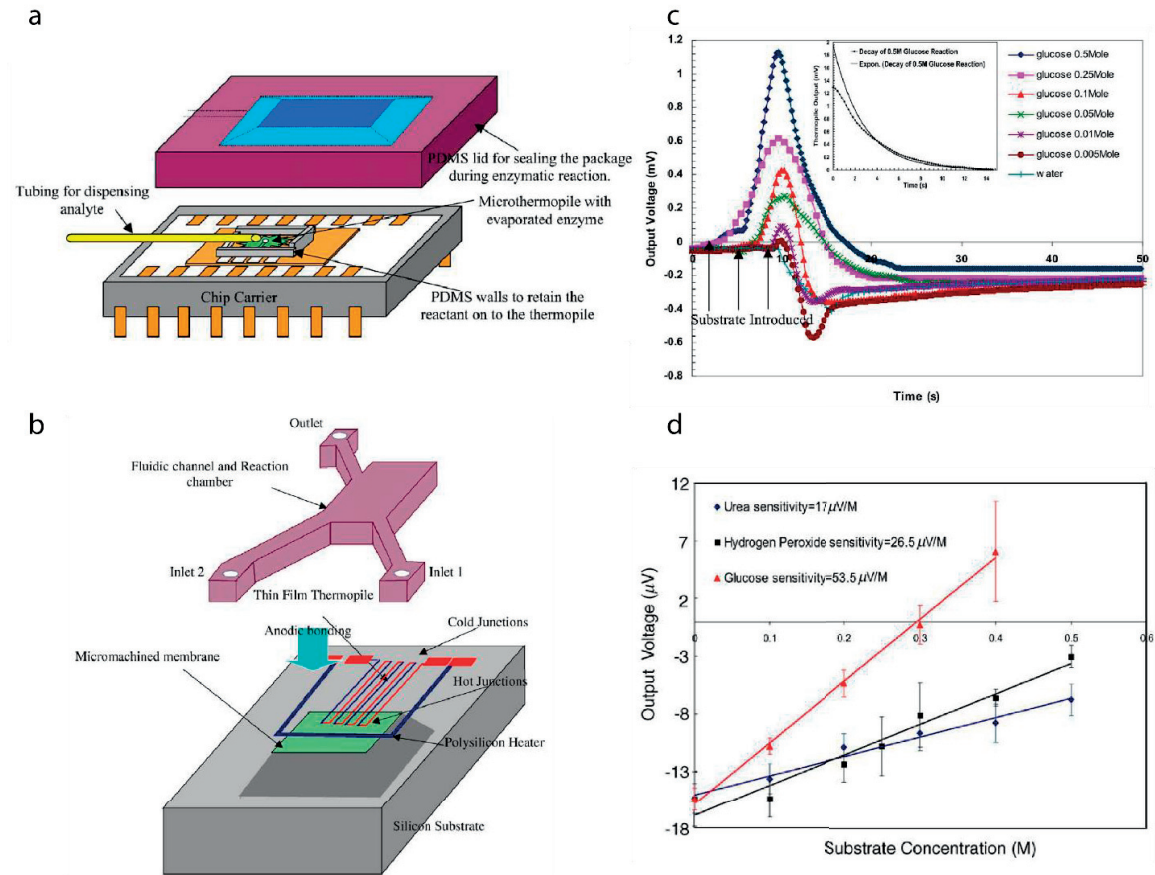


Figure 21 Nanocalorimeter developed by Zhang *et al.* a) Schematics showing the nanocalorimeter used in the open-chamber configuration with a PDMS chamber. b) Schematics showing the nanocalorimeter used in the close-chamber operation mode where a microfluidic glass structure is bonded to the silicon chip. c) Example of measurements carried out in the open-chamber configuration, showing the oxidation of glucose catalyzed by glucose oxidase: first, a droplet of enzyme was let to dry, then subsequent injections of glucoses were carried out, resulting in increasing voltage peaks for increasing concentrations. d) Comparison of the nanocalorimetric sensitivity of the closed-chamber configuration for different enzyme catalyzed reactions (*images reproduced from [117]*).

More complex peripheral microfluidic structures, instead, were fabricated in PDMS. In particular, microvalves and pumps were used for the precise injection of liquid volumes as small as 700 μl . An 80 μm intermediate SU-8 layer was used to planarize the surface and to allow good interfacing between parylene and PDMS microfluidic structures. Moreover, this intermediate layer permitted on-chip vacuum encapsulation of the nanocalorimeter for improved thermal insulation. Further improvement of thermal insulation was achieved by off-chip vacuum encapsulation below the parylene membrane. Figure 22a-c reports some schematics and photographs of such calorimeter. Electrical calibration, carried out using a gold resistive heater located in the measurement chamber and after prefilling the microfluidic structures with water, resulted in a power sensitivity of 7.1 V/W. The thermal conductance was also estimated to be 16 $\mu\text{W/K}$, which is significantly smaller than the one of previously developed nanocalorimeters (ranging from 100 $\mu\text{W/K}$ to 10 mW/K). As a result, the time response was estimated to be 1.3 s, which is higher compared to previously described open-chamber nanocalorimeters, but still smaller than closed-chamber nanocalorimeters working with bigger volumes, such as the one presented by Lerchner *et al.* Additionally, the documented

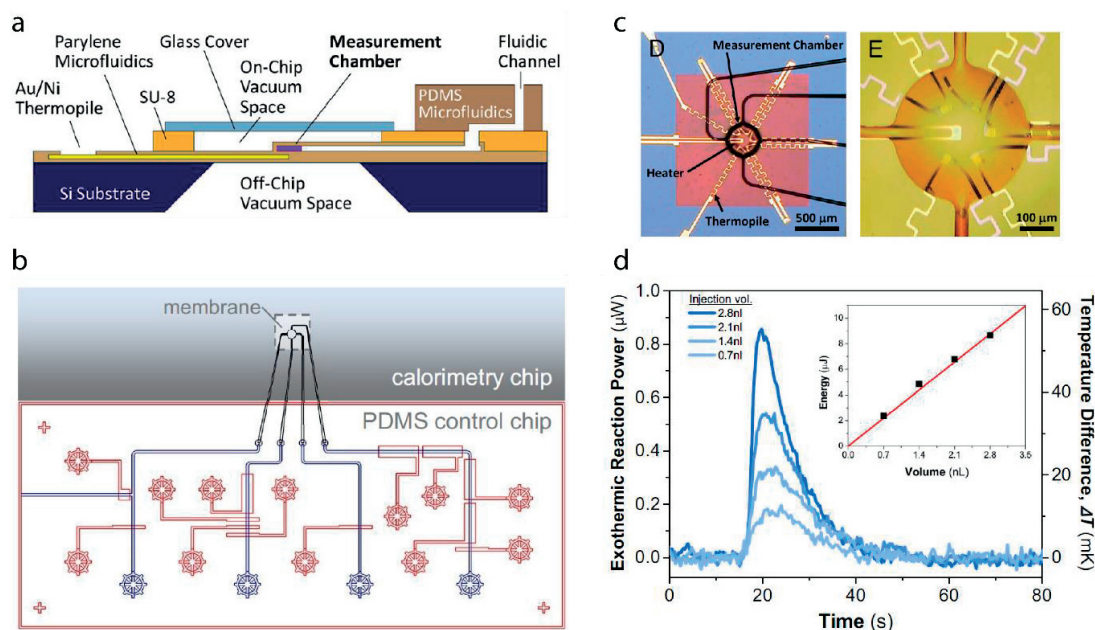


Figure 22 Nanocalorimeter developed by Lee *et al.* a) Cross-sectional schematics showing the different components of the nanocalorimeter developed, including the thermopile sensor, the parylene measurement chamber, the SU-8 intermediate layer and the PDMS microfluidics. b) Top view of the microfluidic structures fabricated in the PDMS layer, showing fluidic pumps and valves. c) Top picture of the sensing area, showing the thermopile and the resistive heater on the parylene membrane. d) Example of measurements showing urea hydrolysis by urease: heat power generated after the injection of increasing volumes (0.7 nl to 2.8 nl) of 50 mM urea solution into the measurement chamber, previously prefilled with urease solution. The inset shows the total energy of reaction calculated for increasing sample volumes injected (*images reproduced from* [113]).

power resolution was 4.2 nW. This nanocalorimeter was used to measure the heat of reaction of urea hydrolysis catalyzed by urease, as reported in Figure 22d, and the heat of mixing of methanol and water. Finally, a twin configuration was also developed consisting of two microfluidic chambers, placed at the cold and hot junctions of the thermopile, respectively. Such solution was proposed to reduce mixing/dilution artefacts [113].

4.2.4 Microfluidic nanocalorimeters for differential measurements

Wang *et al.* presented a thermopile-based nanocalorimeter interfaced with microfluidic structures allowing differential measurements [125], [138], [139]. The thermopile consisted of a 5 μm thick SU-8 membrane on which 50 nickel-chromium thermocouples are connected in series. The resulting temperature sensitivity was about 35 $\mu\text{V}/\text{K}$. Nickel resistive heaters were also included allowing electrical calibration. As shown in Figure 23a, the microfluidic structures consisted of two 1.2 μl PDMS microchambers, the measurement chamber and the reference chamber, respectively, that were connected to microchannels for sample handling. Air gaps were also included in the PDMS in order to increase the thermal insulation, especially between the two microchambers. Electrical calibration was carried out by filling both microchambers with phosphate buffered saline (PBS) and activating the resistive heater underneath the sample chamber. The resulting power sensitivity coefficient was estimated to be 1.2 V/W.

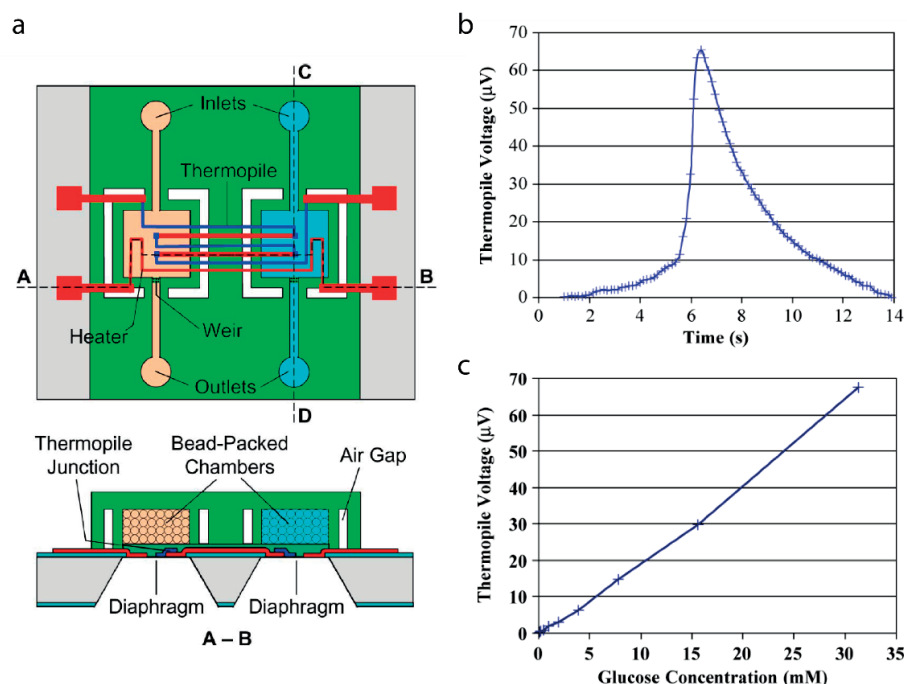


Figure 23 Nanocalorimeter developed by Wang *et al.* a) Schematic view of a closed-chamber nanocalorimeter operated in differential mode. b) Measurement of the oxidation of glucose catalyzed by glucose oxidase, when injecting $0.8 \mu\text{l}$ of 31.3 mM glucose solution into the sample chamber: initially the voltage signal increases as the chamber is being filled, then it decreases as the glucose available in solution is depleted. c) Maximum of the thermopile voltage measured as described in b) for increasing glucose concentrations in a stopped-flow mode (*images reproduced from [125]*).

Such device was used as a glucose sensor where $10 \mu\text{m}$ polystyrene microbeads coated with glucose oxidase and catalase were packed into the two microchambers [125]. Glucose solutions at varying concentrations were flown through the measurement chamber, whereas reference solutions were flown through the other chamber. The estimated sensitivity with respect to glucose detection was $2.2 \mu\text{V}/\text{mM}$ in stopped-flow mode, and $0.24 \mu\text{V}/\text{mM}$ when perfusing with a rate of $0.5 \text{ ml}/\text{h}$. Additionally, considering a thermopile voltage noise of 53 nV , the limit of detection was about 0.025 mM for glucose. Examples of measurements are reported in Figure 23b-c. The same device was also used for differential scanning calorimetry (DSC) [138], [139]. In this case, the measurement chamber was filled with the biochemical sample of interest, whereas the reference chamber was filled with buffer solution. The temperature of the whole device was varied over time. DSC experiments were implemented for the estimation of thermodynamic parameters, such as the enthalpy, the specific heat capacity and the melting temperature, of protein unfolding for lysozyme and ribonuclease A.

Seung-Il Yoon *et al.* also proposed a differential thermopile-based nanocalorimeter interfaced with microfluidic structures [148], [149]. As depicted in Figure 24a, the biggest difference compared to other work presented in literature is that this device is not based on a suspended membrane. In the present case, the nanocalorimeter consisted of a $100 \mu\text{m}$ thick SU-8 layer deposited on a $500 \mu\text{m}$ thick silicon substrate. The thermopile is built up from 42 copper-chrome thermocouples, resulting in a temperature sensitivity of $838.74 \mu\text{V}/\text{K}$. A $2 \mu\text{m}$ thick polyimide layer is used for insulating the thermopile, on the top of which a $300 \mu\text{m}$ thick SU-8 layer is used for defining the microfluidic chambers, in particular the reaction and reference chambers, which are connected with the so-called split

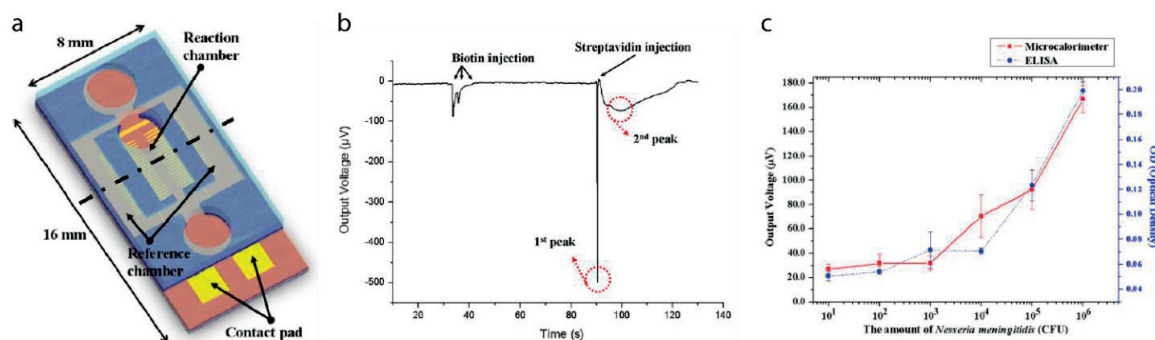


Figure 24 Nanocalorimeter developed by Seung-Il Yoon *et al.* a) Schematic view of the nanocalorimeter, showing the split-flow geometry of the microfluidic channels on top of a thick Si/SU-8 substrate. b) Thermopile voltage resulting from the biotin–streptavidin reaction: 3 μl of 3.4 $\mu\text{g}/\mu\text{l}$ biotin solution was injected three times through the common inlet to obtain a control measurement; then 3 μl of 1.0 $\mu\text{g}/\mu\text{l}$ of streptavidin solution was injected only in the reaction chamber. The first peak indicated in the plot is an injection artefact, whereas the second peak originates from the actual heat of reaction. c) Calorimetric measurement showing the detection of *Neisseria meningitidis* group B for increasing bacteria concentration, and comparison with the optical detection based on ELISA (Enzyme-Linked Immunosorbent Assay) (a and b reproduced from [149], c reproduced from [148]).

flow microchannels. A final layer of PDMS is then bonded to close the system. Such fluidic geometry allowed implementing a differential measurement configuration. In fact, the cold junctions of the thermopile are located underneath the two separate reference chambers, whilst the hot junctions are located underneath the reaction chamber. The typical protocol consisted in injecting the same biochemical solution from a common inlet in both microchambers, in order to record control signals. Then the reactant of interest was loaded only in the reaction chamber from a separate inlet and a voltage signal was recorded. The functionality of the device was demonstrated both for the detection of streptavidin down to 0.01 $\mu\text{g}/\mu\text{l}$ by biotin [149], and for the detection of *Neisseria meningitidis* group B (NMGB) bacteria by the monoclonal antibody HmenB3 [148], as shown in Figure 24b-c.

4.2.5 Differential enthalpy arrays with thermistor sensors

Torres *et al.* have presented a thermistor-based nanocalorimeter working in differential mode, the so-called enthalpy array [126]. This platform was developed for studying molecular interactions, based on a suspended membrane with thermistors as sensing elements and specific electrodes for merging and mixing by electrostatic handling of sample droplets. Figure 25a-b shows the schematic and photograph of a single module of the enthalpy array. The whole array comprises 96 individual modules. The membrane is made of a 12.5 μm polyimide layer on which two distinct sensing areas, one for the measurement and one for the reference, are located. On each area, an amorphous silicon thermistor was fabricated, coated with a protective layer of 300 nm of silicon oxynitride and a 2 μm parylene layer. The temperature coefficient of the thermistor resistance was 0.028 $^{\circ}\text{C}^{-1}$. The two thermistors of the measurement and reference areas, respectively, were connected through a Wheatstone bridge, allowing the differential measurement. Each sensing area consisted of two electrodes separated by a 50 μm gap. The parylene layer provided surface hydrophobicity, which is indispensable for electrostatic sample handling. In particular, for each experiment two 250 nl droplets containing the reagents of interest were dispensed on the two electrodes of the measurement area, whereas control droplets were dispensed on the two electrodes of the reference area. By applying

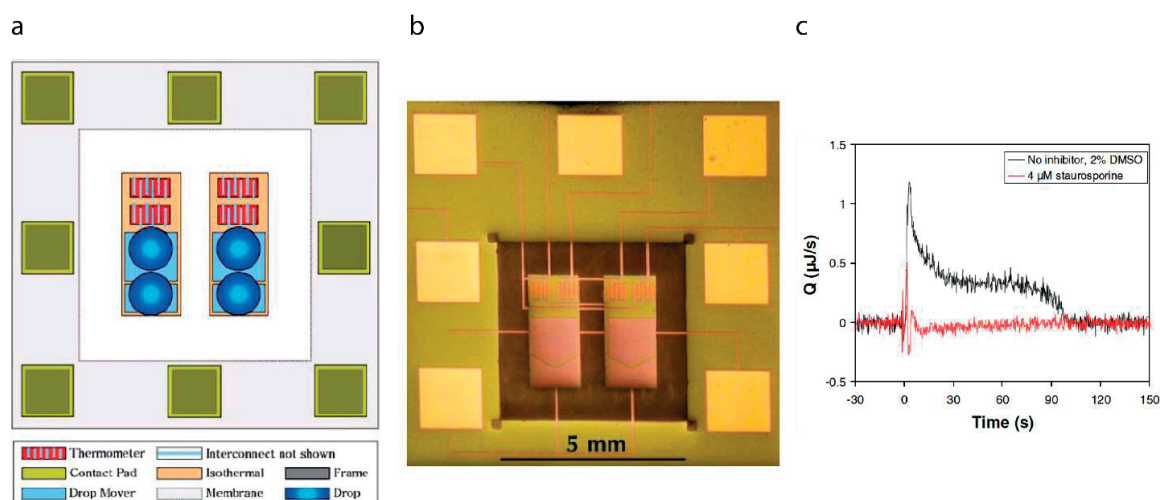


Figure 25 Enthalpy arrays developed by Torres *et al.* a) Schematic view of a single enthalpy module of the 96 array, showing the two sensing areas for the differential measurement, the thermistor thermometer, and the droplets dispensed on the electrodes of the measurement and the reference area. b) Photograph showing the same module. The electrodes of the two sensing areas are suspended on a polyimide membrane. c) Heat power measurement during the phosphorylation of Kempptide by a specific enzyme in absence and presence of an inhibitor (staurosporine) (*a and b reproduced from [126], c reproduced from [119]*).

a voltage of 100 V to the sensing area, droplets extended over the full surface of each sensing area, merged and eventually mixed. The measurement started when activating electrostatic mixing, thus inducing the chemical reaction on the measurement area. The corresponding heat of reaction could be deduced from the voltage signal on the Wheatstone bridge. A temperature difference of 500 μK could be detected, using a reference reaction producing 250 ncal of heat in a 500 nL volume. Initial experiments consisted in measuring the heat produced during protein–ligand binding interactions, such as between RNase A and cytidine 2'-monophosphate and between streptavidin and biotin, during the phosphorylation of glucose by hexokinase, and during mitochondria suspension exposure to DNP.

Further improvements were implemented to increase device sensitivity [118]. In particular, silicon thermistors were substituted by vanadium oxide thermistors, fabricated on a 25 μm thick polyethylene naphthalate (PEN) membrane, replacing the polyimide membrane. The resulting temperature coefficient of resistance of the thermistor was 0.027°C^{-1} . Additionally, a temperature controlled enclosure was added, as well as a plastic cap that was placed on the whole sensing areas to minimize sample evaporation. Moreover, resistive heaters were fabricated on the electrostatic electrodes, allowing electrical calibration. Experiments showed the applicability of such platform for studying enzyme activity and inhibitors effects, such as the example reported in Figure 25c. In particular, experiments were done for measuring the heat produced during trypsin hydrolysis of benzoylarginine ethyl ester (BAEE), and during trypsin inhibition by leupeptin and antipain. Additionally, titration like experiments of 18-crown-6 with barium chloride were performed by dispensing in parallel different concentration on the sensing modules of the enthalpy array. Finally, magnetic mixing was also implemented using magnetic stir bars made of a cobalt-based magnetic alloy [119]. One stir bar was placed on each pair of drops to mix by using a micromanipulator.

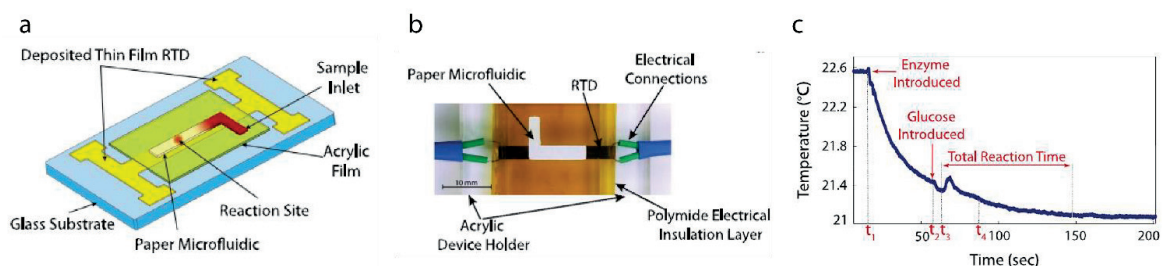


Figure 26 Paper-based calorimeter developed by Davaji *et al.* a) Schematic showing the main components of this calorimeter, including the paper-based channel and the RTD sensor. b) Photograph of the calorimeter, realized on the glass substrate (24 x 60 mm²). c) Glucose detection by glucose oxidase where 2 μ l of glucose oxidase were first dispensed on the reaction site, then 8 μ l of glucose solution was loaded from the sample inlet (*images reproduced from [150]*).

4.2.6 Nanocalorimeter with paper-based microfluidics

A significantly different approach to calorimetric measurements was recently presented by Davaji *et al.* [150]. The device relies on paper-based microfluidics interfaced with a nickel resistive temperature detector (RTD) as sensing element. As shown in Figure 26a-b, the paper-based channel was made of knife-cut chromatography-grade filter paper and was placed on the RTD sensor. The RTD sensor was fabricated on the top surface of a 100 μ m thick glass layer. Additionally, a 5 μ m acrylic film was interposed between the RTD sensor and the paper-based channel, both to provide electrical insulation and as adhesive layer. As for thermistors, measurements with RTD sensors are based on the temperature coefficient of the resistance. However, self-heating may be an issue in this case. For this particular device, a current of 1 mA was applied to measure the RTD resistance, resulting in Joule heating of 0.11 mW. Calibration has to take into account such unwanted effects. From the fluidic point of view, the first reactant was spotted on the center of the channel, then the other reactant was introduced from the sample inlet. The sample was driven by capillary force and reached the first reactant, thus starting the chemical reaction of interest. The functionality of such device was demonstrated for the detection of glucose by glucose oxidase, as shown in Figure 26c, the detection of DNA, and the detection of streptavidin-biotin binding.

4.3 Commercially available nanocalorimeters

At present, the company *Xensor Integration* commercializes several types of nanocalorimeters for a variety of applications [151]. They may be classified into two main groups, according to the membrane they are made of, *i.e.* monocrystalline silicon membranes of 4 to 45 μ m thickness, and silicon-nitride membranes of about 1 μ m thickness. The first type of nanocalorimeters is more suitable for liquid applications as they are more robust. Moreover, as the thermal resistance across the membrane is strongly reduced by the presence of the liquid sample, thicker membranes having lower thermal resistance are acceptable. The second type of nanocalorimeters are characterized by a high thermal resistance to the environment and a very small time constant, due to the low overall specific heat capacity. As a result, such nanocalorimeters are more suitable for experiments in gaseous environments, for using small samples and for fast scanning calorimetry. An overview of the different chip developments was given by van Herwaarden [152], [122].

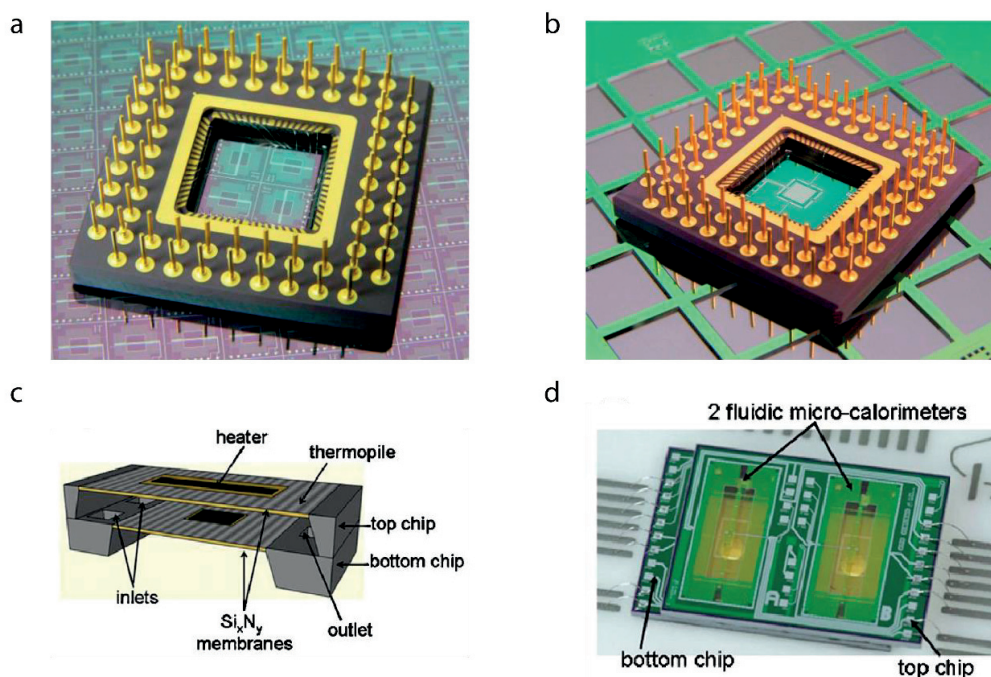


Figure 27 Nanocalorimeters developed by *Xensor Integration*. a) Photograph as reported in the datasheet of the model XEN-LCMquad with four independent sensors (see appendix). b) Photograph of the model XEN-NCM9924 with a single sensor on a thicker membrane. c) Schematics of a recently developed nanocalorimeter, integrating a closed microchamber for flow-through implementation. d) Photograph of two nanocalorimeters on the same chip of the same type as described in c) (*a and b reproduced from the datasheet, see appendix; c and d reproduced from [153]*).

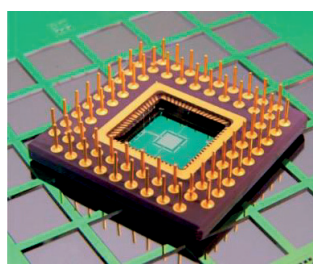
Considering the nanocalorimeters for liquid applications, two main types, the XEN-LCM2506 and the XEN-NCM9924, are available [151]. The first type is made of a monocrystalline silicon membrane of 4 to 8 μm in thickness and 3.5 x 3.5 mm^2 in size. It has 160 monocrystalline silicon-aluminum thermocouples in series giving a temperature (also called intrinsic) sensitivity of 50 to 80 mV/K and a power sensitivity of 8 V/W (as specified on the datasheet, reported in Appendix A). The hot junctions of the thermopile are arranged around a central region, on which also diffused p-type silicon heaters are microfabricated, whereas the cold junctions of the thermopile are in thermal contact with the chip rim. A similar product is the XEN-LCMquad shown in Figure 27a, which contains four XEN-LCM2506 chips arranged in a 2 x 2 array. The XEN-NCM9924 chip (see Figure 27b) is considered the heavy-duty sensor, as the membrane is thicker (22 to 45 μm thick) and the chip is bigger (8.3 x 8.3 mm^2 in size). Its integrated silicon-aluminum thermopile provides an intrinsic sensitivity of 50 mV/K and a power sensitivity of 1.2-2.4 V/W . It also features a diffused p-type silicon heater, and two aluminum heaters, which are separated by a dielectric layer from the thermopile. This latter product has been chosen for the development of the nanocalorimetric platform in this work, and it is the sensing core of such platform.

More recently a nanocalorimeter with an integrated microchamber was developed, allowing flow-through implementation to study the thermal properties of biochemical samples [153]. As shown in Figure 27c-d, the calorimeter consists of a stack of two sensor chips with a 300 μm spacing forming a 2.5 μl microchamber. Both sensor chips are made of a 2 μm thick silicon nitride membrane, on which p-type polycrystalline silicon (polySi) heaters and 136 p-polySi/n-polySi thermocouples are

fabricated. The reported power sensitivity of this device is 5 V/W. Two fluidic inlets and one outlet are machined in the rim holding the bottom membrane. Such nanocalorimeter has been tested in scanning mode where an alternating voltage with frequency f_0 is applied to the heater on the bottom membrane, thus inducing an alternating heat wave with a frequency $2 \times f_0$ that is detected by the upper thermopile. Thermal properties of the sample, such as thermal conductivity and diffusivity, may be derived from amplitude and phase measurements of the propagating heat wave [153].

Chapter 5 Development of the new calorimetric platform

This chapter is dedicated to the description of the design and development stages of the nanocalorimetric platform for biological studies. In particular, the development of such platform required both an accurate mechanical and thermal design, and fine-tuning of the temperature control system. The platform is built around a commercial thermopile-based sensor chip (see photograph on the right), on which an open-well reservoir holding the sample is directly positioned. Both elements are located inside a temperature controlled isothermal holder, enabling to set a specific temperature in a highly accurate and stable manner.



Some sections (in particular sections 5.4 and 5.5) of this chapter have been reported in following journal article [154] and conference proceedings [155]:

Nanocalorimetric platform for accurate thermochemical studies in microliter volumes (2015)

R. Padovani, T. Lehnert, R. Trouillon, and M. A. M. Gijs

RSC Advances, vol. 5, no. 118, pp. 97133–97142

DOI: 10.1039/C5RA22248F

A microcalorimetric platform for studying the heat produced by chemical reactions in microlitre volumes (2015)

R. Padovani, T. Lehnert, and M. A. M. Gijs

Proc. of 19th International Conference on Miniaturized Systems for Chemistry and Life Sciences (microTAS 2015)

Gyeongju, Korea.

We first point out the design rules that drive the development of this platform and that originate from specific requirements for biological applications. Then governing equations for the heat transfer phenomena involved are presented, followed by some fundamental considerations on nanocalorimetric sensing. Design and assembly of the nanocalorimetric platform will be presented next, as well as the computational thermal simulations, which had been carried out to identify the appropriate design of the isothermal holder. Finally, the isothermal holder and the integrated temperature control system will be discussed in more detail.

5.1 General system requirements for biological nanocalorimetric sensing

5.1.1 Nanocalorimeter sensitivity

The sensitivity of the nanocalorimetric platform should be high enough to allow measurements of metabolic heat produced by living organisms, such as mammalian cells, and also by multicellular organisms, such as nematodes. Such type of measurements aims to estimate basal metabolic heat production, and also the quantification of heat changes under stimulated conditions. Heat power generated by living organisms typically range from 1 pW/cell to 1 nW/cell depending on the cell type [14], [96], [97], and can reach few tens of nW for nematodes [108], [156]. More specifically, Table 2 gives an overview of microcalorimetric measurements of metabolic heat power values for different types of cells reported in literature.

Living cell or organism	Heat production rate
Escherichia coli [14]	1 pW/bacterium
Staphylococcus aureus [14]	3 pW/bacterium
3T3 mouse fibroblasts [96], [157]	17 pW/cell
HeLa-53G [96], [158]	31 pW/cell
Rat white adipocytes [96], [159]	40 pW/cell
Human melanoma H1477 [96], [160]	80 pW/cell
Hamster brown adipocytes [96], [161]	110 pW/cell
Keratinocytes [96], [162]	134 pW/cell
Rat hepatocytes [96], [163]	329 pW/cell
Human myocardial cells [14]	2 nW/cell
C. elegans nematodes [108]	≈13 nW/worm

Table 2 Basal heat power generated by living cells and organisms measured by microcalorimetry.

Furthermore, the total heat produced by a biosample is limited by the sample volume and the seeding density of the organism in the calorimeter reservoir. For nanocalorimeters using sample volumes in the nl to μl range, cellular concentrations in the order of 10^6 cells/ml are used and typical total heat power values are expected to be in the range from hundreds of nW to tens or hundreds of μW . Considering stimulated conditions, information on heat production variations due to biochemical compounds, such as oligomycin or carbonyl cyanide-4-(trifluoromethoxy)phenylhydrazone (FCCP), are not easily found in literature. Instead, more consistent information on the effects of such compounds on oxygen consumption rates is available. For example, the exposure of different types of mammalian cells to FCCP may induce an increase of oxygen consumption from basal to FCCP-induced condition over a very wide range, *i.e.* from about 10% to as high as 300%, as measured by the

Seahorse Bioscience Extracellular Flux Analyzer in different studies [164]–[166]. Unfortunately, it is not possible to directly correlate such data with the metabolic heat production. Nevertheless, such information may provide some hints on the degree of variation expected in metabolic heat production.

5.1.2 Temperature stability and thermal gradients

The nanocalorimetric sensing principle is based on detecting thermal gradients originating from heat produced by a chemical or biological sample. Any thermal gradient in the absence of the sample would result in an undesired background or baseline signal. Therefore, thermal gradients inside the isothermal holder, in particular close to the sensing area, have to be minimized. Residual thermal gradients can be identified by appropriate thermal computational simulations and careful design of the isothermal holder.

The isothermal holder or housing of the nanocalorimetric chip should be held at constant temperature in a very stable manner over time. In fact, the isothermal holder thermalizes the whole system at a specific setpoint temperature, and also works as a heat sink for the thermopile sensor chip. Even minor fluctuations of the temperature of the heat sink may generate fluctuations in temperature gradients over the sensing area and, thus, instabilities in the background signal. For highly sensitive heat power measurements, below the μW range, temperature control and stability must be optimized, typically in the mK range.

Furthermore, it should be emphasized that heat generated by the sample must flow through the sensing area, *i.e.* the nanocalorimetric membrane, to the heat sink in order to be detected. This thermal path must therefore be carefully considered and alternative thermal paths that give rise to heat loss have to be minimized to achieve high sensitivity.

5.1.3 Thermal time constants of the system

Two thermal time constants are relevant for the nanocalorimetric platform, (i) the sensing time constant and (ii) the thermalization time constant.

(i) The sensing time constant of the nanocalorimetric system corresponds to the time response of the sensor with respect to heat generated by the sample. It should be fast enough to detect dynamic events of (bio-)chemical processes. Considering metabolic processes which are relatively slowly changing [14], a sensing time constant in the order of tens of seconds is acceptable [90].

(ii) The thermalization time constant corresponds to the time required by the whole system to reach the setpoint temperature, and it strongly depends on the thermal inertia of the platform. This time constant should be small in order to minimize the waiting time before starting the experiment. Such prerequisite is particularly critical when working with biological samples, especially when working with living organisms. For example, mammalian cells are kept in cell culture incubators at 37 °C, with a carbon dioxide content fixed to 5% and the humidity set to 95%. Also calorimetric experiments on cells have to be performed at a setpoint temperature of 37 °C, however this condition can not be

guaranteed during sample loading and system temperature stabilization. A temperature stabilization time of up to 30 minutes is generally acceptable. It must be noted that a smaller thermal inertia of the system would reduce the time constant but also reduces damping of ambient temperature fluctuations, making accurate thermal stabilization more difficult. A good compromise must be found between these two conflicting conditions.

5.2 Governing physical equations for heat transfer phenomena

Heat transfer phenomena play a critical role in the development of the nanocalorimetric platform. The fundamental principles and equations governing the three mechanisms of heat transfer, *i.e.* conduction, convection, and radiation, will be outlined. Understanding of the individual contributions is of importance for computational simulations and performance optimization of the platform.

5.2.1 Heat transfer by conduction

Heat transfer by conduction occurs across any temperature gradient in the system. Heat conduction is the result of the transfer of kinetic energy between atoms or molecules [130]. The collision mechanisms and probabilities vary considerably between gases, liquids and solids, which explains their different thermal conductivities [130]:

- Gases are characterized by a large mean free path, resulting in few possible collisions. In general, gases are poor thermal conductors. Gaps in thermal systems filled with gas, *e.g.* air, may even serve as thermally insulating spaces, especially if low gas pressure is used.
- In solids, energy transfer occurs through lattice vibrations. The presence of impurities and defects in the lattice causes local distortions, slowing down the energy transfer. In general amorphous solids have lower thermal conductivity than crystalline solids. Additionally, in metals heat conduction is strongly enhanced by freely moving electrons.
- Liquids have an intermediate behavior from the point of view of heat conduction. Atoms and molecules are closer to each other compared to gases, but are not confined in defined positions.

According to Fourier's law of heat conduction, the heat transfer rate or heat flow q_x (measured in $\text{J}\cdot\text{s}^{-1}$) in x -direction normal to a cross-sectional area A (m^2) is proportional to the temperature gradient $\partial T/\partial x$ ($\text{K}\cdot\text{m}^{-1}$), with the proportionality coefficient corresponding to the thermal conductivity k ($\text{W}\cdot\text{m}^{-1}\cdot\text{K}^{-1}$):

$$q_x = -kA \frac{\partial T}{\partial x}$$

Equation 5:1 – Fourier's law of heat conduction

The negative sign in Equation 5:1 accounts for the fact that heat obviously always flows from higher temperature regions to lower temperature regions. Considering a one-dimensional planar system

with constant properties, heat conduction through an element of thickness dx , may be expressed by the following energy balance [167]. This equation also takes into account the presence of a heat source in the considered element:

$$q_x + \dot{q} A dx = \rho c A \frac{\partial T}{\partial t} dx + q_{x+dx}$$

Equation 5:2 – Energy balance for an element of thickness dx

where q_x ($\text{J}\cdot\text{s}^{-1}$) is the heat flow into the element at position x and q_{x+dx} ($\text{J}\cdot\text{s}^{-1}$) is the heat flow out of the element at position $x+dx$, respectively, \dot{q} ($\text{J}\cdot\text{s}^{-1}\cdot\text{m}^{-3}$) is the heat generated within the element per unit volume, ρ ($\text{kg}\cdot\text{m}^{-3}$) is the density of the material, c is the specific heat capacity of the material ($\text{J}\cdot\text{K}^{-1}\cdot\text{kg}^{-1}$), and $\partial T/\partial t$ ($\text{K}\cdot\text{s}^{-1}$) is the partial time derivative of the temperature of the element.

Combining Equation 5:1 with Equation 5:2 results in the following differential equation for the time-dependent temperature distribution in a one-dimensional planar system:

$$\frac{\partial}{\partial x} \left(k \frac{\partial T}{\partial x} \right) + \dot{q} = \rho c \frac{\partial T}{\partial t}$$

Equation 5:3 – Heat conduction equation for a one-dimensional system

Extending Equation 5:3 to a three-dimensional system results in:

$$\frac{\partial}{\partial x} \left(k \frac{\partial T}{\partial x} \right) + \frac{\partial}{\partial y} \left(k \frac{\partial T}{\partial y} \right) + \frac{\partial}{\partial z} \left(k \frac{\partial T}{\partial z} \right) + \dot{q} = \rho c \frac{\partial T}{\partial t}$$

Equation 5:4 – Heat conduction equation for a three-dimensional system

The last equation describes the general case of the heat transfer by conduction, and thus was used for the computational simulations that will be discussed in section 5.5 of this chapter.

5.2.2 Heat transfer by convection

Heat transfer by convection is the result of heat transfer, in particular cooling, from a solid surface through the motion of the surrounding fluid (liquid or gas) [130]. Depending on the cause of such fluid motion, it is possible to distinguish:

- Natural or free convection, when buoyancy effects in the fluid are causing a fluid motion that cools a warm solid body immersed in the fluid. Fluid near the solid surface, having higher temperature and lower density than the surrounding fluid, moves upward and is replaced by colder and denser fluid from the surroundings. Therefore, such fluid motion carries away the heat from the hotter surface, thus progressively cooling it.

- Forced convection, when an external force causes the fluid motion, *e.g.* a fan that cools the surface of a solid.

In particular, considering the fluid motion over a surface, it is possible to distinguish two main regions: the fluid region far from the surface, where motion is not affected by the presence of the surface, and a boundary layer close to the surface where the fluid velocity approaches zero at the solid surface.

Newton's law of cooling describes the mechanism of convection as [167]:

$$q = h A (T_s - T_\infty)$$

Equation 5:5 – Newton's law of cooling

where q ($\text{J}\cdot\text{s}^{-1}$) is the heat transfer rate, h ($\text{W}\cdot\text{m}^{-2}\cdot\text{K}^{-1}$) is the convective heat transfer coefficient, and A (m^2) is the surface area. T_s (K) is the temperature of the fluid at the solid surface, and T_∞ (K) is the temperature of the freely moving fluid region, far from the solid surface.

The convective heat transfer coefficient h is an important parameter in this context. It depends on many factors, such as the fluid type, the size and shape of the solid surface, the orientation (for example vertical or horizontal surface), and the presence of turbulences. Tabulated values in literature can be found, specifying the different experimental conditions [167], or estimations can be made based on Reynolds and Nusselt numbers [167]. In most case, however, h has to be determined experimentally. As for the heat conduction equation, also Equation 5:5 represents an important input for the computational simulations that will be described.

5.2.3 Heat transfer by radiation

The Stefan-Boltzmann law describes the energy loss of a warm black body by electromagnetic radiation. The heat transfer rate per unit area E ($\text{J}\cdot\text{s}^{-1}\cdot\text{m}^{-2}$) from an object to the surroundings can be written as [130]:

$$E = \varepsilon \sigma T_s^4$$

Equation 5:6 – Stefan-Boltzmann law

where ε is the emissivity of the object's surface, σ is the Stefan-Boltzmann constant ($5.669 \cdot 10^{-8} \text{W}\cdot\text{m}^{-2}\cdot\text{K}^{-4}$) and T_s (K) is the object's temperature.

Moreover, considering the balance between the thermal radiation emitted by the object and the thermal radiation absorbed from the surroundings, the net radiative heat transfer rate is:

$$q = \varepsilon \sigma A (T_s^4 - T_{sur}^4)$$

Equation 5:7 – Radiative heat transfer between an object and the surroundings

where A (m^2) is the area of the object's surface and T_{sur} (K) is the temperature of the surroundings.

For the specific experimental conditions of the nanocalorimetric platform, convective heat transfer plays the major role in cooling the system. For this reason, radiative heat transfer is not included in the following computational simulations.

5.3 Theoretical background for thermopile-based heat flow calorimetry

5.3.1 Thermopile sensing principle

The working principle of the thermocouple sensor is based on the thermoelectric conversion of a thermal gradient into a voltage. More specifically, it relies on the Seebeck effect [128], [129]. The Seebeck effect corresponds to the observation that a voltage builds up when a temperature gradient is applied to a material, in particular a metallic conductor. This physical phenomenon is related to the fact that temperature gradients affect the local diffusivity and density of the electrons, thus resulting in a voltage gradient, also called Seebeck voltage V_s [130]. In a simple cylindrical wire, the Seebeck voltage V_s (V) is directly proportional to the temperature difference ΔT (K) between the hotter and the colder end of the conductor. This relationship is expressed through the Seebeck coefficient $s(T)$ ($\text{V}\cdot\text{K}^{-1}$), as:

$$V_s = s(T) \cdot \Delta T$$

Equation 5:8 – Seebeck voltage - temperature difference relationship

The Seebeck coefficient $s(T)$ is a function of temperature and depends on the electronic properties of the conductor. It is also affected by the presence of defects or contaminants in the conductor. As an example, the Seebeck coefficient of platinum is approximately $-5 \mu\text{V}/\text{K}$ at room temperature.

In practice, the absolute Seebeck coefficient of a material is difficult to measure, as generally wires of different materials have to be connected together. A junction of two conductors A and B forms a thermocouple, and the voltage drop across this series connection has to be taken into account. In order to use a thermocouple for temperature sensing, a configuration as shown in Figure 28a has to be considered. On one side, the junction of conductors A and B, typically called hot junction, forms the sensing spot in contact with the sample. On the other side, both ends of the thermocouples are fixed on a heat sink, where conductors A and B are connected to the measurement device, through a copper wire, for instance. As these junctions, also named cold or reference junctions, are at constant and equal temperature, they do not affect the temperature measurement. The voltage across the thermocouple can then be expressed by introducing:

$$V_A = s_A \cdot \Delta T$$

$$V_B = s_B \cdot \Delta T$$

Equation 5:9 – Seebeck voltage and coefficients defined for two conductors A and B

where V_A (V) and V_B (V) are the Seebeck voltages across the conductor A and B, s_A ($V \cdot K^{-1}$) and s_B ($V \cdot K^{-1}$) are the Seebeck coefficients for each conductor, and ΔT (K) is the temperature difference between the hot and cold junctions.

Then the corresponding voltage V_{TC} (V) across the thermocouple is:

$$V_{TC} = V_A - V_B = s_A \cdot \Delta T - s_B \cdot \Delta T = s_{AB} \cdot \Delta T$$

Equation 5:10 – Seebeck voltage - temperature difference relationship for a thermocouple

where s_{AB} ($V \cdot K^{-1}$) is the relative Seebeck coefficient.

For nanocalorimetric devices, the measurement sensitivity is increased by series connections of thermocouples, also called thermopiles. A thermopile is a series connection of wires or thin-film leads of alternating conductors A and B. The corresponding configuration is shown in Figure 28b. Half of the junctions (hot junctions) are located on the sensing area with a temperature T_{HOT} , the other ones (cold junctions) are connected to a heat sink with temperature T_{COLD} , and serve as reference. The resulting voltage V_{TP} (V) generated by the thermopile is:

$$V_{TP} = n \cdot s \cdot \Delta T$$

Equation 5:11 – Seebeck voltage for a thermopile made of n thermocouples connected in series

where n is the number of thermocouples connected in series, s is the relative Seebeck coefficient for the specific thermocouple ($V \cdot K^{-1}$), and $\Delta T = T_{HOT} - T_{COLD}$ (K) is the temperature difference between hot junctions and cold junctions. As mentioned previously, the temperature sensitivity S_T (or simply S) ($V \cdot K^{-1}$) of a calorimeter is given by $S_T = n \cdot s$. In order to use this temperature sensing mechanism it is crucial to minimize temperature fluctuations of the cold junctions and to minimize unwanted thermal gradients in the device.

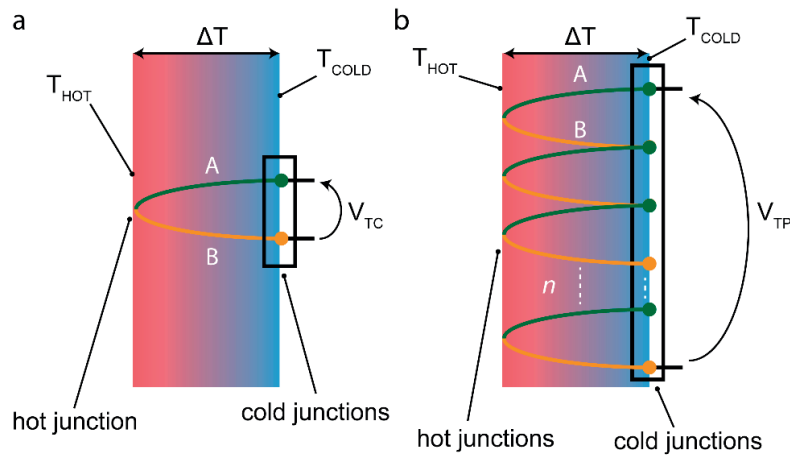


Figure 28 Working principle of thermoelectric sensing. a) Schematic of a thermocouple made of two materials A and B connected together. Because of the presence of the temperature gradient $\Delta T = T_{HOT} - T_{COLD}$, a voltage V_{TC} between the two cold junctions is generated. b) Schematic for a thermopile made of a series connection of n thermocouples, exposed to a temperature difference ΔT . The resulting voltage V_{TP} is equal to $n \cdot V_{TC}$.

5.3.2 Working principle of heat flow calorimetry

In conventional heat flow calorimetry sensing relies on a thermopile element connecting the reaction vessel to the heat sink. On the one hand, it works as the preferential thermal path between the vessel and the surroundings, and on the other hand, it senses the temperature difference between hot and cold regions. For a heat flow calorimeter, the rate P [$\text{J}\cdot\text{s}^{-1}$] of heat produced/absorbed by the sample may be expressed by the following heat power equation [168]:

$$P = \frac{dQ}{dt} + C \frac{dT_{HOT}}{dt}$$

Equation 5:12 – Heat power equation for heat flow calorimetry

where dQ/dt ($\text{J}\cdot\text{s}^{-1}$) is the heat flow between the sample and the heat sink, C ($\text{J}\cdot\text{K}^{-1}$) is the heat capacity of the system, including reaction vessel, sample and thermopile, and dT_{HOT}/dt ($\text{K}\cdot\text{s}^{-1}$) is the rate of temperature change of the reaction vessel. The second part of the equation on the right-hand side accounts for the fact that part of the energy produced by a sample is used to heat up the system.

Assuming that the heat sink, and thus the cold junctions, are kept at constant temperature (*i.e.* $dT_{COLD}/dt = 0$), Equation 5:12 may be re-written as:

$$P = \frac{dQ}{dt} + C \frac{d(T_{HOT} - T_{COLD})}{dt} = \frac{dQ}{dt} + C \frac{d\Delta T}{dt}$$

Equation 5:13 – Re-written heat power equation for heat flow calorimetry

where ΔT (K) is the temperature difference between hot and cold junctions. In the ideal case, all the heat produced/absorbed by the sample would flow exclusively through the thermopile, as described by the following heat flow equation:

$$\frac{dQ}{dt} = \frac{1}{R_{th}} \cdot \Delta T$$

Equation 5:14 –Heat flow equation for an ideal thermopile

where R_{th} ($\text{K}\cdot\text{s}\cdot\text{J}^{-1}$) is the thermal resistance of the thermopile, and ΔT (K) is the temperature difference between hot and cold junctions. The temperature sensing function of the thermopile can be considered by combining Equation 5:11 with Equation 5:13 and Equation 5:14, and the resulting equation is the so-called Tian's equation:

$$P = \varepsilon \cdot \left(V_{TP} + \tau \frac{dV_{TP}}{dt} \right)$$

Equation 5:15 – Tian's equation

where ε ($\text{W}\cdot\text{V}^{-1}$) is defined by $\varepsilon = 1/(n\cdot s\cdot R_{th})$, being n the number of thermocouples connected in series, s ($\text{V}\cdot\text{K}^{-1}$) is the relative Seebeck coefficient of the thermocouple, V_{TP} (V) is the thermopile voltage, and τ (s) is the sensing time constant defined as $\tau = R_{th}\cdot C$. The Tian's equation describes the relationship between the measured voltage V_{TP} and the heat power P generated by the sample [9], [168]. At steady state, the heat power P is directly proportional to the thermopile voltage V_{TP} , through the proportionality coefficient ε . By calibration it is possible to estimate the proportionality coefficient, which is typically reported as the power sensitivity coefficient $PS = \varepsilon^{-1}$.

Tian's equation may be applied to nanocalorimeters, considering that in this case the heat flow is strongly determined by the membrane which holds the sample and the thermopile. The thermal resistance R_{th} may be increased by reducing the membrane thickness, thus through $PS = n\cdot s\cdot R_{th}$, a higher power sensitivity PS can be expected. However, for thinner membranes unwanted alternative thermal paths may become more relevant, which in term reduce the nanocalorimetric sensitivity. A compromise has to be found, and somehow thicker membranes with lower thermal resistance may be preferred to achieve high sensitivity. In any case, residual thermal paths must be minimized. From the considerations above, we also notice that a nanocalorimeter with high power sensitivity PS requires a high number n of thermocouples connected in series and thermocouple materials with a high relative Seebeck coefficient s . Applying these criteria to nanocalorimeters is not always straightforward. In particular, the number of thermocouples connected in series is limited by the size and geometry of the nanocalorimeter, and the choice of possible materials for the thermocouple also depends on the membrane material [14].

5.3.3 Signal-to-noise ratios for different configurations

The second term of Tian's equation accounts for the transient state, *i.e.* a sample temperature change, due to a biochemical reaction, for instance. As already mentioned, the sensing time constant τ is directly proportional to the thermal resistance R_{th} and to the heat capacity C of the nanocalorimeter. Calorimetric applications may be classified in principle into two fields, *i.e.* the study of fast processes or of slow events. Reactions are considered fast if the reaction time is much smaller than the sensing time constant, and, vice versa, slow processes have a longer reaction time compared to the calorimeter time constant [140]. These two cases are presented in Figure 29.

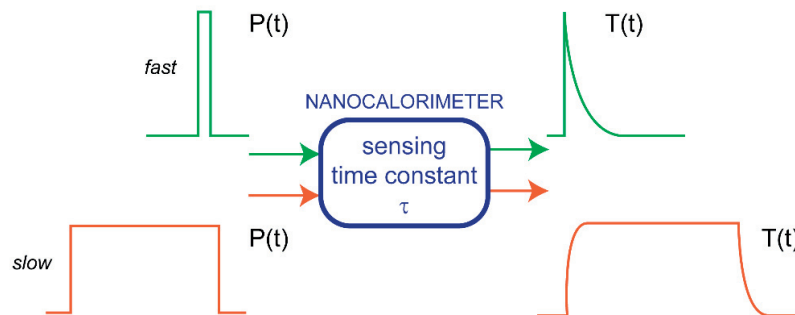


Figure 29 Fast and slow processes with respect to the sensing time constant τ .

In the first case of fast temperature variations, the nanocalorimeter works almost in adiabatic mode, as the heat flow through the membrane may be neglected. In such conditions, the signal-to-noise ratio (SNR) may be calculated as [140], [169]:

$$SNR = \frac{V_{TP}}{V_n} = \frac{S_T \Delta T_{ad}}{V_n} = \frac{S_T}{V_n} \cdot \frac{q}{C} = \frac{S_T}{V_n} \cdot \frac{cV\Delta H}{\rho c_p V + C_a} \approx \frac{S_T}{V_n} \cdot \frac{c\Delta H}{\rho c_p}$$

Equation 5:16 – SNR of nanocalorimetric measurements for fast processes

where V_{TP} (V) is the measured signal, V_n (V) is the voltage noise, S_T ($V \cdot K^{-1}$) is the temperature sensitivity of the nanocalorimeter, ΔT_{ad} (K) is the adiabatic temperature change, q (J) is the heat generated by the sample, C ($J \cdot K^{-1}$) is the total heat capacity, c ($mol \cdot m^{-3}$) is the reactant concentration, V (m^3) is the sample volume, ΔH ($J \cdot mol^{-1}$) is the reaction enthalpy, ρ ($kg \cdot m^{-3}$) is the sample density, c_p ($J \cdot kg^{-1} \cdot K^{-1}$) is the specific heat capacity of the sample, and C_a ($J \cdot K^{-1}$) is the heat capacity of the nanocalorimeter excluding the sample. As can be seen on the right-hand side of Equation 5:16, for a heat capacity C_a of the nanocalorimeter being very small ($C_a < 1$ mJ/K), the volume of the sample drops out and does not directly affect SNR, which mainly depends on the temperature sensitivity S_T of the device. For this reason, this type of nanocalorimeter is suitable for very small sample volumes, down to the nL volume range and below.

The calculation of the SNR for slow processes, instead, may be reported as follows:

$$SNR = \frac{V_{TP}}{V_n} = \frac{PS \cdot P}{V_n} = \frac{PS}{V_n} \cdot rV\Delta H$$

Equation 5:17 – SNR of nanocalorimetric measurements for slow processes

where PS ($V \cdot W^{-1}$) is the heat power sensitivity, P ($J \cdot s^{-1}$) is the heat power generated by the sample, and r ($mol \cdot m^{-3} \cdot s^{-1}$) is the reaction rate. In this case, the SNR is proportional to the sample volume, making extreme reduction of sample volumes less advantageous [140], [169].

In the specific case of the nanocalorimeter developed in the present work, our main interest focuses on the investigation of slow biological processes. In fact, the sensing time constant τ of the nanocalorimeter is about 10 s (see section 5.5.4), which is much smaller than the reaction time of typical metabolic processes which are in the order of minutes. In this case, it is possible to neglect the transient term of Equation 5:15 and to write a simplified version of Tian's equation:

$$P = \varepsilon \cdot V_{TP} = \frac{1}{nSR_{th}} V_{TP}$$

Equation 5:18 – Simplified version of Tian's equation

Specifically, the documented temperature sensitivity $S_T = n \cdot s$ for the commercial nanocalorimeter (XEN-NCM 9924 chip, *Xensor Integration*) used in this work is equal to 50 mV/K. Additionally, sample volumes of few tens of μl have been used in order to obtain good SNR.

5.4 Design and assembly of the nanocalorimetric platform

5.4.1 Main components of the platform

According to the requirements listed in section 5.1, the nanocalorimetric platform has been designed and developed as sketched in Figure 30. In particular, it comprises the following components:

- a sensor chip which is the core of the nanocalorimetric platform. In Figure 30 only the outer frame of the chip, that is fixed on a PCB board, is visible;
- a polycarbonate (PC) sample reservoir glued onto a polystyrene (PS) membrane, allowing sample loading on the thermopile sensor without contamination of the sensor itself;
- the aluminum isothermal holder, built up from three parts which are assembled together, and an additional aluminum plate on the top. The sensor chip is located in the center of the holder. This aluminum housing has multiple functions, such as allowing uniform thermalization, being a heat sink for the thermopile, and enabling shielding of external electrical noise;
- components of the temperature control system, in particular a temperature sensor (the PID resistive sensor) and a resistive heater (the PID heater). Both resistors are connected to an external Proportional-Integral-Derivative (PID) controller;
- two poly(methylmethacrylate) (PMMA) plates (bottom and top of the holder);
- an outer PMMA box is also used to provide additional thermal insulation with respect to ambient temperature fluctuations (not included in the sketch).

Figure 31 shows a photograph of the actual fabricated and assembled nanocalorimetric platform. The platform is shown closed as used during the measurements. Thus, only the outer parts are visible, which include the aluminum parts of the isothermal holder, the PMMA plates and the PID heater (orange foil in the figure). All the mechanical parts, including the polycarbonate sample reservoir, the aluminum components of the isothermal holder and the PMMA parts, have been fabricated by the EPFL Workshop *Atelier de l'Institut de microtechnique*, according to the three-dimensional drawings provided.

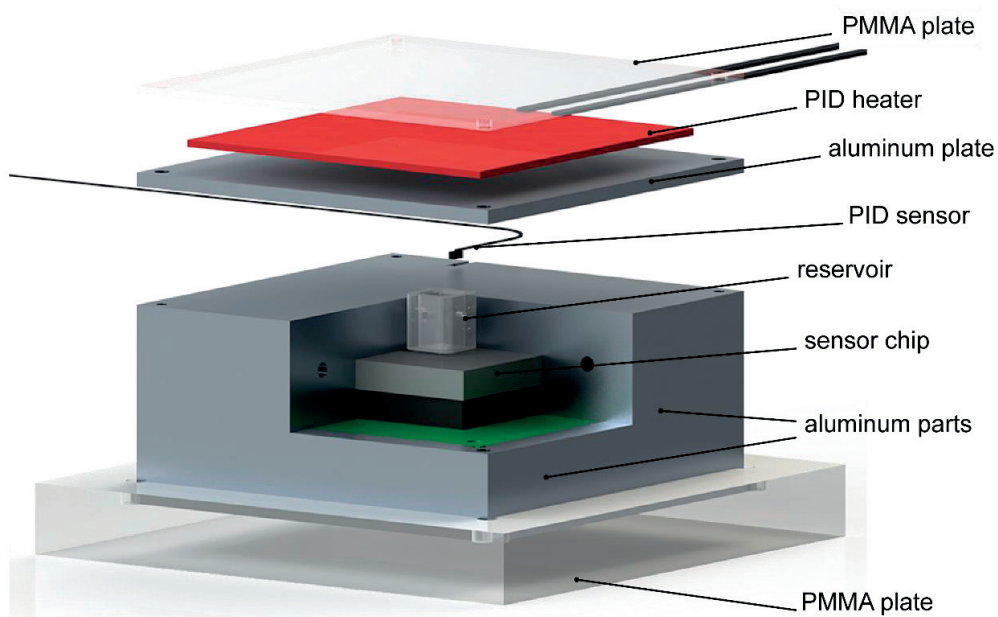


Figure 30 Three-dimensional sketch of the nanocalorimetric platform, consisting mainly of a membrane-based sensor chip, a PC sample reservoir positioned on the sensor membrane, and several aluminum parts clamped together (outer size 60 x 60 mm²). The PID temperature control is achieved thanks to a flat polyimide heater (PID heater) on top and a platinum temperature sensor (PID sensor) positioned inside the isothermal holder.

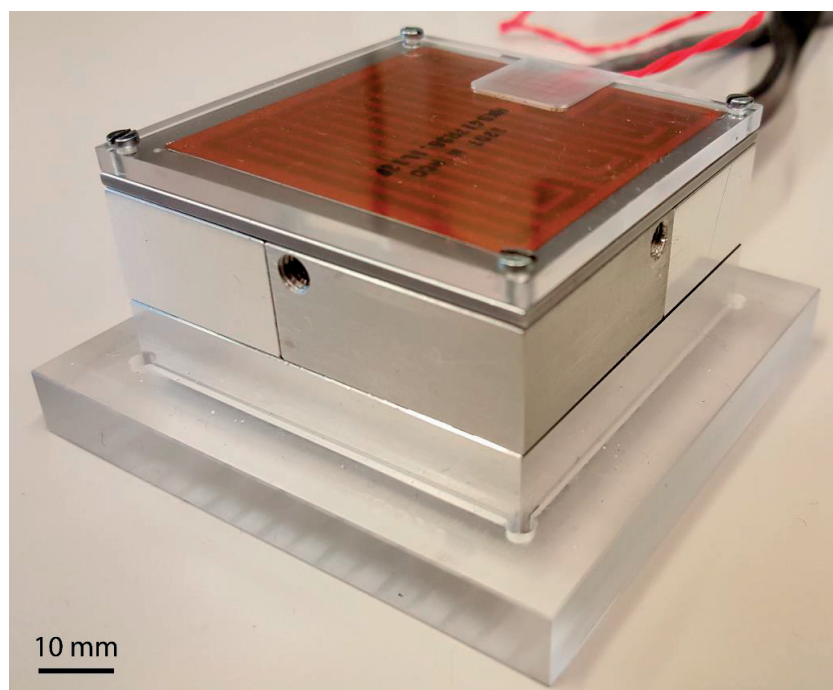


Figure 31 Photograph of the developed nanocalorimetric platform. The three aluminum parts are visible, together with the top aluminum plate, as well as the PMMA parts (bottom and top plates). The flat PID resistive heater (orange in the picture) is clamped between the top aluminum plate and the top PMMA plate.

5.4.2 Specifications of the sensor chip

We chose to use a commercially available sensor, in particular the XEN-NCM 9924 chip from *Xensor Integration*. This sensor chip has already been optimized for use with liquid samples, and examples of their application, that are comparable with our approach, are reported in literature [76]. Focusing on the development of a new platform and possible biological applications, this choice appeared to be more efficient. Design and development of a specific custom-made sensor may be considered for future more advanced applications. The XEN-NCM 9924 chip has been chosen as its membrane size (area of $8.3 \times 8.3 \text{ mm}^2$) is compatible with the reservoir size required for sample volumes to be investigated (typically in the range of a few μl). This sensor has already been introduced in Chapter 4. More specifically, the aluminum-silicon thermopile of this chip is fabricated on a $22 \text{ }\mu\text{m}$ thick monocrystalline silicon membrane which is sitting on a thicker silicon rim. Figure 32a shows the sensor chip upside down with respect to its actual positioning when mounted in the platform. The thermopile membrane at the center is glued to a Pin-Grid Array (PGA) to allow contacting all components fabricated on the membrane. The bottom face of the membrane, visible in Figure 32a, holds all integrated thin-film elements, such as the serpentine aluminum resistive heaters at the center and the thermopile, whereas the hidden top face is the one interfacing with the sample reservoir.

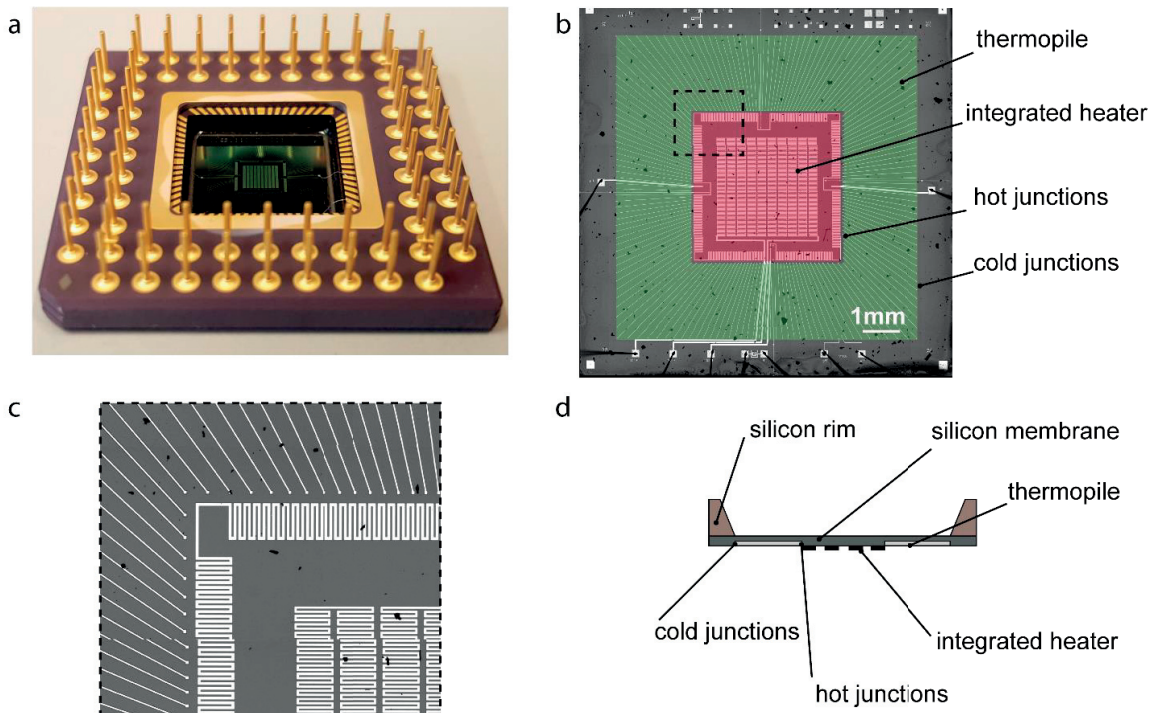


Figure 32 The thermopile sensor (XEN-NCM 9924, *Xensor Integration*). a) Photograph of the sensor chip, positioned upside down. The bottom face of the membrane is visible in the center of the frame, where the components, such as the resistive heaters, are fabricated. The ceramic Pin-Grid Array (PGA), to which the membrane is glued, is also shown. b) Bottom view of the thermopile sensor chip, indicating the position of hot and cold junctions of the silicon-aluminum thermopile (highlighted in green) and of the integrated aluminum heaters (highlighted in red) on the monocrystalline silicon membrane (area $8.3 \times 8.3 \text{ mm}^2$). c) Close-up view of a region on the sensing membrane, as indicated by the dashed line in b), showing radially distributed lines corresponding to the thermocouples, and to two different serpentine resistive heaters. d) Cross-sectional sketch of the thermopile sensor chip, showing also the silicon rim.

As shown in Figure 32b, and in the closer view in Figure 32c, the thermopile is made of a series of thermocouples which are radially distributed around a central square area of about $4 \times 4 \text{ mm}^2$. The hot junctions of the thermopile, which define the sensing area, are located on the inner part of the membrane, while the cold junctions are in thermal contact with the rim.

Using the serpentine thin film heater integrated on the central area of the membrane (see Figure 32b-c) is the most direct method for electrical calibration of the thermopile sensor, avoiding most effects of heat loss through other thermal pathways than the sensor membrane. Figure 32d shows a cross-sectional view of the sensor chip with the actual orientation when in operation. The membrane cavity is oriented upside and the fabricated components are on the bottom face of the membrane. The top face of the membrane is the one interfaced with the PS membrane of the sample reservoir.

The full datasheet of the sensor is reported in Appendix A, whereas the most relevant specifications are summarized in Table 3.

Thermopile sensor specifications (at 22 °C)	
membrane size	$8.3 \times 8.3 \text{ mm}^2$
membrane thickness	22 μm
power sensitivity in air at 1013 mbar	1.2 – 2.4 V/W
thermopile resistance	50 k Ω
thermopile temperature sensitivity	50 mV/K
heater resistance (R1-R3)	0.25 k Ω

Table 3 Summary of relevant specifications of XEN-NCM 9924 chip, as reported in the datasheet by *Xensor Integration*.

5.4.3 Sample reservoir and injection system

The sample reservoir is made of a $7 \times 7 \text{ mm}^2$ PC well with an inner size of $5 \times 5 \text{ mm}^2$, which is glued on the bottom to a 25 μm thick PS membrane (*Goodfellow Cambridge Ltd.*), as depicted in Figure 33a. The reservoir is positioned on the sensor membrane so that the sensor is not contaminated by the sample and may be reused for several experiments. Figure 33b shows a photograph of the open nanocalorimetric platform, with the sample reservoir sitting on the sensing membrane, located in the center of the ceramic frame and the PGA. The PGA of the sensor chip assembly is connected through a standard connector (black in the photograph) to the PCB board.

Minimizing the thermal resistance between sample and the sensor membrane is crucial for highly-sensitive heat detection. Therefore, a thin film of thermal grease (*Thermigrease TG 20025, Müller GmbH*) is applied to the interface of the two surfaces. Fluidic connections to the reservoir are provided by polytetrafluoroethylene (PTFE) thin tubing (0.30 x 0.76 mm PTFE microtube, *Fisher Scientific*) that is inserted through holes fabricated into the isothermal holder and in the side walls of the reservoir. As the tubing is in direct contact with the isothermal holder and is filled with the reagents at the beginning of each experiment, the sample is thermalized prior to its injection, minimizing thermal injection artefacts.

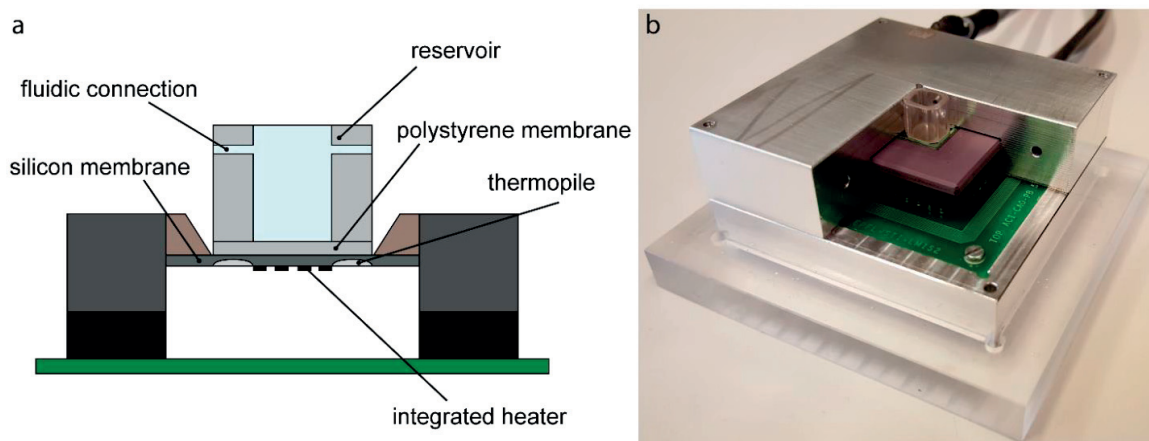


Figure 33 Sample reservoir located on the top of the thermopile membrane. a) Cross-sectional view of the core of the platform, showing the 25 μm polystyrene membrane at the bottom of the sample reservoir, which is in direct contact with the sensor membrane. Fluidic connections are fabricated on the sidewalls of the reservoir and are aligned to the corresponding holes in the aluminum holder providing direct access from the outside. b) Photograph of the nanocalorimetric platform, taken after opening the platform and removing one of the three assembled aluminum parts. The polycarbonate reservoir sitting on the membrane at the center of the sensor chip is visible. (The holes in the aluminium parts visible in the photograph are for closing the system with screws, the fluidic connections are hidden by the reservoir).

Additionally, the choice of material being used for both the sample reservoir and reservoir membrane was driven by chemical compatibility and biocompatibility, depending on the application involved. Both materials have very high chemical resistance [170], also to solvents, and in particular polystyrene was chosen for the reservoir membrane, as it is, because of its biocompatibility, the material of choice for a wide range of consumables used in cell culture.

5.5 Computational modeling of the nanocalorimetric platform

Computational simulations have been carried out in Comsol Multiphysics[®], modeling the heat transfer phenomena involved in the typical operating range of temperature of the nanocalorimetric platform.

5.5.1 Model definition

A two-dimensional model was developed as shown in Figure 34. This model reproduces the actual size of all parts present in the isothermal holder. Moreover, the relevant physical properties (mass density ρ , thermal conductivity k and specific heat capacity c_p) of the different materials involved are specified, including the silicon sensor chip membrane, the PS reservoir membrane, the PC reservoir, the aluminum parts, the PMMA top plate, as well as the partially water-filled reservoir (sample), and the air gaps. Additionally, the model includes also the ceramic chip frame, the printed circuit board and the copper pins of the sensor chip contacts. Table 4 summarizes the different material parameters used in the model. Most of the thermal properties are already available in the Comsol material database, including the temperature-dependent behavior for air and water. The thermal properties for the PS reservoir membrane, as well as for the PC reservoir were obtained from tabulated values [170].

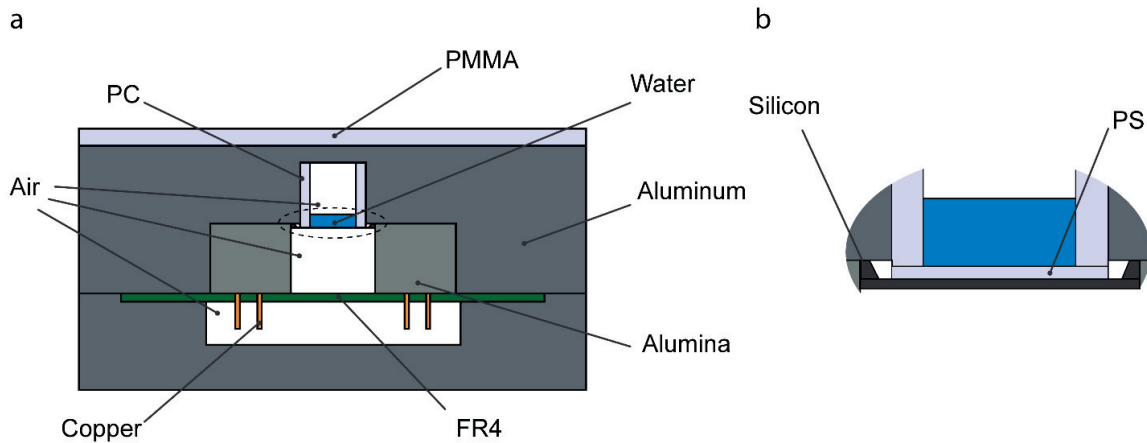


Figure 34 Materials assigned to the different parts of the model. a) Full view of the device. b) Closed-up view to show the location of the silicon membrane of the thermopile sensor (dashed line in a), and the PS membrane of the reservoir.

For modeling, the Comsol module for *Heat Transfer in Solids* was used. Simulation is based on the heat conduction equation (Equation 5:4), which was applied to a two-dimensional system in our case. A free triangular mesh was used for all parts of the model, using a predefined mesh element size (parameter chosen: *extremely fine*).

Materials	Density ρ (kg/m ³)	Thermal conductivity k (W/(m·K))	Specific heat capacity c_p (J/(kg·K))
Air	<i>temperature dependence as from Comsol material database</i>		
Alumina	3900	27	900
Aluminum	2700	160	900
Copper	8700	400	385
FR4 (Circuit Board)	1900	0.3	1369
PC	1201	0.2	1200
PMMA	1190	0.19	1420
PS	1050	0.12	1200
Silicon	2330	163	703
Water	<i>temperature dependence as from Comsol material database</i>		

Table 4 Thermal properties of materials, as specified in the computational modelling.

The boundary conditions applied to the model may be listed as follows:

- Temperature T_0 as initial value of all parts present in the model.
- Heat source Q_{HEATER} applied at the interface between the top aluminum surface and the PMMA plate (as indicated in Figure 35). It is a flat constant heat source modeling the PID heater used for heating the isothermal holder.
- Heat source Q_{SAMPLE} , which models the heat generated locally by the sample.

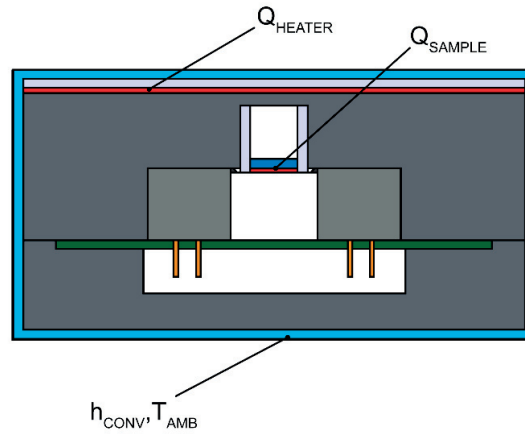


Figure 35 Boundary conditions applied to the model.

- Convective cooling, applied to all external surfaces of the holder, modeling the natural convection occurring on the surfaces exposed to air at ambient temperature T_{AMB} . This boundary condition takes into account Newton’s law of cooling (Equation 5:5). In particular, for free convection of air, the convective heat transfer coefficient h_{CONV} was set to $10 \text{ W}/(\text{m}^2\cdot\text{K})$, based on average tabulated values taken for literature.

Four main types of studies have been carried out, which will be described in the following. Table 5 summarizes the actual boundary conditions that have been applied.

Boundary conditions	Effect of the external heat source Q_{HEATER}	Effect of heat generated by the sample Q_{SAMPLE}	Transient study: constant Q_{HEATER}	Transient study: constant Q_{SAMPLE}
T_0	20 °C	25 °C	20 °C	25 °C
Q_{HEATER}	initial: $130 \text{ W}/\text{m}^2$ final: $505 \text{ W}/\text{m}^2$	$0 \text{ W}/\text{m}^2$	$145 \text{ W}/\text{m}^2$	$0 \text{ W}/\text{m}^2$
Q_{SAMPLE}	$0 \text{ W}/\text{m}^3$	initial: $10^2 \text{ W}/\text{m}^3$ final: $10^5 \text{ W}/\text{m}^3$	$0 \text{ W}/\text{m}^3$	$10^3 \text{ W}/\text{m}^3$
Convective cooling	$h=10 \text{ W}/\text{m}^2\text{K}$ $T_{AMB}=20 \text{ °C}$	$h=10 \text{ W}/\text{m}^2\text{K}$ $T_{AMB}=25 \text{ °C}$	$h=10 \text{ W}/\text{m}^2\text{K}$ $T_{AMB}=20 \text{ °C}$	$h=10 \text{ W}/\text{m}^2\text{K}$ $T_{AMB}=25 \text{ °C}$

Table 5 Boundary conditions applied for the different computational studies.

5.5.2 Effect of the external heat source

The first stationary study aimed at investigating the range of heat power Q_{HEATER} , that should be applied to the PID heater in order to reach and to maintain a given target temperature. For this purpose, a parametric sweep on Q_{HEATER} was carried out, considering a stepwise increase of the heat power per unit area values from $130 \text{ W}/\text{m}^2$ to $505 \text{ W}/\text{m}^2$ (step increase of $15 \text{ W}/\text{m}^2$). Results are summarized in Figure 36a. In particular, a linear behavior is observed when plotting the temperature of the isothermal holder at the center of the sensing area vs the heat power Q_{HEATER} . Depending on the experiments to be carried out, the temperatures of 25 °C and 37 °C are of particular interest. In order to be able to reach these temperatures, the applied heat power per unit area Q_{HEATER} should be around $145 \text{ W}/\text{m}^2$ and $500 \text{ W}/\text{m}^2$, respectively. Considering a heating surface of $50 \times 50 \text{ mm}^2$, the heat power required is in the order of a few watts.

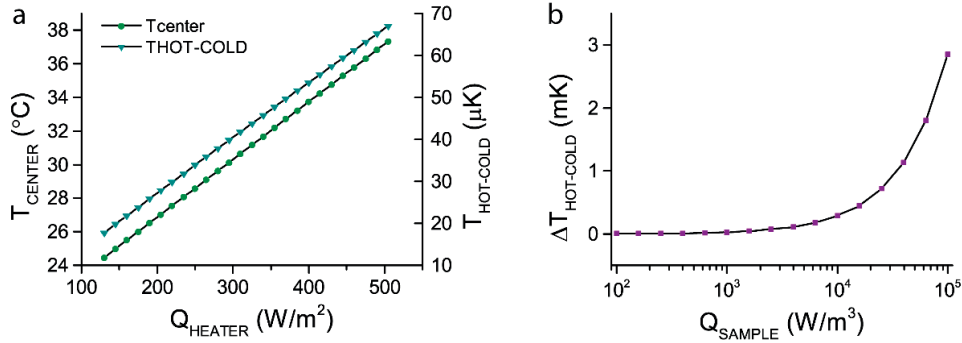


Figure 36 Computational results for steady-state studies. a) Temperature at the center of the sensing area and temperature difference calculated, based on the temperature on the two positions where the hot and cold junctions are located in the real case, vs the heat power Q_{HEATER} applied to the isothermal holder to reach the setpoint temperature. b) Temperature difference between hot and cold junctions resulting from the production of the heat power Q_{SAMPLE} by the sample (logarithmic scale in the plot).

Furthermore, the temperature difference $\Delta T_{\text{HOT-COLD}}$ between hot and cold junctions on the membrane has been considered. This temperature difference is calculated as the difference of the temperature values taken at the position where the hot and cold junctions are actually located. As it can be observed from Figure 36a, with increasing external heat power, the temperature difference $\Delta T_{\text{HOT-COLD}}$ increases as well. This is intuitively expected as, when heating to higher temperature with respect to the ambient temperature, the temperature gradient inside the isothermal holder also increases. As this thermal gradient is not related to sample heating, it generates a baseline voltage signal on the thermopile. By taking into account the temperature sensitivity of the thermopile sensor, it is possible to obtain a first estimate of such background signal. From the specifications by *Xensor Integration* (see Appendix A) and as summarized in Table 3, the thermopile sensor used in this nanocalorimetric platform has a temperature sensitivity of 50 mV/K. Considering that the simulated temperature differences $\Delta T_{\text{HOT-COLD}}$ arising when heating up to 25 °C and 37 °C are around 20 μK and 65 μK , respectively, the estimated background voltage signals are in the order of few μV .

5.5.3 Effect of heat generated by the sample

A second stationary study was carried out, by assuming the platform temperature to be stabilized at the setpoint temperature of 25 °C and by applying a parametric sweep to the heat generated by the sample Q_{SAMPLE} . The aim of such study was to have an estimate of the temperature differences $\Delta T_{\text{HOT-COLD}}$ resulting from the production of heat by the sample. Considering a range of heat power per unit volume from 10^2 W/m^3 to 10^5 W/m^3 , which corresponds to total heat power from around 60 nW to 60 μW (for a sample volume of 50 μl), the simulated temperature difference $\Delta T_{\text{HOT-COLD}}$ is reported in Figure 36b. In particular, for very low heat power (60 nW) the temperature difference $\Delta T_{\text{HOT-COLD}}$ is in the order of few μK . For intermediate values of heat power (6 μW), the temperature difference $\Delta T_{\text{HOT-COLD}}$ rises to hundreds of μK , and finally for high heat power (60 μW), the temperature difference $\Delta T_{\text{HOT-COLD}}$ is in the order of few mK. By considering the temperature sensitivity of the thermopile sensor, the expected voltage signal resulting from the production of heat by the sample may be up to a few hundreds of μV .

5.5.4 Estimation of the thermal time constants

The time-dependent studies were carried out to estimate the two time constants of the system, the thermalization time constant, and the sensing time constant, as mentioned in section 5.1.3. The first one describes how fast the system reaches a stable temperature setpoint. The latter estimates how fast the temperature difference $\Delta T_{HOT-COLD}$ stabilizes in response to heat generated by the sample.

The first transient study aimed both at simulating the thermal gradient observed when heating up the isothermal holder to 25 °C, and at quantifying the time scale for reaching the setpoint temperature. For this study, the only heat source applied is the flat constant heat source in the upper part of the holder Q_{HEATER} , which is switched on at $t = 0$ at 145 W/m². The results are summarized in Figure 37. Figure 37a shows the temperature distribution at two different time points showing the evolution of the thermal gradients in the platform over time. Shortly after switching on the heat source ($t = 1$ min) the temperature of the holder is still very close to the initial temperature (20°C). However, a significant thermal gradient of up to about 60 mK arises in the sensing area (visible in the magnification inset of the sensing area at $t = 1$ min). This gradient in the sensing area decreases as the holder approaches the setpoint temperature, as shown in the same figure (for $t = 120$ min). The corresponding curves for the average temperature T_{CENTER} in the sensing area (taken at the center of the sensing area) and for the thermal gradient $\Delta T_{HOT-COLD}$ between hot and cold junctions as a function of time are shown in Figure 37b. Assuming an exponential approach of the temperature T_{CENTER} from 20 °C to the final target temperature T_F of 25 °C, the temperature profile may be described as:

$$T_{CENTER} = T_{AMB} + (T_F - T_{AMB}) \cdot (1 - e^{-t/\tau'})$$

Equation 5:19 – Transient temperature profile assuming heating up to the setpoint temperature T_{CENTER}

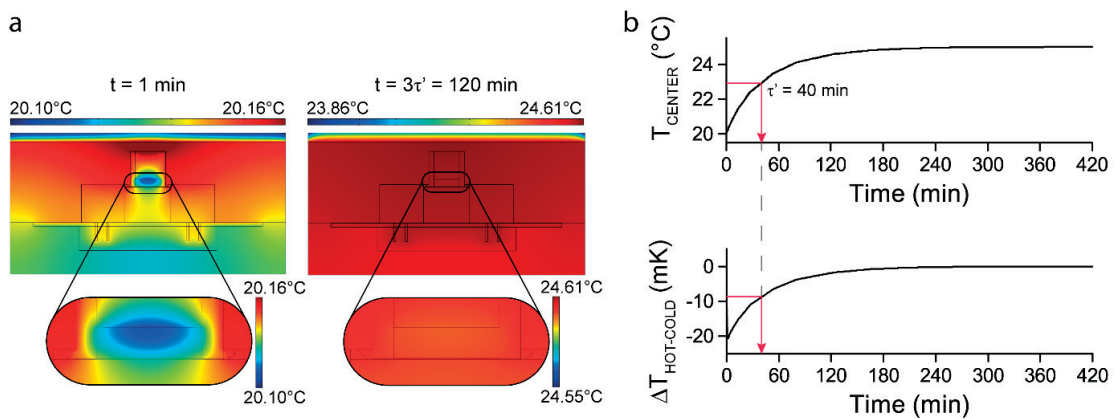


Figure 37 Time-dependent computational results when simulating heating the isothermal holder by the flat heater Q_{HEATER} (equal to 145 W/m²) to 25 °C. a) Temperature gradient immediately after switching on Q_{HEATER} ($t = 1$ min, $T_{AMB} = 20$ °C) and after heating for a characteristic time equal to $3\tau'$ ($t = 120$ min). The time constant τ' is estimated to be 40 min. b) (i) Temperature evolution over time in the center area of the chip membrane, when applying the heat source Q_{HEATER} . (ii) Corresponding temperature difference $\Delta T_{HOT-COLD}$ between hot and cold junctions.

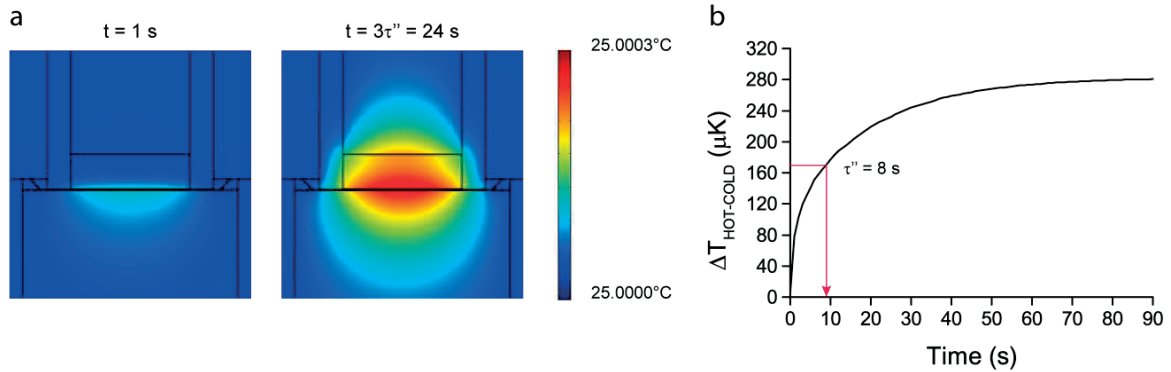


Figure 38 Time-dependent evolution of the temperature in the sensing area after applying the constant local heat source $Q_{\text{SAMPLE}} = 10^4 \text{ W/m}^3$ generated by the sample in the reservoir, starting from a platform temperature that is stabilized at 25°C . a) Simulated temperature gradient immediately after switching on the heat source ($t = 1 \text{ s}$), and after a characteristic time equal to $3\tau''$ ($t = 24 \text{ s}$). b) Corresponding temperature difference $\Delta T_{\text{HOT-COLD}}$ between hot and cold junctions of the thermopile over time. The second time constant of the system τ'' is about 8 s .

where τ' (s) is the time constant of the system. The time constant τ' may thus be defined as the time $t = \tau'$ at which the temperature T_{CENTER} is equal to $T_{\text{AMB}} + 0.63(T_{\text{F}} - T_{\text{AMB}})$. The estimated value for the system is 40 min , which is acceptable for common biological experiments. After $3\tau'$ the system has approached the setpoint temperature and thermal gradients over the sensing area are negligible, as can be observed on the second inset of Figure 37b.

The characteristic time constant τ'' , which corresponds to the response time of the system upon heat generated by a sample located on the sensing membrane, was determined in a second transient study. Fast sensing response times improve the time resolution of dynamic measurements of heat-generating samples or reactions. This simulation was carried out by assuming the platform temperature to be stabilized at 25°C and by applying a local heat source Q_{SAMPLE} of 10^4 W/m^3 at $t = 0$. Assuming an exponential approach of the temperature gradient $\Delta T_{\text{HOT-COLD}}$ to equilibrium, the time constant τ'' may be defined as in the previous case (see Equation 5:19) and it has been determined to be 8 s . The temperature distribution in the sensing area is shown in Figure 38a (for $t = 1 \text{ s}$ and $t = 3\tau'' = 24 \text{ s}$), while the corresponding time evolution of the temperature gradient $\Delta T_{\text{HOT-COLD}}$ between hot and cold junctions is shown in Figure 38b. The results of this second transient study demonstrate that the sensing response time is adequate for good time-resolved detection of most chemical/biochemical processes and that maximum thermal gradients of a few mK are expected for tens of μW of heat power generated by the sample.

5.6 The isothermal holder and temperature control system

5.6.1 Design and functions of the isothermal holder

The sensor chip is incorporated into an isothermal holder that provides a temperature-regulated environment (external dimensions of $60 \times 60 \times 30 \text{ mm}^3$). As already depicted in Figure 30, the silicon sensor rim of the sensor chip is tightly clamped between two aluminum parts to provide a good thermal contact. A temperature controller (Model 335, *Lake Shore Cryotronics, Inc.*), which is operated in a closed loop PID mode, is used to stabilize the temperature of the isothermal holder at the

setpoint value. The temperature control system includes also a temperature sensor (PID sensor) and an electrical heater (PID heater). The PID sensor is a miniature platinum sensor ($1.6 \times 1.2 \text{ mm}^2$) with $1000 \ \Omega$ nominal resistance at 0°C (Pt1000 class A, *IST Innovative Sensor Technology*). A small groove in the aluminum part that is in direct contact with the sensor chip accommodates the PID sensor. Good thermal contact is achieved by clamping the sensor with an aluminum plate (1 mm thick). The PID controlled heater is a flat polyimide square heater ($50.8 \times 50.8 \text{ mm}^2$, $36.1 \ \Omega$ resistance, *Minco*) which is fixed on top of the aluminum plate by a PMMA plate (3 mm thick). The PMMA plate also reduces heat loss to the external environment.

The isothermal holder has three main functions:

- It allows to thermalize the system at a specific setpoint temperature. This is achieved thanks to the integration of the PID temperature control system, which is described in the following section, with the isothermal holder.
- It works as a heat sink for the thermopile sensor. As mentioned, the aluminum parts are in good thermal contact with the sensor rim, which in turn is in thermal contact with the cold junctions of the thermopile. Thus, the cold junctions are kept at a constant temperature through the temperature control of the isothermal holder. The stability of the temperature control system is particularly critical, as already observed in section 5.1.2, as temperature fluctuations negatively affect the appropriate thermopile readout.
- It works as a Faraday cage allowing electrical shielding of the thermopile voltage signal to be measured. As voltage signals as low as a few μV are expected to be measured, interference with external noise sources may negatively affect the SNR. To avoid this, the shielding of the

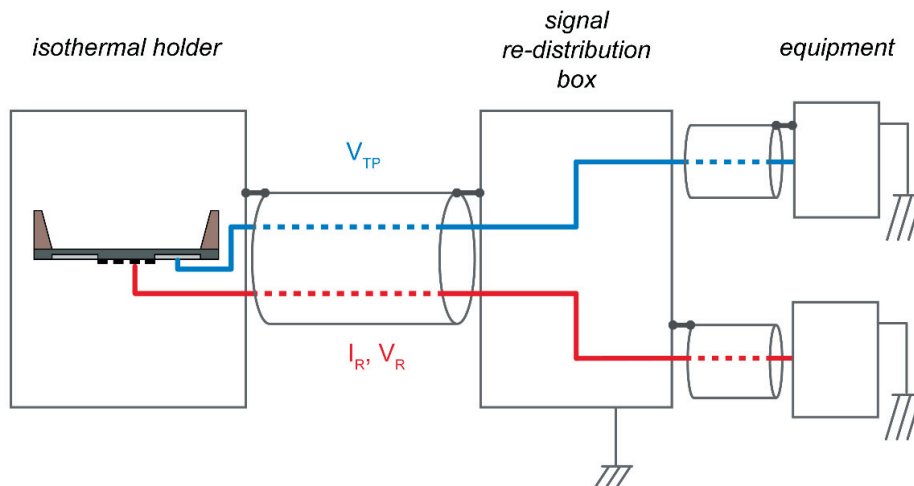


Figure 39 Schematic explaining shielding of the nanocalorimetric platform. The isothermal holder (depicted as a grey rectangle) with the thermopile sensor, the metal chassis (depicted as a grey rectangle) of the signal re-distribution box, as well as the shields of the cable in between both devices (for the thermopile voltage signal V_{TP} and for the resistive heater signals I_R and V_R) are connected to a common ground. In order to avoid ground loops, the shields of the separate twisted cables for the signals V_{TP} and I_R , V_R connecting the respective equipment are interrupted at specific locations.

whole system, from the thermopile sensor to the electronic readout by a commercial nanovoltmeter, was carefully designed. Figure 39 depicts the electrical shielding strategy of the device, including the metal isothermal holder, shielded twisted cables and a shielded signal distribution box. From there, signals are distributed to the different equipment through shielded twisted cables. Additionally, grounding is achieved through the metal chassis of one of the equipment in use.

5.6.2 Temperature control based on PID algorithm

The closed loop control system implemented in the development of the nanocalorimetric platform is based on a PID algorithm. There are three terms involved in such control: the proportional (P), the integrative (I) and the derivative (D) term.

In order to describe the implementation of such algorithm, first the error signal $e(t)$ is defined as [171]:

$$e(t) = r(t) - y_m(t)$$

Equation 5:20 – Definition of process error signal

where $r(t)$ is the reference signal and $y_m(t)$ is the measured output signal. During operation the control continuously measures the signal $e(t)$ and takes different actions depending on the parameters set.

The proportional term allows the controller to introduce a correction that is proportional to the error signal. Considering the output signal of the controller $u_c(t)$, then [171]:

$$u_c(t) = k_p e(t)$$

Equation 5:21 – Proportional gain definition

where k_p is the proportional gain.

A high proportional gain allows reaching the setpoint temperature faster. Typically, the controller works in an on/off mode when the error signal is high. For example, considering the PID control implemented for the nanocalorimetric platform, the controller switches on maximum heating power on the PID heater when the system temperature is too low compared to the setpoint temperature. Instead, it switches the heating power off when the system temperature is too high. Then, when the temperature is closer to the setpoint temperature, *i.e.* the error signal is smaller, the proportional mode takes action. The thresholds between the three operational modes (on/proportional/off) defines the proportional band around the setpoint temperature. This implementation allows eliminating the typical oscillating behaviour observed with a simple on/off control.

The integral term allows improving the control algorithm, as the output signal of a pure proportional controller has often an offset, *i.e.* a difference between the stable system temperature and the set-point temperature. The controller output signal $u_c(t)$ can thus be defined as [171]:

$$u_c(t) = k_I \int e(\tau) d\tau$$

Equation 5:22 – Integral controller gain definition

where k_I is the integral controller gain.

Therefore, such term relies on the integration with respect to time of the error signal, and the action taken by the controller is proportional to the numerical result of this integration. Considering again the nanocalorimetric platform developed, if no offset exists, then no action is taken by the controller. As soon as an offset is observed, the heating power applied to the PID heater is increased or decreased, depending on the presence of a positive or negative offset, respectively.

The derivative is the third term. In this case, the output signal of the controller is proportional to the rate of change of the error signal, as described by the following equation [171]:

$$u_c(t) = k_D \frac{de}{dt}$$

Equation 5:23 – Derivative control gain definition

where k_D is the derivative control gain.

This latter term is particularly important when the setpoint temperature is changing, as it allows the system temperature to follow closely such changes. Therefore, this term is relevant when using scanning temperature devices. For the nanocalorimetric platform developed, instead, the normal

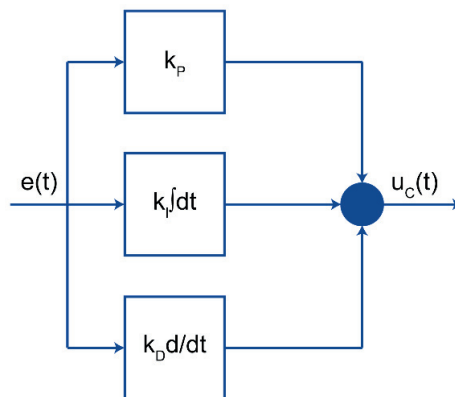


Figure 40 Sketch representing the operation of the PID control system: the output signal of the controller $u_c(t)$ is the sum of the different contributions, *i.e.* the proportional term (k_p), the integrative term (k_I) and the derivative term (k_D), which are applied for correcting the error signal $e(t)$ at the input.

operating mode is at steady state, *i.e.* by setting a constant setpoint temperature for the full length of the experiment. For this reason, the derivative control gain is set to zero for this specific application. Figure 40 summarizes the contributions of all the three terms involved in the PID control.

5.6.3 Integration of the PID control system in the isothermal holder

An important issue in the integration of the PID control system with the isothermal holder is the choice of the location of the PID controlled elements, *i.e.* the PID sensor and the PID heater. Considering that the aim of the implemented PID control is to keep the cold junctions of the thermopile sensor at a stable setpoint temperature, the three locations, *i.e.* the cold junctions location, the PID sensor location and the PID heater location, should be as close as possible, in order to obtain a good accuracy of temperature reading and fast feedback. Additionally, the PID sensor may be located either closer to the PID heater or closer to the cold junctions. The first configuration allows minimizing fluctuations around the setpoint temperature, under steady state conditions. The second configuration allows a better readout of the cold junctions temperature under transient conditions or when the controller is used in temperature scanning mode. However, in the second case, as the PID sensor and heater are more distant, a time lag during the control exists due to thermal inertia, resulting in undershooting and overshooting, which negatively affects the temperature stability of the system. For this reason, the location of the PID sensor for the present application was chosen closer to the PID heater, in order to minimize thermal inertia in the control and to allow high temperature stability.

The second step in the integration of the PID control system was tuning the PID control gain parameters (k_P , k_I and k_D). There are different methods of tuning [171], and all are based on experimental observations of the effects when changing the PID control gains. The “*guess and check*” method was used in this context, which can be summarized by the following actions:

1. Setting the integrative and derivative term to zero. A pure proportional control is active, and the proportional gain may be stepwise increased, in order to reach faster the setpoint temperature. In fact, for too low proportional gains the setpoint temperature will be approached too slowly. On the other hand, for too high proportional gains, instabilities may take place, such as oscillation of the system temperature.
2. The integrative term is introduced to eliminate temperature instabilities and/or possible offsets. Such term should be gradually increased too, as it increases the overshoot. In particular, overshoot is always present in fast stabilizing system, and a compromise should be found for an acceptable overshoot.
3. The derivative term is set to 0. As already observed in section 5.6.2, steady state systems, which are not continuously changing the setpoint temperature, do not require such term.

The tuning of the PID control gains should be done for each setpoint temperature of interest, as different heat power ranges may be applied to the PID heater. Table 6 summarizes the PID control

gains, as defined for the system used in our experiments, tuned for working at the setpoint temperatures of 25 °C, foreseen for calorimetric measurements on chemical reactions, and 37 °C as used for biological experiments. In particular, the three terms P , I and D are defined as reported in the controller user manual:

$$\text{heater output} = P \left(e + I \int e \cdot dt + D \frac{de}{dt} \right)$$

Equation 5:24 – PID controller output as defined in the *Lakeshore* PID controller user manual

Setpoint temperature	Heating power range	P	I	D
25 °C	medium	1000	30	0
37 °C	high	500	20	0

Table 6 PID control gains used for the integrated control system at the two setpoint temperatures of 25 and 37 °C.

5.6.4 Platform automation and data acquisition

A software-controlled syringe pump (Nemesys Syringe Pump, *Cetoni GmbH*) is used for automated sample injection of typically 1.5 to 5 μl . The pump was controlled by a dedicated interface. As sketched in Figure 41, all other equipment are controlled through a custom-made program developed in Labview (*National Instruments*), including the temperature controller, a nanovoltmeter (34420A, *Agilent*) for thermopile signal acquisition, and a sourcemeter (2400, *Keithley Instruments*) for implementing the calibration procedure. All data were acquired with a sampling time of 1 sec. Figure 42 shows a photograph of the nanocalorimetric platform, including the necessary equipment. In particular, we have developed two main Labview interfaces (see Appendix B) for controlling the necessary equipment:

- Nanocalorimetric interface: This interface allows running actual nanocalorimetric experiments. This interface controls only the PID controller and it acquires the voltage signal from the thermopile sensor.
- Calibration interface: This interface allows controlling all three equipment, *i.e.* the PID temperature controller, the nanovoltmeter for measuring the thermopile voltage and the sourcemeter for running electrical calibration with a resistive heater. In particular, this interface allows setting a current or a voltage to the resistive heater through the sourcemeter and measuring the corresponding voltage or current, respectively. Raw signals are always acquired, and only subsequently data processing, such as filtering and averaging, is applied.

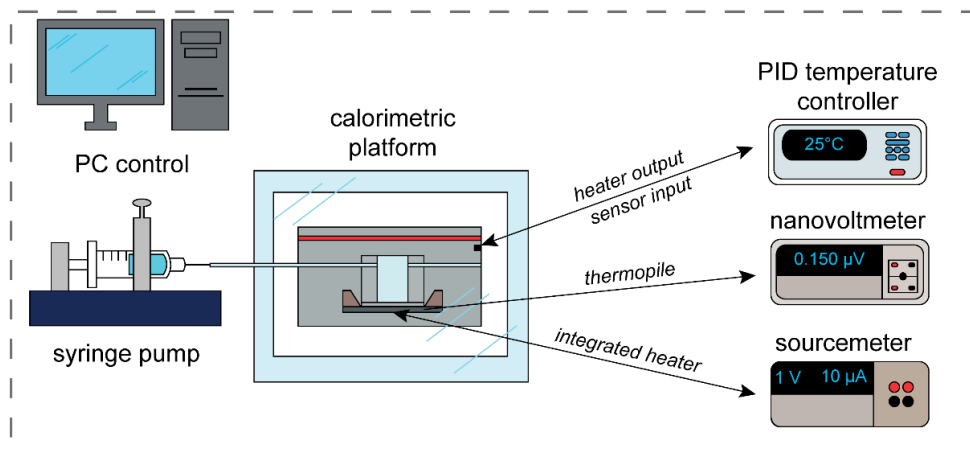


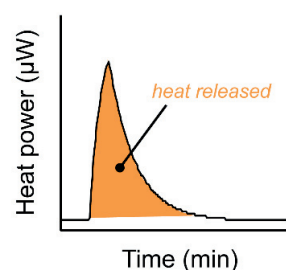
Figure 41 Different elements of the nanocalorimetric platform for fluidic sample injection, electrical signal acquisition and temperature control. The control of the full system is automatized through a Labview (*National Instruments*) interface.



Figure 42 Photograph showing the nanocalorimetric platform and the necessary equipment. Acquisition equipment are on the right-hand side (from the top to the bottom): the nanovoltmeter, the sourcemeter and the temperature controller. On the back of the picture, the signal distribution box is visible. The syringe pump used for sample injection is on the left side. The foreground shows the nanocalorimetric platform, including the outer PMMA box surrounding the aluminium holder, which is used for additional insulation from external temperature fluctuations.

Chapter 6 Characterization and validation of the nanocalorimetric platform

This chapter reports on the characterization and validation of the newly developed nanocalorimetric platform working with sample volumes of a few tens of μl . The platform has a very high temperature stability, down to ± 1 mK over a period of about one hour for a setpoint temperature of 25 $^{\circ}\text{C}$. A maximum power sensitivity of 2.7 V/W was determined by electrical calibration, as well as a limit of detection of 70 nW. An experimental sensing time constant of 6 seconds was estimated by using a resistive heater. The platform functionality was demonstrated by a thermodynamic study of the mixing enthalpy of 1-propanol in water (a typical measurement curve is shown on the right hand side) and by a kinetic study of the glucose oxidase-catalyzed oxidation of glucose.



Some sections of this chapter have been reported in following journal article [154] and conference proceedings [155]:

Nanocalorimetric platform for accurate thermochemical studies in microliter volumes (2015)

R. Padovani, T. Lehnert, R. Trouillon, and M. A. M. Gijs

RSC Advances, vol. 5, no. 118, pp. 97133–97142

DOI: 10.1039/C5RA22248F

A microcalorimetric platform for studying the heat produced by chemical reactions in microlitre volumes (2015)

R. Padovani, T. Lehnert, and M. A. M. Gijs

Proc. of 19th International Conference on Miniaturized Systems for Chemistry and Life Sciences (microTAS 2015)

Gyeongju, Korea.

This chapter reports the experimental results obtained with the nanocalorimetric platform. First, the platform is evaluated, both in terms of temperature stability and in terms of thermopile voltage stability. Second, two different configurations of electrical calibration are presented, *i.e.* by using the resistive heater integrated on the chip membrane, and by using an external resistive heater immersed in the sample reservoir. The power sensitivity was calculated and the limit of detection was estimated. Validation of the nanocalorimetric platform was performed by the measurement of the heat power released/absorbed during well-known (bio-)chemical reactions, *i.e.* the mixing of 1-propanol in water and the oxidation of glucose catalyzed by glucose oxidase. Data processing and analysis for better comparison of the experimental data with literature is described in detail. Finally, preliminary heat power measurements were carried out on *C. elegans* nematodes, and initial results are reported showing the potential of this technology for the study of metabolic heat produced by living organisms.

6.1 Characterization of the platform stability

The initial characterization of the nanocalorimetric platform was carried out at two specific temperatures, 25 °C and 37 °C, as used for experiments involving many (bio-)chemical reactions and for experiments on specific biological samples, respectively. To evaluate the platform stability, the target temperature and PID parameters were set through the Labview interface, via which the PID sensor temperature T_{PID} and the thermopile voltage V_{TP} were acquired. In this experimental configuration, no sample reservoir was placed on the chip membrane.

6.1.1 Platform thermalization and temperature stability

As described in Chapter 5, the PID control parameters have been optimized to obtain a good compromise between fast response time for the thermalization of the platform as a whole with minimum oscillations around the setpoint temperature. Figure 43a shows the temperature T_{PID} acquired by the PID sensor over time for a target temperature of 25 °C. The setpoint temperature of 25 °C is reached after 10-15 min, whereas a maximum temperature fluctuation of ± 0.001 °C around 25.000 °C is observed after 20 min, indicating an extremely good thermal stability of the platform. The temperature stability of the platform should, in principle, be defined by $\pm \sigma_T$, where σ_T is the standard deviation of T_{PID} in the time window of interest. However, in our setup the accuracy of measurement was in fact limited by the resolution of the temperature read-out (± 1 mK, see the magnified inset in Figure 43a), thus we consider this limit to estimate the temperature stability.

The difference observed between the computationally estimated time constant for thermal stabilization of the system ($\tau' = 40$ min, see Chapter 5, section 5.5.4) and the experimental thermalization time ($\tau' \approx 20$ min) arises from the fact that we considered a constant heat source Q_{HEATER} in the thermal simulation, corresponding to the minimum heat power required to reach the target temperature. Instead, in the experimental condition, the PID controller temporarily applies a much higher power and controls the heater dynamically to reach and maintain the setpoint temperature. Faster thermalization can therefore be expected.

The temperature stability at 37 °C, and the corresponding temperature T_{PID} , are shown in Figure 43b. Also in this case the temperature stabilizes after 10-15 min, and a maximum stability of the order of ± 1 mK is achieved after 20 min. In fact, as it is possible to observe in the inset of Figure 43b, the temperature oscillates mainly in the temperature range between 37.000 and 37.001 °C, even though more frequently somewhat higher temperature fluctuations reaching 37.002 °C are observed. Moreover, also in this case, the accuracy of measurement was essentially limited by the resolution of the temperature read-out.

6.1.2 Thermopile signal stability

The fundamental limit of the thermopile sensor stability was assessed by recording the thermopile voltage V_{TP} after thermalization of the platform at 25°C and 37°C, respectively. For this purpose, a blank chip membrane, *i.e.* without sample reservoir, was used. The thermopile voltage V_{TP} stabilization when setting a platform target temperature of 25 °C is shown in Figure 43c. Higher voltage signals (up to about 40 μ V) are observed in the beginning of the thermalization phase, reflecting thermal gradients generated while heating the platform. The thermopile voltage stabilizes at a lower value once the setpoint temperature is reached and thermal gradients over the sensing area have decreased significantly. This behaviour is confirmed by computational simulations, which have been described in Chapter 5 (section 5.5.4), when simulating the heating of the platform by a flat constant heat source Q_{HEATER} . For this specific experiment, the thermopile voltage V_{TP} has an offset of 7.5 μ V (at 20 min) and a baseline drift of about 0.3 nV/s (for 20 min < t < 40 min). Thus, a baseline subtraction algorithm had to be applied to all subsequent measurements. More specifically, for each measurement the specific offset and baseline drift (linear or non-linear) was experimentally evaluated in a representative range of the experimental $V_{TP}(t)$ curve and then subtracted, resulting in a flat corrected baseline. In Figure 43c, taking σ_V as the standard deviation of the voltage V_{TP} after baseline correction, the voltage signal stability can be estimated as $\pm\sigma_V = \pm 80$ nV. This value sets a lower limit for the detectable sensor signal and, thus, the heat power generated by a sample. As this value is sensitive to the actual experimental conditions, in particular if the sensor chip has been changed, we re-evaluate it before each new series of experiments.

Figure 43d shows the $V_{TP}(t)$ curve when setting a target temperature of 37 °C. In the starting phase of the thermalization process, very high initial voltage signals of the order of few mV are observed. This transient behaviour is due to strong thermal gradients in the system, especially in the chip area, as compared to the previous case. Also the baseline drift is significantly different from the one observed at 25°C. In the specific case reported here, the offset is of 76 μ V at 20 min, and the drift is negative with a value of approximately -8 nV/s in a time window between 20 and 40 min after starting the test. After baseline correction the standard deviation of the voltage V_{TP} may be estimated to be $\pm\sigma_V = \pm 100$ nV. This value is 25% higher compared to the value estimated at 25 °C and, thus, the limit of detection is expected to be slightly worse at 37 °C.

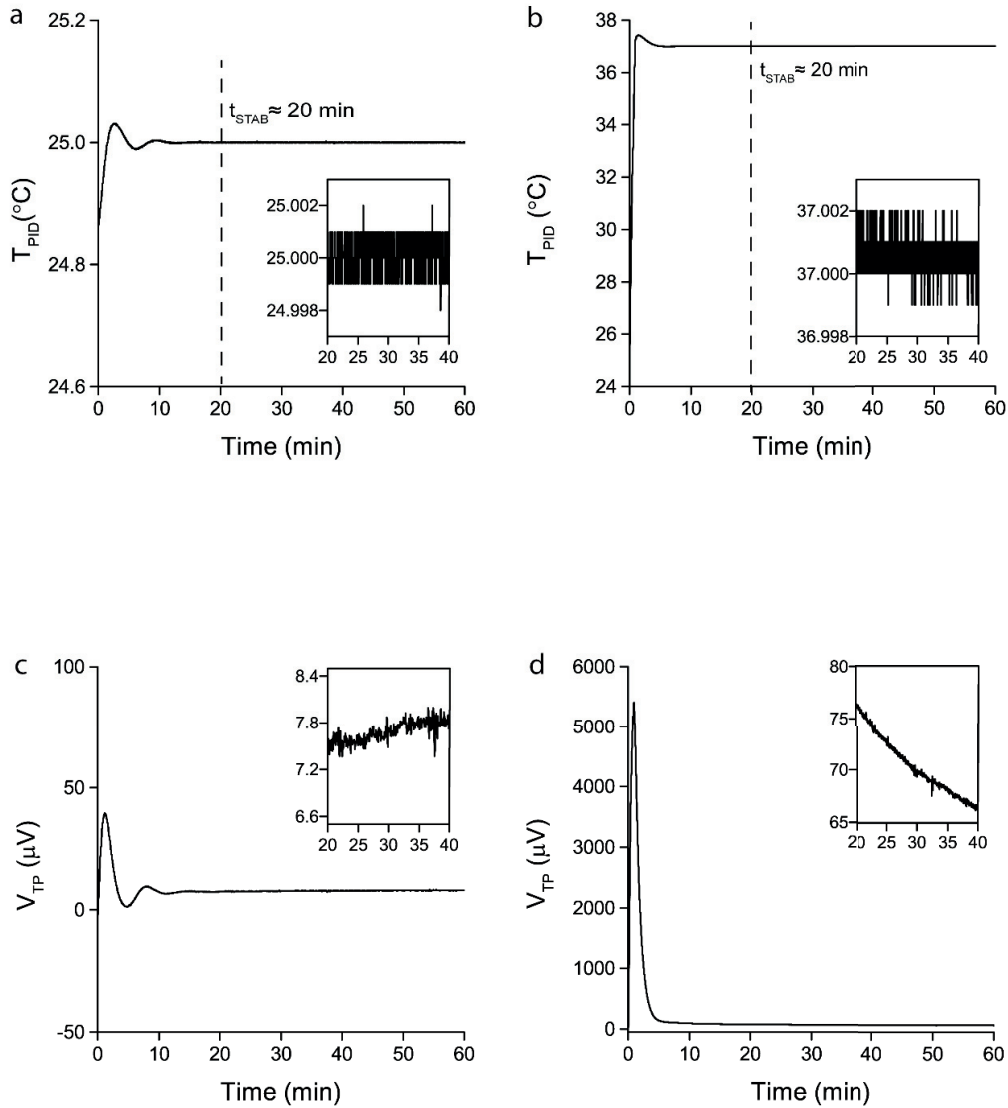


Figure 43 Platform temperature T_{PID} stability and baseline signal V_{TP} acquired by the thermopile sensor at a setpoint temperature of 25 °C and 37 °C, respectively. a) Temperature T_{PID} acquired by the PID sensor over time for a setpoint temperature of 25 °C. The flat heater on the top of the platform is activated at $t = 0$ min. After about $t_{STAB} = 20$ minutes of thermal stabilization, the temperature stability of the platform is $T_{PID} = 25.000 \pm 0.001$ °C (see inset). b) Temperature T_{PID} over time for a setpoint temperature of 37 °C. The temperature stability is again in the range of ± 1 mK (see inset). c) Thermopile voltage V_{TP} over time curve at 25 °C. After full thermalization of the platform ($t > t_{STAB}$), the voltage has a slight baseline drift of 0.3 nV/s (see inset). The voltage signal stability $\pm\sigma_V$ is ± 80 nV after baseline correction. d) Thermopile voltage V_{TP} over time curve at 37 °C. In this case, the baseline drift is -8 nV/s (see inset). After baseline correction, the voltage signal stability $\pm\sigma_V$ is ± 100 nV.

6.2 Electrical calibration and limit of detection

For calibrating the nanocalorimetric platform, the power sensitivity coefficient $PS = V_{TP} / P_R$ has to be determined. This conversion coefficient relates the thermopile voltage signal V_{TP} to the heat power P_R generated by a small heat source on or close to the sample location on the chip membrane. Two different configurations, schematically shown in Figure 44, have been considered. The first one uses the resistive heater integrated on the silicon chip membrane (R_{INT} , no reservoir), while the second one uses an external resistive heater (R_{EXT}), which is a miniaturized negative temperature coefficient (NTC) 100 k Ω thermistor (Micro-BetaCHIP Thermistor Probe (MCD), *Measurement Specialties*) immersed in the reservoir filled with 50 μ l of deionized water. The second calibration procedure mimics more closely the real experimental situation, *i.e.* heat generation by a liquid sample in the reservoir that is placed on the chip membrane. In both cases, gradually increasing electrical power levels were applied to the resistive heaters and converted into heat power by Joule's effect ($P_{R_{INT}}$ and $P_{R_{EXT}}$ for the integrated and external heater, respectively). The corresponding thermopile voltage V_{TP} is measured. This procedure was implemented at the two setpoint temperatures of the nanocalorimetric platform (25 $^{\circ}$ C and 37 $^{\circ}$ C) in order to estimate the power sensitivity coefficients.

Figure 45a shows the electrical calibration sequence for R_{INT} , *i.e.* the applied $P_{R_{INT}}$ values and the resulting V_{TP} signal, at a platform temperature of 25 $^{\circ}$ C. From this type of measurements, the calibration curves for the thermopile voltage V_{TP} were derived. Figure 45b presents the results for both configurations, *i.e.* for the integrated heater R_{INT} and for the external heater R_{EXT} . The corresponding power sensitivity coefficients can be determined as $PS_{R_{INT}} = 2.700 \pm 0.004$ V/W and $PS_{R_{EXT}} = 1.900 \pm 0.008$ V/W, for the internal and external heater, respectively. As expected, the power sensitivity $PS_{R_{INT}}$ is higher, as the heating element and the sensing element are integrated on the same silicon membrane, resulting in very efficient heat power-to-voltage conversion with minimum heat loss. When including a liquid sample reservoir and an external heater, heat losses through alternative thermal paths arise, thus reducing the power sensitivity of the system.

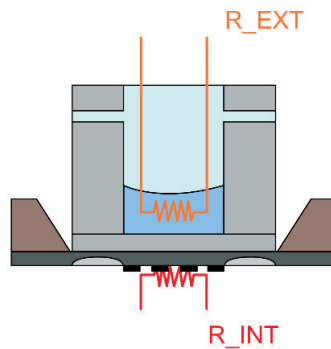


Figure 44 Sketch of the sample reservoir on the silicon membrane, showing the two configurations used for electrical calibration: (i) the resistive thin-film heater integrated directly on the silicon membrane (R_{INT}), or (ii) a miniaturized 100 k Ω thermistor used as resistive heater (R_{EXT}), immersed in the reservoir filled with 50 μ l of deionized water.

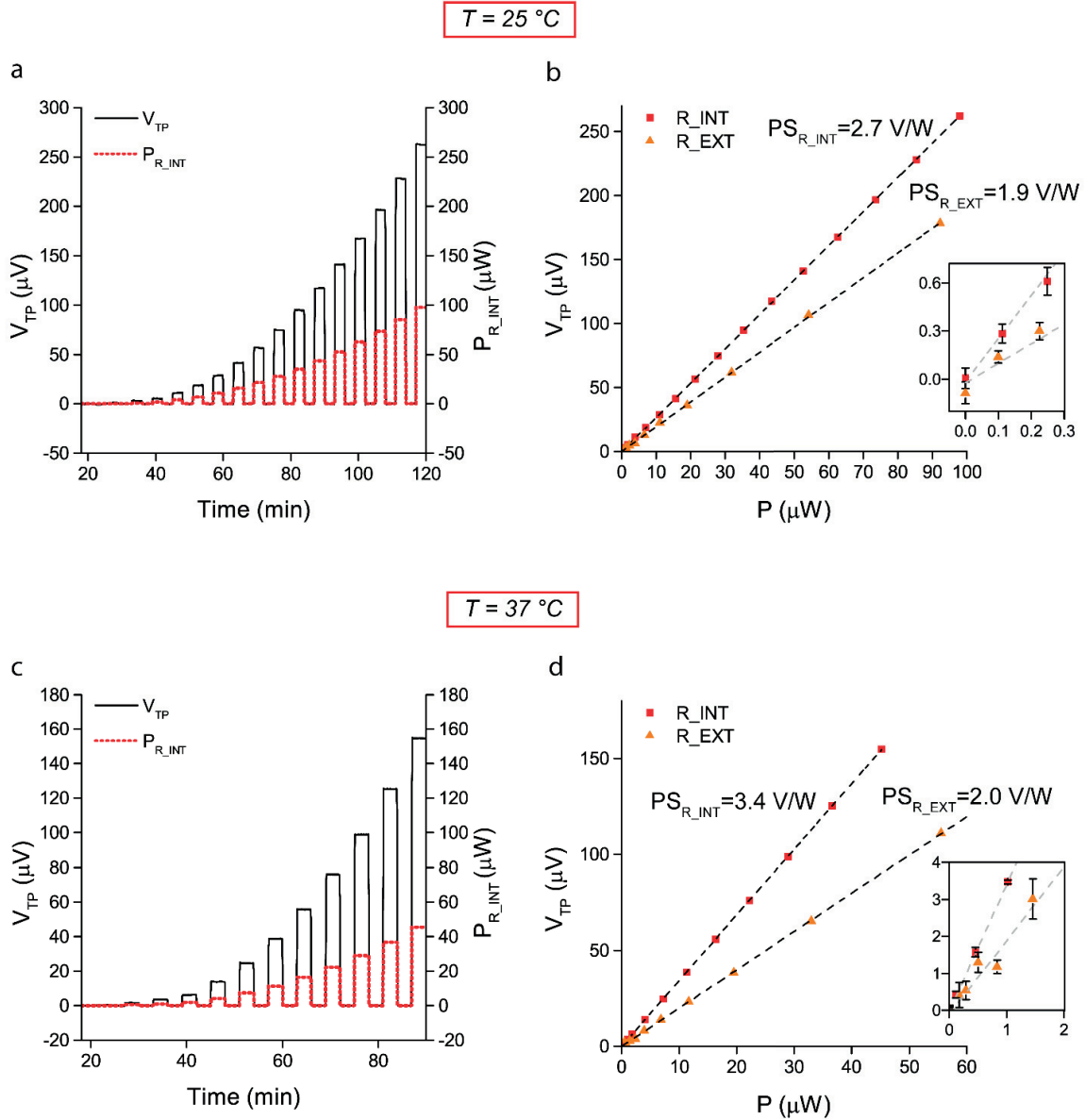


Figure 45 Electrical calibration carried out at 25 °C and 37 °C. a) Thermopile voltage V_{TP} over time curve (full black line), when applying a periodically increasing electrical power to the integrated resistive heater P_{R_INT} (dashed red line), at 25 °C. b) Calibration curves for the integrated heater R_{INT} and for the external heater R_{EXT} , at 25 °C. The corresponding power sensitivities are 2.7 V/W (PS_{R_INT}) and 1.9 V/W (PS_{R_EXT}), respectively. The inset is a close-up of the calibration points for very small heat power (0 – 300 nW) that allows to determine a limit of detection of 70 nW and 170 nW, when using R_{INT} or R_{EXT} , respectively. c) Same sequence as described in a) at 37 °C. d) Calibration curves for R_{INT} and for R_{EXT} at 37 °C. The inset is a close-up of the calibration points for small heat power (0 – 2 μ W) that allows to determine a limit of detection of 100 nW and 500 nW, when using R_{INT} or R_{EXT} , respectively.

The inset in Figure 45b shows the calibration curves for very small heat power (0 – 300 nW), from which we determine a limit of detection (LOD) of the platform $LOD_{INT} \approx 70$ nW for the integrated heater, and $LOD_{EXT} \approx 170$ nW for the external heater. In particular, the LOD was calculated as $3\sigma_P$ for an applied heat power to the resistive heater equal to 0, where $\sigma_P = \sigma_V / PS$ is the standard deviation of the calculated heat power signal, and σ_V is the standard deviation of the thermopile voltage V_{TP} . The first value (LOD_{INT}) can be considered as the ultimate intrinsic limit of detection of the platform, whereas the second value (LOD_{EXT}) corresponds better to a real experimental situation.

Similarly, electrical calibration was carried out also at 37 °C, and results are summarized in Figure 45c-d. In particular, Figure 45c shows a calibration sequence similar to the one performed at 25 °C (reported in Figure 45a), and Figure 45d compares the results obtained with the integrated heater R_{INT} and external heater R_{EXT} , respectively. As already observed when working at 25 °C, the power sensitivity decreases significantly when applying a heat power through the external heater. In this case, the power sensitivity drops from $PS_{R_{INT}} = 3.4 \pm 0.001$ V/W to $PS_{R_{EXT}} = 2.0 \pm 0.001$ V/W, respectively. The estimated limit of detection at 37 °C is $LOD_{INT} \approx 100$ nW for the integrated heater, and $LOD_{EXT} \approx 500$ nW for the external heater.

Additionally, we observe that $PS_{R_{INT}}$ is higher at the setpoint temperature of 37 °C than at 25 °C (3.4 V/W vs 2.7 V/W), whereas $PS_{R_{EXT}}$ is comparable (2.0 V/W vs 1.9 V/W). The first observation may be explained by the fact that the thermal resistance R_{th} of the silicon chip membrane increases in the temperature range from 25°C to 37°C, thus resulting in a higher PS (according to Equation 5:15 in Chapter 5). In fact, using the integrated resistive heater, the heat generated flows mainly to the heat sink by conduction through the membrane. On the other hand, by adding a sample reservoir and an external heater, heat losses through alternative paths may become more important. As expected, we then observe a lower power sensitivity that is less affected by the membrane conductivity temperature dependence.

Figure 46 shows a close-up view of the thermopile voltage signals for very low heat power values applied by means of the integrated resistive heater R_{INT} (without reservoir). In particular, considering a setpoint temperature of 25 °C, Figure 46a shows three V_{TP} response curves for $P_{R_{INT}}$ signals in the range of a few hundreds of nW (110 nW, 250 nW and 440 nW, respectively). These measurements confirm, indeed, that a heat power signal of 110 nW can be safely detected, which is close to the reported LOD for this experimental configuration ($LOD_{INT} \approx 70$ nW). Likewise, also the V_{TP} response curves at 37 °C, shown in Figure 46b (110 nW, 450 nW and 1 μ W, respectively), demonstrate that a heat power signal $P_{R_{INT}}$ of 110 nW could be clearly detected, which is consistent with $LOD_{INT} \approx 100$ nW previously determined for this configuration.

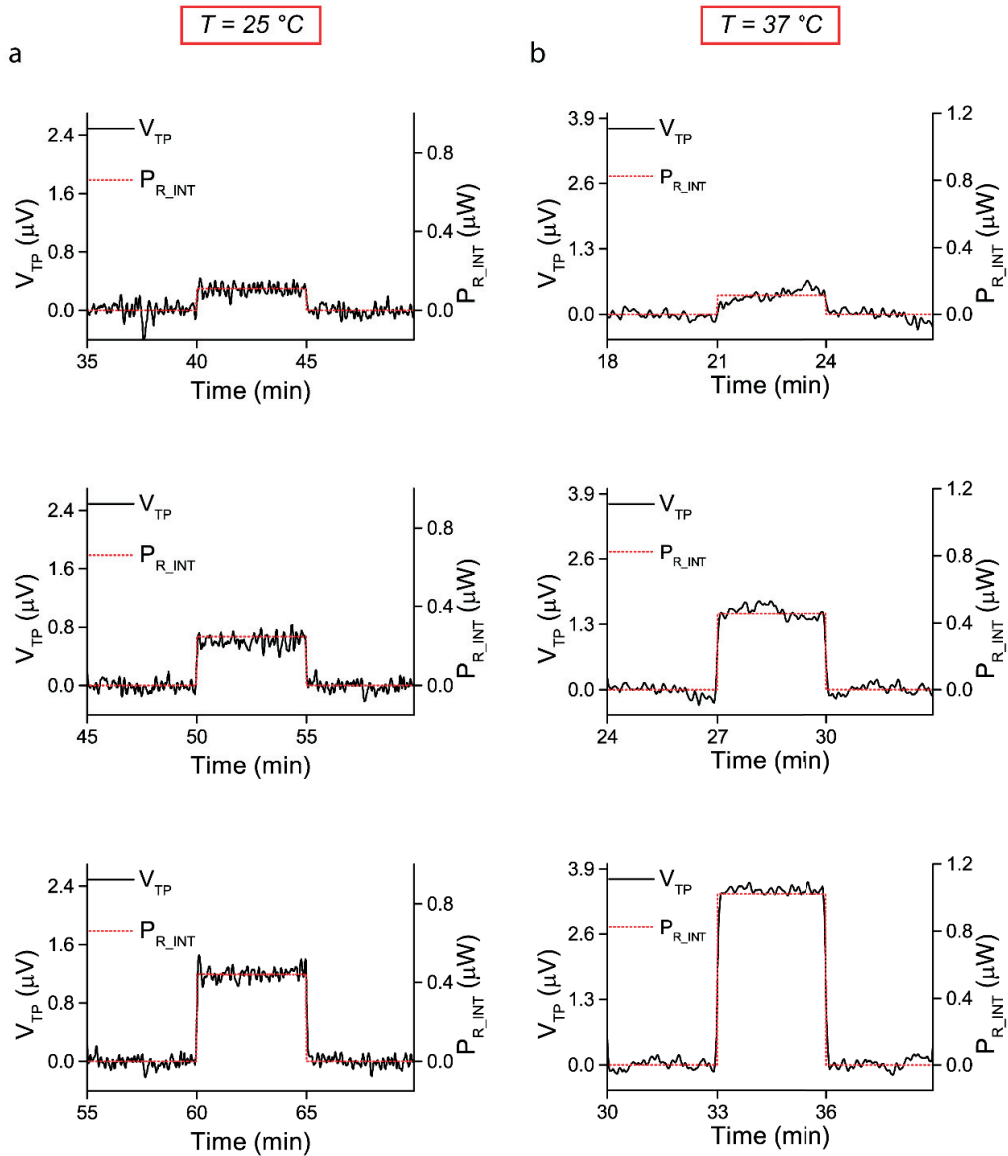


Figure 46 Thermopile voltage signal V_{TP} over time measured when very low heat power signals P_{R_INT} are applied to the integrated resistive heater R_{INT} . a) V_{TP} response curves for increasing heat power P_{R_INT} pulses (110 nW, 250 nW and 440 nW, respectively) when the platform is stabilized at 25 $^{\circ}\text{C}$. b) Measurements carried out at 37 $^{\circ}\text{C}$ for increasing heat power P_{R_INT} pulses (110 nW, 450 nW and 1 μW , respectively).

6.3 Sensing time constant

We estimated the sensing time constant of the nanocalorimeter by using the external resistive heater. As previously defined in Chapter 5 (section 5.1.3), the sensing time constant corresponds to the response of the sensor with respect to heat generated by the sample. For this purpose, similarly to the tests carried out for the electrical calibration, the external resistive heater was immersed in the sample reservoir filled with 50 μl of deionized water. After switching on the heat power through R_{EXT} at time $t = 0$ s, the thermopile voltage V_{TP} increases and approaches a steady state value. In order to quantify the time response of the nanocalorimeter, we may fit the experimental data with the following equation:

$$V_{TP} = V_0 + (V_F - V_0) \cdot (1 - e^{-t/\tau})$$

Equation 6:1 – Transient behaviour of the thermopile voltage after applying a heat power to the external heater

where V_0 (V) is the initial value of the thermopile voltage V_{TP} (V) at $t = 0$, V_F (V) is the steady state value for $t \gg \tau$ and τ (s) is the sensing time constant.

Figure 47 shows the thermopile voltage V_{TP} acquired when a heat power $P_{R_{EXT}} \approx 30 \mu\text{W}$ is generated by the external resistive heater, once the nanocalorimetric platform is stabilized at 25 °C. Fitting of the experimental curve by means of Equation 6:1 allows to estimate a sensing time constant τ of 6.0 ± 0.5 seconds (adjusted coefficient of determination $R^2 = 0.96$). This value is comparable with the previously calculated value of about 8 seconds, based on the computational simulations of the same configuration (see Chapter 5, section 5.5.4).

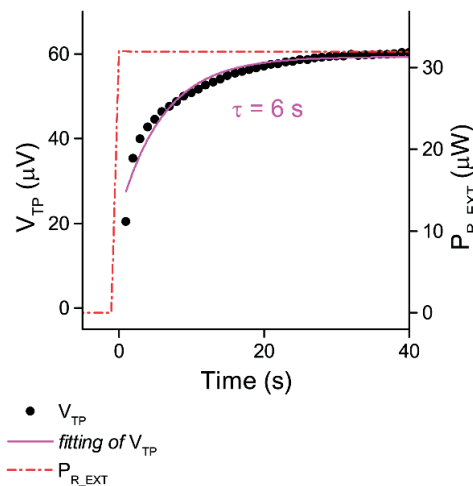


Figure 47 Experimental evaluation of the sensing time constant of the nanocalorimeter at 25 °C. A heat power pulse $P_{R_{EXT}}$ of about 30 μW (dashed red line) was applied at time $t = 0$ s to the external resistive heater R_{EXT} . The thermopile voltage V_{TP} is acquired with a sampling time of 1 second (black dots), and a fitting according to Equation 6:1 resulted in a sensing time constant τ of 6 seconds.

6.4 Quantification of the enthalpy of mixing of 1-propanol in water

As already pointed out by Wadsö *et al.* [172], calibration based on electrically generated heat may cause systematic errors as the induced thermal gradients may not fully reflect the experimental conditions of heat-generating (bio-)chemical reactions. For this reason, a test reaction having well-known thermochemical properties is required to further validate the calibration and the sensing system. Mixing of 1-propanol in deionized water (DIW) at 25 °C was chosen for this purpose.

6.4.1 Mixing of 1-propanol in water

Mixing of 1-propanol in water involves rearranging of intermolecular bonds, in particular hydrogen bonds between water or alcohol molecules, that may break and form in new configurations [173], [174]. As a result, energy is either absorbed or released depending on the interactions taking place. In fact, as reported in Figure 48a, a binary alcohol/water mixture may behave differently for increasing concentrations of the alcohol: for low alcohol mole fractions X (below 0.02 for 1-propanol in water), water-water interactions result in the formation of hydration shells around few alcohol molecules; for intermediate mole fractions (between 0.1 and 0.5 for 1-propanol), extensive hydrogen-bonded networks form between water and alcohol molecules; and for higher mole fractions alcohol clusters of increasing size may form and merge [174].

The excess molar enthalpy H^E of mixing of 1-propanol in water (also called molar heat of mixing H^E) corresponds to the heat absorbed or released per mole of mixed solution when both components are brought together. The thermodynamic properties of this binary mixture have been extensively studied in literature [172], [173], [175], [176]. For the study in this work, experimental data reported by Davis *et al.* were taken as a reference and are presented in Figure 48b [175]. As can be observed

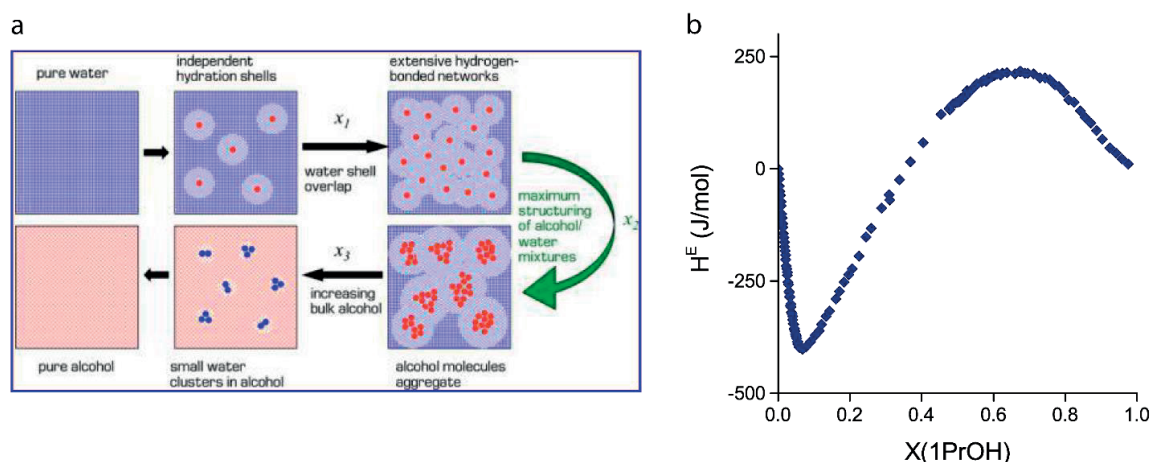


Figure 48 Mixing of 1-propanol in water. a) Schematic showing the mesoscopic molecular interactions taking place when considering a binary alcohol/water mixture at different concentrations (*image reproduced from* [174]). For increasing mole fraction $X(1PrOH)$ of the alcohol in water, different behaviours are observed: for $X < X_1$ water-water molecules interact forming hydration shells; for $X_1 < X < X_2$ hydration structures are less stable and water tends to aggregate around the $-OH$ of the alcohol, forming hydrogen-bonded networks; for $X_2 < X < X_3$ larger alcohol aggregates form; for higher mole fractions isolated water clusters remain. b) Excess molar enthalpy H^E of 1-propanol in water as a function of the mole fraction of 1-propanol $X(1PrOH)$ at 25 °C, as reported by Davis *et al.* in tabulated format [175].

from this figure, mixing of 1-propanol in water is exothermic for mole fractions of 1-propanol $X(1PrOH)$ below 0.4 ($H^E < 0$), while it is endothermic for higher mole fractions ($H^E > 0$). $X(1PrOH)$ is defined as the number of moles of 1-propanol divided by the total number of moles of the mixed solution.

6.4.2 Experimental configuration: single vs sequential injection

The heat of mixing of 1-propanol (1-propanol anhydrous, 99.7%, *Sigma-Aldrich*) in DIW was investigated with the nanocalorimetric platform. The experimental procedure consisted in prefilling the sample reservoir with 45 μl of 1-propanol in water solutions at different initial concentrations. The inlet tubing connected to the reservoir was filled with 5 μl of pure 1-propanol. After a thermalization duration of 20 min to reach the setpoint temperature of 25 $^{\circ}\text{C}$, 5 μl of pure 1-propanol were injected into the reservoir, resulting in a total volume of 50 μl . As the inlet tube passes through the metal block of the platform, the injected volume is well thermalized at 25 $^{\circ}\text{C}$. A single experiment may last less than 30 minutes, which is acceptable when planning several subsequent experiments, and especially in view of biological sample testing ultimately.

An alternative experimental protocol relying on sequential injections was also tested. As before, the reservoir was prefilled with 45 μl of 1-propanol in water solutions at different initial concentrations. However, in this case, the inlet tubing connecting the reservoir was filled with up to 15 μl of pure 1-propanol. After allowing a thermalization time of 20 min to reach the setpoint temperature of 25 $^{\circ}\text{C}$, three sequential injections of 5 μl of pure 1-propanol were implemented. A waiting time of at least 10 minutes was applied between subsequent injections, allowing the thermopile voltage signal to return to the initial baseline and thermalization of the 5 μl sample aliquot at 25 $^{\circ}\text{C}$ before injection. In principle, this multiple injection approach is faster when testing the effect of increasing concentrations of reactants, however, it may be less accurate when aiming at quantifying the enthalpy of mixing, as errors due to integration over sequential peaks will add up. For this reason, the single injection protocol was preferred in the studies described in sections 6.4.4 and 6.5.3.

6.4.3 Evaluation of injection artefacts

Control experiments have been carried out in order to assess possible signal artefacts observed when injecting a 5 μl sample aliquot. In particular, three tests have been carried out. First, 5 μl of DIW were sequentially injected three times into the sample reservoir, prefilled with 45 μl of DIW. A second independent experiment consisted in a sequence of three injections of 5 μl of pure 1-propanol into the reservoir, prefilled with 45 μl of pure 1-propanol. Finally, three 5 μl aliquots of pure 1-propanol were sequentially injected into the reservoir, prefilled with 45 μl of DIW. The final sample volume in all experiments was 60 μl . The thermopile voltage curves over time acquired in the three cases are reported in Figure 49a, Figure 49b and Figure 49c, respectively. We observe that injection of thermalized solutions of the same type (water in water or alcohol in alcohol, respectively) has minor effect compared to actual V_{TP} peaks observed for mixing of 1-propanol in water (see Figure 49c).

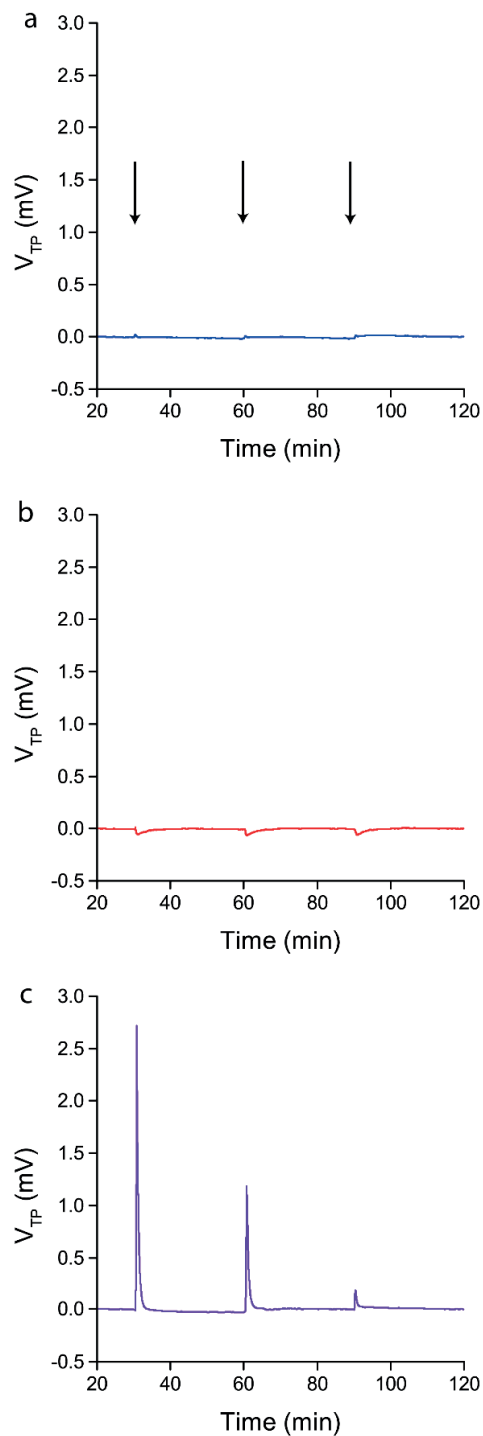


Figure 49 Thermopile voltage V_{TP} acquired when implementing three sequential injections of 5 μl aliquots (at time $t = 30, 60, 90$ min – indicated by the arrows) into the reservoir, prefilled with 45 μl of different solutions. a) Sequential injection of DIW into the reservoir prefilled with DIW. b) Sequential injection of 1-propanol into the reservoir prefilled with 1-propanol. c) Injection of 1-propanol into the reservoir prefilled with DIW. Actual mixing peaks are observable in the latter case, which are clearly more pronounced than the injection artefacts in a) and b).

6.4.4 Detection of mixing of 1-propanol in water

In order to determine the heat of mixing of 1-propanol in DIW, a series of independent experiments was implemented, based on a single 5 μL aliquot injection into the reservoir, which was filled with 45 μL of 1-propanol in water solutions with an initial concentration ranging from 0% to 89% (v/v). The results are shown in Figure 50. In this figure, the initially acquired thermopile voltage $V_{TP}(t)$ was converted into the corresponding heat power signal, expressed as the differential total enthalpy dH_{TOT}^E/dt in Figure 50. The reported dH_{TOT}^E/dt over time curves are observed when the concentration of the 1-propanol solution in the reservoir changes from its initial value to the final value after injection. In particular, for converting V_{TP} into the heat power dH_{TOT}^E/dt (with $dH_{TOT}^E/dt = V_{TP} / PS_{exp}$) a power sensitivity coefficient $PS_{exp} = 0.6 \text{ V/W}$ was applied, which was determined by the chemical calibration method that will be described in the following. In order to carry out measurements for increasing concentrations of 1-propanol in water while keeping the same sample volumes, both for prefilling the reservoir and for injecting, the initial concentration in the reservoir was gradually increased for each experiment (as indicated in Figure 50).

As may be deduced from Figure 50, each experiment consisted of three different phases: (i) temperature stabilization of the platform lasting 20 minutes, during which the initial baseline was acquired (in the figure plotted from $t = 18$ to 20 min); (ii) the injection of 5 μL of pure 1-propanol (at $t = 20$ min), inducing a mixing peak in the heat power signal; (iii) evanescent heat power and acquisition of the final baseline (in the figure from $t = 23$ to 24 min). In particular, the acquisition of both baselines, before and after the mixing peak, was required for the accurate implementation of the baseline subtraction algorithm. This procedure is particularly critical because, as will be described

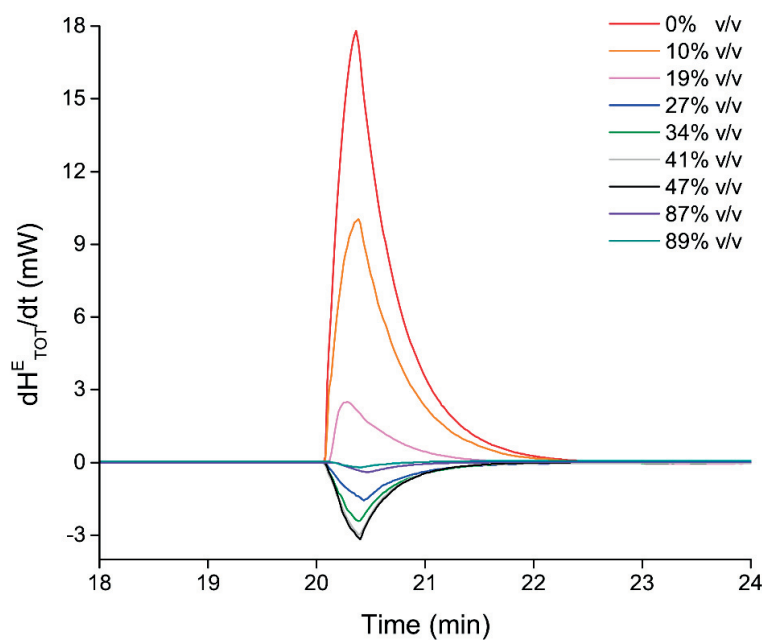


Figure 50 Differential excess enthalpy dH_{TOT}^E/dt over time generated by injecting and mixing 5 μL of pure 1-propanol into 45 μL of 1-propanol solutions at different initial concentrations (values are indicated in the figure). $dH_{TOT}^E/dt(t)$ curves were obtained by converting the measured thermopile voltages V_{TP} using a power sensitivity coefficient of 0.6 V/W.

in the next section, quantification of the enthalpy of mixing H^E is based on the integration over time of the heat power signal.

Finally, the highest initial concentration of 1-propanol in water tested was 89% v/v, corresponding to a final concentration of 90% v/v after injection of 5 μL of pure 1-propanol. Mixing peaks could still be detected at higher concentrations of alcohol, but the presence of a significant drift of the baseline signal after the mixing peak affected the accuracy of the baseline subtraction. This observation may be explained by thermal effects due to evaporation, which become more significant as the concentration of volatile alcohol increases.

6.4.5 Processing of the experimental data for chemical calibration

In order to perform the chemical calibration of the nanocalorimetric platform, some data processing was required for comparing our experimental heat power curves (Figure 50) with literature values. First of all, the excess molar enthalpy $H^E(X)$ curve reported in Figure 48b was differentiated with respect to $X(1PrOH)$ after polynomial fitting, where $X(1PrOH)$ is the mole fraction of 1-propanol in water. The resulting differential molar excess enthalpy dH^E/dX , which is plotted in Figure 51 (full black line), is used as the actual reference curve for comparison with our experimental data.

Data processing implemented on the experimental data consisted in a sequence of steps, which are graphically summarized in Figure 52:

1. the total differential excess enthalpy dH^E_{TOT}/dt is normalized by the number of moles in solution after mixing in order to obtain the corresponding molar value dH^E/dt ;
2. the molar differential excess enthalpy dH^E/dt is integrated with respect to time for each curve shown in Figure 50. The resulting values correspond to the excess molar enthalpy

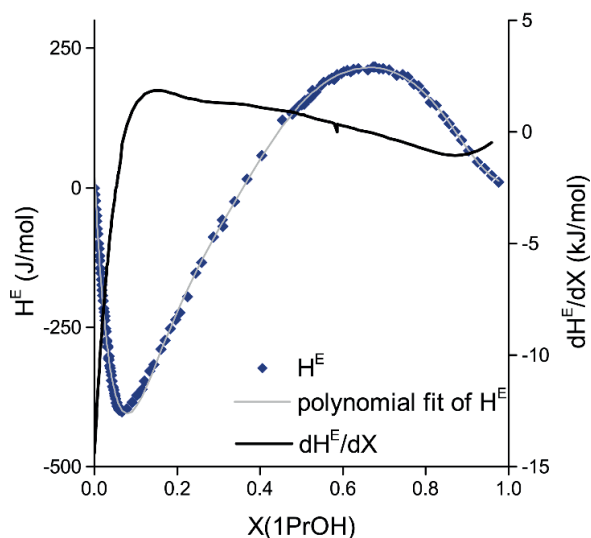


Figure 51 Literature data for the molar excess enthalpy H^E for mixing of 1-propanol in water vs the mole fraction $X(1PrOH)$ (as already reported in Figure 48 [175]). Additionally, the differential molar excess enthalpy dH^E/dX is shown (black solid line), obtained by differentiating the polynomial fit of $H^E(X)$ with respect to the mole fraction $X(PrOH)$ (light grey solid line).

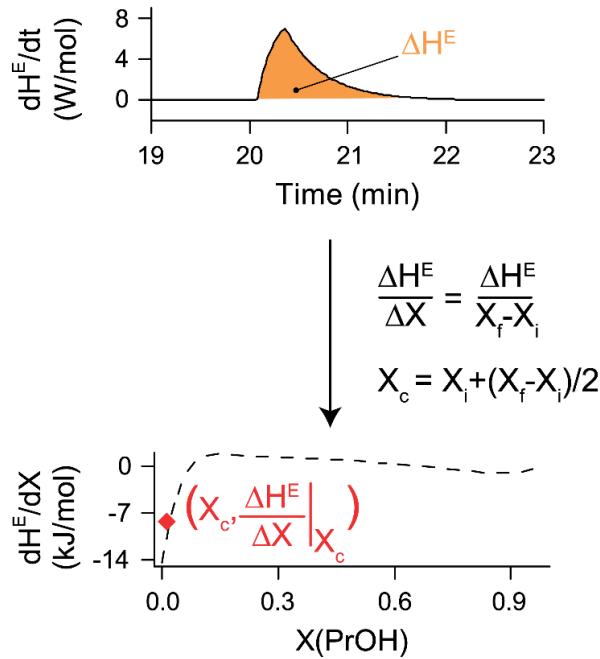


Figure 52 Protocol used for data analysis: the measured $dH^E_{TOT}/dt(t)$ curve is first normalized in order to obtain the molar differential excess enthalpy $dH^E/dt(t)$. Integrating over time results in the molar excess enthalpy change ΔH^E between the initial (X_i) and final (X_f) mole fraction. The central mole fraction X_c is then calculated and used to plot $(X_c, \Delta H^E/\Delta X)$ data points on the differential molar excess enthalpy $dH^E/dX(X)$ reference curve from literature.

change ΔH^E , which is observed when the solution concentration is increased by $\Delta X = X_f - X_i$, *i.e.* from the initial mole fraction X_i to the final mole fraction X_f after injection;

- the molar excess enthalpy change ΔH^E is then divided by the mole fraction difference ΔX to obtain $\Delta H^E/\Delta X$. The central mole fraction $X_c = X_i + (X_f - X_i)/2$ has been calculated in order to plot pairs of values $(X_c, \Delta H^E/\Delta X)$ and to compare these with the dH^E/dX vs X reference curve (Figure 51).

The comparison of experimental $(X_c, \Delta H^E/\Delta X)$ data and literature data for the differential molar excess enthalpy dH^E/dX is shown in Figure 53, where a good match of both data sets can be observed. In order to achieve this overlap, a scaling parameter, corresponding to the power sensitivity coefficient PS_{exp} , had to be determined and applied to the initially recorded thermopile voltage V_{TP} . In this particular case, a PS_{exp} value of 0.6 V/W was found for the most accurate conversion of V_{TP} into the heat power. This protocol corresponds to the chemical calibration of the nanocalorimetric platform. The thus obtained power sensitivity coefficient PS_{exp} is about 3 times lower than the coefficient previously determined with the external heater $PS_{R_EXT} = 2.0$ V/W (at 25°C). This fact underlines the importance of system calibration using liquid chemical reactions, where the heat source is uniformly distributed in the sample reservoir in contrast to localized heat generation by an immersed resistive heater.

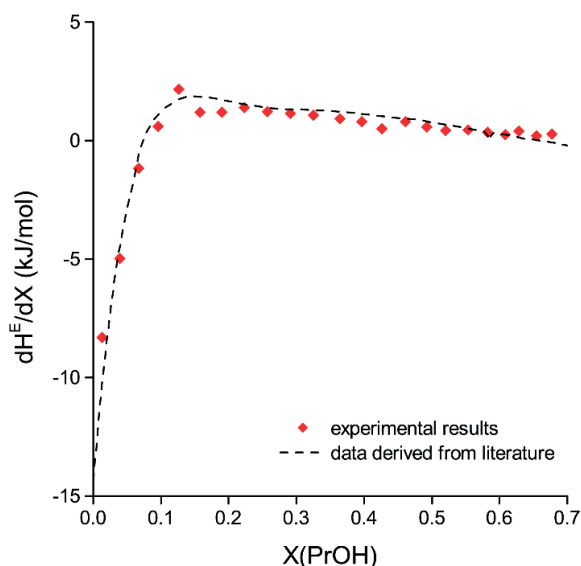


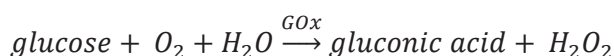
Figure 53 Comparison of the differential molar excess enthalpy dH^E/dX derived from literature [175] (dashed line) with the $(X_c, \Delta H^E/\Delta X)$ values calculated from our experimental data (red dots).

6.5 Enzymatic study of glucose oxidation by glucose oxidase

6.5.1 The reaction mechanism of glucose oxidation

The nanocalorimetric platform was also used to study the enzymatic activity of glucose oxidase (GOx) during the catalytic oxidation of glucose. Glucose oxidase is a flavoprotein, *i.e.* a protein containing flavin adenine dinucleotide (FAD), which is an indispensable redox cofactor enabling the catalytic activity of GOx. In particular, as schematically shown in Figure 54, the redox reaction involved may be divided into two half reactions. First, during the reductive half reaction, β -D-glucose is oxidized to D-glucono- δ -lactone that in turn is non-enzymatically hydrolysed to gluconic acid. At the same time, the FAD cofactor of GOx is reduced to FADH₂. Second, during the oxidative half reaction, FADH₂ is reoxidized to FAD and molecular oxygen is reduced to hydrogen peroxide [177].

The overall reaction may be described as follows [178], [179]:



Equation 6:2 – Oxidation of glucose catalyzed by glucose oxidase

This equation expresses the consumption of glucose, molecular oxygen and water, to obtain gluconic acid and hydrogen peroxide. From the thermodynamic point of view, the overall reaction is exothermic.

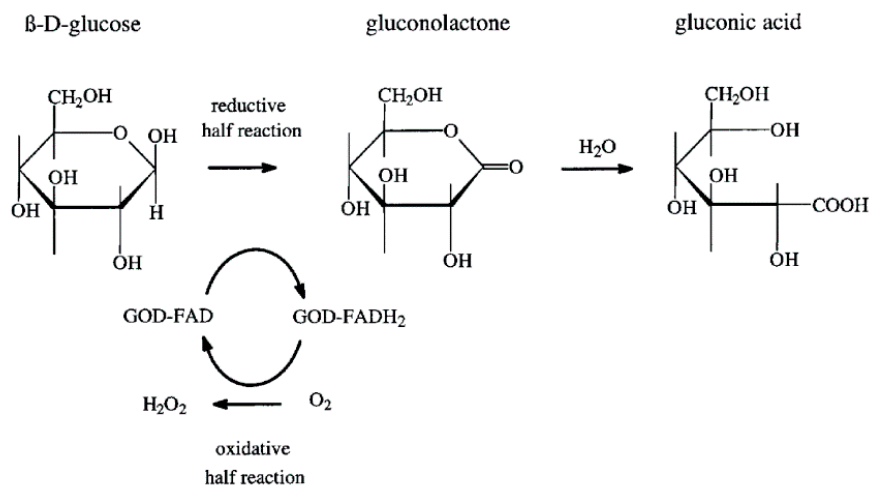


Figure 54 Schematic showing the reaction mechanism of glucose oxidation catalyzed by glucose oxidase (abbreviated as GOD in this figure) (image reproduced from [180]).

6.5.2 Experimental protocol

Solutions were prepared by dissolving glucose (D-Glucose $\geq 99.5\%$, *Sigma-Aldrich*) or GOx (Glucose Oxidase from *Aspergillus niger* 100,000-250,000 Units/g, *Sigma-Aldrich*) in phosphate buffered saline (PBS, pH 7.4, Gibco, *Life Technologies*). Experiments were performed in the presence of dissolved oxygen (DO) under atmospheric conditions, which corresponds to an initial DO concentration of 0.25 mM [181]. The liquid injection procedure for this series of experiments is very similar to the previously applied protocol, except for the liquid volumes used. The reservoir was filled with 25 μl of GOx solution (0 U/ml, 125 U/ml or 250 U/ml in PBS), the tubing was filled with 1.5 μl of concentrated glucose solution in PBS (up to about 700 mmol/l), the platform temperature was set to 25 $^{\circ}\text{C}$ and 30 minutes of thermalization were allowed before injecting the glucose solution. The concentration of the glucose aliquot injected was adjusted so that the initial glucose concentration $[S_0]$ in the reservoir at the beginning of the reaction ranged from 0 to 40 mmol/l. Recalibration of the platform using 1-propanol in water as test reaction with the reduced sample volume (25 μl instead of 50 μl) resulted in an improved power sensitivity PS_{exp} of 1.0 V/W (instead of 0.6 V/W for 50 μl as determined before). A possible explanation for this effect may be that smaller sample volumes represent a heat source that is confined in a space closer to the thermopile sensor, thus heat detection may be more efficient. This power sensitivity coefficient was applied to all glucose oxidation experiments.

6.5.3 Detection of oxidation of glucose catalyzed by GOx

The heat power P (W) released by glucose oxidation corresponds to the heat energy released per unit time, and it is directly proportional to the number of moles of glucose consumed per unit time, *i.e.* the reaction rate V ($\text{mol}\cdot\text{l}^{-1}\cdot\text{s}^{-1}$):

$$P = h \cdot V$$

Equation 6:3 – Proportionality relationship between measured heat power and reaction rate

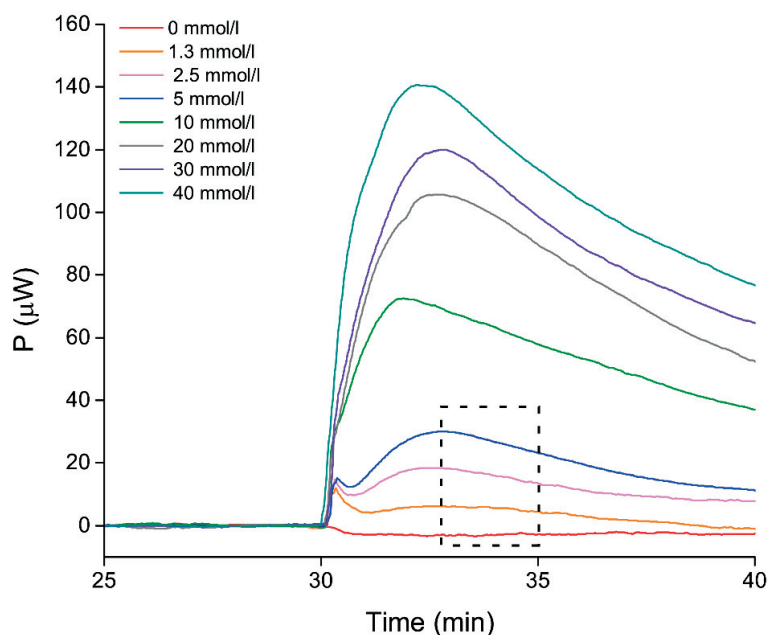


Figure 55 Measurement of glucose oxidation, catalyzed by glucose oxidase at 25 °C. Heat power $P(t)$ curves are obtained from the measured thermopile voltage V_{TP} with a power sensitivity coefficient $PS_{exp} = 1.0$ V/W. The reservoir was initially filled with 25 μ l of glucose oxidase solution (250 U/ml in PBS), and 1.5 μ l of glucose solution (in PBS with varying concentrations) is injected at $t = 30$ min to achieve an initial glucose concentration $[S_0]$ in the reservoir ranging from 0 to 40 mmol/l.

where h ($\text{J}\cdot\text{l}\cdot\text{mol}^{-1}$) is the thermal energy released per mole of glucose consumed per volume unit. As the catalytic activity starts, the heat power measured has the maximum value P_0 , which corresponds to an initial reaction rate V_0 , and then slowly decreases.

Results from a series of measurements are presented in Figure 55, showing the heat power P released over time when glucose with increasing concentration is injected in the glucose oxidase solution ($[GOx] = 250$ U/ml). Shortly after injection (at $t = 30$ min), a rapid increase of the heat power P during diffusive mixing in the reservoir is observed (duration ≈ 1 -2 min), and a maximum (or initial) heat power P_0 is reached which marks the start of the enzymatic reaction. The value of P_0 increases as a function of the initial glucose concentration $[S_0]$ in the reservoir at the beginning of the oxidation reaction (0 to 40 mmol/l).

We also observe that, differently from the previous study when the mixing of 1-propanol in water was investigated, the heat power signal does not return to the initial baseline before injection in the considered time lapse (up to 40 min). This is expected as after the peak maximum P_0 , the reaction is going on, *i.e.* glucose continues to be consumed and heat is produced. By integrating the heat power with respect to time for each glucose concentration (Figure 55), we obtain the released energy $E(t)$ as a function of time. The corresponding graphs are shown in Figure 56.

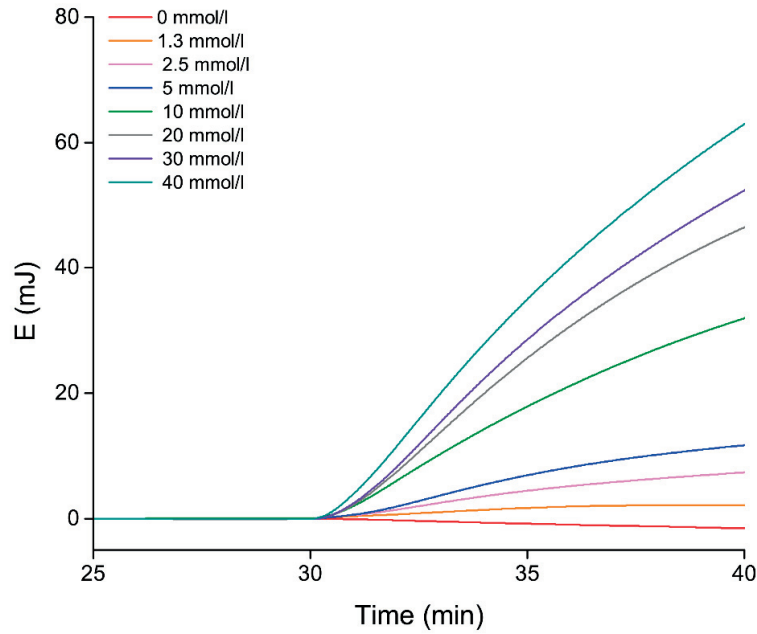


Figure 56 Thermal energy $E(t)$ released during the reaction, obtained by integrating $P(t)$ with respect to time, for different glucose solutions and at a fixed glucose oxidase concentration of 250 U/ml.

6.5.4 Data analysis based on the Michaelis-Menten model

For most enzymatic assays, and typically for GOx-mediated glucose oxidation, the curve obtained by plotting the initial reaction rate V_0 ($\text{mol}\cdot\text{l}^{-1}\cdot\text{s}^{-1}$) as a function of the glucose substrate concentration $[S_0]$ ($\text{mol}\cdot\text{l}^{-1}$) is described by the Michaelis-Menten model, which is based on the following equation [17], [182], [183]:

$$V_0 = V_{max} \cdot \frac{[S_0]}{[S_0] + K_M}$$

Equation 6:4 – Michaelis-Menten equation

where V_{max} ($\text{mol}\cdot\text{l}^{-1}\cdot\text{s}^{-1}$) is the maximum rate attained when all catalytic sites of the enzyme are saturated and K_M ($\text{mol}\cdot\text{l}^{-1}$) is the Michaelis constant. As the heat power P generated is directly proportional to the reaction rate V , the Michaelis-Menten equation can be rewritten as:

$$P_0 = P_{max} \cdot \frac{[S_0]}{[S_0] + K_M}$$

Equation 6:5 – Michaelis-Menten equation rewritten for the heat power

where P_{max} (W) is the asymptotic limit of the P_0 (W) values expected in the saturation range at high glucose concentrations (for $[S_0] \gg K_M$).

By identifying the initial heat power P_0 (*i.e.* the peak values in Figure 55) for each initial glucose concentration $[S_0]$ in the reservoir, the corresponding power vs concentration plot is obtained as presented in Figure 57a. Additional experiments for a GOx concentration of 125 U/ml and for a control experiment (0 U/ml) are also reported. Fitting with the modified Michaelis-Menten equation $P_0([S_0])$ (Equation 6:5), shown as dashed curves in Figure 57a (adjusted $R^2 > 0.97$), allowed to obtain the two distinctive parameters P_{MAX} and K_M . The estimated upper limits P_{MAX} of the heat power are $210 \pm 78 \mu\text{W}$ and $230 \pm 23 \mu\text{W}$ for GOx concentrations of 125 U/ml and 250 U/ml, respectively. More interestingly, the corresponding Michaelis constants K_M are $50 \pm 30 \text{ mmol/l}$ and $25 \pm 5 \text{ mmol/l}$, which correspond to the same range of reported values in literature [177], [184], [185].

Considering the curve for a GOx concentration of 250 U/ml, we can also observe the linear region of the Michaelis-Menten plot for low glucose concentrations (*i.e.* for $[S_0] \ll 25 \text{ mmol/l}$), which is typical of a first order enzyme-substrate reaction, before enzyme saturation becomes important. Figure 57b shows a magnification in the 0-5 mmol/l range of the glucose concentration. In this range, the heat power P_0 and thus the reaction rate V_0 is directly proportional to the initial substrate concentration $[S_0]$. A linear fitting (dashed line; adjusted R^2 equal to 0.96) allows an estimation of the slope α of the fitted line according to the following equation:

$$P_0 = \alpha \cdot [S_0]$$

Equation 6:6 –Linear range of the initial heat power vs initial glucose concentration, for low substrate concentrations

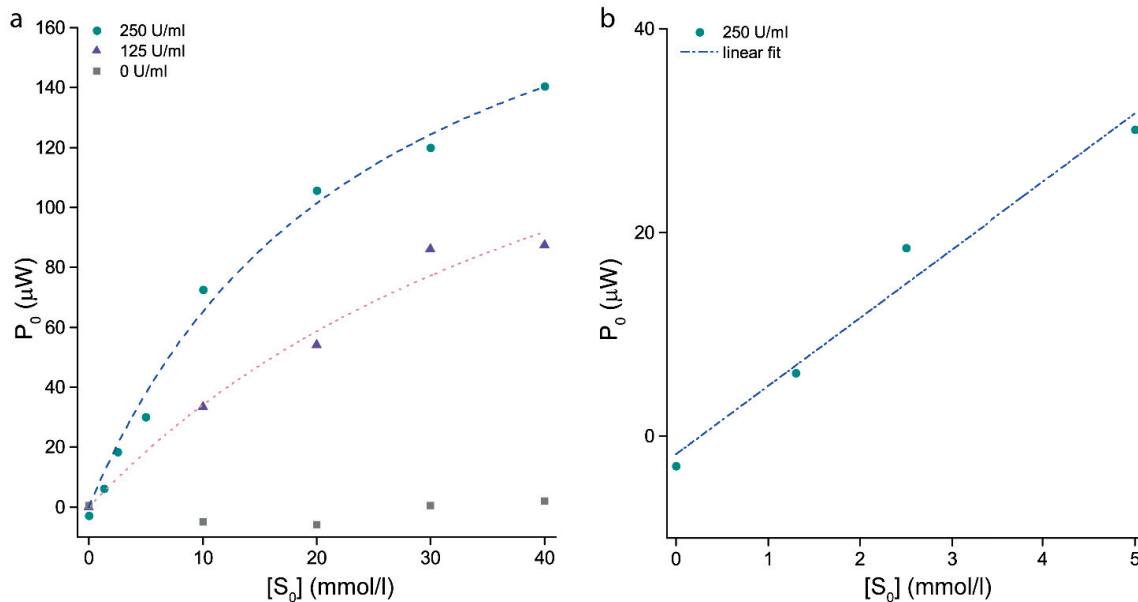


Figure 57 Fitting of the experimental data by the Michaelis-Menten equation. a) Peak values P_0 of the measured heat power as a function of the initial glucose concentration $[S_0]$ in the reservoir, for different glucose oxidase concentrations: 250 U/ml, 125 U/ml and 0 U/ml (control experiment). The experimental data obtained for $[\text{GOx}] = 250 \text{ U/ml}$ and $[\text{GOx}] = 125 \text{ U/ml}$ were fitted using the Michaelis-Menten equation (dashed lines, adjusted $R^2 \approx 0.99$ and 0.97 , respectively). b) P_0 vs $[S_0]$ curve for glucose concentrations below 10 mmol/l (for $[\text{GOx}] = 250 \text{ U/ml}$, from figure a). This emphasizes the linear region of the Michaelis-Menten curve for glucose concentrations smaller than the Michaelis constant K_M . The proportionality coefficient $\alpha \approx 6.68 \mu\text{W} \cdot \text{l} \cdot \text{mmol}^{-1}$ was determined by linear fitting (dashed line, adjusted $R^2 \approx 0.96$).

The estimated value of α from the experimental data is $6.68 \pm 0.79 \mu\text{W}\cdot\text{l}\cdot\text{mmol}^{-1}$. Furthermore, for this type of reactions, the substrate concentration $[S]$ ($\text{mol}\cdot\text{l}^{-1}$) decays exponentially over time as:

$$[S] = [S_0]e^{-k\cdot t}$$

Equation 6:7 – Exponential decay of the substrate concentration over time

where k is the rate constant (s^{-1}). Thus, from Equation 6:3 and Equation 6:7 we deduce that the reaction rate V ($\text{mol}\cdot\text{l}^{-1}\cdot\text{s}^{-1}$) and, consequently, the heat power released P (W) decays exponentially too, as:

$$P = h \cdot V = h \cdot \frac{d[S]}{dt} = -h \cdot k \cdot [S] = -h \cdot k[S_0]e^{-k\cdot t}$$

Equation 6:8 – Exponential decay of the heat power signal over time

Interestingly, the rate constant k (s^{-1}) can be estimated by fitting the experimental data shown in Figure 55. In particular, a short duration after the power peak was chosen (corresponding to the dashed rectangle in Figure 55) to guarantee that the system was still in the conditions close to its initial status and that the first order reaction obtained from the simplification of Michaelis-Menten is still a good approximation. From the exponential fitting in a time window of 2 minutes after the maximal peak and for small glucose concentrations from 1.3 to $5 \text{ mmol}\cdot\text{l}^{-1}$, the estimated average rate constant k is 0.0022 s^{-1} (adjusted $R^2 > 0.80$). Finally, by applying Equation 6:8 to the time instant $t_0 = 0$ of the peak value P_0 (considered as the onset of the reaction, once the system has overcome its mass transport limitation) and knowing the proportionality coefficient α from Equation 6:6, the following relation can be deduced:

$$P_0 = -h \cdot k[S_0] = \alpha[S_0]$$

Equation 6:9 –Proportionality relation between initial heat power P_0 and initial substrate concentration S_0

where h ($\text{J}\cdot\text{l}\cdot\text{mol}^{-1}$) was defined earlier as the heat energy released per mole of glucose consumed per volume unit. As the rate constant k and the proportionality coefficient α have been estimated, h may be calculated which, after dividing by the sample volume of $26.5 \mu\text{l}$, gives the amount of energy released during the reaction per unit of mole, *i.e.* the molar reaction enthalpy. The molar reaction enthalpy estimated with this procedure is $-115 \pm 15 \text{ kJ}\cdot\text{mol}^{-1}$ (for the 250 U/ml GOx solution), which is in good agreement with values available from literature [184].

A posteriori analysis of possible limiting effects of dissolved oxygen depletion, which were documented in literature [184], [186], has also been carried out. Such limitation was not observed experimentally in our case and the results were, indeed, in agreement with literature on the Michaelis-Menten model [183], [184]. Oxygen diffusion from the top surface of the liquid to the bottom of the

reservoir may take up to 4 minutes, if we consider an inner size of the reservoir of $5 \times 5 \text{ mm}^2$, a sample volume of $25 \text{ }\mu\text{l}$, and thus a mean diffusive path of up to 1 mm (a diffusion coefficient D of oxygen in water of $2 \cdot 10^{-5} \text{ cm}^2 \cdot \text{s}^{-1}$ was taken [187] and the mean diffusive time calculated as $t = x^2/2D$). Therefore, re-supply of oxygen over the duration of the experiment is continuously enabled. Moreover, the highest consumption of glucose per minute, which is observed at the maximum reaction rate, may be estimated by dividing the heat power measured (Figure 55) by the molar reaction enthalpy known from literature [184]. Considering a glucose concentration of 5 mmol/l , which is the highest in the linear range of Figure 57b, the thus estimated highest consumption of glucose would be $14 \cdot 10^{-9} \text{ mol/min}$. Consequently, $14 \cdot 10^{-9} \text{ mol} \cdot \text{min}^{-1}$ of oxygen are also consumed, which is of the same order of magnitude as the initial DO moles available in solution ($7 \cdot 10^{-9} \text{ mol}$, assuming 0.25 mM as the initial DO concentration). We can conclude that the continuous replenishment of oxygen from air and the relatively fast diffusion of oxygen may explain the ability to test high glucose concentrations without oxygen-limiting effects. This is particularly true in the linear range of the Michaelis-Menten model, as no linearity between heat power signal and glucose concentration would have been observed if oxygen was limiting the reaction. In contrast, we cannot exclude that oxygen depletion may be partially taking place in the saturation regime of the Michaelis-Menten model (glucose concentration higher than $5 \text{ mmol} \cdot \text{l}^{-1}$), even though the system follows the expected theoretical behaviour for such reaction. Finally, the combination of glucose oxidase with the oxygen-regenerating enzyme catalase may be foreseen in future to create less limiting experimental conditions from the oxygen depletion point-of-view.

This validation of the nanocalorimetric platform demonstrates its applicability to the thermodynamic study of chemical reactions, by measuring the enthalpy change of reaction, but also to the kinetic study of biochemical and, in particular, enzymatic assays. The versatility of the platform makes it an excellent tool for studying unknown biochemical reactions and, more interestingly, the effects of chemical compounds on specific enzymatic reactions. This is particularly relevant in the field of pharmacology, as enzymes are considered one of the major drug targets [188]. Another interesting application is in field of toxicological studies, where enzyme inhibition by pollutants or toxins may be investigated and even be used as sensing mechanism for the determination of sample contamination [189].

6.6 Preliminary metabolic experiments on *C. elegans* nematodes

6.6.1 Preparation of the *C. elegans* nematode suspension

The final goal of the development of the nanocalorimetric platform is the investigation of metabolic heat production by a population of cells or by multicellular organisms. In this context, a nanocalorimetric experiment has been carried out on *C. elegans* nematodes.

The *C. elegans* nematode is a roundworm used as a model organism in life science research, especially in the field of developmental biology. In fact, it has a rapid life cycle of three days (from birth to adulthood), it is transparent and small in size (an adult is about 1.0 mm long), and it is easy to culture in laboratory [190]. Additionally, it is relatively easy to manipulate genetically and its whole

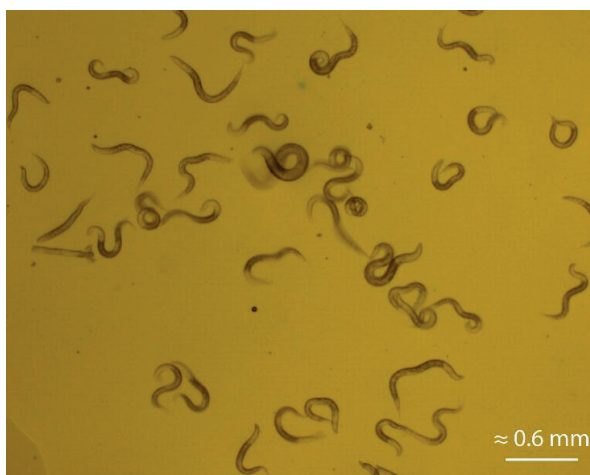


Figure 58 Suspension of *C. elegans* nematodes in S Medium, consisting mainly of worms at the larval stage (L3-L4).

genome has been sequenced [191]. Finally, *C. elegans* nematodes may be used as a model to study human diseases, thanks to the high number of human disease-related genes sharing homology with *C. elegans* genes [192].

For our experiments, wild-type *N2* worms were cultured in the laboratory according to standard procedures, *i.e.* by transferring them regularly on fresh agar plates prepared with Nematode Growth Medium (NGM). Furthermore, the NGM agar was seeded on the surface with *Escherichia coli* bacteria (*E. coli*, OP50) as food source for the worms [193]. *C. elegans* nematodes were kept in an incubator at 20 °C during their whole life. Right before running an experiment, worms were collected from the NGM agar plates and suspended in S Medium, which is a buffer solution often used for worm suspensions. Figure 58 shows a picture of a worm suspension.

6.6.2 Experimental configuration

The goal of our experiment was to assess a possible effect of glucose uptake by the worms on the metabolic heat production. The sample reservoir on the nanocalorimetric chip was prefilled with 25 μl of worm suspension in S Medium, whereas the inlet tubing connected to the reservoir was filled with 2 μl of 75 mM of glucose solution in S Medium. A target temperature of 25 °C was set and 25 min of thermalization time was allowed to reach temperature stability. Then 2 μl of glucose solution were injected, resulting in a total volume of 27 μl in the reservoir with a final glucose concentration of 5.5 mM. The injected volume was well thermalized prior to the injection, as the inlet tube was in good thermal contact with the metal block of the platform.

Additionally, two control experiments were carried out under the same experimental conditions. The worm suspension was replaced by pure S Medium solution in one case, and by S Medium contaminated with *E. coli* in the other case. The reason driving the choice of this second control experiment comes from the observation that by collecting the worms from the NGM agar plate also a certain amount of *E. coli* is collected. Thus, in order to be able to evaluate specifically the effect of glucose injection on the worms, a separate experiment assessing the effect of glucose injection on

E. coli is required. For this purpose, NGM agar plates seeded with *E. coli* but not with worms were used for preparing the S Medium solution contaminated by *E. coli*.

6.6.3 Preliminary heat power measurements on worms

Figure 59 shows preliminary results of the heat power measurements carried out on a suspension of worms in S Medium.

The thermopile voltage was converted to the corresponding heat power through the power sensitivity coefficient PS_{exp} . Here we used the value that was previously determined for a sample volume of 25 μL ($PS_{exp} = 1.0 \text{ V/W}$, *i.e.* the same value that was used for the glucose oxidation studies). The baseline for the worm experiment and the two control experiments was set to zero for the time window prior to injection of glucose. Immediately after the injection, a short peak is observed in all cases (duration less than 1 minute), corresponding to a temporary injection artefact. This is not particularly critical for the metabolic heat power measurements, as we are interested in a longer time window. Furthermore, it is possible to observe that the heat power signals after injection (for $t > 26 \text{ min}$) are clearly above the initial baseline. This difference may, therefore, be attributed to an effect of glucose in the suspension. The heat signal increase is most significant for the worm suspension, which is consistent with the assumption that worms, which are consuming glucose, may produce more metabolic heat. Glucose injection also has a distinct but less pronounced effect on the *E. coli* suspension. On the other hand, the signal also increases for glucose injection in pure S Medium, which is possibly due to heat produced by mixing and dissolution. This effect should be also present in the worm and *E. coli* experiments. In order to give a preliminary estimate of the glucose injection effect on worms, we may consider the difference in the heat power signal of the

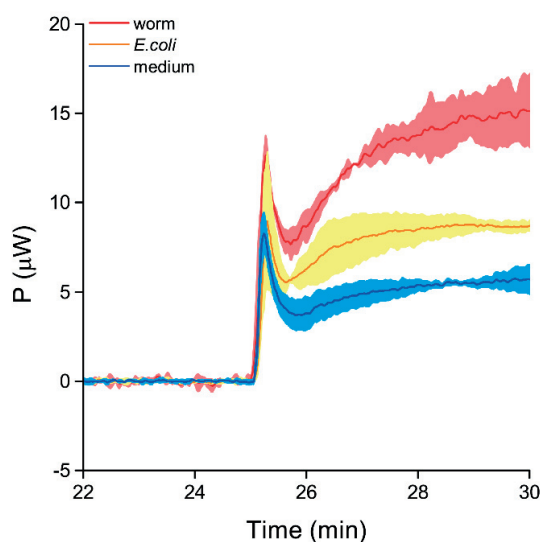


Figure 59 Preliminary results of heat power measurements carried out on *C. elegans* nematodes. After thermalization of the platform, 2 μL of 75 mM of glucose solution in S Medium were injected in the sample reservoir (at $t = 25 \text{ min}$). The reservoir was initially prefilled with 25 μL of three different samples: (i) worm suspension (red curve), (ii) *E. coli* suspension (orange curve), and (iii) S Medium solution (blue curve). The solid lines are the average of 2 worm experiments, and the average of 3 for the control experiments, respectively. The highlighted area corresponds to \pm the standard deviation.

worm suspension and of the *E. coli* suspension. In average, the heat power difference between the two conditions is about 6 μW after 5 minutes from the glucose injection. We estimate that the sample volume of 25 μl in the reservoir contains a few hundreds of worms (corresponding to about 10 worms/ μl), thus we may conclude that the heat power measured is about few tens of nW/worm, which is in the same order of magnitude as data on worm metabolic heat production, reported in literature [156].

The aim of this proof-of-concept experiment was to demonstrate the applicability of the newly developed nanocalorimetry platform to the study of metabolically produced heat by living organisms. Indeed, extensive optimization of this type of protocol should be carried out before being able to provide any biological interpretation of the results. The experiment carried out here was based on a mixed population of worms at different development stages. Future experiments should be planned after optimizing the preparation of the worm suspension, targeting both a consistent number of worms for each experiment, as well as age-synchronized populations. In fact, it has been reported that metabolic parameters change for the different developmental stages of the worms [194]. Age synchronization is possible by standard techniques when growing the worms on agar plates [193], and this may not only allow to obtain more reproducible results, but possibly also to discriminate between metabolic heat production of worms at different developmental stages. Additionally, interesting experiments may be also carried out for higher glucose concentrations, in particular, at concentrations corresponding to the diabetic range in humans [195].

6.7 Concluding remarks

In this chapter we have presented the characterization and the validation of the newly developed nanocalorimetric platform. In particular, the temperature stability and thermalization time were estimated to be ± 1 mK and 20 minutes, respectively, which are both adequate when compared to the system requirements, as presented in detail in Chapter 5. Additionally, a sensing time constant of 6 seconds was experimentally determined. This experimental result is in good agreement with the computational result, obtained by heat transfer simulations as described in section 5.5.3.

The electrical calibration procedures allowed to determine the limit of detection of the platform, which is about 70 nW and 170 nW at 25 $^{\circ}\text{C}$ when using an integrated resistive heater and an external heater, immersed in a prefilled sample reservoir, respectively. The comparison between these two values allows to have a first estimate of the heat losses phenomena taking place under actual experimental conditions. More specifically, only part of the heat power, which is generated electrically via the external resistive heater in the sample reservoir, is conducted towards the sensing area and contributes to the generation of the temperature gradient, which is then recorded by the thermopile. A certain amount of the generated heat power is lost to the environment because of alternative thermal paths. From this point of view, interfaces between the different components of the nanocalorimetric platform are particularly critical and the presence of air gaps may be detrimental, for instance between the polystyrene membrane of the sample reservoir and the thermopile silicon membrane. For this reason, particular care was taken when assembling the different parts of the platform and thermal grease was used at the critical interface between the two membranes.

The experimental results obtained during calibration demonstrate the applicability of such platform for the investigation of chemical or biological processes having a thermal signature, which is at least in the order of hundreds of nW. This is the case of the chemical and biochemical studies, which have been carried out subsequently. In particular, the mixing of 1-propanol in water was chosen as the test reaction for refining the calibration, which was previously done using the external resistive heater. In fact, as already observed in section 6.4 and extensively reported in literature, electrical calibration alone may lead to relevant systematic errors. In fact, for the same thermal power released during electrical calibration or during a chemical test, the thermal gradients generated in the sensing area may be significantly different. For instance, factors that may contribute to these differences are the location of the external resistive heater in the sample reservoir, and the mixing efficiency of the reagents when injected in the reservoir. As a result, the use of test reactions with well-known thermal profiles is indispensable for accurate calibration [172]. In the specific case of the developed nanocalorimetric platform, the power sensitivity obtained by using the mixing of 1-propanol in water as test reaction has been estimated to be three times lower when compared to the corresponding value, obtained by electrical calibration.

Additionally, as already mentioned, the quantification of the enthalpy of mixing was possible for an initial concentration of 1-propanol in water up to 89% v/v. The reason for this limitation was the increasing effect of evaporation, which became more and more significant for increasing concentration of volatile alcohol. As the sample reservoir consists of an open vessel, evaporation may have an effect on the nanocalorimetric measurements, in particular it may induce a drift in the signal baseline. Small effects compared to the expected mixing peaks in the thermopile signal, may be corrected by applying the baseline subtraction algorithm to the raw data. However, if evaporation becomes more important, mixing peaks may be still detected, but the quantification of the reaction enthalpy is not accurate anymore due to the strong baseline drift. For this reason, the calibration was based on experimental results for 1-propanol in water concentrations, which baselines were reasonably stable.

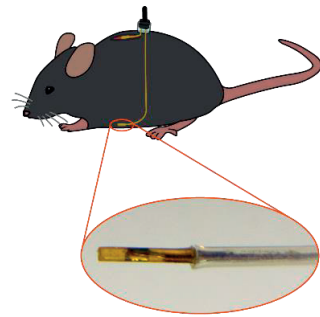
Further validation of the platform was carried out by investigating another well-know reaction, the oxidation of glucose catalyzed by glucose oxidase. This biochemical reaction is well described by the Michaelis Menten model, as reported in section 6.5.4 and it allowed to confirm the applicability of such platform to the study of enzymatic assays. In particular, when considering the heat power peaks vs the initial concentration of substrate, both the linear range and the saturation range of the typical enzymatic system following the Michaelis Menten model were identified. Additionally, the calculated values of Michaelis constants agree well with reported values from literature, as well as the estimated enthalpy of oxidation of glucose catalyted by glucose oxidase. These results demonstrate that the nanocalorimetric platform may be use for the quantitative investigation of the reaction enthalpy for a wide range of applications.

Finally, we have reported preliminary results on the measurement of metabolic heat production by a population of *C. elegans* nematodes. This proof-of-concept opens the way for more advanced met-

abolic studies on living organisms, especially for the investigation of metabolic changes during ageing or during exposure to specific biomolecules, for example glucose. The biological applications using this nanocalorimetric platform target the study of metabolism on a population of biological organisms or cells. This type of investigation allows measuring directly the metabolic heat, as an average over the population, and correlating it to other important metabolic parameters, such as the oxygen consumption and carbon dioxide production, enabling a more complete understanding of the biological process of interest. For instance, this is particularly promising when investigating chemically induced uncoupling phenomena, such as previously described in section 2.2.1, as the expected effect of uncoupling is, indeed, the increased production of metabolic heat. The design and development of the nanocalorimetric platform was driven by this field of application. Instead, the study of metabolic heat at the single-organism level has not been targeted. In fact, the system requirements are significantly different when comparing these two fields of research. Metabolic investigation at the population-level requires sample volumes of at least few tens of μl and a limit of detection in the range of a few tens of nW would be sufficient. In contrary, metabolic studies at the single-organism level require a much lower limit of detection in the order of few nW, which is achieved through extreme sample miniaturization, as small as few hundreds of pJ, and thus enhanced sample insulation, for example through vacuum incapsulation, as reported in literature [86].

Chapter 7 Localized temperature measurements during cold exposure for *in vivo* metabolic studies

This chapter presents the new method developed for localized and accurate *in vivo* temperature measurements at two different sites in a mouse body. Two miniaturized temperature sensors have been successfully implanted in the brown adipose tissue and in the abdomen of C57BL6/J mice, in order to assess directly possible local metabolic variations. Temperature was continuously acquired during mouse cold exposure to 6 °C for maximum 6 hours. Experimental results highlighted two different phenotypes in terms of metabolic resistance to cold. These results were qualitatively explained by computational simulation, performed considering a simplified physical thermal model of the mouse body.



All sections of this chapter have been adapted from the following journal article [196]:

Miniaturized implantable sensors for *in vivo* localized temperature measurements in mice during cold exposure (2016)
R. Padovani, T. Lehnert, P. Cettour-Rose, R. Doenlen, J. Auwerx, M. A. M. Gijs.
Biomedical Microdevices, vol. 18, no. 1, pp. 1–9
DOI: 10.1007/s10544-015-0028-9

This chapter reports on *in vivo* temperature measurements performed in mice at two specific sites of interest in the animal body over a period of several hours. In particular, the aim of this work was to monitor mouse metabolism during cold exposure, and to record possible temperature differences between the body temperature measured in the abdomen and the temperature of the brown adipose tissue (BAT) situated in the interscapular area. This approach is of biological interest as it may help unravelling the question whether biochemical activation of BAT is associated with local increase in metabolic heat production. For that purpose, miniaturized thermistor sensors have been accurately calibrated and implanted in the BAT and in the abdominal tissue of mice. Both procedures, *i.e.* the sensor preparation and calibration as well as the implant, are described in detail in this chapter. The temperature measurements on mice, exposed to cold (6°C) for a maximum duration of 6 hours, are then reported and discussed. In particular, these measurements have been carried out after one week since the surgery to allow the mice to recover. Control measurements with a conventional rectal probe confirmed good performance of both sensors. Moreover, two different mouse phenotypes could be identified, distinguishable in terms of their metabolic resistance to cold exposure. This difference was analyzed from the thermal point of view by computational simulations, which are presented as well. They are based on a simplified physical model of the mouse body, which allowed to reproduce the global evolution of hypothermia and also to explain qualitatively the temperature difference between abdomen and BAT locations. While with our approach, we have demonstrated the importance and feasibility of localized temperature measurements on mice, further optimization of this technique may help better identify local metabolism variations.

7.1 Setup for *in vivo* measurements and sensor preparation

The inbred C57BL6/J mouse strain, that is commonly used for metabolic studies, was chosen for our *in vivo* experiments. To measure local variations of mouse metabolism, two sensitive and miniaturized temperature sensors are implanted in each mouse, as depicted in Figure 60a. One sensor is positioned in the interscapular BAT, underneath the larger white adipose tissue depot (as sketched in Figure 60b), in order to measure directly temperature variations in the BAT. The second sensor is sutured in the abdominal cavity. This sensor provides a reference measurement for the body temperature of the mouse far from the BAT. As a control, a third conventional sensor (Thermometer BIO-TK 9882, *Bioseb*; and Thermometer Probe RET-3 Probe, *Physitemp*) is used to acquire periodically rectal measurements of the body temperature.

The implanted miniaturized sensors are negative temperature coefficient (NTC) thermistors with a nominal resistance of 100 k Ω at 25°C (Micro BetaCHIP Probe, *Measurement Specialties*). These sensors, featuring a sensing tip with a polyimide cover for improved moisture protection and biocompatibility, are suitable for laboratory animal research. The coated sensor tip is 0.5 mm in diameter and 3 mm long, as shown in Figure 61a. The sensor lead wires (0.1 mm in diameter) are made of nickel and are covered by a polyester insulation. Such thin lead wires have very low thermal conduction, thus limiting the impact of adjacent tissues on local temperature measurements. The lead wires of both sensors are cut to an appropriate length so that the subcutaneous path runs

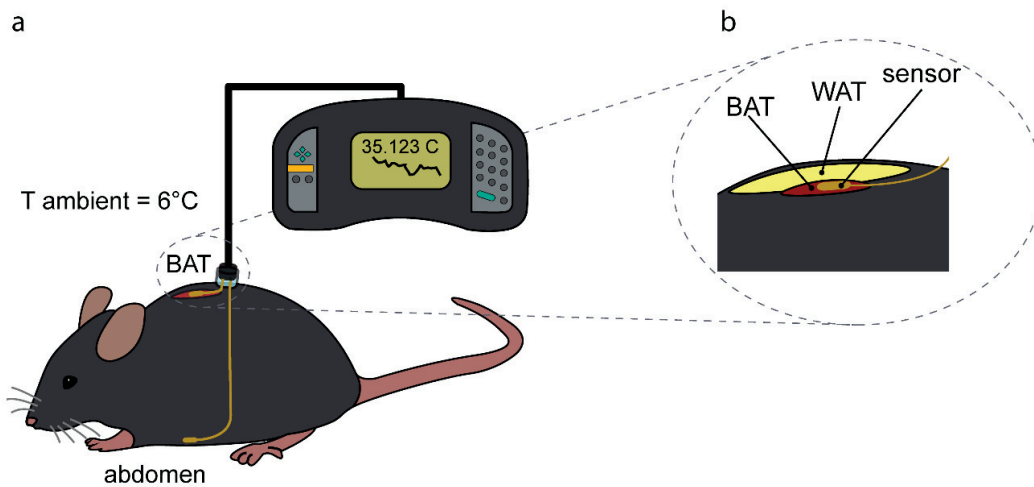


Figure 60 Principle of the *in vivo* temperature measurement on a mouse. a) Schematic view showing the thermistor sensors implanted in the mouse abdomen to record the overall body temperature, and in the brown adipose tissue (BAT). The measurement readout is done via a connector that is surgically fixed on the back of the mouse. After a period of one week for recovery from surgery, the two sensors are continuously read out during cold exposure at 6°C. b) Close-up view of the sensor insertion point in the BAT in the interscapular region underneath the white adipose tissue (WAT) layer.

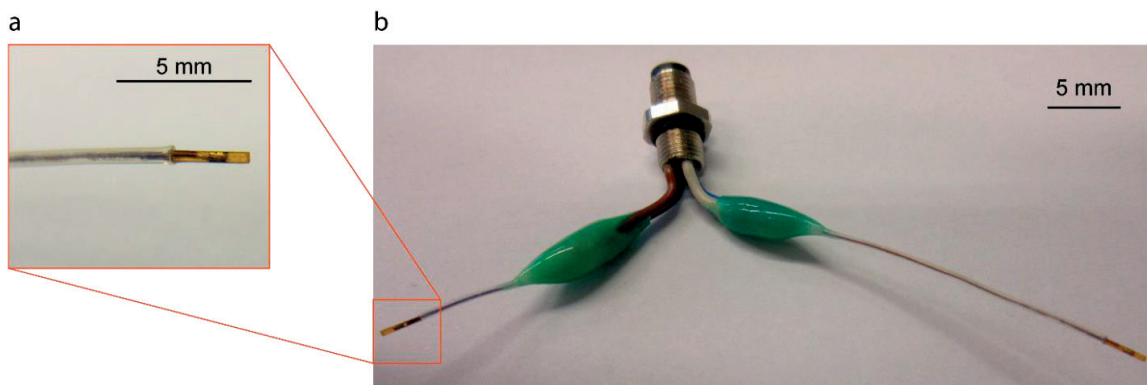


Figure 61 View of the miniaturized temperature sensor assembly. a) Close-up view of the sensor tip, which is 0.5 mm in diameter and 3 mm in length. b) Photograph of the sensor assembly prepared for implant: a pair of sensors is soldered to a common 4-pin connector, then reinforced with dental cement and covered with medical silicon (green colour) to guarantee biocompatibility.

smoothly from the specific implant site to the insertion point on the back of the mouse (1 cm long for the BAT sensor and 3 cm long for the abdominal sensor, respectively). Additionally, in order to improve the mechanical resistance of lead wires, biocompatible thin plastic tubing (Bohlander PTFE tubing, *Sigma-Aldrich*) is used to cover lead wires over the full length, except the sensing tip. At the insertion point, both sensors are connected to a common 4-pin connector (panel-mount plug pole no. 4, *Binder*). The soldered junctions are then reinforced and insulated by embedding them in a layer of dental cement (RelyX Unicem2 Automix, *3M ESPE*). Figure 61b shows an assembly of two sensors and a connector. At this point, once the sensors are calibrated (see section below), the assembly is inserted into a standard infusion connector (Dacron mesh button, *Instech Laboratories*) that is sutured on the back of the mouse. Just before the implant, the dental cement layer is covered by an additional layer of medical silicone (Kwik-Cast Silicone Elastomer, *World Precision Instrument*) to avoid any inflammatory reaction of the mouse tissue. This setup allows convenient connection and disconnection of the sensors to the measuring equipment (1560 Black Stack, *Fluke Hart Scientific*). This is a critical point considering that the mice should be left recovering from the surgery for one week without any constraints and stress that may affect mouse temperature and circadian rhythms.

7.2 Sensor calibration

For accurate temperature measurements, the sensors have been calibrated before the implant. For this purpose, as is shown in Figure 62, we designed and developed a setup for precise temperature control and stabilization. All the mechanical parts were fabricated by the EPFL Workshop *Atelier de l'Institut de microtechnique*, according to the 3D designs provided.

The main part of this platform consists of an aluminum plate (110 mm x 80 mm x 5 mm) that has specific grooves to accommodate the implantable sensors to be calibrated, one larger groove for a

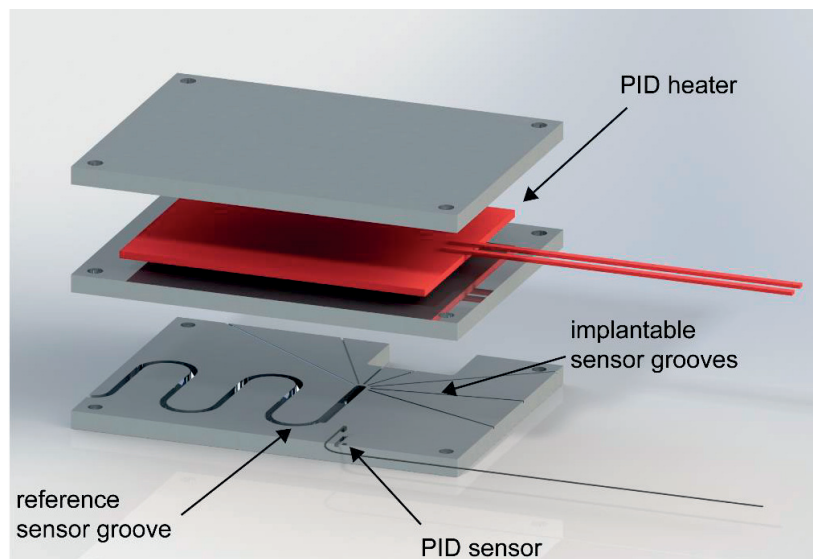


Figure 62 Exploded view of the custom-built aluminum holder used to set calibration temperatures by means of a PID controller. Specific temperature calibration points in the range of 25 °C to 42 °C were set with a stability of ± 1 mK over a period of 30 min. For each setpoint, the temperature value T_{ref} of a calibrated thermistor reference sensor and the resistance value R_{sens} of each implantable sensor were acquired.

calibrated reference sensor (thermistor probe 5611T, *Fluke Hart Scientific*) and a small pocket for a platinum resistive temperature sensor (Pt1000, *IST Innovative Sensor Technology*) required for temperature regulation of the system. The temperature control relies on a proportional-integral-derivative (PID) control loop including a PID controller (Model 335, *Lake Shore Cryotronics*), a flat resistive heater (polyimide heater 68.1 x 87.4 mm, nominal resistance 36.3 Ω , *Minco*) and the platinum temperature sensor. A second aluminum plate is interposed between the sensors and the resistive heater in order to provide a uniform temperature distribution while heating, and to avoid direct contact of the sensors with the heater. Finally, a third plate is used to clamp the assembled setup together. A tight clamp is critical to hold the different sensors in place and to provide good thermal contact for efficient temperature regulation of the calibration platform. Temperature and resistance values of the sensors are recorded simultaneously at a sample rate of 0.5 Hz by using a commercial thermometer readout (1560 Black Stack, *Fluke Hart Scientific*).

Calibration of the sensors has been carried out according to the Steinhart-Hart equation [197] that fits most accurately the temperature vs resistance curve for thermistors [198]:

$$T^{-1} = A + B \ln R + C (\ln R)^3$$

Equation 7:1 – Steinhart-Hart equation

where A , B , and C are the calibration coefficients, T (K) is the temperature of the platform, and R (Ω) is the sensor resistance.

For calibration, the sensor plate temperature is set subsequently to three different temperatures (27 °C, 33 °C and 42 °C). The temperature stability at the setpoint may be as good as ± 1 mK. For

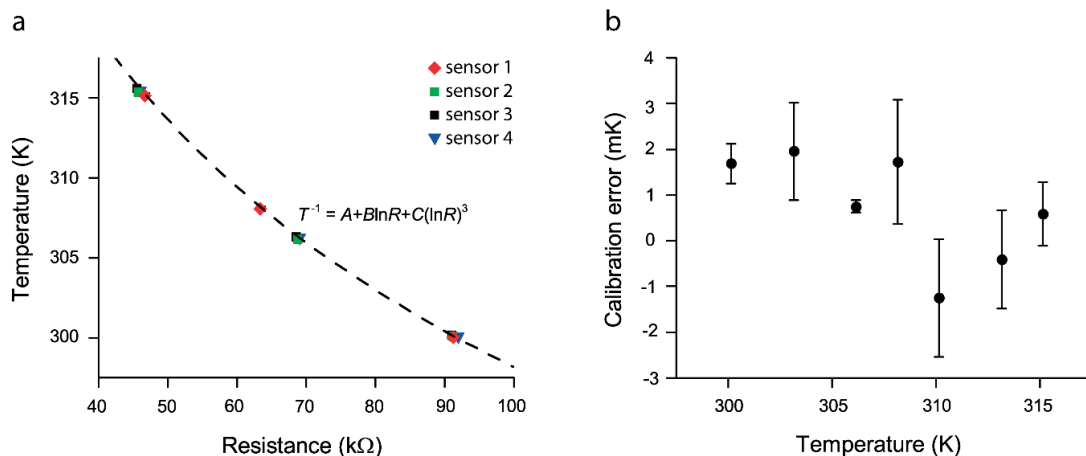


Figure 63 Calibration of the temperature sensors. a) Calibration curve based on the Steinhart-Hart equation obtained by fitting three pairs of (R_{sens}, T_{sens}) values per sensor (assuming $T_{sens} = T_{ref}$). b) Calibration error curve at different temperatures, in order to verify the accuracy of the thus-calibrated sensors, by comparing the temperature values T_{ref} from the thermistor reference sensor with the temperature values T_{sens} from the implantable sensors (mean \pm standard deviation). The maximum experimental calibration error is about 2 ± 1 mK.

each setpoint, the reference sensor temperature T_{ref} is recorded, as well as the corresponding resistance R_{sens} of each implantable sensor. Since the platform was designed to guarantee a uniform temperature distribution, especially within the sensing area, we can assume that the reference sensor temperature T_{ref} corresponds well to the temperature T_{sens} of the implantable sensors. Knowing three pairs of (R_{sens}, T_{sens}) values, the three calibration coefficients in Equation 7:1 may be calculated for each implantable sensor by solving the corresponding simultaneous equations. An example of data fitting using the Steinhart-Hart equation is shown in Figure 63a. Subsequently, the calibration error may be evaluated by setting the platform to different temperatures within the calibration range and by recording both, T_{ref} and T_{sens} . The maximum absolute error is then calculated as the difference in the temperature values recorded by the two types of sensors. As depicted in Figure 63b, this error is typically in the range of a few mK which is far below other possible fluctuations that occur during *in vivo* measurements.

7.3 Animal model: from surgery to cold test

7.3.1 Animals

C57BL/6J wild-type mice, a strain that is widely used for studies on energy metabolism, were used for our *in vivo* experiments. In particular, male C57BL/6J mice aged between 8 and 12 weeks were used. At the EPFL Center of Phenogenomics, mice were housed in groups in cages (Green Line® GM500 IVC type, Tecniplast) at 22°C +/- 2°C room temperature, with 12h:12h dark-light cycle and with a relative humidity of 55% +/- 10%. Mice had *ad-libitum* access to food (Kliba 3242) and acidified water (Prominet® CH system). All conducted procedures conformed to Swiss National Institutional Guidelines on Animal Experimentation and were approved through a license by the Swiss Veterinary Office Committee for Animal Experimentation (*license: VD2696*).

7.3.2 Surgical procedure and sensor implant

During the implant surgery, mice were anesthetized by isoflurane inhalation (induction 4-5%, maintenance 1.5-2%) and kept on a warm thermoregulated surgical plate, in order to maintain body temperature. Eye gel (Lacryvisc, Alcon) was used to keep mouse eyes hydrated during the surgery. Moreover, at the beginning and at the end of the surgery, buprenorphine (0.1 mg/kg) was injected subcutaneously, in order to minimize pain-induced stress and improve post-surgical recovery.

Sensors were sutured into place by using surgical wires. In particular, the longer sensor was sutured in the abdominal cavity, while the shorter one was positioned in the interscapular brown adipose tissue. Sensor wires run subcutaneously till the insertion point, where the outer connector was positioned on the back of the mouse and fixed by using surgical staples.

After surgery, each mouse was housed individually in the same type of cage, in order to prevent animals to harm each other. An analgesic (paracetamol, 2 mg/ml) dissolved in water was also provided during the first three days. Body weight was monitored daily in order to evaluate post-surgical recovery, and the surgical scar was inspected to identify possible signs of inflammation. Mice were left recovering from the surgery for one week before running the cold test.

7.3.3 Cold test protocol

To study cold-induced thermogenesis mice were placed in a cold room at 6 °C and each mouse was kept in its own cage individually, in order to avoid any possible interconnection between mice that may harm them or break the implant. No food was provided and temperature was continuously monitored by the implanted miniaturized sensors. Regularly temperature was also acquired with a standard rectal probe. These measurements allowed to have a control for the temperature measured by the implanted sensors, and to guarantee that mice never reached the minimal body temperature accepted by the animal experimentation license. After cold testing, mice were euthanized by carbon dioxide inhalation and the implants were recovered.

Both surgical procedures and cold tests were carried out by trained personnel of the *Center of Phenogenomics* of EPFL in their facility.

7.4 Experimental results during cold exposure

Eleven C57BL6/J wild type mice were implanted with the miniaturized temperature sensors and were subjected to the cold test at 6 °C, after recovering for one week from the surgery. Measurements were taken simultaneously for up to 4 mice (1 mouse per cage) with a sample rate of 0.5 Hz using a commercial thermometer readout system (1560 Black Stack, *Fluke Hart Scientific*). Raw data were post-processed by filtering in order to reduce short-term fluctuations, which may originate from electrical contact artefacts due to mouse movement.

Two different mouse phenotypes have been identified after cold exposure of the animals. The majority of mice (8 out of 11) were able to sustain a body temperature higher than the minimal accepted temperature (31 °C) for about 6 hours, *i.e.* the initially planned duration of the cold test (this class of mice is named phenotype 1 in the following). A smaller group (3 out of 11), instead, experienced a more marked body temperature drop and cold exposure had to be interrupted after 4 hours as the minimal acceptable body temperature of 31 °C was reached (this class of mice is named phenotype 2).

The temperature data recorded by the abdominal and the BAT sensors for both phenotypes are shown in Figure 64a and Figure 64b, respectively. Reported data points correspond to the average value of 8 (phenotype 1) or 3 (phenotype 2) measurements. The average rectal temperature, recorded with the conventional probe at an interval of roughly 60 min, is also indicated. For both mouse phenotypes, the initial body temperature was 36.2 ± 0.5 °C, as measured with the implanted sensors, whereas the rectal probe value was slightly higher for phenotype 1. This observation confirms that the sensors were operational after surgery and the one-week lasting recovery period after implant. Regarding the temperature evolution during the cold test, temperature recordings with the abdominal sensors were in good agreement with the rectal probe. Both reflect the body temperature of the mice. Slight systematic differences are observed ($\Delta T_{\text{ABDO-RECT}} \approx 0.2 - 1$ K for phenotype 1, and $\Delta T_{\text{ABDO-RECT}} \approx 0.1 - 0.4$ K for phenotype 2) for which several reasons, *e.g.* different sensor positions, varying thermal contact with the surrounding tissue, stress during rectal measurement etc., may be considered.

The temperature at the BAT location in the mouse, as plotted in Figure 64a and Figure 64b, could also be reliably recorded for the 11 mice. The BAT curves reflect the same global evolution as the abdominal curves, *i.e.* a slower decrease for phenotype 1 and a sharper temperature drop for phenotype 2. The average negative temperature difference $\Delta T_{BAT-ABDO}$ was calculated by subtracting the abdominal from the BAT temperature for each measurement point. The corresponding values are shown in Figure 64c and Figure 64d. For both phenotypes, we observe an approximately linear decrease of $\Delta T_{BAT-ABDO}$ down to a final temperature difference $\Delta T_{BAT-ABDO} \approx -2$ °C, reflecting faster cooling of the BAT than the abdomen during cold exposure. Whereas $\Delta T_{BAT-ABDO}$ is close to zero for phenotype 1 at the beginning of the cold test, the measured BAT temperature is slightly higher for phenotype 2, resulting in a crossover of the abdominal and the BAT curve after about 60 min. In principle, this observation could reflect an enhanced metabolic and thermal activity of the BAT upon cold exposure. However, taking into account the full set of measurements, it is most likely that systemic errors occurring during the recordings might have shifted the BAT or abdominal temperature curves.

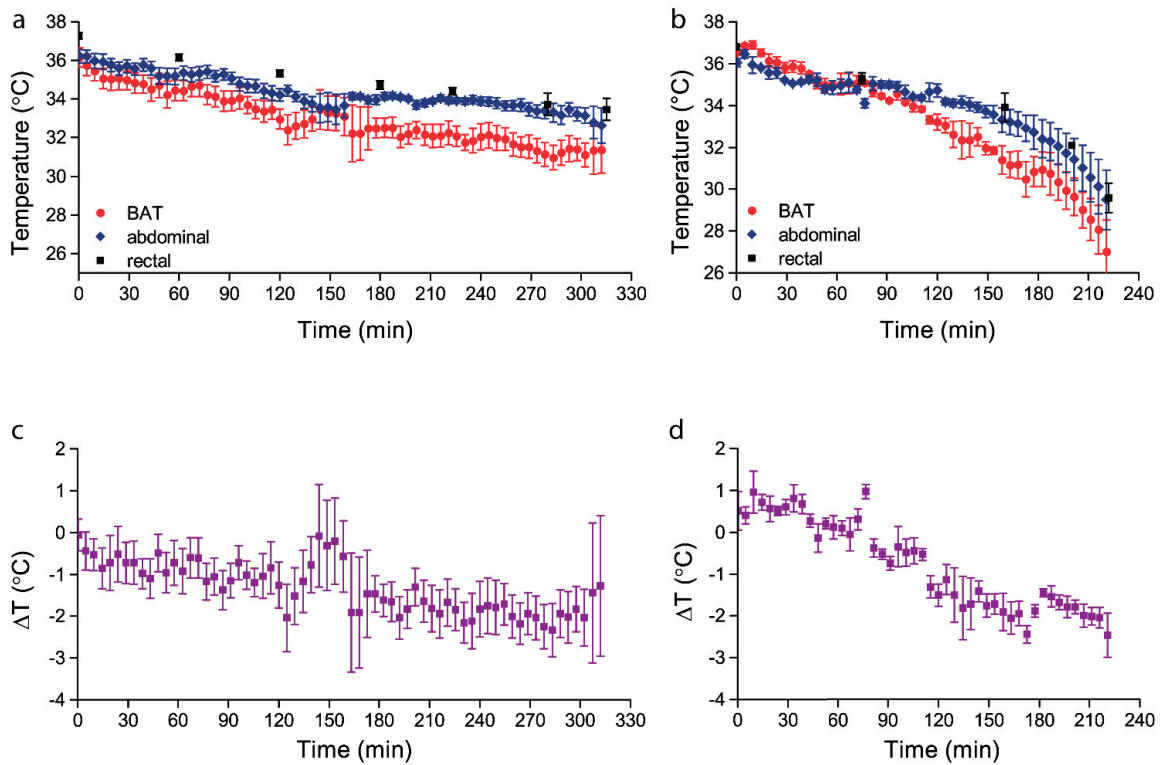


Figure 64 *In vivo* temperature measurements during cold exposure at 6 °C for the two different mice phenotypes. a) Average temperature plot for 8 mice of phenotype 1, showing a tendency to hypothermia. Temperature was continuously measured by the implantable sensors positioned in the abdomen and in the BAT. Rectal temperature was also acquired using a conventional rectal probe as a control measurement. b) Average temperature plot for 3 mice of phenotype 2, highlighting a lower resistance to hypothermia (cold exposure lasted less than 4 hours as the mice reached the minimal body temperature allowed). c) Average temperature difference $\Delta T = T_{BAT} - T_{ABDO}$ for phenotype 1, calculated by subtracting the abdomen temperature from the BAT temperature. After more than 5 hours of cold exposure the temperature difference is about -2 °C, indicating faster cooling of the BAT with respect to the abdomen. d) Average temperature difference ΔT for phenotype 2 showing a stronger but also nearly linear decrease over time (data points with error bars: mean \pm standard error of mean, over all mice of a given phenotype).

For instance, temperature measurements are very sensitive to the thermal contact of the sensor with the surrounding tissue, which is affected by mouse movements in the cage during the test.

Cold test experiments on mice have been reported in literature, but results are not directly comparable because of the great variability of *in vivo* experimentations. For example, it is known that, for C57BL6/J wild type mice (the same strain as used in our experiments), the mouse body temperature varies along the day/night rhythm [61]. Moreover, the positioning of the temperature sensors may have a significant impact on the measured temperature values. In our study, great care was taken to implant the miniaturized sensors directly in the BAT, while in previous studies sensors were sutured either underneath the BAT or subcutaneously on the top of it [68]–[70].

7.5 Computational heat transfer modeling

7.5.1 Model definition

We consider a simplified thermal model of the mouse body to elucidate qualitatively the effect of heat production and heat loss on the body temperature and to facilitate the interpretation of the experimental *in vivo* results during cold exposure. Figure 65 depicts the basic model used for that purpose. The mouse body is considered as an ellipsoid with uniform physical properties having a size comparable to the real animal (volume $\approx 35 \text{ cm}^3$). Values for material properties of the biological tissue have been chosen as reported in literature, in particular for the density ($\rho = 1050 \text{ kg/m}^3$), the thermal conductivity ($k = 0.4 \text{ W/mK}$), and the specific heat capacity ($c_p = 3657 \text{ J/kg K}$) [199].

The boundary conditions applied to the model may be listed as follows:

- Heat source $Q_M(t)$, which is uniform over the whole mouse body, modelling the body metabolism;
- Body temperature T_{M0} as the initial temperature of the mouse body. It was set to 36.2°C , which corresponds to the average experimental initial temperature.
- Natural convection, applied to the external surface of the ellipsoid, which is responsible for cooling during cold exposure at $T_c = 6^\circ\text{C}$. A heat transfer coefficient h can, thus, be defined to describe heat loss of the mouse body at its surface to the external environment. For mice

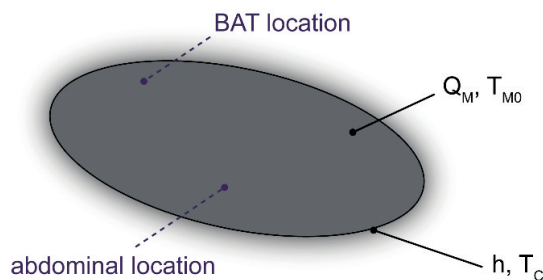


Figure 65 Heat transfer computational simulation. The mouse body was modeled as an ellipsoid, considering an overall mouse metabolic rate $Q_M(t)$ and an initial body temperature T_{M0} prior to cold exposure. Additional boundary conditions are determined by natural convection at the surface of the ellipsoid with a heat transfer coefficient h and an external temperature $T_c = 6^\circ\text{C}$.

a value of $h = 2.8 \text{ W/m}^2\text{K}$ was specified, that was estimated from the thermal insulation of mouse fur [200]. This boundary condition takes into account Newton's law of cooling (introduced in Chapter 5, Equation 5:5).

The resulting thermal gradients give rise to heat transfer by thermal conduction from the inner body to the surface. Thus, the simulations are based on the heat conduction equation for a three-dimensional system, which has been introduced in Chapter 5 (Equation 5:4).

The 3D numerical simulations have been performed using Comsol Multiphysics® aiming at monitoring the body temperature distribution and evolution over time. A free triangular mesh was used for the model, using a predefined mesh element size (parameter chosen: *extremely fine*). With respect to thermal simulation, the two mouse phenotypes differ from each other, as different body metabolism $Q_M(t)$ curves have to be applied to approximate the experimental data.

7.5.2 Simulating the thermal behavior of mouse phenotype 1

For simulating phenotype 1, showing a slower and more linear decrease of the body temperature upon cold exposure than phenotype 2, best fitting was achieved by considering a constant metabolic heat production. As indicated in Figure 66a, we applied a value of $Q_M = 0.42 \text{ W}$, which corresponds to estimated mouse metabolic rates reported in literature [70]. Figure 66b shows the transient temperature distributions on the external surface of the ellipsoid after two different time lapses, *i.e.* a few seconds after the beginning of cold exposure, and after 330 minutes, respectively. Cooling is

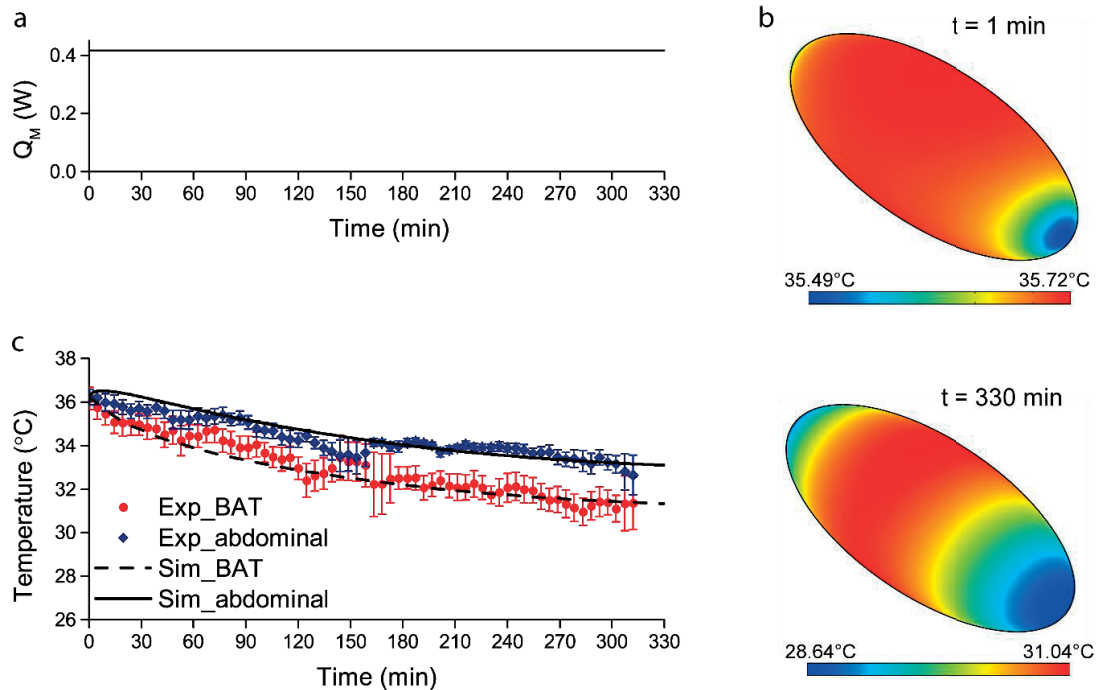


Figure 66 Comparison between computational and experimental results for mouse phenotype 1. a) Constant body metabolic rate implemented in the model ($Q_M = 0.42 \text{ W}$). b) Simulation of the temperature gradients on the body surface at different time lapses, considering $t = 0 \text{ min}$ as the starting point of cold exposure. c) Comparison of experimental and simulated temperature over time data for abdominal and BAT sensor locations. Simulated temperature values are taken at a distance of about 8 mm from the surface, both for the BAT and the abdominal temperature.

faster at the extremities of the ellipsoid where a temperature gradient of 2.4 °C builds up with respect to the central area of the body surface. Finally, Figure 66c shows the comparison of the simulated body temperature with the experimental results. The two simulated curves are temperature values calculated at the locations in the ellipsoid that correspond to the abdominal and BAT sensor positions in the mouse body, about 8 mm distant from the body surface. The general decreasing trend of the abdominal and BAT experimental temperature curves can be well reproduced. The temperature difference between BAT and abdomen can also, in principle, be found in the simulated curves. In the simulation, the temperature difference builds up quickly to about $\Delta T \approx 0.5$ K after starting the cold exposure and remains nearly constant over time. Using a very simple model as in our case, however, we can not expect accurate agreement of the absolute values and between detailed features of simulated and experimental curves. Nevertheless, it is remarkable that the overall evolution of the body and BAT temperatures can be explained by taking into account only a few basic physical assumptions. In our model, the difference between abdominal and BAT temperature is only determined by the different locations of the corresponding sensors, *i.e.* by the merely physical effect of faster heat loss at peripheral regions of the mouse body. More accurate quantitative matching of simulated and experimental values can be expected by a refinement of the mouse model, for instance by taking into account the different tissues and corresponding thermal properties.

7.5.3 Simulating the thermal behavior of mouse phenotype 2

Computational results for mouse phenotype 2 are summarized in Figure 67. As this phenotype showed a much lower resistance with respect to cold exposure, thus a faster decrease in body temperature after about 2 hours, we modified our assumption on the metabolic heat source. As shown in Figure 67a, the metabolic heat source $Q_M(t)$ applied was set to a constant value of 0.42 W (as for the previous model) up to 150 minutes of cold exposure. Thereafter, in order to take into account a possible breakdown of the metabolic heat production, we assumed that $Q_M(t)$ decreases linearly at a rate of 0.0025 W/min. All other parameters are the same as for phenotype 1.

Figure 67b shows the temperature distributions on the body surface at two different time lapses (a few seconds after the beginning of the cold exposure, and after 230 minutes, respectively), whereas Figure 67c shows the comparison between the experimental and computational data. Again, qualitatively, the overall shape of the temperature curves is well reproduced. Considering a breakdown in the metabolic heat production allows better fitting of the experimental data for phenotype 2 than if a constant heat source would have been considered as for phenotype 1.

7.5.4 Concluding remarks on phenotype difference and BAT activity

As the mice are inbred and hence genetically identical, there is no underlying genetic difference that can explain the differences in thermal behaviour between the two phenotypes. Environmental factors may have played a role, in particular the average body weight (BW) of mice for the two phenotypes has been calculated: phenotype 1 has a BW equal to 28.0 ± 1.0 g, while phenotype 2 has a BW of 29.4 ± 1.0 g. The BW difference was analyzed by Student's t-Test providing a p -value of

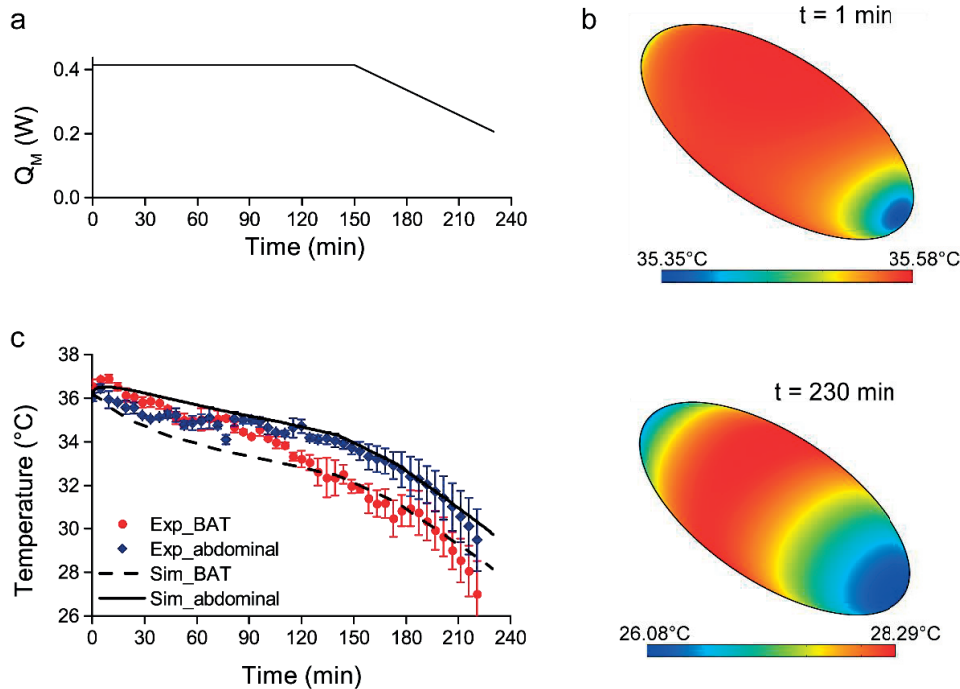


Figure 67 Comparison between computational and experimental results for mouse phenotype 2. a) Body metabolic rate $Q_M(t)$ implemented in the model. In order to take into account the breakdown of the cold resistance for phenotype 2, the body metabolic rate $Q_M(t)$ was set constant up to 150 minutes of cold exposure ($Q_M = 0.42$ W), and then decreases linearly. b) Temperature gradients on the body surface simulated at different time lapses, considering $t = 0$ min as the starting point of cold exposure. c) Comparison of the experimental and simulated temperature plots showing good qualitative correspondence.

0.06. However, defining the exact physiological causes of the difference in body weight and cold resistance will require further analysis of body composition (fat versus lean mass), food intake, food efficiency, activity and movement, as well as a detailed analysis of serum and tissue metabolites (e.g. glucose, free fatty acids, triglycerides). Our miniaturized temperature sensors will be extremely useful for evaluating possible effects of changes in these different parameters on brown adipose tissue activation and heat production.

Summarizing, based on the *in vivo* experimental results obtained, we are not able to speculate on any biological effect related to a possible activation of metabolic heat production in the BAT during cold exposure. Moreover, if we take into account the computational results of the simplified thermal model of a mouse, we have been able to qualitatively reproduce the thermal behavior of the two phenotypes by varying only the heat source simulating the whole body metabolic rate. No term was applied to simulate the local BAT metabolic activity. A brief discussion on possible improvements of *in vivo* experiments in order to obtain biologically relevant and reliable interpretations is reported in the conclusion in Chapter 8.

Chapter 8 Conclusion and Outlook

8.1 Results overview and discussion

The objective of this thesis work was the development and implementation of new technologies, enabling eventually the thermal investigation of biochemical processes and/or of metabolic processes in living organisms, such as bacteria, cells and multicellular organisms, and also small animals. This field of research is particularly promising and challenging at the same time. On the one hand, it has the potential to allow quantitative studies of complex biological phenomena and to provide innovative and faster analysis through the thermal signature of the reaction or organism under investigation. On the other hand, temperature measurements require a meticulous and systematic design of experiments, in order to be able to obtain conclusive results and biologically relevant interpretations. Two different technological approaches have been presented in the frame of this thesis.

8.1.1 Specifications of the nanocalorimetric platform

A nanocalorimetric platform was developed allowing heat power measurements during chemical and *in vitro* biochemical reactions under well-defined experimental conditions. The design and characterization of the platform was presented and its main experimental features were reported: (i) high temperature stability of the isothermal housing in the mK range over a period of about one hour, (ii) a thermalization time of only 20 minutes for reaching the setpoint temperatures of 25 °C or 37 °C, and (iii) a fast sensing response time of a few seconds for heat power generated by the sample. Electrical calibration based on using a resistive heater integrated in the nanocalorimetric sensor chip allowed to determine a limit of detection of 70 nW at 25 °C. Instead, electrical calibration based on an external resistive heater immersed in the 50 μ l sample reservoir was used to simulate heat generated by a chemical reaction in a liquid sample. Using such configuration, we obtained a limit of detection of 170 nW at 25 °C. The good performance of the nanocalorimetric platform was successfully demonstrated in the study of both the thermodynamics and the kinetics of (bio-) chemical reactions. In particular, the quantification of the heat of mixing of 1-propanol in water and the study of the enzymatic activity of glucose oxidase provided results, which are in good agreement with literature data. Also preliminary heat power measurements on a suspension of *C. elegans* nematodes showed the applicability of our platform to metabolic studies on living organisms.

The use of a miniaturized and highly sensitive chip-based thermopile sensor in our nanocalorimetric platform, combined with the optimized design of an isothermal housing, proved to be advantageous for sensitive and time-efficient calorimetric measurements. Briefly, by comparing with the main specifications of commercial isothermal microcalorimeters (as described in Chapter 3), several advantages of our nanocalorimetric platform may be emphasized. First, the sample volume used in

our platform is at least 20 times smaller compared to the ml sample volume required for typical microcalorimetric ampoules. This is a significant advantage, if expensive samples and/or samples that are only available in limited quantity are investigated. Nevertheless, we reached a limit of detection of a few hundreds of nW, which is of the same order of magnitude as for commercial microcalorimeters. Additionally, the thermalization time required to reach stability before initiating an experiment is drastically reduced, *i.e.* from several hours for commercial equipment to about 20 minutes for the presented nanocalorimetric platform. Regarding biological samples, the short thermalization time plays in favor of preserving sample quality during an experiment.

A detailed comparison with nanocalorimetric systems that have been presented in literature (as described in Chapter 4) is more difficult due to the wide range of different approaches and specifications. As an example, we may consider the calorimetric system presented by Lerchner *et al.* working with the same range of sample volumes (a few tens of μl) as our platform [88]. This nanocalorimeter was used extensively for metabolic studies on bacteria and biofilms and had a limit of detection of 50 nW, *i.e.* about three times lower than our platform. However, the low limit of detection achieved by Lerchner *et al.* required the development of a highly sophisticated temperature control system based on two nested thermostats with multiple sensing and heating elements. For the development of the nanocalorimetric platform presented here, instead, we favored a simpler design of both, the isothermal housing and the temperature control system. Moreover, the sample reservoir is easily accessible in our case, meaning that sample and reagent solutions can either be pre-loaded or injected directly into the reservoir via an external thermalized conduct, thus allowing very versatile experimental protocol definitions. We therefore believe that our approach provides a good compromise between high sensitivity, versatility and user-friendliness. These features are critical when aiming more extensive use of this powerful sensing technique in advanced biology studies, and particularly in molecular and cell biology.

8.1.2 *In vivo* localized temperature sensing in mice

Furthermore, we have conducted a study for assessing the thermal activity of biological processes *in vivo*, which aimed in particular at highly localized temperature measurements in mice for investigating the metabolic activity of the interscapular brown adipose tissue (BAT). Several series of *in vivo* mice cold tests have been carried out in the course of this work at the EPFL Center of Phenogenomics (EPFL SV CPG-GE) and the results have been presented in the last part of this thesis. For the purpose of this study, we used miniaturized thermistor sensors of 0.5 mm in diameter that were suitable for implant in animals because of their miniaturized cylindrical shape, the extremely thin connecting leads and the biocompatible polyimide coating. For this feasibility study, two miniaturized temperature sensors were implanted simultaneously in two different sites, *i.e.* the BAT interscapular depot and the abdomen, respectively. Due to general constraints of animal testing and specific challenges related to the implementation of a new technology, experiments were based on groups of a small number (up to four each) of wild-type mice (strain C57BL/6J). Prior to implant, the sensors have been calibrated using a highly stable and accurate custom-made temperature controlled platform, resulting in a sensor accuracy of 2 mK. The sensors were successfully implanted and allowed the continuous recording of the temperature values at the two locations for several

hours during cold exposure of the mice to an ambient temperature of 6 °C. The recorded set of temperature curves revealed a general tendency to hypothermia, and two different phenotypes could be distinguished with respect to their capacity to withstand cold exposure. A simple physical model was used for thermal computational simulation of the mouse body temperature. This model was sufficient to reproduce the general shape of the recorded temperature curves. Finally, our findings did not allow to draw any specific and biologically relevant conclusion on the metabolic activity of the BAT during cold exposure. The assumed body metabolic rate over time dependence was identified as the main critical parameter that shapes the behavior of the two different phenotypes. In particular, our observations suggest that resistance to prolonged cold exposure may be explained by maintaining a constant body metabolic rate.

8.2 Future opportunities

8.2.1 Microfluidic integration and new applications of the nanocalorimetric platform

At present, our system relies on passive diffusive mixing of small aliquots injected into the on-chip sample reservoir. Even if the reservoir dimensions are relatively small, our experiments revealed some limitations due to slow diffusive mixing. Faster mixing is key to further improvements of the platform performance. One way to achieve this goal is to combine a custom-designed microfluidic chip system with the sensor chip. The present platform design is already compatible with such an implementation.

For instance, a microfluidic mixer may be designed for further studies of biochemical reactions, such as enzyme-catalyzed assays. Such design comprises inlets for separate injection of reagents and possibly a serpentine-like channel confined within the sensing area of the thermopile chip. Alternatively, another type of microfluidic design may be envisaged for working with living organisms. On-chip culturing of organism, such as bacteria or cells, is of great interest to study the thermal fingerprint of growing populations under different conditions. For such applications, the microfluidic chip may consist of a central culture chamber, located directly on top of the sensing area of the thermopile chip. Adjacent microchannels would allow the introduction and uniform flow of reagents through the culture chamber. Such an approach would also overcome a major limitation of typical isothermal microcalorimeters consisting in the undesired alteration of the culture medium in closed ampoules. In fact, a microfluidic chip enables the replenishments of nutrients, and also of oxygen, and the removal of waste byproducts resulting from the metabolic activity of the organism. Finally, microfluidic integration may allow experimental protocols based on alternative operational modes. For instance, alternating injections of control and sample solutions improves the baseline acquisition and subtraction algorithm before and after the heat power signal measurement. Also sequential measurements may be implemented more easily.

In view of future biological applications, the presented nanocalorimetric platform holds great potential in several fields of research. First of all, our study of enzyme-based glucose oxidation demonstrated that nanocalorimetry has high potential in the field of drug design to investigate the mech-

anism of action of specific compounds, such as possible drug candidates targeting enzymatic reactions [188]. Similarly, in environmental biology, contaminants or pollutants have often an inhibitory effect on enzyme activity, for instance, heavy metals are known to have such effect on glucose oxidase [189]. The nanocalorimetric platform may be used either to study the mechanism of inhibition of specific pollutants, or even as a sensing system for quantifying the degree of pollution of contaminated samples. The evaluation of the general shape of the heat power curve (*e.g.* maximum peak, rate constant, etc.) acquired during the enzymatic assays in presence or absence of interfering compounds, may reveal important information on underlying mechanisms. Additionally, the application of the nanocalorimetric platform to the field of biosensing is, indeed, promising and examples from literature already demonstrated the possibility to directly monitor protein-protein binding as well as DNA hybridization [136]. However, as heat is a non-specific signal, accurate sample preparation would be required, especially when aiming at working with complex biological samples, in order to avoid misleading interpretation of the results.

A wide and still emerging field for nanocalorimetric studies is the metabolic activity of mammalian cells. As discussed in Chapter 2, mitochondria are the key organelles of cellular metabolism and uncoupling pathways of cellular respiration are still not completely established. Metabolic heat power measurements, when correlated with other types of measurements, in particular oxygen consumption data, may help to provide a more complete understanding of mitochondrial respiration and its alterations. Conventional biological protocols to quantify bioenergetic parameters consist in exposing living organisms to different compounds interfering with mitochondrial respiration (such as FCCP, oligomycin, rotenone, etc.). Such protocols may be adapted for the nanocalorimetric platform and microfluidic integration is particularly useful for this purpose.

A new and very promising field for nanocalorimetric applications is the study of the metabolic activity of multicellular organisms. In our work, we were able to show promising preliminary measurements on *C. elegans* nematodes. In future, it may be interesting to conduct more extended and systematic studies of *C. elegans* metabolism, not only in wild type worms, but also in transgenic worms that are relevant models for specific metabolic diseases in humans [201].

8.2.2 Improvements and applications of *in vivo* localized temperature sensing

The work presented in this thesis demonstrates the feasibility of localized *in vivo* temperature measurements in laboratory mice for direct and selective monitoring of metabolic heat production. The use of highly miniaturized sensors, however, may be subjected to a certain number of systematic errors related mainly to problems of reliable fixation and of positioning of the sensors in the tissue of interest. Good and stable thermal contact between tissue and sensor is a prerequisite for low-noise, accurate and reproducible temperature measurements. Furthermore, considering the size of the BAT, especially the relatively small thickness of this tissue (few millimeters in mice), surgery itself for sensor implant and accurate positioning inside or in close contact with the tissue is also a critical issue for this type of study. At present, this problem can only be solved by an experienced surgeon. From the technological point of view, different approaches may be tested to overcome some of these issues. First, the sensor size may be optimized and a compromise between the two

conflicting approaches, *i.e.* spatial resolution and reliability of the localized temperature measurements, may be found. On the one hand, using slightly larger sensors might be advantageous for secured handling and improved thermal contact, thus enhancing reliability. On the other hand, considering larger capsule-like implantable temperature sensors used in literature (the smallest of them being 2 mm in diameter and 14 mm long) [66], [70], it would be rather difficult or even impossible to insert such a sensor completely into the small BAT. Thus, spatial resolution may not be sufficient and only an average temperature between BAT and neighboring tissues could be measured. A second significant improvement would be the implementation of telemetric data transmission chips connected to the sensors, thus avoiding permanent external wire connections of the mouse throughout the cold test experiment. Such wire connections are cumbersome and exert mechanical stress on the mouse body and on the implanted sensors. Even more important, such constraints may increase the stress experienced by the mouse, possibly resulting in uncontrolled increase or variations of the body temperature.

Finally, the present study sets the basis for further biological investigation of BAT activation during cold test exposure, which may be addressed by evaluating the effect of diet or pharmaceutical compounds, such as beta-adrenergic agents. Systematic biological studies are often based on the response of specific transgenic mice. In our case, for instance, the investigation of mice strains showing overexpression, inactivation or downregulation of BAT activity would be of great interest to determine the role and importance of the BAT tissue. Ultimately, our approach may provide insights in the study of new therapies, for instance for obesity, type 2 diabetes, and related metabolic disorders.

Appendix A

In the following two pages, part of the datasheet of liquid nanocalorimeters, fabricated by *Xensor Integration*, is reported, giving detailed specifications for the nanocalorimeter XEN-NCM 9924, which has been used in the development of the nanocalorimetric platform.

Liquid Nanocalorimeters XEN-NCM9924 / -LCM2506 / -LCMquad

3 Technical data

3.1 Specifications

Table 2.1 Specifications (ambient temperature 22 °C)

	XEN-LCM 2506	XEN-LCM quad	XEN-NCM 9924	XEN-TCG 3880			
Parameter	typ	typ	typ	typ	unit	symbol	notes
Dimensions							
housing size	29x29x7	29x29x7	29x29x7	3.3x2.5x0.3	mm ³		
chip dimensions	5x5	4 of 5x5	10x10		mm ²		
membrane size	3.5x3.5	3.5x3.5	8.3x8.3		mm ²		
membrane thickness	4-8	4-8	22-45	1	µm		
Output							
in air at 1013 mbar	8	8	1.2-2.4	30	V/W		
in still water	4	4	-	-	V/W		
Time constant							
in air				9	ms		τ
in vacuum				36	ms		
Stability							
short term				100	ppm		
long term				1000	ppm		
Thermopile							
resistance	150	150	50	55	kΩ	R_{Tp}	
effective sensitivity				1.3	mV/K	S_{Tp}	
intrinsic sensitivity	50-80	50-80	50	2.4	mV/K		
temp coefficient				0.05	%/K		
Heater							
resistance	0.8	0.8	0.44	0.6	kΩ	R_{heat}	
resistance R1-R2	-	-	1.0	-	kΩ	R_{heat}	Alu heater
resistance R1-R3	-	-	0.25	-	kΩ	R_{heat}	Alu heater
temperature coefficient				0.1	%/K		
Thermal resistance							
membrane				100	kK/W		
temperature coefficient					%/K		
membrane + gas				23	kK/W		
temperature coefficient				-0.08	%/K		
chip to housing					K/W		
Maximum heating voltage							
in air				2.5	V		U_{heat}
in vacuum				1	V		
Sensor ambient temp							
minimum				-273	°C		
maximum				240	°C		
Heater max temp							
				250	°C		

Xensor Integration bv

Distributieweg 28
2645 EJ Delfgauw
The Netherlands

Phone +31 (0)15-2578040
Fax +31 (0)15-2578050
Email info@xensor.nl

Founded 18 May 1988
Trade reg. 27227437
Site www.xensor.nl

Smart Sensor Devices

ABN-AMRO 60 50 40 311
IBAN NL42ABNA0605040311
VAT NL 009122746 B01

Liquid Nanocalorimeters XEN-NCM9924 / -LCM2506 / -LCMquad

XEN-NCM9924: 68 pins 11x11 PGA cavity down

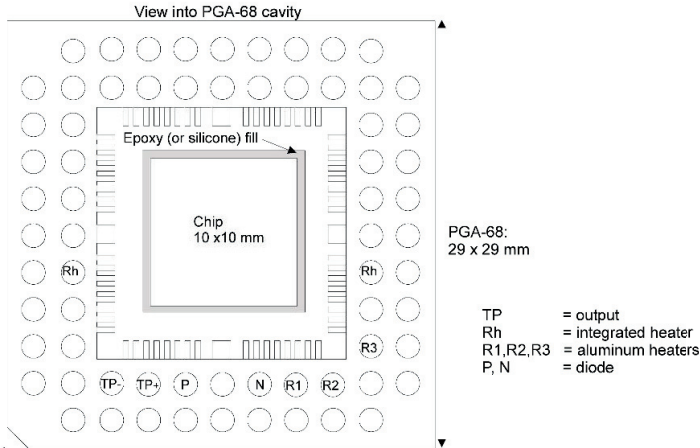
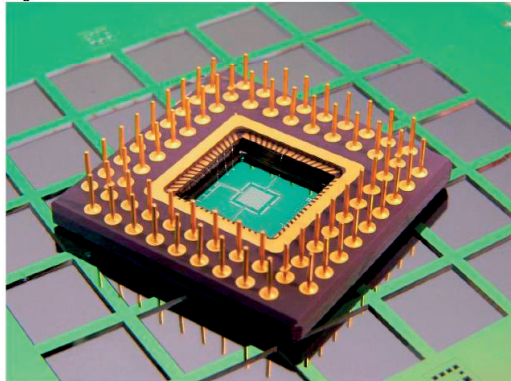


Figure 2.4 Electronics side of XEN-NCM9924



Xensor Integration bv

Distributieweg 28
2645 EJ Delfgauw
The Netherlands

Phone +31 (0)15-2578040
Fax +31 (0)15-2578050
Email info@xensor.nl

Founded 18 May 1988
Trade reg. 27227437
Site www.xensor.nl

Smart Sensor Devices

ABN-AMRO 60 50 40 311
IBAN NL42ABNA0605040311
VAT NL 009122746 B01

copyright Xensor Integration

12 October 2010

page 7 of 11

Appendix B

As already mentioned in Chapter 5, two main Labview interfaces have been developed for controlling the necessary equipment of the nanocalorimetric platform:

1. The nanocalorimetric interface, which controls the Proportional-Integrative-Derivative (PID) controller and acquires the voltage signal from the thermopile sensor. Figure 68 reports a screenshot of this interface. In particular, two main sections may be distinguished. The first section is dedicated to the definition of all the settings required for both equipment, *i.e.* the temperature controller (Model 335, *Lake Shore Cryotronics, Inc.*) and the nanovoltmeter (34420A, *Agilent*). Together with the settings for proper communication between Labview and the equipment (VISA and serial configuration) and for general data acquisition (sampling rate and total number of samples), required settings include the *P, I, D* optimized parameters, the setpoint temperature, the heater power range, the PID sensor input and the voltage measurement type. The second section of the interface is dedicated to real time visualization of experimental measurements, *i.e.* the temperature measured by the PID sensor and the voltage acquired by the thermopile sensor.
2. The calibration interface, which controls the PID temperature controller, the nanovoltmeter for measuring the thermopile voltage and the sourcemeter (2400, *Keithley Instruments*) for running electrical calibration with a resistive heater. Figure 69 reports the corresponding screenshot. Also in this case two sections are present. The first one is dedicated to the definition of all required settings. Compared to the previous interface, this interface requires settings for the sourcemeter, including the source mode, by applying either a current or a voltage to the resistive heater, and the list of current or voltage values considered. The second section, instead, allows the real time visualization of the experimental data. Compared to the previous interface, the voltage and corresponding current measured on the resistive heater are also reported, which allowed the calculation of the heat power dissipated by Joule's effect by the resistive heater.

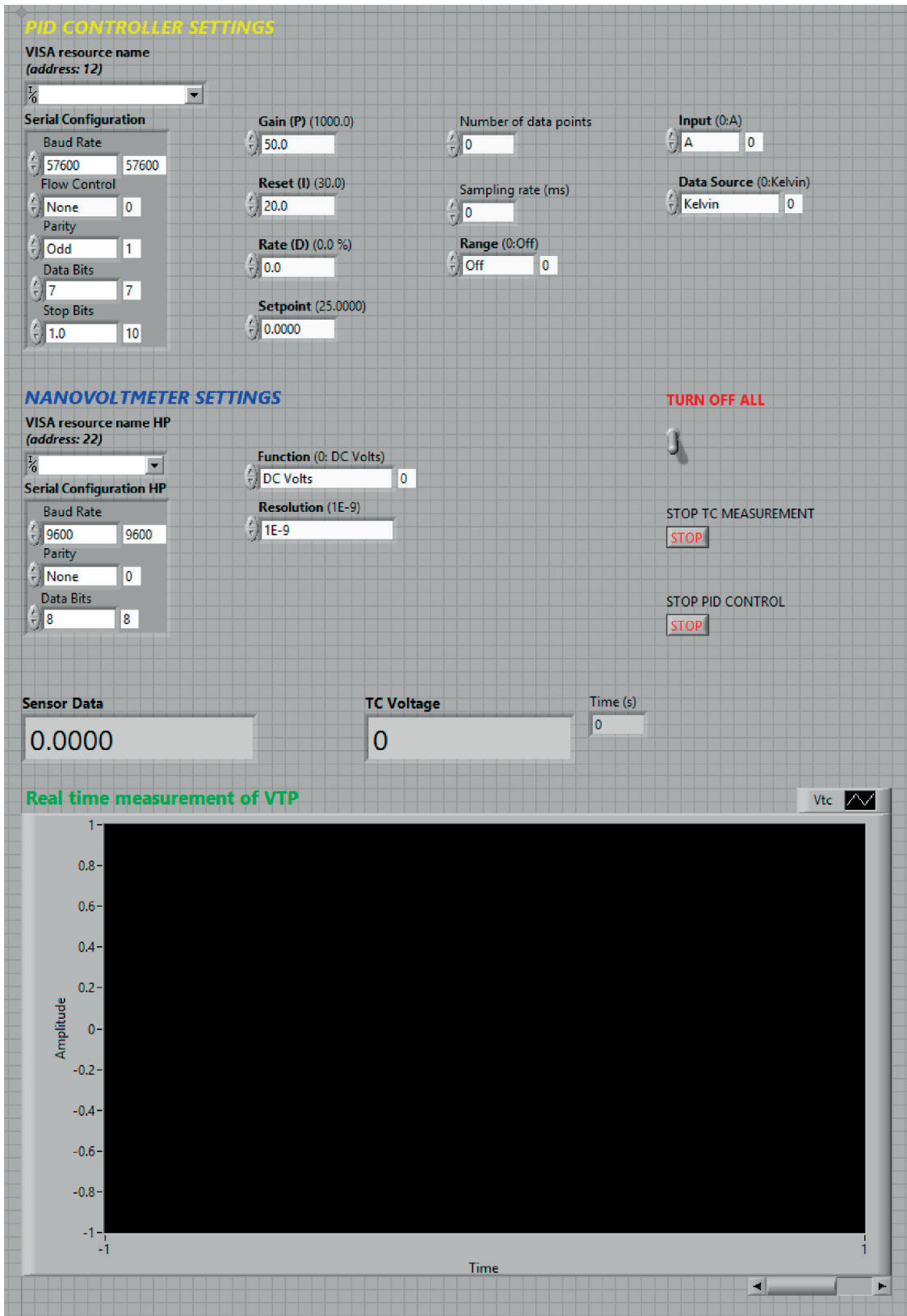


Figure 68 Screenshot of the nanocalorimetric interface.

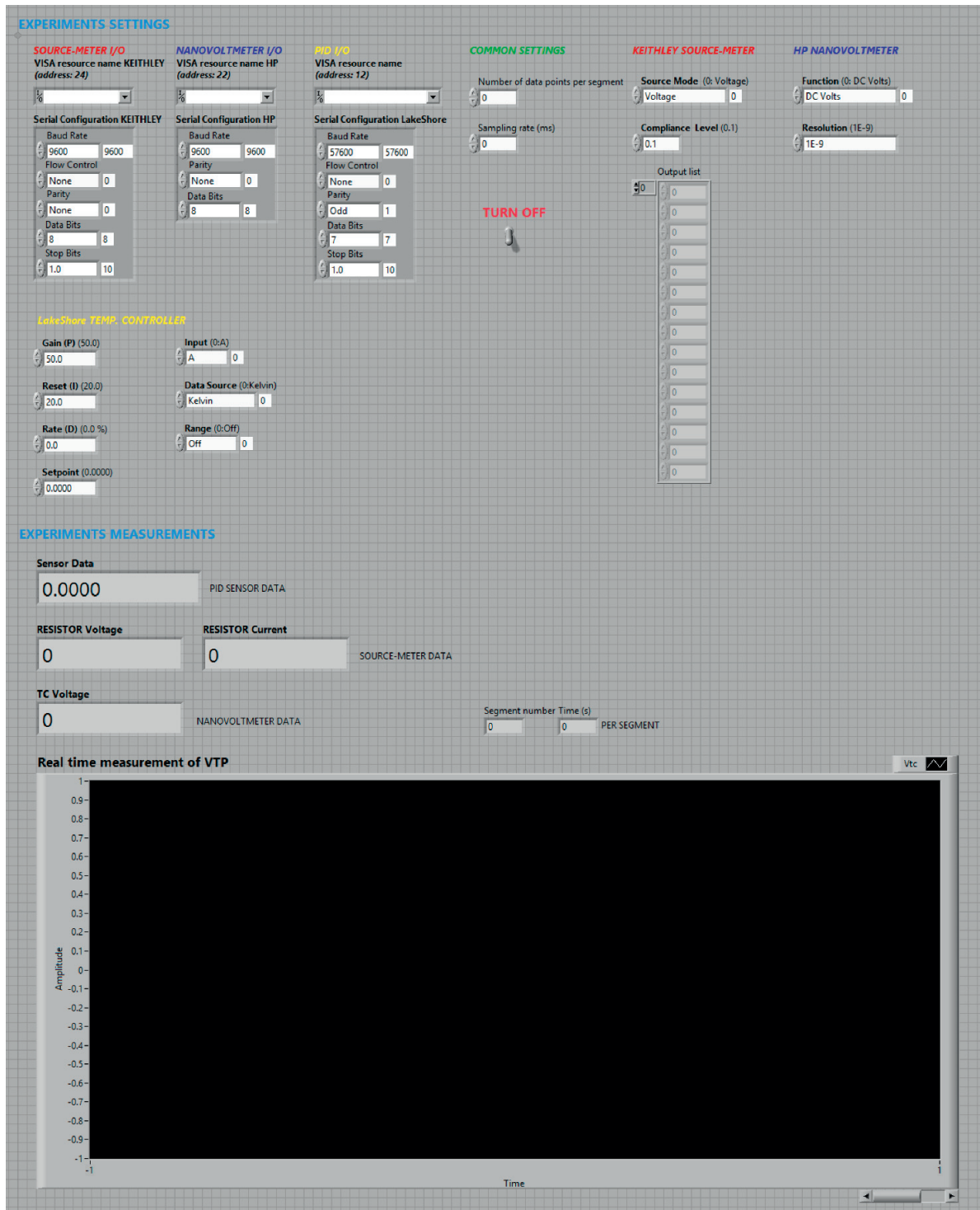


Figure 69 Screenshot of the calibration interface.

References

- [1] D. L. Nelson and M. M. Cox, *Lehninger Principles of Biochemistry*, 6th edition edition. New York: W. H. Freeman, 2013.
- [2] V. Rottiers and A. M. Näär, "MicroRNAs in Metabolism and Metabolic Disorders," *Nat. Rev. Mol. Cell Biol.*, vol. 13, no. 4, pp. 239–250, Mar. 2012.
- [3] S. R. Pieczenik and J. Neustadt, "Mitochondrial dysfunction and molecular pathways of disease," *Exp. Mol. Pathol.*, vol. 83, no. 1, pp. 84–92, Aug. 2007.
- [4] M. T. Lin and M. F. Beal, "Mitochondrial dysfunction and oxidative stress in neurodegenerative diseases," *Nature*, vol. 443, no. 7113, pp. 787–795, Oct. 2006.
- [5] J. B. Chaires, "Calorimetry and Thermodynamics in Drug Design," *Annu. Rev. Biophys.*, vol. 37, no. 1, pp. 135–151, 2008.
- [6] A. E. Beezer, "An outline of new calculation methods for the determination of both thermodynamic and kinetic parameters from isothermal heat conduction microcalorimetry," *Thermochim. Acta*, vol. 380, no. 2, pp. 205–208, Dec. 2001.
- [7] M. L. Bianconi, "Calorimetry of enzyme-catalyzed reactions," *Biophys. Chem.*, vol. 126, no. 1–3, pp. 59–64, Mar. 2007.
- [8] M. I. Recht, F. E. Torres, D. D. Bruyker, A. G. Bell, M. Klumpp, and R. H. Bruce, "Measurement of enzyme kinetics and inhibitor constants using enthalpy arrays," *Anal. Biochem.*, vol. 388, no. 2, pp. 204–212, May 2009.
- [9] A. E. Beezer, *Biological microcalorimetry*. London: Academic Press Inc. Ltd, 1980.
- [10] I. Wadsö, "Bio-calorimetry," *Trends Biotechnol.*, vol. 4, no. 2, pp. 45–51, Feb. 1986.
- [11] O. Braissant, D. Wirz, B. Göpfert, and A. U. Daniels, "Use of isothermal microcalorimetry to monitor microbial activities," *FEMS Microbiol. Lett.*, vol. 303, no. 1, pp. 1–8, 2010.
- [12] O. Braissant, D. Wirz, B. Göpfert, and A. U. Daniels, "Biomedical Use of Isothermal Microcalorimeters," *Sensors*, vol. 10, no. 10, pp. 9369–9383, Oct. 2010.
- [13] N. C. Garbett and J. B. Chaires, "Thermodynamic Studies for Drug Design and Screening," *Expert Opin. Drug Discov.*, vol. 7, no. 4, pp. 299–314, Apr. 2012.
- [14] T. Maskow, T. Schubert, A. Wolf, F. Buchholz, L. Regestein, J. Buechs, F. Mertens, H. Harms, and J. Lerchner, "Potentials and limitations of miniaturized calorimeters for bioprocess monitoring," *Appl. Microbiol. Biotechnol.*, vol. 92, no. 1, pp. 55–66, Oct. 2011.

- [15] J. Lerchner, A. Wolf, H.-J. Schneider, F. Mertens, E. Kessler, V. Baier, A. Funfak, M. Nietzsche, and M. Krügel, "Nano-calorimetry of small-sized biological samples," *Thermochim. Acta*, vol. 477, no. 1–2, pp. 48–53, Oct. 2008.
- [16] M. R. Villarreal, "File:Animal mitochondrion diagram en (edit).svg," *Wikipedia Commons*. [Online]. Available: [https://commons.wikimedia.org/wiki/File:Animal_mitochondrion_diagram_en_\(edit\).svg](https://commons.wikimedia.org/wiki/File:Animal_mitochondrion_diagram_en_(edit).svg). [Accessed: 10-Jan-2016].
- [17] J. M. Berg, J. L. Tymoczko, and L. Stryer, *Biochemistry: International Edition*, International, of 6th revised. New York: W.H. Freeman & Co Ltd, 2006.
- [18] B. Alberts, A. Johnson, J. Lewis, M. Raff, K. Roberts, and P. Walter, *Molecular Biology of the Cell*, 4th ed. Garland Science, 2002.
- [19] S. A. Detmer and D. C. Chan, "Functions and dysfunctions of mitochondrial dynamics," *Nat. Rev. Mol. Cell Biol.*, vol. 8, no. 11, pp. 870–879, Nov. 2007.
- [20] B. Westermann, "Bioenergetic role of mitochondrial fusion and fission," *Biochim. Biophys. Acta BBA - Bioenerg.*, vol. 1817, no. 10, pp. 1833–1838, Oct. 2012.
- [21] P. Mitchell, "Chemiosmotic coupling in energy transduction: A logical development of biochemical knowledge," *J. Bioenerg.*, vol. 3, no. 1–2, pp. 5–24, May 1972.
- [22] P. Mitchell, "Vectorial Chemistry and the Molecular Mechanics of Chemiosmotic Coupling: Power Transmission by Proticity. The Ninth CIBA Medal Lecture," *Biochem. Soc. Trans.*, vol. 4, no. 3, pp. 399–430, 1976.
- [23] B. M. Spiegelman and J. S. Flier, "Obesity and the Regulation of Energy Balance," *Cell*, vol. 104, no. 4, pp. 531–543, Feb. 2001.
- [24] D. Ricquier, "Respiration uncoupling and metabolism in the control of energy expenditure," *Proc. Nutr. Soc.*, vol. 64, no. 01, pp. 47–52, Feb. 2005.
- [25] S. Rousset, M.-C. Alves-Guerra, J. Mozo, B. Miroux, A.-M. Cassard-Doulier, F. Bouillaud, and D. Ricquier, "The Biology of Mitochondrial Uncoupling Proteins," *Diabetes*, vol. 53, no. suppl 1, pp. S130–S135, Feb. 2004.
- [26] M. Jastroch, A. S. Divakaruni, S. Mookerjee, J. R. Treberg, and M. D. Brand, "Mitochondrial proton and electron leaks," *Essays Biochem.*, vol. 47, pp. 53–67, 2010.
- [27] D. G. Nicholls and S. J. Ferguson, *Bioenergetics, Fourth Edition*, 4 edition. Amsterdam: Academic Press, 2013.
- [28] G. B. Pinchot, "The Mechanism of Uncoupling of Oxidative Phosphorylation by 2,4-Dinitrophenol," *J. Biol. Chem.*, vol. 242, no. 20, pp. 4577–4583, Oct. 1967.

- [29] R. Benz and S. McLaughlin, "The molecular mechanism of action of the proton ionophore FCCP (carbonylcyanide p-trifluoromethoxyphenylhydrazone)," *Biophys. J.*, vol. 41, no. 3, pp. 381–398, Mar. 1983.
- [30] E. Colman, "Dinitrophenol and obesity: An early twentieth-century regulatory dilemma," *Regul. Toxicol. Pharmacol.*, vol. 48, no. 2, pp. 115–117, Jul. 2007.
- [31] C. M. L. Burnett and J. L. Grobe, "Dietary effects on resting metabolic rate in C57BL/6 mice are differentially detected by indirect (O₂/CO₂ respirometry) and direct calorimetry," *Mol. Metab.*, vol. 3, no. 4, pp. 460–464, Jul. 2014.
- [32] J. Marín-García, *Mitochondria and Their Role in Cardiovascular Disease*. Boston, MA: Springer US, 2013.
- [33] Seahorse Bioscience, "Seahorse XFp Extracellular Flux Analyzer," *Seahorse Bioscience - Making Cell Metabolism Even Easier*. [Online]. Available: <http://www.seahorsebio.com/products/instruments/xfp.php>. [Accessed: 01-Jan-2016].
- [34] S. M. Sarge, G. W. H. Höhne, and W. Hemminger, Eds., "Calorimeters," in *Calorimetry*, Wiley-VCH Verlag GmbH & Co. KGaA, 2014, pp. 125–212.
- [35] R. G. da Silva and A. S. Campos Maia, *Principles of Animal Biometeorology*, vol. 2. Springer, 2013.
- [36] J. Wu, P. Cohen, and B. M. Spiegelman, "Adaptive thermogenesis in adipocytes: Is beige the new brown?," *Genes Dev.*, vol. 27, no. 3, pp. 234–250, Feb. 2013.
- [37] M. E. Symonds, Ed., *Adipose Tissue Biology*. New York, NY: Springer New York, 2012.
- [38] A. Park, W. K. Kim, and K.-H. Bae, "Distinction of white, beige and brown adipocytes derived from mesenchymal stem cells," *World J. Stem Cells*, vol. 6, no. 1, pp. 33–42, Jan. 2014.
- [39] M. Saito, Y. Okamatsu-Ogura, M. Matsushita, K. Watanabe, T. Yoneshiro, J. Nio-Kobayashi, T. Iwanaga, M. Miyagawa, T. Kameya, K. Nakada, Y. Kawai, and M. Tsujisaki, "High Incidence of Metabolically Active Brown Adipose Tissue in Healthy Adult Humans Effects of Cold Exposure and Adiposity," *Diabetes*, vol. 58, no. 7, pp. 1526–1531, Jul. 2009.
- [40] M. J. Vosselman, W. D. van Marken Lichtenbelt, and P. Schrauwen, "Energy dissipation in brown adipose tissue: From mice to men," *Mol. Cell. Endocrinol.*, vol. 379, no. 1–2, pp. 43–50, Oct. 2013.
- [41] J. E. Walker, "ATP Synthesis by Rotary Catalysis (Nobel lecture)," *Angew. Chem. Int. Ed.*, vol. 37, no. 17, pp. 2308–2319, Sep. 1998.
- [42] J. Nedergaard and B. Cannon, "How brown is brown fat? It depends where you look," *Nat. Med.*, vol. 19, no. 5, pp. 540–541, May 2013.

- [43] C. Cohade, M. Osman, H. K. Pannu, and R. L. Wahl, "Uptake in Supraclavicular Area Fat ('USA-Fat'): Description on 18F-FDG PET/CT," *J. Nucl. Med.*, vol. 44, no. 2, pp. 170–176, Feb. 2003.
- [44] J. Nedergaard, T. Bengtsson, and B. Cannon, "Unexpected evidence for active brown adipose tissue in adult humans," *Am. J. Physiol. - Endocrinol. Metab.*, vol. 293, no. 2, pp. E444–E452, Aug. 2007.
- [45] M. Saito, "Brown adipose tissue as a therapeutic target for human obesity," *Obes. Res. Clin. Pract.*, vol. 7, no. 6, pp. e432–e438, Dec. 2013.
- [46] J. Nedergaard and B. Cannon, "The Changed Metabolic World with Human Brown Adipose Tissue: Therapeutic Visions," *Cell Metab.*, vol. 11, no. 4, pp. 268–272, Apr. 2010.
- [47] S. P. Vickers, H. C. Jackson, and S. C. Cheetham, "The utility of animal models to evaluate novel anti-obesity agents," *Br. J. Pharmacol.*, vol. 164, no. 4, pp. 1248–1262, Oct. 2011.
- [48] K. C. Bicego, R. C. H. Barros, and L. G. S. Branco, "Physiology of temperature regulation: Comparative aspects," *Comp. Biochem. Physiol. A. Mol. Integr. Physiol.*, vol. 147, no. 3, pp. 616–639, Jul. 2007.
- [49] C. J. Gordon, "Thermal physiology of laboratory mice: Defining thermoneutrality," *J. Therm. Biol.*, vol. 37, no. 8, pp. 654–685, Dec. 2012.
- [50] IUPS Thermal Commission, "Glossary of terms for thermal physiology," *J. Therm. Biol.*, vol. 28, no. 1, pp. 75–106, Jan. 2003.
- [51] J. A. Levine, "Measurement of energy expenditure," *Public Health Nutr.*, vol. 8, no. 7a, pp. 1123–1132, Oct. 2005.
- [52] J. B. de V. Weir, "New methods for calculating metabolic rate with special reference to protein metabolism," *J. Physiol.*, vol. 109, no. 1–2, pp. 1–9, Aug. 1949.
- [53] M. H. Tschöp, J. R. Speakman, J. R. S. Arch, J. Auwerx, J. C. Brüning, L. Chan, R. H. Eckel, R. V. Farese Jr, J. E. Galgani, C. Hambly, M. A. Herman, T. L. Horvath, B. B. Kahn, S. C. Kozma, E. Maratos-Flier, T. D. Müller, H. Münzberg, P. T. Pfluger, L. Plum, M. L. Reitman, K. Rahmouni, G. I. Shulman, G. Thomas, C. R. Kahn, and E. Ravussin, "A guide to analysis of mouse energy metabolism," *Nat. Methods*, vol. 9, no. 1, pp. 57–63, Jan. 2012.
- [54] C. M. L. Burnett and J. L. Grobe, "Direct calorimetry identifies deficiencies in respirometry for the determination of resting metabolic rate in C57Bl/6 and FVB mice," *Am. J. Physiol. Endocrinol. Metab.*, vol. 305, no. 7, pp. E916–924, Oct. 2013.
- [55] J. R. Speakman, "Measuring energy metabolism in the mouse – theoretical, practical, and analytical considerations," *Integr. Physiol.*, vol. 4, p. 34, 2013.

- [56] P. Lomax, "Measurement of 'Core' Temperature in the Rat," *Nature*, vol. 210, no. 5038, pp. 854–855, May 1966.
- [57] D. D. Bae, P. L. Brown, and E. A. Kiyatkin, "Procedure of rectal temperature measurement affects brain, muscle, skin and body temperatures and modulates the effects of intravenous cocaine," *Brain Res.*, vol. 1154, pp. 61–70, Jun. 2007.
- [58] S. Poole and J. D. Stephenson, "Core temperature: Some shortcomings of rectal temperature measurements," *Physiol. Behav.*, vol. 18, no. 2, pp. 203–205, Feb. 1977.
- [59] T. J. J. Zethof, J. A. M. Van Der Heyden, J. T. B. M. Tolboom, and B. Olivier, "Stress-induced hyperthermia in mice: A methodological study," *Physiol. Behav.*, vol. 55, no. 1, pp. 109–115, Jan. 1994.
- [60] M. Sanchez-Alavez, S. Alboni, and B. Conti, "Sex- and age-specific differences in core body temperature of C57Bl/6 mice," *Age Dordr. Neth.*, vol. 33, no. 1, pp. 89–99, Mar. 2011.
- [61] C. J. Gordon, "Quantifying the instability of core temperature in rodents," *J. Therm. Biol.*, vol. 34, no. 5, pp. 213–219, Jul. 2009.
- [62] B. Conti, M. Sanchez-Alavez, R. Winsky-Sommerer, M. C. Morale, J. Lucero, S. Brownell, V. Fabre, S. Huitron-Resendiz, S. Henriksen, E. P. Zorrilla, L. de Lecea, and T. Bartfai, "Transgenic Mice with a Reduced Core Body Temperature Have an Increased Life Span," *Science*, vol. 314, no. 5800, pp. 825–828, Nov. 2006.
- [63] S. Gatti, J. Beck, G. Fantuzzi, T. Bartfai, and C. A. Dinarello, "Effect of interleukin-18 on mouse core body temperature," *Am. J. Physiol. - Regul. Integr. Comp. Physiol.*, vol. 282, no. 3, pp. R702–R709, Mar. 2002.
- [64] E. M. Knight, T. M. Brown, S. Gümüşgöz, J. C. M. Smith, E. J. Waters, S. M. Allan, and C. B. Lawrence, "Age-related changes in core body temperature and activity in triple-transgenic Alzheimer's disease (3xTgAD) mice," *Dis. Model. Mech.*, vol. 6, no. 1, pp. 160–170, Jan. 2013.
- [65] S. DeBow and F. Colbourne, "Brain temperature measurement and regulation in awake and freely moving rodents," *Methods*, vol. 30, no. 2, pp. 167–171, Jun. 2003.
- [66] BMDS, "Transponders," *Bio Medic Data Systems: Lab Animal Identification*. [Online]. Available: <http://www.bmds.com/products/transponders/ipptt-300>. [Accessed: 10-Jan-2016].
- [67] J. D. Crane, E. P. Mottillo, T. H. Farncombe, K. M. Morrison, and G. R. Steinberg, "A standardized infrared imaging technique that specifically detects UCP1-mediated thermogenesis in vivo," *Mol. Metab.*, vol. 3, no. 4, pp. 490–494, Jul. 2014.
- [68] M. L. Gantner, B. C. Hazen, J. Conkright, and A. Kralli, "GADD45 γ regulates the thermogenic capacity of brown adipose tissue," *Proc. Natl. Acad. Sci. U. S. A.*, vol. 111, no. 32, pp. 11870–11875, Aug. 2014.

- [69] M. J. Harms, J. Ishibashi, W. Wang, H.-W. Lim, S. Goyama, T. Sato, M. Kurokawa, K.-J. Won, and P. Seale, "Prdm16 Is Required for the Maintenance of Brown Adipocyte Identity and Function in Adult Mice," *Cell Metab.*, vol. 19, no. 4, pp. 593–604, Apr. 2014.
- [70] D. M. Lateef, G. Abreu-Vieira, C. Xiao, and M. L. Reitman, "Regulation of body temperature and brown adipose tissue thermogenesis by bombesin receptor subtype-3," *Am J Physiol Endocrinol Metab*, no. 306, pp. E681–E687, 2014.
- [71] N. Kataoka, H. Hioki, T. Kaneko, and K. Nakamura, "Psychological Stress Activates a Dorsomedial Hypothalamus-Medullary Raphe Circuit Driving Brown Adipose Tissue Thermogenesis and Hyperthermia," *Cell Metab.*, vol. 20, no. 2, pp. 346–358, May 2014.
- [72] TA Instruments, "Isothermal calorimetry," *TA Instruments: Thermal Analysis & Analyzers*. [Online]. Available: <http://www.tainstruments.com/product.aspx?id=260&n=1&siteid=11>. [Accessed: 10-Jan-2016].
- [73] O. Braissant and A. "Dan. Daniels, "Closed Ampoule Isothermal Microcalorimetry for Continuous Real-Time Detection and Evaluation of Cultured Mammalian Cell Activity and Responses," in *Mammalian Cell Viability*, M. J. Stoddart, Ed. Humana Press, 2011, pp. 191–208.
- [74] A. Lavoisier and P.-S. Laplace, *Mémoire sur la Chaleur*. Paris, France: Académie des Sciences, 1780.
- [75] S. A. Thorén, J. Suurkuusk, and B. Holma, "Operation of a multichannel microcalorimetry system in the micro-submicrowatt region: some methodological aspects," *J. Biochem. Biophys. Methods*, vol. 18, no. 2, pp. 149–156, Mar. 1989.
- [76] A. W. van Herwaarden, "Overview of calorimeter chips for various applications," *Thermochim. Acta*, vol. 432, no. 2, pp. 192–201, Jul. 2005.
- [77] A. Lavoisier, *Traité de Chimie*. Paris, France: Académie des Sciences, 1801.
- [78] T. H. Lodwig and W. A. Smeaton, "The ice calorimeter of Lavoisier and Laplace and some of its critics," *Ann. Sci.*, vol. 31, no. 1, pp. 1–18, Jan. 1974.
- [79] A. Tari, *The Specific Heat of Matter at Low Temperatures*. World Scientific, 2003.
- [80] M. E. Brown, *Handbook of Thermal Analysis and Calorimetry: Principles and Practice*. Elsevier, 1998.
- [81] Laboratory of Thermophysical Properties, "Caloric properties," *Laboratory of Thermophysical Properties*. [Online]. Available: <http://www.ltp-oldenburg.de/index.php/caloric-properties.html>. [Accessed: 10-Feb-2016].
- [82] I. Wadsö, "Isothermal microcalorimetry in applied biology," *Thermochim. Acta*, vol. 394, no. 1–2, pp. 305–311, Oct. 2002.

- [83] Setaram, "3D CALVET CALORIMETRY," *SETARAM Instrumentation - Calorimetry & Thermal Analysis*. [Online]. Available: http://www.setaram.com/product_categories/calorimetry/calorimetry-calorimetry/. [Accessed: 10-Jan-2016].
- [84] THT, "Micro Reaction Calorimeter," *Thermal Hazard Technology - Home*. [Online]. Available: <http://www.thermalhazardtechnology.com/products/micro+reaction+calorimeter>. [Accessed: 10-Jan-2016].
- [85] E. A. Johannessen, J. M. R. Weaver, P. H. Cobbold, and J. M. Cooper, "Heat conduction nanocalorimeter for pl-scale single cell measurements," *Appl. Phys. Lett.*, vol. 80, no. 11, pp. 2029–2031, Mar. 2002.
- [86] W. Lee, W. Fon, B. W. Axelrod, and M. L. Roukes, "High-sensitivity microfluidic calorimeters for biological and chemical applications," *Proc. Natl. Acad. Sci. U. S. A.*, vol. 106, pp. 15225–30, 2009.
- [87] J. Xu, R. Reiserer, J. Tellinghuisen, J. P. Wikswo, and F. J. Baudenbacher, "A Microfabricated Nanocalorimeter: Design, Characterization, and Chemical Calibration," *Anal. Chem.*, vol. 80, no. 8, pp. 2728–2733, Apr. 2008.
- [88] J. Lerchner, A. Wolf, G. Wolf, V. Baier, E. Kessler, M. Nietzsche, and M. Krügel, "A new microfluid chip calorimeter for biochemical applications," *Thermochim. Acta*, vol. 445, no. 2, pp. 144–150, Jun. 2006.
- [89] W. Lee, Lee, and Koh, "Development and applications of chip calorimeters as novel biosensors," *Nanobiosensors Dis. Diagn.*, vol. 2012, pp. 17–29, Apr. 2012.
- [90] L. M. Ahmad, B. Towe, A. Wolf, F. Mertens, and J. Lerchner, "Binding event measurement using a chip calorimeter coupled to magnetic beads," *Sens. Actuators B Chem.*, vol. 145, no. 1, pp. 239–245, Mar. 2010.
- [91] I. Wadsö and L. Wadsö, "Systematic errors in isothermal micro- and nanocalorimetry," *J. Therm. Anal. Calorim.*, vol. 82, no. 3, pp. 553–558, Nov. 2005.
- [92] M. Monti, "Application of microcalorimetry to the study of living cells in the medical field," *Thermochim. Acta*, vol. 172, pp. 53–60, Dec. 1990.
- [93] A. M. James, *Thermal and Energetic Studies of Cellular Biological Systems*. Bristol: Wright, 1987.
- [94] M. Monti and I. Wadsö, "Microcalorimetric Measurements of Heat Production in Human Erythrocytes I. Normal Subjects and Anemic Patients," *Scand. J. Clin. Lab. Invest.*, vol. 32, no. 1, pp. 47–54, Jan. 1973.
- [95] M. Monti, L. Brandt, J. Ikomi-Kumm, H. Olsson, and I. Wadö, "Metabolic Activity of Lymphoma Cells and Clinical Course in Non-Hodgkin Lymphoma (NHL)," *Scand. J. Haematol.*, vol. 27, no. 5, pp. 305–310, Nov. 1981.

- [96] R. B. Kemp, "Calorimetric studies of heat flux in animal cells," *Thermochim. Acta*, vol. 193, pp. 253–267, Dec. 1991.
- [97] R. B. Kemp, "Developments in cellular microcalorimetry with particular emphasis on the valuable role of the energy (enthalpy) balance method," *Thermochim. Acta*, vol. 219, pp. 17–41, May 1993.
- [98] G. B. West, W. H. Woodruff, and J. H. Brown, "Allometric scaling of metabolic rate from molecules and mitochondria to cells and mammals," *Proc. Natl. Acad. Sci. U. S. A.*, vol. 99, no. Suppl 1, pp. 2473–2478, Feb. 2002.
- [99] C. Murigande, S. Regenass, D. Wirz, A. U. Daniels, and A. Tyndall, "A Comparison Between (3H)-thymidine Incorporation and Isothermal Microcalorimetry for the Assessment of Antigen-induced Lymphocyte Proliferation," *Immunol. Invest.*, vol. 38, no. 1, pp. 67–75, Jan. 2009.
- [100] Z. Heng, Z. Congyi, W. Cunxin, W. Jibin, G. Chaojiang, L. Jie, and L. Yuwen, "Microcalorimetric study of virus infection; The effects of hyperthermia and 1b recombinant homo interferon on the infection process of BHK-21 cells by foot and mouth disease virus," *J. Therm. Anal. Calorim.*, vol. 79, no. 1, pp. 45–50, Jan. 2005.
- [101] W. Liu, F. Chaspoul, D. B. Lefranc, L. Decome, and P. Gallice, "Microcalorimetry as a tool for Cr(VI) toxicity evaluation of human dermal fibroblasts," *J. Therm. Anal. Calorim.*, vol. 89, no. 1, pp. 21–24, Jul. 2007.
- [102] A. Doostmohammadi, A. Monshi, M. H. Fathi, S. Karbasi, O. Braissant, and A. U. Daniels, "Direct cytotoxicity evaluation of 63S bioactive glass and bone-derived hydroxyapatite particles using yeast model and human chondrocyte cells by microcalorimetry," *J. Mater. Sci. Mater. Med.*, vol. 22, no. 10, pp. 2293–2300, Jul. 2011.
- [103] J. Monod, "The Growth of Bacterial Cultures," *Annu. Rev. Microbiol.*, vol. 3, no. 1, pp. 371–394, 1949.
- [104] O. Braissant, A. Bachmann, and G. Bonkat, "Microcalorimetric assays for measuring cell growth and metabolic activity: Methodology and applications," *Methods*, vol. 76, pp. 27–34, Apr. 2015.
- [105] A. Trampuz, S. Salzmann, J. Antheaume, and A. U. Daniels, "Microcalorimetry: a novel method for detection of microbial contamination in platelet products," *Transfusion (Paris)*, vol. 47, no. 9, pp. 1643–1650, Sep. 2007.
- [106] U. von Ah, D. Wirz, and A. Daniels, "Isothermal micro calorimetry - a new method for MIC determinations: results for 12 antibiotics and reference strains of *E. coli* and *S. aureus*," *BMC Microbiol.*, vol. 9, p. 106, 2009.

- [107] U. von Ah, D. Wirz, and A. U. Daniels, "Rapid Differentiation of Methicillin-Susceptible *Staphylococcus aureus* from Methicillin-Resistant *S. aureus* and MIC Determinations by Isothermal Microcalorimetry," *J. Clin. Microbiol.*, vol. 46, no. 6, pp. 2083–2087, Jun. 2008.
- [108] B. P. Braeckman, K. Houthoofd, A. De Vreese, and J. R. Vanfleteren, "Assaying metabolic activity in ageing *Caenorhabditis elegans*," *Mech. Ageing Dev.*, vol. 123, no. 2–3, pp. 105–119, Jan. 2002.
- [109] K. Houthoofd, B. P. Braeckman, I. Lenaerts, K. Brys, A. De Vreese, S. Van Eygen, and J. R. Vanfleteren, "Ageing is reversed, and metabolism is reset to young levels in recovering dauer larvae of *C. elegans*," *Exp. Gerontol.*, vol. 37, no. 8–9, pp. 1015–1021, Aug. 2002.
- [110] T. Manneck, O. Braissant, Y. Haggemüller, and J. Keiser, "Isothermal Microcalorimetry To Study Drugs against *Schistosoma mansoni*," *J. Clin. Microbiol.*, vol. 49, no. 4, pp. 1217–1225, Apr. 2011.
- [111] X.-M. RONG, Q.-Y. HUANG, D.-H. JIANG, P. CAI, and W. LIANG, "Isothermal Microcalorimetry: A Review of Applications in Soil and Environmental Sciences," *Pedosphere*, vol. 17, no. 2, pp. 137–145, Apr. 2007.
- [112] L. Wadsö and F. Gómez Galindo, "Isothermal calorimetry for biological applications in food science and technology," *Food Control*, vol. 20, no. 10, pp. 956–961, Oct. 2009.
- [113] W. Lee, W. Fon, B. W. Axelrod, and M. L. Roukes, "High-sensitivity microfluidic calorimeters for biological and chemical applications," *Proc. Natl. Acad. Sci. U. S. A.*, vol. 106, pp. 15225–30, Aug. 2009.
- [114] J. Lerchner, A. Wolf, H.-J. Schneider, F. Mertens, E. Kessler, V. Baier, A. Funfak, M. Nietzsche, and M. Krügel, "Nano-calorimetry of small-sized biological samples," *Thermochim. Acta*, vol. 477, no. 1–2, pp. 48–53, Oct. 2008.
- [115] F. Yi and D. A. La Van, "Nanoscale thermal analysis for nanomedicine by nanocalorimetry," *Wiley Interdiscip. Rev. Nanomed. Nanobiotechnol.*, vol. 4, no. 1, pp. 31–41, 2012.
- [116] J. Lerchner, A. Wolf, G. Wolf, V. Baier, E. Kessler, M. Nietzsche, and M. Krügel, "A new microfluid chip calorimeter for biochemical applications," *Thermochim. Acta*, vol. 445, no. 2, pp. 144–150, Jun. 2006.
- [117] Y. Zhang and S. Tadigadapa, "Calorimetric biosensors with integrated microfluidic channels," *Biosens. Bioelectron.*, vol. 19, no. 12, pp. 1733–1743, Jul. 2004.
- [118] M. I. Recht, D. D. Bruyker, A. G. Bell, M. V. Wolkin, E. Peeters, G. B. Anderson, A. R. Kolatkar, M. W. Bern, P. Kuhn, R. H. Bruce, and F. E. Torres, "Enthalpy array analysis of enzymatic and binding reactions," *Anal. Biochem.*, vol. 377, no. 1, pp. 33–39, Jun. 2008.

- [119] M. I. Recht, F. E. Torres, D. D. Bruyker, A. G. Bell, M. Klumpp, and R. H. Bruce, "Measurement of enzyme kinetics and inhibitor constants using enthalpy arrays," *Anal. Biochem.*, vol. 388, no. 2, pp. 204–212, May 2009.
- [120] F. Mariana, F. Buchholz, J. Lerchner, T. R. Neu, H. Harms, and T. Maskow, "Chip-calorimetric monitoring of biofilm eradication with antibiotics provides mechanistic information," *Int. J. Med. Microbiol.*, vol. 303, no. 3, pp. 158–165, Apr. 2013.
- [121] E. A. Johannessen, J. M. R. Weaver, L. Bourova, P. Svoboda, P. H. Cobbold, and J. M. Cooper, "Micromachined Nanocalorimetric Sensor for Ultra-Low-Volume Cell-Based Assays," *Anal. Chem.*, vol. 74, no. 9, pp. 2190–2197, May 2002.
- [122] A. W. van Herwaarden, "Overview of calorimeter chips for various applications," *Thermochem. Acta*, vol. 432, no. 2, pp. 192–201, Jul. 2005.
- [123] V. Baier, R. Födisch, A. Ihring, E. Kessler, J. Lerchner, G. Wolf, J. M. Köhler, M. Nietzsche, and M. Krügel, "Highly sensitive thermopile heat power sensor for micro-fluid calorimetry of biochemical processes," *Sens. Actuators Phys.*, vol. 123–124, pp. 354–359, Sep. 2005.
- [124] S.-K. Nam, J.-K. Kim, S.-C. Cho, and S.-K. Lee, "Design and Characterization of a High Resolution Microfluidic Heat Flux Sensor with Thermal Modulation," *Sensors*, vol. 10, no. 7, pp. 6594–6611, Jul. 2010.
- [125] L. Wang, D. M. Sipe, Y. Xu, and Q. Lin, "A MEMS Thermal Biosensor for Metabolic Monitoring Applications," *J. Microelectromechanical Syst.*, vol. 17, no. 2, pp. 318–327, 2008.
- [126] F. E. Torres, P. Kuhn, D. D. Bruyker, A. G. Bell, M. V. Wolkin, E. Peeters, J. R. Williamson, G. B. Anderson, G. P. Schmitz, M. I. Recht, S. Schweizer, L. G. Scott, J. H. Ho, S. A. Elrod, P. G. Schultz, R. A. Lerner, and R. H. Bruce, "Enthalpy arrays," *Proc. Natl. Acad. Sci. U. S. A.*, vol. 101, no. 26, pp. 9517–9522, Jun. 2004.
- [127] T. Maskow, T. Schubert, A. Wolf, F. Buchholz, L. Regestein, J. Buechs, F. Mertens, H. Harms, and J. Lerchner, "Potentials and limitations of miniaturized calorimeters for bioprocess monitoring," *Appl. Microbiol. Biotechnol.*, vol. 92, no. 1, pp. 55–66, Oct. 2011.
- [128] T. J. Seebeck, "Magnetische Polarisierung der Metalle und Erze durch Temperatur-Differenz," in *Abhandlungen der Königlich Preussischen Akademie der Wissenschaften*, Berlin: Deutsche Akademie der Wissenschaften zu Berlin, 1825, pp. 265–373.
- [129] T. J. Seebeck, "Ueber die Magnetische Polarisierung der Metalle und Erze durch Temperatur-Differenz," in *Annalen der Physik und Chemie, Volume 6*, Berlin: Barth J. A., 1826, pp. 1–20, 133–160, 253–286.
- [130] J. V. Nicholas and D. R. White, *Traceable Temperatures: An Introduction to Temperature Measurement and Calibration*, 2 edition. Chichester: John Wiley & Sons, Ltd, 2001.

- [131] J. S. Steinhart and S. R. Hart, "Calibration curves for thermistors," *Deep Sea Res. Oceanogr. Abstr.*, vol. 15, no. 4, pp. 497–503, Aug. 1968.
- [132] B. Lubbers and F. Baudenbacher, "Isothermal Titration Calorimetry in Nanoliter Droplets with Subsecond Time Constants," *Anal. Chem.*, vol. 83, no. 20, pp. 7955–7961, Oct. 2011.
- [133] K. Verhaegen, K. Baert, J. Simaels, and W. Van Driessche, "A high-throughput silicon microphysiometer," *Sens. Actuators Phys.*, vol. 82, no. 1–3, pp. 186–190, May 2000.
- [134] J. Xu, R. Reiserer, J. Tellinghuisen, J. P. Wikswo, and F. J. Baudenbacher, "A Microfabricated Nanocalorimeter: Design, Characterization, and Chemical Calibration," *Anal. Chem.*, vol. 80, no. 8, pp. 2728–2733, Apr. 2008.
- [135] E. A. Johannessen, J. M. R. Weaver, P. H. Cobbold, and J. M. Cooper, "A Suspended Membrane Nanocalorimeter for Ultralow Volume Bioanalysis," *IEEE Trans. NANOBIOSCIENCE*, vol. 1, no. 1, pp. 29–36, Mar. 2002.
- [136] L. M. Ahmad, B. Towe, A. Wolf, F. Mertens, and J. Lerchner, "Binding event measurement using a chip calorimeter coupled to magnetic beads," *Sens. Actuators B Chem.*, vol. 145, no. 1, pp. 239–245, Mar. 2010.
- [137] B. S. Kwak, B. S. Kim, H. H. Cho, J. S. Park, and H. I. Jung, "Dual thermopile integrated microfluidic calorimeter for biochemical thermodynamics," *Microfluid. Nanofluidics*, vol. 5, no. 2, pp. 255–262, Aug. 2008.
- [138] B. Wang and Q. Lin, "Temperature-modulated differential scanning calorimetry in a MEMS device," *Sens. Actuators B Chem.*, vol. 180, pp. 60–65, Apr. 2013.
- [139] L. Wang, B. Wang, and Q. Lin, "Demonstration of MEMS-based differential scanning calorimetry for determining thermodynamic properties of biomolecules," *Sens. Actuators B Chem.*, vol. 134, no. 2, pp. 953–958, Sep. 2008.
- [140] J. Lerchner, A. Wolf, G. Wolf, and I. Fernandez, "Chip calorimeters for the investigation of liquid phase reactions: Design rules," *Thermochim. Acta*, vol. 446, no. 1–2, pp. 168–175, Jul. 2006.
- [141] E. A. Johannessen, J. M. R. Weaver, P. H. Cobbold, and J. M. Cooper, "Heat conduction nanocalorimeter for pl-scale single cell measurements," *Appl. Phys. Lett.*, vol. 80, no. 11, pp. 2029–2031, Mar. 2002.
- [142] B. Cannon and J. Nedergaard, "Brown Adipose Tissue: Function and Physiological Significance," *Physiol. Rev.*, vol. 84, no. 1, pp. 277–359, Jan. 2004.
- [143] T. Maskow, J. Lerchner, M. Peitzsch, H. Harms, and G. Wolf, "Chip calorimetry for the monitoring of whole cell biotransformation," *J. Biotechnol.*, vol. 122, no. 4, pp. 431–442, Apr. 2006.

- [144] F. Buchholz, J. Lerchner, F. Mariana, U. Kuhlicke, T. R. Neu, H. Harms, and T. Maskow, "Chip-calorimetry provides real time insights into the inactivation of biofilms by predatory bacteria," *Biofouling*, vol. 28, no. 3, pp. 351–362, 2012.
- [145] F. M. Morais, F. Buchholz, T. Hartmann, J. Lerchner, T. R. Neu, B. Kiesel, H. Harms, and T. Maskow, "Chip-calorimetric monitoring of biofilm eradication with bacteriophages reveals an unexpected infection-related heat profile," *J. Therm. Anal. Calorim.*, vol. 115, no. 3, pp. 2203–2210, 2014.
- [146] T. Hartmann, N. Barros, A. Wolf, C. Siewert, P. L. O. Volpe, J. Schemberg, A. Grodrian, E. Kessler, F. Hänschke, F. Mertens, and J. Lerchner, "Thermopile chip based calorimeter for the study of aggregated biological samples in segmented flow," *Sens. Actuators B Chem.*, vol. 201, pp. 460–468, Oct. 2014.
- [147] A. Wolf, T. Hartmann, M. Bertolini, J. Schemberg, A. Grodrian, K. Lemke, T. Förster, E. Kessler, F. Hänschke, F. Mertens, R. Paus, and J. Lerchner, "Toward high-throughput chip calorimetry by use of segmented-flow technology," *Thermochim. Acta*, vol. 603, pp. 172–183, Mar. 2015.
- [148] S.-I. Yoon, M.-H. Lim, S.-C. Park, J.-S. Shin, and Y.-J. Kim, "Neisseria Meningitidis Detection Based on a Microcalorimetric Biosensor With a Split-Flow Microchannel," *J. Microelectromechanical Syst.*, vol. 17, no. 3, pp. 590–598, 2008.
- [149] S.-I. Yoon, S.-C. Park, and Y.-J. Kim, "A micromachined microcalorimeter with split-flow microchannel for biochemical sensing applications," *Sens. Actuators B Chem.*, vol. 134, no. 1, pp. 158–165, Aug. 2008.
- [150] B. Davaji and C. H. Lee, "A paper-based calorimetric microfluidics platform for bio-chemical sensing," *Biosens. Bioelectron.*, vol. 59, pp. 120–126, Sep. 2014.
- [151] Xensor Integration, "Home," *Xensor Integration*. [Online]. Available: <http://www.xensor.nl/>. [Accessed: 01-Jan-2015].
- [152] A. W. van Herwaarden, P. M. Sarro, J. W. Gardner, and P. Bataillard, "Liquid and gas microcalorimeters for (bio)chemical measurements," *Sens. Actuators Phys.*, vol. 43, no. 1–3, pp. 24–30, May 1994.
- [153] T. Adrega and A. W. van Herwaarden, "Chip calorimeter for thermal characterization of biochemical solutions," *Sens. Actuators Phys.*, vol. 167, no. 2, pp. 354–358, Jun. 2011.
- [154] R. Padovani, T. Lehnert, R. Trouillon, and M. A. M. Gijs, "Nanocalorimetric platform for accurate thermochemical studies in microliter volumes," *RSC Adv.*, vol. 5, no. 118, pp. 97133–97142, 2015.

- [155] R. Padovani, T. Lehnert, and M. A. M. Gijs, "A microcalorimetric platform for studying the heat produced by chemical reactions in microlitre volumes," in *Proc. of 19th International Conference on Miniaturized Systems for Chemistry and Life Sciences (microTAS 2015)*, Gyeongju, Korea, 2015.
- [156] B. P. Braeckman, K. Houthoofd, and J. R. Vanfleteren, "Assessing metabolic activity in aging *Caenorhabditis elegans*: concepts and controversies," *Aging Cell*, vol. 1, no. 2, pp. 82–88, Dec. 2002.
- [157] P. Lönnbro and A. Schön, "The effect of temperature on metabolism in 3T3 cells and SV40-transformed 3T3 cells as measured by microcalorimetry," *Thermochim. Acta*, vol. 172, pp. 75–80, Dec. 1990.
- [158] S. M. Mcguinness, D. A. Roess, and B. G. Barisas, "Acute toxicity effects of mercury and other heavy metals on HeLa cells and human lymphocytes evaluated via microcalorimetry," *Thermochim. Acta*, vol. 172, pp. 131–145, Dec. 1990.
- [159] P. Nilsson-Ehle and G. Nordin, "Microcalorimetric studies on the total metabolic activity of fat cells," *Int. J. Obes.*, vol. 9 Suppl 1, pp. 169–172, 1985.
- [160] M. G. Nordmark, J. Laynez, A. Schön, J. Suurkuusk, and I. Wadsö, "Design and testing of a new microcalorimetric vessel for use with living cellular systems and in titration experiments," *J. Biochem. Biophys. Methods*, vol. 10, no. 3–4, pp. 187–202, Dec. 1984.
- [161] J. Nedergaard, B. Cannon, and O. Lindberg, "Microcalorimetry of isolated mammalian cells," *Nature*, vol. 267, no. 5611, pp. 518–520, Jun. 1977.
- [162] U. Reichert and B. Schaarschmidt, "Heat evolution of cultured human keratinocytes," *Experientia*, vol. 42, no. 2, pp. 173–174, Feb. 1986.
- [163] L. Nässberger, E. Jensen, M. Monti, and C. H. Florén, "Microcalorimetric investigation of metabolism in rat hepatocytes cultured on microplates and in cell suspensions," *Biochim. Biophys. Acta*, vol. 882, no. 3, pp. 353–358, Jul. 1986.
- [164] A. Loft, I. Forss, M. S. Siersbæk, S. F. Schmidt, A.-S. B. Larsen, J. G. S. Madsen, D. F. Pisani, R. Nielsen, M. M. Aagaard, A. Mathison, M. J. Neville, R. Urrutia, F. Karpe, E.-Z. Amri, and S. Mandrup, "Browning of human adipocytes requires KLF11 and reprogramming of PPAR γ superenhancers," *Genes Dev.*, vol. 29, no. 1, pp. 7–22, Jan. 2015.
- [165] A. Jais, E. Einwallner, O. Sharif, K. Gossens, T. T.-H. Lu, S. M. Soyal, D. Medgyesi, D. Neureiter, J. Paier-Pourani, K. Dalgaard, J. C. Duvigneau, J. Lindroos-Christensen, T.-C. Zapf, S. Amann, S. Saluzzo, F. Jantscher, P. Stiedl, J. Todoric, R. Martins, H. Oberkofler, S. Müller, C. Hauser-Kronberger, L. Kenner, E. Casanova, H. Sutterlüty-Fall, M. Bilban, K. Miller, A. V. Kozlov, F. Krempler, S. Knapp, C. N. Lumeng, W. Patsch, O. Wagner, J. A. Pospisilik, and H. Esterbauer, "Heme Oxygenase-1 Drives Metaflammation and Insulin Resistance in Mouse and Man," *Cell*, vol. 158, no. 1, pp. 25–40, Jul. 2014.

- [166] I. Ismailoglu, Q. Chen, M. Popowski, L. Yang, S. S. Gross, and A. H. Brivanlou, "Huntingtin protein is essential for mitochondrial metabolism, bioenergetics and structure in murine embryonic stem cells," *Dev. Biol.*, vol. 391, no. 2, pp. 230–240, Jul. 2014.
- [167] J. P. Holman, *Heat Transfer*, 10 edition. Boston: McGraw-Hill Education, 2009.
- [168] P. Bäckman, M. Bastos, D. Hallén, P. Lönnbro, and I. Wadsö, "Heat conduction calorimeters: time constants, sensitivity and fast titration experiments," *J. Biochem. Biophys. Methods*, vol. 28, no. 2, pp. 85–100, Mar. 1994.
- [169] J. Lerchner, T. Maskow, and G. Wolf, "Chip calorimetry and its use for biochemical and cell biological investigations," *Chem. Eng. Process. Process Intensif.*, vol. 47, no. 6, pp. 991–999, Jun. 2008.
- [170] Goodfellow, "Goodfellow - All the materials you need for Scientific and Industrial Research and Manufacturing," *Goodfellow*. [Online]. Available: <http://www.goodfellow.com/>.
- [171] M. A. Johnson, "PID Control Technology," in *PID Control*, M. A. Johnson and M. H. Moradi, Eds. Springer London, 2005, pp. 1–46.
- [172] I. Wadso and R. N. Goldberg, "Standards in isothermal microcalorimetry (IUPAC Technical Report)," *Pure Appl. Chem.*, vol. 73, no. 10, pp. 1625–1639, 2001.
- [173] D. Peeters and P. Huyskens, "Endothermicity or exothermicity of water/alcohol mixtures," *J. Mol. Struct.*, vol. 300, pp. 539–550, Dec. 1993.
- [174] R. Li, C. D'Agostino, J. McGregor, M. D. Mantle, J. A. Zeitler, and L. F. Gladden, "Mesoscopic Structuring and Dynamics of Alcohol/Water Solutions Probed by Terahertz Time-Domain Spectroscopy and Pulsed Field Gradient Nuclear Magnetic Resonance," *J. Phys. Chem. B*, vol. 118, no. 34, pp. 10156–10166, Aug. 2014.
- [175] M. I. Davis and E. S. Ham, "Analysis and interpretation of excess molar properties of amphiphile + water systems: Part 2. Comparisons of the propanol isomers in their aqueous mixtures," *Thermochim. Acta*, vol. 190, no. 2, pp. 251–258, Nov. 1991.
- [176] M. I. Davis, J. B. Rubio, and G. Douh ret, "Excess molar enthalpies of 2-propanol + water at 25°C," *Thermochim. Acta*, vol. 259, no. 2, pp. 177–185, Aug. 1995.
- [177] S. B. Bankar, M. V. Bule, R. S. Singhal, and L. Ananthanarayan, "Glucose oxidase — An overview," *Biotechnol. Adv.*, vol. 27, no. 4, pp. 489–501, Jul. 2009.
- [178] M. F. Chaplin and C. Bucke, *Enzyme Technology*. Cambridge: CUP Archive, 1990.
- [179] A. Crueger and W. Crueger, "Glucose Transforming Enzymes," in *Microbial Enzymes and Biotechnology*, Second., W. M. Fogarty and C. T. Kelly, Eds. Essex: Elsevier Science Publishers, 1990, pp. 177–226.

- [180] S. Witt, G. Wohlfahrt, D. Schomburg, H. J. Hecht, and H. M. Kalisz, "Conserved arginine-516 of *Penicillium amagasakiense* glucose oxidase is essential for the efficient binding of beta-D-glucose.," *Biochem. J.*, vol. 347, no. Pt 2, pp. 553–559, Apr. 2000.
- [181] D. Kondepudi and I. Prigogine, "Thermodynamics of Solutions," in *Modern Thermodynamics*, John Wiley & Sons, Ltd, 2014, pp. 207–229.
- [182] K. A. Johnson and R. S. Goody, "The Original Michaelis Constant: Translation of the 1913 Michaelis–Menten Paper," *Biochemistry (Mosc.)*, vol. 50, no. 39, pp. 8264–8269, Oct. 2011.
- [183] L. Michaelis and M. L. Menten, "Die Kinetik der Invertinwirkung," *Biochem. Z.*, vol. 49, pp. 333–369, 1913.
- [184] R. Hüttl, K. Bohmhammel, K. Pritzkat, and G. Wolf, "Problems associated with using thermal measurement principles in enzymatic reactions," *Thermochim. Acta*, vol. 229, pp. 205–213, Dec. 1993.
- [185] R. Wilson and A. P. F. Turner, "Glucose oxidase: an ideal enzyme," *Biosens. Bioelectron.*, vol. 7, no. 3, pp. 165–185, 1992.
- [186] B. Danielsson, K. Gadd, B. Mattiasson, and K. Mosbach, "Enzyme thermistor determination of glucose in serum using immobilized glucose oxidase," *Clin. Chim. Acta*, vol. 81, no. 2, pp. 163–175, Dec. 1977.
- [187] P. Han and D. M. Bartels, "Temperature Dependence of Oxygen Diffusion in H₂O and D₂O," *J. Phys. Chem.*, vol. 100, no. 13, pp. 5597–5602, Jan. 1996.
- [188] J. G. Robertson, "Mechanistic Basis of Enzyme-Targeted Drugs," *Biochemistry (Mosc.)*, vol. 44, no. 15, pp. 5561–5571, Apr. 2005.
- [189] A. Amine, H. Mohammadi, I. Bourais, and G. Palleschi, "Enzyme inhibition-based biosensors for food safety and environmental monitoring," *Biosens. Bioelectron.*, vol. 21, no. 8, pp. 1405–1423, Feb. 2006.
- [190] D. L. Riddle, T. Blumenthal, B. J. Meyer, and J. R. Priess, Eds., *C. elegans II*, 2nd ed. Cold Spring Harbor (NY): Cold Spring Harbor Laboratory Press, 1997.
- [191] A. K. Corsi, B. Wightman, and Chalfie, "A Transparent window into biology: A primer on *Caenorhabditis elegans*," *WormBook C Elegans Res. Community*, pp. 1–31, Jun. 2015.
- [192] G. A. Silverman, C. J. Luke, S. R. Bhatia, O. S. Long, A. C. Vetica, D. H. Perlmutter, and S. C. Pak, "Modeling Molecular and Cellular Aspects of Human Disease using the Nematode *Caenorhabditis elegans*," *Pediatr. Res.*, vol. 65, no. 1, pp. 10–18, Jan. 2009.
- [193] T. Stiernagle, "Maintenance of *C. elegans*," *WormBook C Elegans Res. Community*, Feb. 2006.

-
- [194] B. P. Braeckman, K. Houthoofd, and J. R. Vanfleteren, "Intermediary metabolism," *Worm-Book C Elegans Res. Community*, pp. 1–24, Feb. 2009.
- [195] A. Schlotterer, G. Kukudov, F. Bozorgmehr, H. Hutter, X. Du, D. Oikonomou, Y. Ibrahim, F. Pfisterer, N. Rabbani, P. Thornalley, A. Sayed, T. Fleming, P. Humpert, V. Schwenger, M. Zeier, A. Hamann, D. Stern, M. Brownlee, A. Bierhaus, P. Nawroth, and M. Morcos, "C. elegans as Model for the Study of High Glucose– Mediated Life Span Reduction," *Diabetes*, vol. 58, no. 11, pp. 2450–2456, Nov. 2009.
- [196] R. Padovani, T. Lehnert, P. Cettour-Rose, R. Doenlen, J. Auwerx, and M. a. M. Gijs, "Miniaturized implantable sensors for in vivo localized temperature measurements in mice during cold exposure," *Biomed. Microdevices*, vol. 18, no. 1, pp. 1–9, Dec. 2015.
- [197] J. S. Steinhart and S. R. Hart, "Calibration curves for thermistors," *Deep Sea Res. Oceanogr. Abstr.*, vol. 15, no. 4, pp. 497–503, Aug. 1968.
- [198] M. D. Alexander and K. T. B. MacQuarrie, "Toward a Standard Thermistor Calibration Method: Data Correction Spreadsheets," *Ground Water Monit. Remediat.*, vol. 25, no. 4, pp. 75–81, 2005.
- [199] F. A. Duck, *Physical Properties of Tissues. A Comprehensive Reference Book*. London: Academic Press, 1990.
- [200] L. E. Mount, "Metabolic rate and thermal insulation in albino and hairless mice," *J. Physiol.*, vol. 217, no. 2, pp. 315–326, Sep. 1971.
- [201] M. Markaki and N. Tavernarakis, "Modeling human diseases in *Caenorhabditis elegans*," *Bio-technol. J.*, vol. 5, no. 12, pp. 1261–1276, Dec. 2010.

Curriculum Vitae

PERSONAL INFORMATION



Rima PADOVANI

Route du Chasseur 40
1008 Prilly, Switzerland
padovani.rima@gmail.com
+41 (0)78 708 53 81

Date of Birth: 17.10.1984
Nationality: Italian and Algerian
Holder of B Permit

EDUCATION

- 2011 - present **Ph.D., Microsystems and Microelectronics**
École Polytechnique Fédérale de Lausanne (EPFL), Lausanne, Switzerland
- 2006 - 2009 **M.Sc., Biomedical Engineering, 110/110 cum laude**
Polytechnic of Turin, Turin, Italy
- 2003 - 2006 **B.Sc., Biomedical Engineering, 110/110 cum laude**
Polytechnic of Turin, Turin, Italy

WORK EXPERIENCE

- 2011 - present **Research and teaching assistant, Microsystems and Microelectronics**
École polytechnique fédérale de Lausanne (EPFL), Lausanne, Switzerland
- Activities:** Design, simulation, development of thermal microsystems. Development of experimental setup and of software interfaces for automatic data acquisition. Design of biological protocols for miniaturized devices. Cleanroom microfabrication. Scientific writing. Teaching in EPFL Cleanroom for undergraduate students.
- 2009 - 2011 **Research assistant, Microfluidic Platforms**
Biomedical Diagnostic Institute, Dublin, Ireland
- Activities:** Design and development of microfluidic devices. Microfabrication/CNC Micromachining. Integration with sensing elements. Cell culturing.

SKILLS

- Technical** Microfabrication/Polymer CNC Micromachining. Surface characterization. Standard electronic laboratory instrumentation. Brightfield and fluorescence microscopy. Cell culture.
- Computational** Solidworks. AutoCAD. Matlab. Labview. C programming. Assembler programming. Comsol Multiphysics. CoventorWare. Origin. ImageJ. Adobe Illustrator CS6 and Photoshop CS6.
- Language** English (Fluent). French (Fluent). Italian (Mother Tongue). Arabic (Basic).

AWARDS

2008 Alta Scuola Politecnica Diploma (Polytechnic of Milan and Polytechnic of Turin)

PUBLICATIONS

Journal *Nanocalorimetric platform for accurate thermochemical studies in microliter volumes (2015)*

R. Padovani, T. Lehnert, R. Trouillon, and M. A. M. Gijs

RSC Advances, vol. 5, no. 118, pp. 97133–97142

DOI: 10.1039/C5RA22248F

Miniaturized implantable sensors for in vivo localized temperature measurements in mice during cold exposure (2016)

R. Padovani, T. Lehnert, P. Cettour-Rose, R. Doenlen, J. Auwerx, M. A. M. Gijs.

Biomedical Microdevices, vol. 18, no. 1, pp. 1–9

DOI: 10.1007/s10544-015-0028-9

Conference *A microcalorimetric platform for studying the heat produced by chemical reactions in microlitre volumes (2015)*

R. Padovani, T. Lehnert, and M. A. M. Gijs

Proc. of 19th International Conference on Miniaturized Systems for Chemistry and Life Sciences (microTAS 2015) Gyeongju, Korea.

